Reconstruction, Characterization, and Micromechanics of Polycrystalline Nickel-Based Superalloy at Mesoscopic Scale

Swansea University
Prifysgol Abertawe

Bingbing Chen

Faculty of Science and Engineering
Swansea University

Submitted to Swansea University in fulfilment of the requirements for the Degree of
Doctor of Philosophy

June 2023

To my beloved family, wife and all friends. . .

Declarations

This work has not previously been accepted in substance for any degree and is not being concurrently submitted in candidature for any degree.

Signed BINGBING CHEN ..... (candidate)

Date 15/06/2023 .....

This thesis is the result of my own investigations, except where otherwise stated. Other sources are acknowledged by footnotes giving explicit references. A bibliography is appended.

Signed BINGBING CHEN ..... (candidate)

Date 15/06/2023 .....

I hereby give consent for my thesis, if accepted, to be available for photocopying and for inter-library loans, and for the title and summary to be made available to outside organizations.

Signed BINGBING CHEN ..... (candidate)

Date 15/06/2023 .....

The university's ethical procedures have been followed and, where appropriate, the ethical approval has been granted.

Signed BINGBING CHEN ..... (candidate)

Date 15/06/2023 .....

Acknowledgements

I sincerely appreciate my supervisor, Prof. Chenfeng Li, for his systematic guidance, support, and inspiration at all stages of my PhD. He is my guide both in life and research. He has changed my destiny.

Abstract

In recent years, extensive correlation studies have been conducted between microstructure characterizations and macroscopic properties and performance in polycrystalline materials. These studies have revealed that the mechanical properties, including stress-strain curve, stress and strain response (peak strength, effective stress, crack damage stress, ultimate tensile strength, yield stress, Von Mises stress, Tresca stress, effective strain, cumulative effective plastic strain, etc.), and elastic and plastic anisotropy, are closely connected to and significantly affected by morphological (grain size, grain size heterogeneity, grain shape, etc.) and crystallographic (grain orientation, etc.) features. Meanwhile, the influence of microstructure characterization on the mechanical performance of polycrystals has also been examined by researchers. It has been well established that ductile failure initiation and growth in polycrystals are extremely sensitive to crystallographic (grain orientation, etc.) and grain boundary (coincidence site lattice (CSL), misorientation, tilt and twist angle, etc.) conditions.

However, in current practice, studies of the microstructure effect on ductile failure have certain limitations. For example, the research methodologies are mainly limited to representative volume elements (RVEs)-based experimental observations or crystal plasticity numerical simulations. In practice, the microstructure characterizations exhibit some degree of randomness during deformation processing, and microstructure randomness reveals polycrystalline materials' probabilistic properties and performance. Consequently, the vast size and number of the microstructure RVE necessary to build the process–structure–properties–performance (PSPP) linkages is computationally prohibitive and challenging to investigate. Meanwhile, the simplified polycrystalline microstructures, such as single crystals, bicrystals, Voronoi and ellipsoid polycrystals, fail to capture all the statistical microstructure characterizations of the heterogeneous grains. Furthermore, to the author's knowledge, these features that influence ductile failure are still contentious, and the association between microstructure characterizations and ductile failure in polycrystals is not yet wholly researched. In addition, it is difficult to quantify the impact of microstructure on ductile failure in polycrystalline materials without a straightforward and efficient method. In the end, the datasets between microstructural characteristics and ductile failure are unlikely to be built without sufficient data.

This research comprehensively investigated the recent progress in microstructure reconstruction and characterization (MCR) of polycrystalline materials. After that, the patch-based texture synthesis reconstruction algorithm was proposed to perfectly capture the statistical microstructure characterizations of the heterogeneous grains. The crystal plasticity finite element (CPFEM) method that can reflect the stress-strain response in nickel-based superalloy was established to reveal the ductile failure mechanisms. Then, the established CPFEM model combined with explicit characterization algorithms was used to perform quantitative analysis on Inconel 718 superalloy to fully understand the macroscopic properties and performance responses (ultimate tensile strength (UTS), Von Mises stress, ductile failure initialization and propagation) in terms of morphological, crystallographic, and boundary characteristics. Finally, the patch-based texture synthesis coupled with explicit characterization algorithms was developed to determine the ductile failure sets using the microstructural parameters, such

as grain orientation and boundary characters. Research conclusions can be excellent guidance for microstructure sensitive design (MSD), materials knowledge system (MKS), uncertainty quantification (UQ), and surrogate crystal plasticity modeling (SCPM) in polycrystalline materials.

Table of contents

List of figures **xiii**

List of tables **xix**

List of algorithms **xix**

List of symbols **xxi**

1 Introduction **1**

2 Literature review: experimental reconstruction and microstructure characterization in polycrystalline materials **9**

2.1 Introduction 9
2.2 Experimental reconstruction 11
2.2.1 Destructive reconstruction 12
2.2.2 Non-destructive reconstruction 15
2.3 Microstructure characterization 18
2.3.1 First-order statistics 20
2.3.2 Second and higher order statistics 37
2.3.3 Reduced-order representations 38

3 Literature review: physical and geometric reconstruction in polycrystalline materials **47**

3.1 Introduction 47
3.2 Physical reconstruction 48
3.2.1 Cellular automata 50
3.2.2 Monte Carlo approaches 52
3.2.3 Vertex methods 53
3.2.4 Phase field models 56

3.2.5 Level set models . . . 58
3.3 Geometric reconstruction . . . 60
3.3.1 Shape-based reconstruction . . . 60
3.3.2 Ellipsoid packing . . . 64
3.3.3 Texture synthesis . . . 69
3.3.4 Others . . . 71

4 Novel strategies for texture synthesis models applied to microstructure representation of polycrystalline materials 75
4.1 Introduction . . . 75
4.2 Orientation coloring . . . 76
4.2.1 Background . . . 76
4.2.2 Perfectly colored orientations . . . 77
4.3 Texture synthesis . . . 82
4.3.1 Patch-based texture synthesis . . . 82
4.3.2 Mapping orientations from the IPF coloring . . . 90
4.4 Applications . . . 95
4.4.1 Microstructure characterizations . . . 95
4.4.2 Comparison studies . . . 103
4.5 Conclusions . . . 104

5 Explicit characterization algorithms for texture synthesis models applied to microstructure representation of polycrystalline materials. 105
5.1 Introduction . . . 105
5.2 Algorithm A: Grain nucleation and growth . . . 105
5.3 Algorithm B: Constrained grain orientation generation . . . 107
5.4 Algorithm C: Constrained grain boundary generation . . . 117
5.5 Conclusions . . . 118

6 Micromechanical simulation in nickel-based superalloys 119
6.1 Introduction . . . 119
6.2 Micromechanical simulation of the single crystal model . . . 120
6.2.1 Micropillar compression test . . . 120
6.2.2 Single crystal plasticity constitutive model . . . 121
6.2.3 Finite element implementation of the single crystal plasticity constitutive model . . . 124
6.3 Calibration of the single crystal plasticity constitutive model parameters . . . 129

6.4 Verification of the single crystal plasticity constitutive model 131
6.5 Micromechanical simulation of the RVE model 131
6.6 Conclusions 133

7 Processing-structure-properties-performance linkages in nickel-based superalloys 135
7.1 Introduction 135
7.2 Micromechanical simulation of the ductile failure 136
7.2.1 Ductile failure mechanism 136
7.2.2 Finite element implementation of the ductile failure 137
7.3 Correlation study between the microstructure characterizations and the ductile failure 139
7.3.1 Grain size 139
7.3.2 Grain orientation 140
7.3.3 Grain boundary 140
7.4 Ductile failure sets of statistical microstructure characterizations 147
7.5 Conclusions 148

8 Conclusions 151
8.1 Conclusions 151
8.2 Perspectives 153

References 155

List of figures

1.1 Schematic illustration of multiple scales for Ni-based superalloys (used extensively in gas turbine engines). Adapted from [195, 126, 45, 5], Copyright (2015,2016,2021,2021), with permission from Elsevier. 2
1.2 Mean-field versus full-field approach. Reprinted from [96], with permission from Springer. 2
1.3 Schematic illustration of image-based computational materials engineering. 3
1.4 Schematic illustration of solving the inverse problem where the performance requirements are examined first, and then the creation of new materials is backed out at the end. 4
1.5 Overview of the characterization and reconstruction linkage in optimal performance design. 7

2.1 Schematic of the grid and vertex-edge-face discretization in the digital reconstruction of polycrystalline materials: (a) grid discretization; (b) vertex-edge-face discretization; (c1-c4) flowchart of vertex-edge-face discretization for a single grain. (d1-d4) flowchart of vertex-edge-face discretization for a polycrystalline internal structure. 10
2.2 Imaging techniques in polycrystalline materials: the destructive and non-destructive classification and their approximate spatial resolution. 12
2.3 The flow diagram of destructive reconstruction. Adapted from [124], Copyright (2008), with permission from Elsevier. 13
2.4 The flow diagram of non-destructive reconstruction 15
2.5 Schematic illustration of the local state in polycrystalline materials. 22
2.6 Schematic illustration of the three-dimensional orientation space: (a) the Euler angles form, and (b) the axis-angle form. Generated from the open-source software MTEX [19]. 23

2.7 Schematic illustration of the fundamental zone for the orientation and misorientation axis-angle spaces of point group $O(432)$. Generated from the open-source software MTEX [19]. 25
2.8 Schematic illustration of low-angle and high-angle grain boundaries. Generated from the open-source software MTEX [19]. 26
2.9 Schematic illustration of the CSL boundaries. Generated from the open-source software MTEX [19]. 27
2.10 Schematic illustration of the grain boundary plane distribution. Generated from the open-source software DREAM.3D [137]. 28
2.11 Illustrations of the balance of interfacial energies at triple junctions. Reprinted from [368], with permission from Springer. 29
2.12 Schematic illustration of the triple lines and quadruple points. Adapted from [435], Copyright (2014), with permission from Elsevier. 35
2.13 Schematic illustration of the orientation distribution function. Generated from the open-source software MTEX [19]. 36

3.1 Overview of digital reconstruction methods in mesoscopic polycrystalline materials for building PSPP linkages. 48
3.2 Illustration of the 3D cellular automata with square cells. Two common types of neighborhood for a cell are illustrated: von Neumann neighborhood and Moore neighborhood 51
3.3 Illustration of a 2D grain structure mapped onto a square lattice. All lattice sites belonging to a common grain share the same lattice index S_i. Grain boundaries are drawn with thicker lines. 52
3.4 Vertex model representation of polycrystalline microstructure. a triple junction between three boundaries have the interface energies $\gamma_{1,2,3}$ and the separation angles $\varphi_{1,2,3}$. The nodes are indicated by circles and the local velocity v of a node is shown. 54
3.5 Schematic representation of a grain microstructure using the orientation parameters η_k. Grain boundaries are indicated with solid lines. 56
3.6 Schematic representation of a grain microstructure using the level set function $\phi_i(\boldsymbol{x},t)$. Grain boundaries are indicated with white lines. 58
3.7 Schematic presentation of the reconstructed polycrystalline microstructures with simplistic regular morphologies: (a) Cubes, (b) Truncated octahedrons, and (c) Rhombic dodecahedrons; 61

3.8 Schematic presentation of the grid and vertex-edge-face-volume discretization for Voronoi polyhedral. Generated from the open-source software Neper [351]. 62
3.9 Schematic presentation of the multi-meshing and re-meshing of 3D large-scale Voronoi polyhedrons. Generated from the open-source software Neper [351]. 63
3.10 Ellipsoid generation: (a) EBSD scan, (b) ellipse fitting, (c) ellipsoid projection. 65
3.11 Schematic presentation of the reconstructed polycrystalline microstructures through ellipsoid packing. Generated from the open-source software DREAM.3D [137]. 65
3.12 Schematic presentation of the reconstructed polycrystalline microstructures with elongated grains. Generated from the open-source software DREAM.3D [137]. 66
3.13 Schematic presentation of the reconstructed polycrystalline microstructures from 3D experimental data. Generated from the open-source software DREAM.3D [137]. 67
3.14 Schematic presentation of the reconstructed 3D polycrystalline microstructures from experimental 2D polycrystalline microstructures through texture synthesis. Adapted from [176], Copyright (2020), with permission from Elsevier. 70
3.15 Schematic presentation of the reconstructed 3D polycrystalline microstructures through phase recovery (a), simulated annealing (b), principal component analysis (c), nonlinear dimensionality reduction (d), and transfer learning (e). Adapted from [117, 126, 413, 242, 50], Copyright (2008,2016,2004,2010,2020,), with permission from Elsevier. 72

4.1 Flowchart of the standard IPF (e.g., the normal direction) coloring for the $m\bar{3}m$ symmetry group. 80
4.2 Illustrations of the IPF color key considering the point groups. 83
4.3 Illustrations of the IPF color key considering the point groups. 84
4.4 Illustrations of the IPF color key considering the point groups. 85
4.5 Illustrations of the IPF color key considering the point groups. 86
4.6 Illustration of the patch-based texture synthesis (PTS) algorithm with the raster-scan order. 87

4.7 Illustration of the imaging quilting (IQ) algorithm: (a) patch-based texture synthesis without imaging quitting; (b) patch-based texture synthesis with imaging quitting. 89
4.8 Precomputed curves: (a) the $H-\rho$, (b) the $S-L$, and (c) the $L-\theta$. 92
4.9 Flowchart of converting the RGB triplet into the symmetrically equivalent crystal direction $\boldsymbol{h}$. 93
4.10 Illustration of the proposed azimuthal angle φ defined by the $\boldsymbol{RD}$ and $\boldsymbol{ND}$ in the crystal coordinate system. 94
4.11 Illustration of the flowchart for calculating the $f(\varphi_k|(\rho_i,\ \theta_j))$, using the $m\bar{3}m$ symmetry group as an example. 94
4.12 Illustrations of converting the RGB triplets into the orientation dataset in the synthesized images $\boldsymbol{Y}$. 96
4.13 Illustration of the orientation dataset in the original image (a) and synthesized domains (b). 97
4.14 The microstructure characterizations of the original orientation dataset for an FCC nickel-based Inconel 718 superalloy. 98
4.15 The flowchart of grain size distributions for the synthesized orientation dataset. 99
4.16 The merge-and-split rules in grain size characterizations: (a) the grain merge algorithm for error elimination, (b) the grain split algorithm for bias correction. 101
4.17 Illustration of the grain orientation distributions for the synthesized grain orientation dataset. 102
4.18 Comparisons of microstructural reconstruction and characterization using Voronoi tesselation, ellipse packing, and improved PTS schemes. 103

5.1 Flowchart of the explicit characterization algorithms procedure. Each algorithm's governing principles, objectives, and required inputs are enumerated. 106
5.2 Flowchart of the grain nucleation and growth algorithm. 108
5.3 The grain size distributions at different evolutionary time steps. 109
5.4 Flowchart of the constrained grain orientation generation algorithm. 110
5.5 Illustrations of the grain orientation distributions under the same morphological conditions in each microstructure evolution step: (a1-a3) the morphological conditions, (b1-b3) the grain orientation distributions. 111
5.5 Illustrations of the grain orientation distributions under the same morphological conditions in each microstructure evolution step: (a4-a6) the morphological conditions, (b4-b6) the grain orientation distributions. 112
5.6 Flowchart of the constrained grain boundary generation algorithm. 114

5.7 Illustrations of the grain boundary conditions under the same morphological and crystallographic information in each microstructure evolution step: (a1-a3) the morphological conditions; (b1-b3) the grain orientation distributions; (c1-c3) the grain boundary distributions. 115
5.7 Illustrations of the grain boundary conditions under the same morphological and crystallographic information in each microstructure evolution step: (a1-a3) the morphological conditions; (b1-b3) the grain orientation distributions; (c1-c3) the grain boundary distributions. 116

6.1 Illustration of the single crystal micropillar in the unconfined compression testing. 120
6.2 The original and calibrated stress-strain curves in the unconfined micropillar compression testing. 121
6.3 The CPFEM model for the single crystal micropillar structure. 124
6.4 Calibration of the single crystal plasticity constitutive model parameters for the nickel-based Inconel 718 superalloy. 130
6.4 Stress-strain data from measurements and simulations of unconfined compression tests from single crystal micropillars. 132
6.5 The reconstructed polycrystalline nickel-based Inconel 718 superalloy with different RVE sizes. 133
6.6 The simulated stress-strain curves with different RVE sizes under the uniaxial tension condition. 134
6.7 The compared stress-strain curves between the RVE polycrystalline simulation and the uniaxial tension experiment. 134

7.1 Illustration of damage evolution with $d = 0.1$. 137
7.2 The CPFEM model of the ductile failure simulation for the 2D polycrystalline RVE of the Inconel 718 superalloy. 138
7.3 Prediction of damage initiation and propagation controlled by accumulated equivalent plastic strain. 139
7.4 Flowchart of the microstructure characterization influences on ductile failure. 140
7.5 Illustrations of explicit characterization algorithms with increased grain sizes. 141
7.6 Illustrations of the grain size distributions with increased grain sizes. 141
7.7 Illustrations of the Von Mises stress-time step curves with increased grain sizes. 142
7.8 Illustrations of the ductile failure localizations with increased grain sizes. . 142
7.9 Illustrations of explicit characterization algorithms with varying grain orientations. 143

7.10 Illustrations of the Von Mises stress-time step curves with varying grain orientations. 143
7.11 Illustrations of the ductile failure localizations with varying grain orientations. 144
7.12 Illustrations of the explicit characterization algorithms with varying grain boundary conditions. 145
7.13 Illustrations of the grain size distributions with varying grain boundary conditions. 146
7.14 Illustrations of the Von Mises stress-time step curves with varying grain boundary conditions. 146
7.15 Illustrations of the ductile failure localizations with varying boundary conditions. 147
7.16 Illustration of expanding or shrinking the grain size distribution. 148
7.17 Flowchart of ductile failure properties subset related to grain orientation. . . 149
7.18 Flowchart of ductile failure performance subset related to grain boundary. . 149

List of tables

1.1 Examples of microstructural effects on properties and performance in polycrystalline materials 3

2.1 Illustrations of volume fraction in polycrystalline microstructure 23
2.2 Characterization with polycrystalline microstructure 24
2.3 Illustrations of grain topology in polycrystalline microstructure 34
2.4 Reduced-order algorithms for characterization representation in polycrystalline materials 46

4.1 Summary of parameterizations of orientation 77
4.2 Point groups are distinguished by lattice type, standard or extended color distribution. k specifies the relative order of the various groups. Neither the standard nor the extended color distribution is appropriate for $\bar{3}, \bar{4}$ and $\bar{1}$. 81

6.1 Material properties of nickel-based Inconel 718 superalloy used in simulations . . 130

List of Algorithms

1 An algorithm for patch-based texture synthesis 82
2 An algorithm for image quilting 89
3 An algorithm for merging grains 100
4 An algorithm for splitting grains 103
5 An algorithm for constrained grain orientation generation 109
6 An algorithm for constrained grain boundary generation 113

List of symbols

3DXRD three-dimensional X-ray diffraction microscopy

AM Additive manufacturing

ATP Atom probe tomography

CDBN Convolutional deep belief network

CGBG Constrained grain boundary generation

CGOG Constrained grain orientation generation

CME Computational materials engineering

CNN Convolutional neural network

CP Crystal plasticity

CPFEM Crystal plasticity finite element method

CSL Coincidence site lattice

DAXM Differential-aperture X-ray microscopy

DCT Diffraction contrast tomography

DFT Discrete Fourier transform

DL Deep learning

DR Digital representation

EBSD Electron backscattering diffraction

ESR Equivalent sphere radius

FCC Face-centered cubic

FFT Fast Fourier transform

FIB Focused ion beam

FS Fundamental sector

GBCD Grain boundary character distributions

GBED Grain boundary energy distribution

GNBs Geometrically necessary boundaries

GNDs Geometrically-necessary dislocations

GNN Graph neural network

GSBs Grain size bins

GSD Grain size distribution

GSHF Generalized spherical harmonic function

GVD Grain volume distribution

HAGB high-angle grain boundary

HEDM high-energy X-ray diffraction microscopy

HSL Hue-saturation-lightness

HSV Hue-saturation-value

ICME Integrated computational materials engineering

IDBs Incidental dislocation boundaries

IPF Inverse pole figure

IQ Imaging quilting

IRIAs Induced realistic instantiation algorithms

ISE Ion-induced secondary electron

LAGB Low-angle grain boundary

MC Monte Carlo

MCP Minimum cost path

MCR Microstructure reconstruction and characterization

MKS Materials knowledge system

ML Machine learning

MODF Misorientation distribution function

MPS multiple-point simulations

MRF Markov random field

MSD Microstructure sensitive design

MSE Materials science and engineering

MTF Micro-texture function

ODF Orientation distribution function

OIM Orientation imaging microscopy

OM Optical microscopy

PCA Principal component analysis

PHCM Parametrically homogenized constitutive model

PSP Processing-structure-properties

PTS Patch-based texture synthesis

PSPP Process–structure–properties–performance

RGB Red-green-blue

RVE Representative volume element

SCPM Surrogate crystal plasticity modeling

SEM Scanning electron microscopy

SERVEs Statistically equivalent representative volume elements

SIMS Secondary ion mass spectroscopy

SM Spectral method

SSDs statistically-stored dislocations

SM Synthetic microstructure

TEM Transmission electron microscopy

TS Texture synthesis

UQ Uncertainty quantification

UTS Ultimate tensile strength

VAE Variational autoencoder

Chapter 1

Introduction

Polycrystalline materials consist of aggregates of grains with varying lattice orientations and sizes separated by grain boundaries. The most common materials are polycrystalline, including metals [302, 304, 376], alloys [431, 337, 336], rocks [141, 459] and ceramics [310, 11], etc. Controlled by the processing history, the grains exhibit heterogeneous (Fig. 1.1) and multiscale (Fig. 2.5) characteristics. A notable example is the heat treatment of metals. Grains are deformed and coarsened during the compaction, solidification, rolling, extrusion, and recrystallization process, resulting in random grain distributions in boundary, morphology and crystallography. Grains' physical and geometric reconstruction during the processing undoubtedly changes polycrystalline microstructures' anisotropic behaviour and further governs their macroscopic mechanical response (Table 1.1). To establish a vital link among processing-structure-properties (PSP), materials science and engineering (MSE) have developed into a distinct field of research. Here, the mechanical experiments have been conducted, the significant features of microstructure have been characterized, and the empirical databases between microstructural characteristics and macroscopic mechanical properties have been built to facilitate the selection of material structure and processing for suitable specific engineering requirements [125].

Empirical, trial-and-error methods of analyzing, designing and discovering materials in the MSE are costly and time-consuming. The computational materials engineering (CME), in particular, multiscale modeling of heterogeneous materials in a representative volume element (RVE), is more appealing [276, 28]. As illustrated in Fig. 1.2, two computational homogenization approaches are used in polycrystalline materials: the mean-field and full-field methods [96, 119]. Before the computational implementation in CME, analyzing realistic microstructures is critical for achieving PSP connections. With the development of imaging technology (Fig. 2.2), especially for orientation imaging microscopy (OIM) analysis in polycrystalline materials, the concept of image-based multiscale modeling has

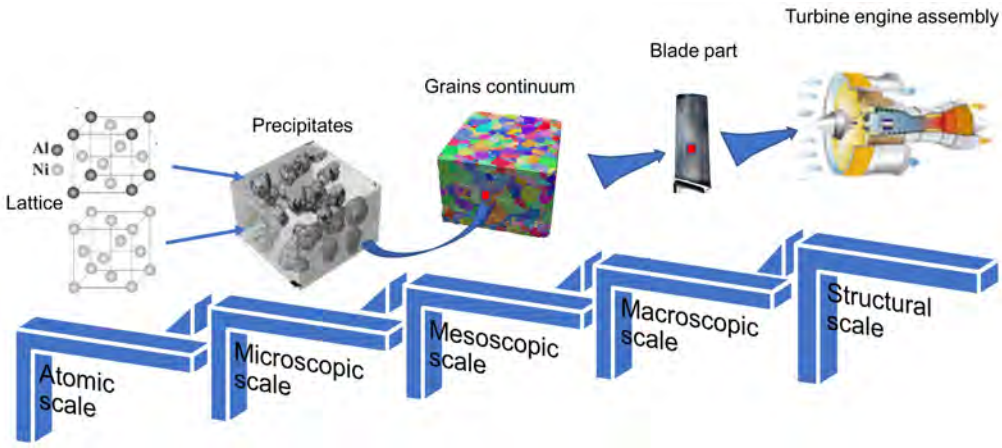

Fig. 1.1 Schematic illustration of multiple scales for Ni-based superalloys (used extensively in gas turbine engines). Adapted from [195, 126, 45, 5], Copyright (2015,2016,2021,2021), with permission from Elsevier.

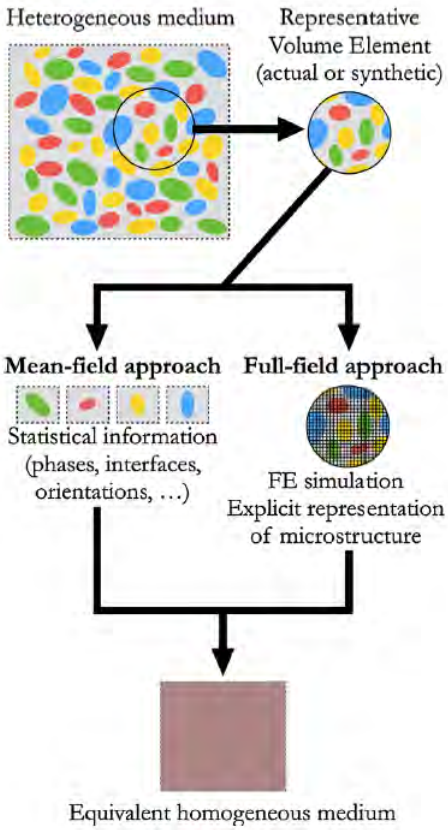

Fig. 1.2 Mean-field versus full-field approach. Reprinted from [96], with permission from Springer.

Table 1.1 Examples of microstructural effects on properties and performance in polycrystalline materials

Microstructure characterizations	Macroscopic properties and performance
Morphology (grain size, grain size heterogeneity, grain shape, etc.)	Fatigue indicator parameters [411, 462]; Ductile failure criterion [62, 80]; Free surface roughening [68]; Stress-strain curve [62, 192, 462, 68, 302, 44, 4]; Strain hardening [302]; Elastic and plastic anisotropy [302, 439, 92]; Yield stress [443, 302, 4, 430, 92, 225]; Ultimate tensile strength [443, 4]; Peak strength [141]; Fatigue crack damage stress [141]; Fatigure crack initiation stress [141]; von Mises Stress [44]; Ductile fracture stress and strain [62, 68]; Tresca stress [439]; Strain deviation [46]; Cumulative effective plastic strain [411]; Elastic modulus [141, 439, 92]; Poisson's ratio [141]
Crystallography (Schmid factor, orientation, etc.)	Fatigue crack initiation and growth [469, 54]; Ductile failure initiation and growth [55, 75]; Ductile failure criterion [73]; Yield stress [7, 144]; Elastic and plastic anisotropy [439, 92]; Stress triaxiality localization [55]; Strain localization [46]; Effective stress and strain [231]
Boundary (coincidence site lattice (CSL), misorientation, tilt and twist angle, etc.)	Fatigue crack initiation and growth [277, 469, 411, 54, 307]; Ductile failure initiation and growth [62, 72]; Strain localization [46, 307];

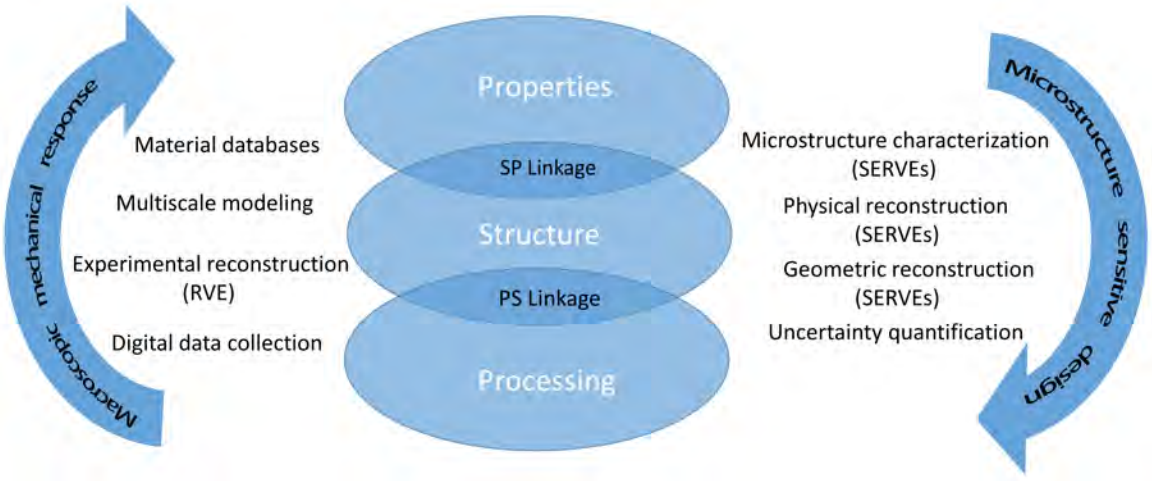

Fig. 1.3 Schematic illustration of image-based computational materials engineering.

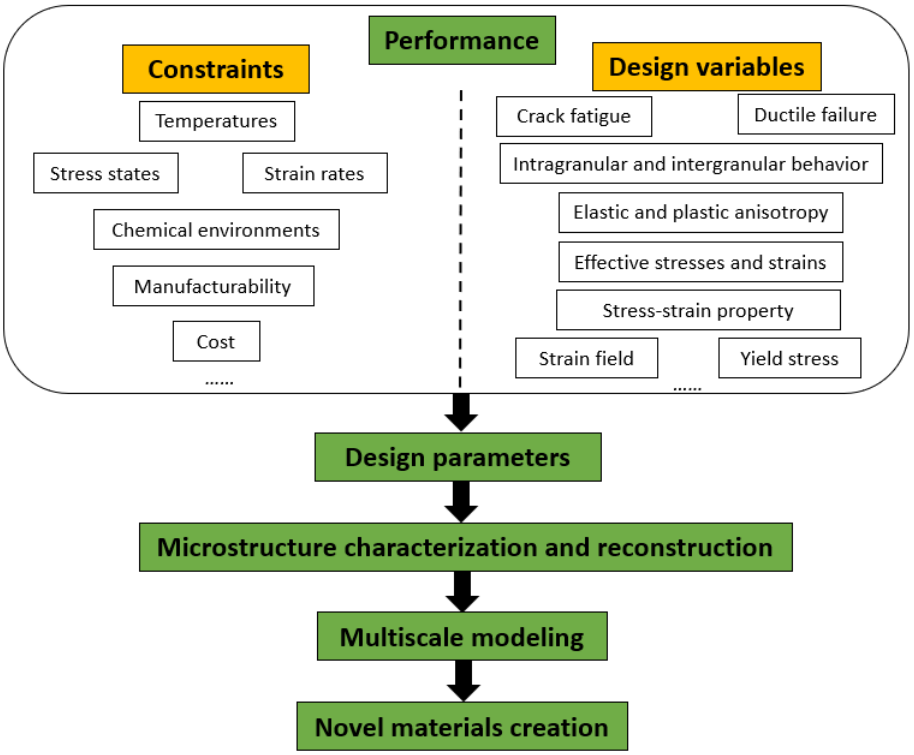

Fig. 1.4 Schematic illustration of solving the inverse problem where the performance requirements are examined first, and then the creation of new materials is backed out at the end.

been established. It generally begins with microstructure reconstruction and characterization (MCR) through experimental data collection and imaging processing. Based on this generated digital data, multiscale modeling is then conducted (Fig. 1.3).

The CME establishes the PSP relationships in a cause-and-effect manner, and their calculations do not include the life-cycle performance. In the emerging field of integrated computational materials engineering (ICME) [159], researchers seek to derive the properties, structure, and processing conditions directly from a performance specification (Fig. 1.4). Thus, the PSP relationships in CME should be updated as the process–structure–properties–performance relationships (PSPP) in ICME. ICME focuses on connecting the multiple length scales (vertical ICME) or bridging the sequential materials processing (horizontal ICME) [159]. In this work, we highlight recent progress in MCR associated with ICME. MCR plays a vital role in achieving the PSPP linkages, especially in the optimal performance design [51, 303]. As illustrated in Fig. 1.5, MCR can be roughly classified into physical and geometric types [28, 215]. The microstructure characterization provides a reliable quantitative analysis of design parameters. In addition, the physical reconstruction establishes the PS linkage based on a physical description of the manufacturing process governing the microstructure for-

mation. Meanwhile, geometric reconstruction generates the individual grains as a realistic virtual microstructure for subsequent properties calculation. As mentioned before, the grains exhibit some degree of randomness during processing regarding microstructure characterizations (Table 2.2). Microstructure randomness reveals polycrystalline materials' probabilistic properties and performance. To perform ICME in this way, one should first reconstruct an ensemble of microstructure samples, often termed statistically equivalent representative volume elements (SERVEs) [316, 116, 276], to capture the randomness, evaluate their properties to build PSPP linkages, and conduct statistical analysis for optimal performance design. Therefore, in this context, MCR refers to the statistical representation of its possible inherent randomness, and reconstruction is the process of generating an ensemble of statistically equivalent microstructure samples. Characterization and reconstruction are complementary. The reconstructed microstructure embodies the prescribed characteristics, which can reconstruct statistically equivalent microstructure. Besides the correlation analysis mentioned before (Table 4), SERVEs-based MCR has also been widely used in properties prediction [222, 293, 430], parametrically homogenized constitutive model (PHCM) [208, 323, 207] and microstructure-sensitive design (MSD) [116, 349, 7, 462, 430, 144] (Fig. 1.5).

After generating MCR in polycrystalline materials, the next step for building PSPP linkages is to specify the relationship between microstructure characterizations and macroscopic properties and performance. Ductile failure as a phenomenon is often observed in polycrystalline materials. In recent years, extensive correlation studies have been conducted between microstructure characterization and macroscopic ductile failure (Table 4). However, in current practice, studies of the microstructure effect on ductile failure have certain limitations. For example, the research methodologies are mainly limited to representative volume elements (RVEs)-based experimental observations or crystal plasticity numerical simulations. In practice, the microstructure characterizations exhibit some degree of randomness during deformation processing, and microstructure randomness reveals polycrystalline materials' probabilistic properties and performance. Consequently, the vast size and number of the microstructure RVE necessary to build the process–structure–properties–performance (PSPP) linkages is computationally prohibitive and challenging to investigate. Meanwhile, the simplified polycrystalline microstructures, such as single crystals [75, 72], bicrystals [72], Voronoi [62, 192, 75], and ellipsoid polycrystals, fail to capture all the statistical microstructure characterizations of the heterogeneous grains. Furthermore, to the author's knowledge, these features that influence ductile failure are still contentious, and the association between microstructure characterizations and ductile failure in polycrystals is not yet wholly researched. In addition, it is difficult to quantify the impact of microstructure on ductile failure in polycrystalline materials without a straightforward and efficient method. In

the end, the datesets for microstructural characteristics and ductile failure are unlikely to be built without sufficient data.

This research comprehensively investigated the recent progress in microstructure reconstruction and characterization (MCR) of polycrystalline materials. After that, the patch-based texture synthesis reconstruction algorithm was proposed to perfectly capture the statistical microstructure characterizations of the heterogeneous grains. The crystal plasticity finite element (CPFEM) method that can reflect the stress-strain response in nickel-based superalloy was established to reveal the ductile failure mechanisms. Then, the established CPFEM model combined with explicit characterization algorithms was used to perform quantitative analysis on Inconel 718 superalloy to fully understand the macroscopic properties and performance responses (ultimate tensile strength (UTS), Von Mises stress, ductile failure initialization and propagation) in terms of morphological, crystallographic, and boundary characteristics. Finally, the patch-based texture synthesis coupled with explicit characterization algorithms was developed to determine the ductile failure sets using the microstructural parameters, such as grain orientation and boundary characters. Research conclusions can be excellent guidance for microstructure sensitive design (MSD), materials knowledge system (MKS), uncertainty quantification (UQ), and surrogate crystal plasticity modeling (SCPM) in polycrystalline materials.

The remainder of the thesis is structured into seven Chapters. Chapter 2 and Chapter 3 aim at comprehensive literature reviews of MCR in polycrystalline materials. Chapter 4 focuses on the SERVEs-based texture synthesis reconstruction. Chapter 5 provides the details of the explicit characterization algorithms. Chapter 6 elaborates on the micromechanical simulation in nickel-based Inconel 718 superalloys. The quantitative analysis between macroscopic properties and performance responses and microscopic characterizations in nickel-based Inconel 718 superalloys is conducted in Chapter 7. This is followed by the ductile failure sets using the most relevant microstructural parameters. A summary is provided in the final Chapter.

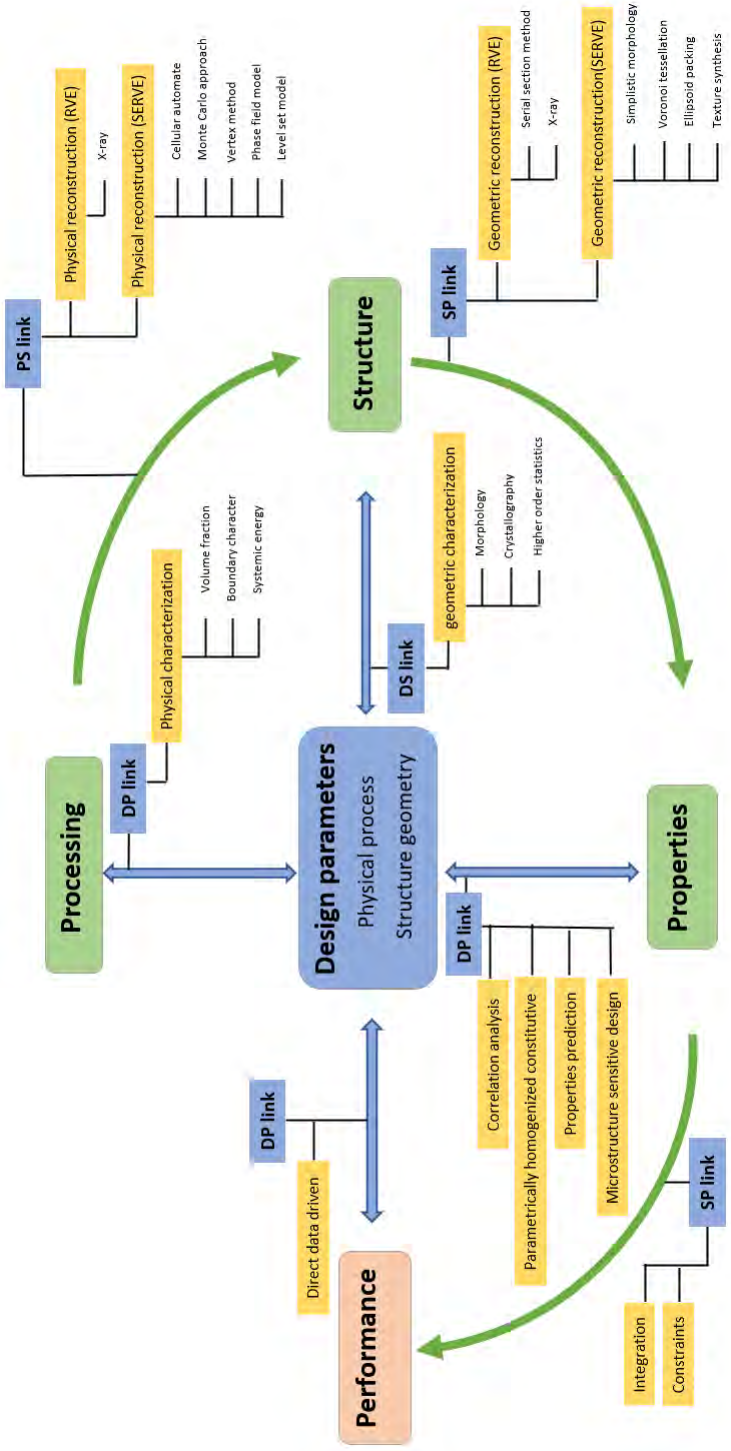

Fig. 1.5 Overview of the characterization and reconstruction linkage in optimal performance design.

Chapter 2

Literature review: experimental reconstruction and microstructure characterization in polycrystalline materials

2.1 Introduction

With the development of imaging technologies, especially for orientation imaging microscopy (OIM) analysis like X-ray diffraction and electron backscattering diffraction in polycrystalline materials, the concept of digital representation has been established. The mesoscopic digital representation (DR) (Fig. 1.1) of polycrystalline materials is of extreme importance in ICME. On the one hand, the mesoscopic DR can be used as a representative volume element (RVE) for multiscale modeling in polycrystalline materials [28, 276]. On the other hand, the DR at the mesoscopic scale gives us information about how the grains are arranged, which helps us understand the detailed morphological, crystallographic, and boundary characterizations [51]. The digital representation based on imaging techniques, also known as experimental reconstruction, can be further divided into destructive and non-destructive types. They are both used in building the PSPP linkages in polycrystalline materials (Fig. 3.1).

After digitally representing polycrystalline materials, the next step is to discretize the whole analyzed space so that the grain morphology can be accurately identified. In general, there are two methods for implementing discretization: (a) grid discretization and (b) vertex-edge-face discretization [372, 125] (Fig. 2.1). The grid-based method uses regular shape units to discretize the entire domain. On the other hand, the vertex-edge-volume method

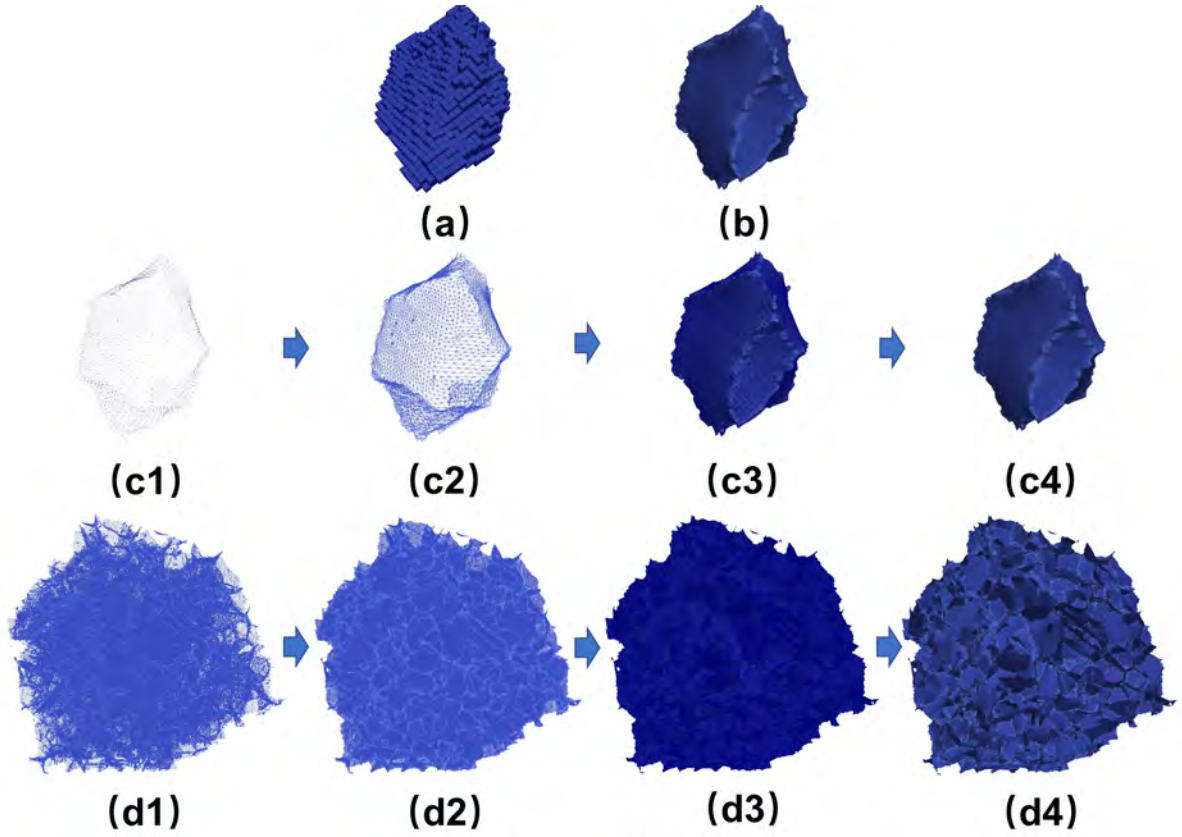

Fig. 2.1 Schematic of the grid and vertex-edge-face discretization in the digital reconstruction of polycrystalline materials: (a) grid discretization; (b) vertex-edge-face discretization; (c1-c4) flowchart of vertex-edge-face discretization for a single grain. (d1-d4) flowchart of vertex-edge-face discretization for a polycrystalline internal structure.

starts from the discretized vertices to provide the coordinate points for generating grain edges. After that, the grain faces originating from the grain edges construct the grain volumes in the space. The grid-based method is independent of the grain shapes. It is easy to perform and widely used in data collection for experimental reconstruction. Nevertheless, grain morphologies represented by grain discretization are restricted to basic domain geometries and frequently influenced by grid anisotropy. In contrast, the vertex-edge-face discretization is highly dependent on the grain shape. It can represent the most significant degree of grain morphologies, like the grain topology and boundary, and is widely used in the interface representation in polycrystalline materials.

This Chapter provides an overview of the two ways of experimental reconstruction: destructive and non-destructive. Specific attention will be focused on each methodology's steps, innovations, strengths and weaknesses. Besides, a detailed illustration of the two categories of characterization: first-order and higher-order description, is also presented.

Similarly, the application and innovations of microstructure characterization will be examined in detail.

2.2 Experimental reconstruction

There are many imaging techniques capable of providing information in the polycrystalline microstructure. Generally speaking, these techniques could fall into three categories:

- Plan-section microscopy techniques: such as optical microscopy (OM) [230], scanning electron microscopy (SEM) [262, 280] and their derivatives (ion-induced secondary electron (ISE)) [320], secondary ion mass spectroscopy (SIMS) [99], etc.).
- Tomographic techniques: using X-rays [169, 249, 244], atom probe tomography (ATP) [194], electron tomography in transmission electron microscopy (TEM) [278, 285], etc.
- Orientation imaging techniques: involving X-ray and neutron diffraction [20], electron backscattering diffraction (EBSD) [392], etc.

The plan-section microscopy and tomography can perceive the variance in atomic number and concentration, so it has an advantage in detecting the morphological features in the polycrystalline microstructure, e.g., grain boundaries, multiple phases, twins, precipitates, inclusions and voids. The orientation imaging techniques could measure the lattice orientation information via Bragg diffraction, so it has an advantage in segmenting the crystallographic features over limited scales. There are mainly two techniques used in the experimental reconstruction: destructive and non-destructive. The destructive reconstruction, also known as serial sectioning, acquires data through the serial removal of material sections. The non-destructive reconstruction obtains data principally via a suite of transmission images from various projection angles. The destructive techniques characterized by commonly founded imaging instruments are more prevalent and accessible in experimental reconstruction. However, the practice uses up the specimen and could be time-consuming. Moreover, the reconstruction accuracy is unstable and highly dependent on the slice thickness. The non-destructive schemes keep samples intact after the experiment but involve high-intensity sources. Fig. 2.2 shows the classification of imaging techniques based on their spatial resolution and capability to be non-destructive.

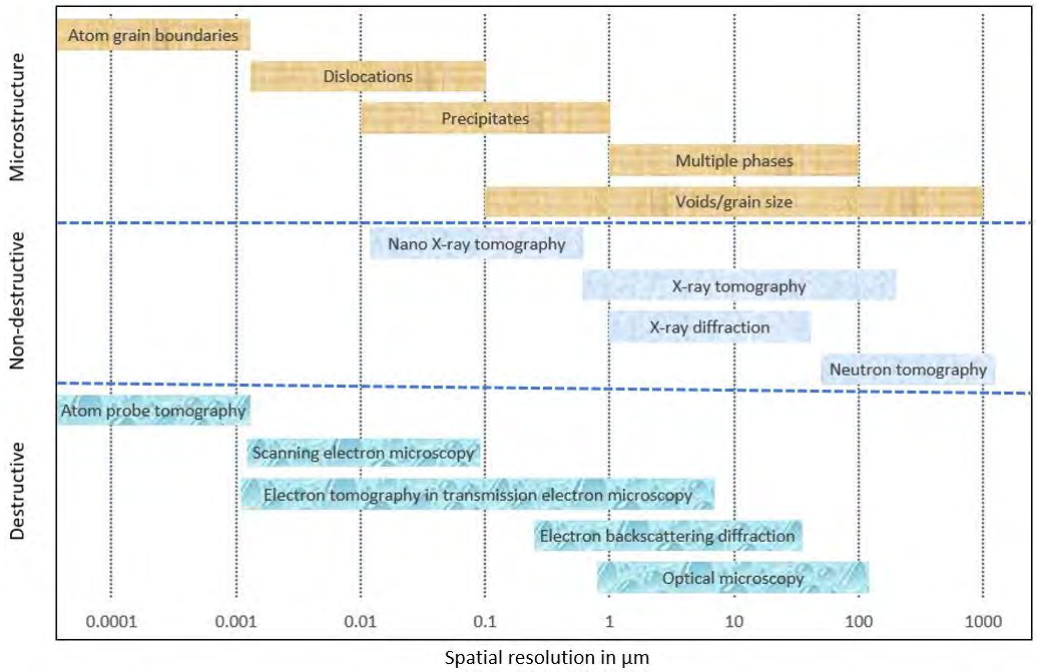

Fig. 2.2 Imaging techniques in polycrystalline materials: the destructive and non-destructive classification and their approximate spatial resolution.

2.2.1 Destructive reconstruction

In the destructive reconstruction methods, early attempts to reconstruct 2D microstructure were successful. Obviously, the 3D characterizations, e.g. the grain size, shape, neighbor distributions affected by the spatial connectivity, can not be precisely quantified from the 2D images. In recent decades, the serial sectioning methodology that collects and assembles 2D microstructure data has been successfully developed to acquire the 3D characterization data. This method is generally achieved by three primary steps:

- Data collection: collecting continuous 2D characterization data for future 3D reconstruction through either manual or automated approaches (Fig. 2.3). Manual collections can be traced back to the 1960s [209]. It begins with preparing repetitive, thickness-constant, falt sections through sputtering, ablating, polishing, etching, cutting, etc., and ends until the sample volume reaches the desired value. The imaging techniques involved could be the utilization of OM, TEM [285] and SEM to image grain boundaries, multiple phases, precipitates or the employment of EBSD to characterize the grain orientation information [229, 402]. The repetitious nature of the manual collection is ideally suitable for automation utilizing instruments. Automation can improve efficiency [189] and reduce data variability concerning image sharpness and serial section

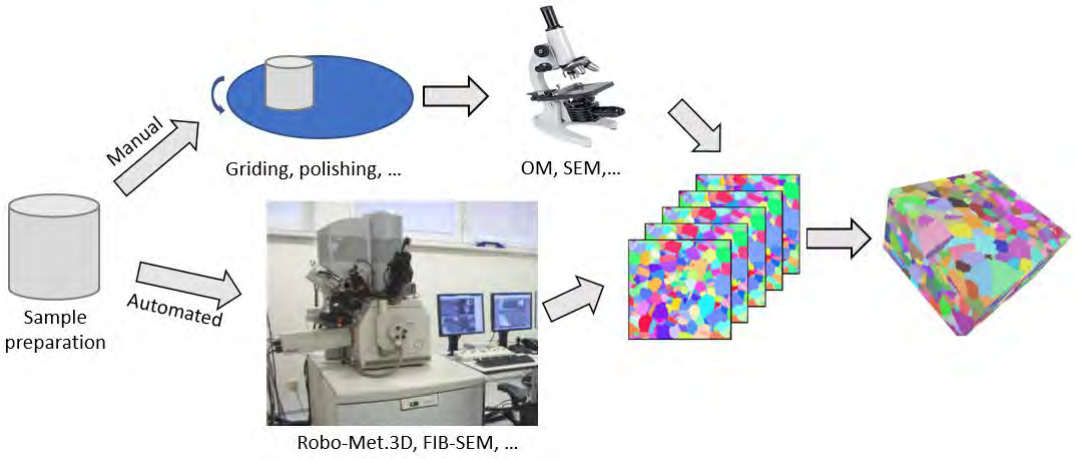

Fig. 2.3 The flow diagram of destructive reconstruction. Adapted from [124], Copyright (2008), with permission from Elsevier.

thickness [136]. Currently, there are three automation devices for serial sectioning experiments: the Alkemper and Voorhees micromiller [9], Robo-Met.3D [405, 404] and focused ion beam–scanning electron microscopes (FIB-SEM) [433, 434]. The Alkemper and Voorhees micromiller and Robo-Met.3D characterized by optical microscopy (OM) yield sufficient micron-level precision, making them widely used in imaging millimetre scale features, e.g., dendrites, dispersoids and voids [188]. The main difference between the Alkemper and Voorhees micromiller and Robo-Met.3D is that Robo-Met.3D utilizes a more precise polishing scheme for thin section preparation rather than micro milling in the Alkemper and Voorhees micromiller. The FIB-SEM founded on scanning electron microscopy (SEM) can achieve accurate featural characterization in micron and submicron scale, e.g., grains and precipitates. Also, it can provide more refined serial sections with approximately 10-15 nm thickness through closed-loop control measurement [25, 157]. In addition, other imaging techniques, such as electron backscattering diffraction (EBSD) [433, 136] for crystallographic information and ion-induced secondary electron (ISE) [320] for chemical spectra mapping, can be incorporated to provide a comprehensive microstructure characterization.

- Data processing: combing the collected 2D data files into the entire 3D stack via data alignment and data segmentation. During the data collection step, scaling, translation and rotation between serial sections can occur and thus must be aligned via the transformation matrix in Equation (2.1).

$$T = RPS \tag{2.1}$$

$$R = \begin{bmatrix} cos(\theta) & -sin(\theta) & 0 \\ sin(\theta) & cos(\theta) & 0 \\ 0 & 0 & 1 \end{bmatrix}; \quad P = \begin{bmatrix} 1 & 0 & P_x \\ 0 & 1 & P_y \\ 0 & 0 & 1 \end{bmatrix}; \quad S = \begin{bmatrix} S_x & 0 & 0 \\ 0 & S_y & 0 \\ 0 & 0 & 1 \end{bmatrix};$$

where S is the scaling matrix, P is the translation matrix R is the rotation matrix. Two primary methods have been used in data alignment. The first is the use of fiducial marks associated with manual and automated apparatus. The second scheme involves applying image processing techniques. As for fiducial markers, [210] utilized the multiple hardness indentations to present an independent reference for data-position correction. [441] glued a chip to the sample to provide both in-depth and plane removal information. [402] proposed machining patterns directly onto the samples to record their spatial position relative to the automation device. Regarding image processing techniques, methods including mutual information [339], least-square difference fitting and image convolutions [138, 398] have been introduced to determine the terms in the Equation (2.1). When it comes to specialized data, such as EBSD, [124] created a misorientation-related parameter to correct the misalignment in consecutive sections. [467] developed an alignment tool based on the orientational correlation function.

The next step following data alignment is data segmentation to identify and separate the features of interest, i.e.,, multiple phases, grain boundariespitates, precipitates, etc. Taking the grain feature as an example [136, 134, 124], it is segmented as the set of voxels whose misorientation angle (Equation 2.10) is under a certain threshold.

$$\theta = min \left| cos^{-1} \left[\frac{tr(S_c g_A g_B^{-1} S_c) - 1)}{2} \right] \right| \tag{2.2}$$

where g_A and g_B are the orientation of seed voxel A and its neighbour B in a grain (Table 4.1), S_c is the the crystal symmetry operator, θ is the misorientation angle between voxel A and B, $(\varphi_1, \phi, \varphi_2)$ are the Bunge Euler angles of the voxel. Besides the thresholding method, other segmentation techniques, including the watershed transformation [440, 283], Euclidean distance transformation [291], etc., have also been widely used in polycrystalline structure. The selection of specific segmentation techniques relies on the research features. For further information, readers are directed towards the books by [401] and [377].

- Space discretization: specifying the domain of the feature using either grid or vertex-edge-face discretization. The grain-based discretization methods are mainly applied in the data collection and data processing, and they play a role as input into the vertex-edge-face discretization schemes. There are two chief techniques conducted in the

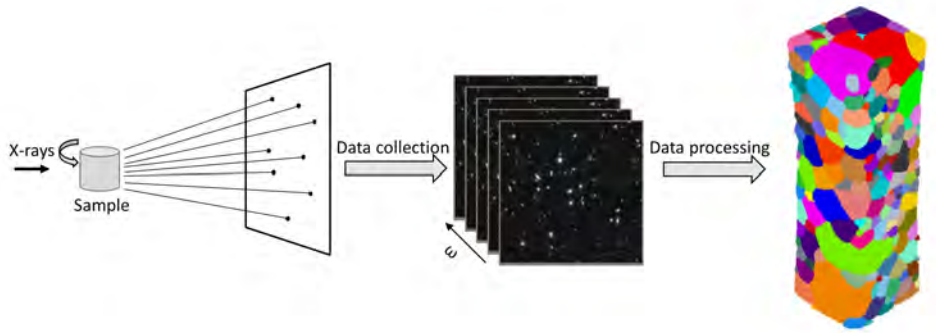

Fig. 2.4 The flow diagram of non-destructive reconstruction

vertex-edge-face scheme: the marching cubes algorithm [253] and the CAD-based surfing fitting [136]. The marching cubes algorithm [228, 388] can take reasonable consideration about the topological information of single grains (quadruple junctions, triple junctions edges and grain surfaces). It begins with substituting voxels with marching cubes, then the intersection of isosurface, and ends with the smoothing and mesh decimation algorithm [391]. The CAD-based surfing fitting [43, 124] can provide a smooth representation of the grain surface. It starts with identifying the set of boundary voxels, then the fitting of spline or polynomial surface, and ends with the overlaps and gaps cleaning through overlaying the initial voxel data.

2.2.2 Non-destructive reconstruction

The non-destructive schemes do not require the removal of material sections in the data collection step. Instead, they mainly combine a range of 2D projection images under continuous small angles to generate the 3D digital microstructures (Fig. 2.4). The process of the non-destructive is similar to the serial sectioning method. But the algorithms involved are entirely different. Details are illustrated below:

- Data collection: collecting a series of 2D projection data either in morphological or crystallographic information. The morphological information emphasises the employment of X-ray and neutron tomography for grain boundaries reconstruction by absorption and phase-contrast techniques. The absorption contrast mechanism, such as the X-ray attenuation [183], measures the intensity distribution in the sample projections via the synchrotron radiation at appropriate X-ray energies and a detector for suitable size and resolution. The grain boundaries can not be detected directly via the absorption contrast due to the limited sub-nanometre width unless it is decorated with a thin layer of a second phase. This is exemplified in works introduced by [315]

for wetted grain boundaries, by [257, 335] for infiltrated edges with liquid Gallium. The phase-contrast system evolving from Fresnel diffraction [400, 77], apart from the monochromaticity, requires the X-ray beam's spatial coherence. Illustrations include diffraction enhanced X-ray imaging [66], hard synchrotron radiation X rays [78], and X-ray phase imaging with a grating interferometer [450]. The coherent X-ray imaging techniques exhibiting two orders of sensitivity increase can detect the interphase boundaries unperceivable in absorption contrast very well [79]. Examples of this are the study carried out by [77] for precipitates identification, by [78] for two-phase (austenitic, ferritic) structure segmentation in stainless steel.

In crystallographic information, the focus is the utilization of X-ray Bragg diffraction for orientation-based grain reconstruction. Illustrations involve the differential-aperture X-ray microscopy (DAXM) [221, 227, 168], the three-dimensional X-ray diffraction microscopy (3DXRD) [347, 344, 345], the diffraction contrast tomography (DCT) [261, 181, 202, 259]. The DAXM combines polychromatic synchrotron X-ray microbeam and charge-coupled device X-ray area detector to measure intra- and intergranular orientations and grain sizes. DAXM data are collected in a point-to-point way through the stepping of profiling wire with submicrometre resolution. The 3DXRD, also termed high-energy X-ray diffraction microscopy (HEDM), has been established at Denmark's Risϕ National Laboratory to reconstruct 3D maps of grain orientations and boundaries. The 3DXRD use a monochromatic planner beam equipped with three detectors: two semitransparent near-field detectors and one far-field detector. Given this, the 3DXRD techniques can be further classified as near-field and far-field methods [345]. The former utilizes the near-field detector with a few micrometres resolution [224, 415]. In contrast, the latter employs the far-field detector with lower resolution (50-200μm) [272, 275]. 3DXRD collects the 2D projection data on detectors by measuring the cross-sections near the center of the sample under various rotation angles. The layers with the same thickness are perpendicular to the vertical axis. The DCT has been developed by [202], in collaboration with the Denmark's Risϕ group [261, 181, 259], and it inherits the principles of projections reconstruction from 3DXRD. The DCT collects data with full 360° scans using a monochromatic wide beam and one near-field detector. The larger beam setup and standard tomographic detector save the scanning and analysis times and make it possible to combine with the X-ray tomography. For example, [259, 260, 258] combined the DCT with X-ray tomographic imaging to prsent a complete data collection in both morphological and crystallographic information.

- Data processing: combing the collected 2D projection data to generate the 3D polycrystalline microstructure incorporating both morphological and crystallographic informa-

tion. The data processing procedures are highly dependent on data collection, such as the conventional filtered backprojection reconstruction for the absorption sources, the filtered backpropagation algorithms for the Fresnel diffraction sources and polycrystal indexing schemes for Bragg diffraction sources. For detailed introductions, readers are referred to the books by [184] and [344]. There are some open-source packages for data processing, including the 3DXRD software IceNine [415, 239] and DCT software (https://sourceforge.net/projects/dct/). Reconstruction of the polycrystalline microstructure needs the incorporation of both morphological and crystallographic information. The primary steps of combined reconstruction are summarized as follows:

- Preprocessing: applying the background removal and normalization procedures to the collected projection images encompassing both the direct and diffracted beams [181, 261]. Firstly, the morphological microstructures are reconstructed from direct beam data via the filtered backprojection reconstruction algorithm. These are followed by the removal of projection images founded on the morphological background and the calculation of diffraction contrast intensity originating from the direct and diffracted beam. Finally, the composite images are formed by the normalization of intensities among the direct and nondirect areas.
- Spots segmentation: identifying the spots through segmentation methods [181, 261] and determining their properties, such as the position, shape and integrated intensity.
- Diffraction determination: establishing the geometry of related diffracted X-rays (e.g., plane normal and scattering vector). The ray-tracing method can be used in the situation of several near-field detectors, and the Friedel pairs are utilized in the data acquisition with full 360° rotation [259, 260, 258]. As for far-field detectors, the diffractions are determined assuming that all grains are located at the nucleus of rotation.
- Indexing: seeking the orientation matrices of the grains and classifying the scattering vectors based on the grain of origin. The indexing programs, including Grainindex [224], Grainspotter [389] and the software by [41], focus on the calculation of the theoretical scattering vectors from a specified orientation.
- Grain reconstruction: reconstructing the 3D grain boundary network from indexed orientations. Several approaches have been established for grain reconstruction: a) forward-projection [415], b) algebraic reconstruction technique [346], and c) GrainSweeper [390].

  - Postprocessing: Integrating the reconstructed data incorporating both the morphological and crystallographic information [260]. The morphological and crystallographic data are first aligned through the scaling, translation and rotation operations. Then the imaging segmentation techniques (e.g., region growth algorithm, 3D watershed algorithm, etc.) are implemented to extract the features of interest, such as the grain boundaries, precipitates and multiple phases.

- Space discretization: specifying the domain of the feature using either grid or vertex-edge-face discretization. Similar to destructive reconstruction, the grain-based discretization methods are mainly applied in the data processing step, and two primary techniques are performed in the vertex-edge-face scheme: the marching cubes algorithm [201] and the CAD-Based surfing fitting [259, 258]. There exist some software packages in reference to the vertex-edge-face based discretization for destructive reconstruction, including the OOF2 [364] and Amira (http://www.amiravis.com/).

2.3 Microstructure characterization

At the microscopic scale of polycrystals, each material point in a representative volume element (RVE) is closely associated with a distinct local state, h. The local state h [116, 316, 8] is described as a combination of concurrent local properties. Using an annealed multi-phase alloy as an example (Fig. 2.5), the local state may involve the thermodynamic phase identifier, the phase's elemental composition, boundary character, systemic energy and the crystal lattice orientation (Table 4.1) [360, 372, 327]. The local states and their properties present in the microstructure can vary significantly as one moves from one representative volume element (RVE) to another. Meanwhile, the local state h is considered a component of the local state space H, which contains all possible local states located at any spatial point in a given material Cartesian space $\mathbf{\Omega}$. For example, the local state space for the thermodynamic phases $\alpha, \beta, ...$ could be defined as a discrete set $H = \{\alpha, \beta, ...\}$, and the crystal lattice orientation, g, could be described as a continuous three-dimensional space (Fig. 2.6), expressed in the Euler angles form as

$$H = \{h = g(\varphi_1, \phi, \varphi_2) | \quad 0 \leq \varphi_1 < 2\pi, \quad 0 \leq \phi < \pi, \quad 0 \leq \varphi_2 < 2\pi\} \tag{2.3}$$

or in the axis-angle form

$$H = \{h = g(\theta, \boldsymbol{n}) = g(x, y, z) | \quad x^2 + y^2 + z^2 \leq r\} \tag{2.4}$$

To adequately express polycrystalline microstructure in a statistical form, a microstructure function $m(\boldsymbol{x},h)$ [116, 316, 8, 186] is introduced to integrate the local state information on the product space $(\boldsymbol{\Omega} \times H)$:

$$m(\boldsymbol{x},h)dh = \frac{V_{h\pm\frac{dh}{2}}(\boldsymbol{x})}{V(\boldsymbol{x})}, \quad \int_{h\in H} m(\boldsymbol{x},h)dh = 1, \quad \frac{1}{vol(\boldsymbol{\Omega})}\int_{\boldsymbol{x}\in\boldsymbol{\Omega}}\int_{h\in H} m(\boldsymbol{x},h)dhd\boldsymbol{x} = 1 \quad (2.5)$$

where $V(\boldsymbol{x})$ indicates the volume of the measured polycrystals constrained at spatial locations $\boldsymbol{x}$, $V_{h\pm\frac{dh}{2}(\boldsymbol{x})}$ is the part of $V(\boldsymbol{x})$ associated with local states within element $(h-\frac{dh}{2}, h+\frac{dh}{2})$, and dh is an invariant measure of the local state space. When the local state space is defined as a discrete set $H = \{\alpha,\beta,...\}$, and each spatial point $\boldsymbol{x}$ of a specific sample volume $\boldsymbol{\Omega}_i$ (thermodynamic phase, grain, subgrain, twin, void etc.), is limited to a single local state, the microstructure function can also be expressed in the indicator functions [429, 116, 232] form:

$$\chi^i(\boldsymbol{x}) = \begin{cases} 1 & if\ h(\boldsymbol{x}) = i \\ 0 & otherwise \end{cases} \quad (2.6)$$

In reality, the imaging techniques in the experimental reconstruction always measure the polycrystalline microstructure on a discrete grid. Therefore, the microstructure function can be extracted by discretizing the Cartesian and local state space into individual bins [116, 232, 186, 329, 198, 293], denoted as

$$\begin{gathered} m(\boldsymbol{x},h)\Delta h \approx \sum_{n=1}^{N}\sum_{\boldsymbol{s}=0}^{\boldsymbol{S}-\boldsymbol{I}} m_{\boldsymbol{s}}^n \chi_n(h)\chi_{\boldsymbol{s}}(\boldsymbol{x}) \\ 0 \le m_{\boldsymbol{s}}^n, \quad \sum_{n=1}^{N} m_{\boldsymbol{s}}^n = 1, \quad \sum_{\boldsymbol{s}=0}^{\boldsymbol{S}-\boldsymbol{I}} m_{\boldsymbol{s}}^n = V^n\boldsymbol{S}, \quad n = 1,2,...,N, \quad \boldsymbol{s} = 0,1,2,...,\boldsymbol{S}-\boldsymbol{I} \end{gathered} \quad (2.7)$$

where the indicator functions $\chi_i()$ are defined analogously to Equation 2.7 such that it is equivalent to one if and only if the value belongs to the bin labeled I and zero otherwise, m_s^n denotes the condensed form of the discrete microstructure function, Δh indicates the size of the local state space bin used. n and s are indexes of the labeled bins in Cartesian and local state space, N and S are the number of individual bins in Cartesian and local state space, and V^n is related to the volume fraction of local state n in the polycrystalline microstructure. Historically, the microstructure characterization can be classified into two categories: first-order and higher-order description. The first-order description is often referred to the one-point statistics and considers only the information on the distinct local states. Higher-order statistical description involves the spatial distribution of the local states.

2.3.1 First-order statistics

First-order statistics provide information about the likelihood of finding a specific local state at a single point sampled from the material. This data is best represented as distribution functions in the local state space. According to the different emphasis of local state h, the one-point statistics are further subdivided into two large groups: physical and geometric. Physical characterization shall be recognized as the appropriate input for physical reconstruction. Simultaneously, the geometric characterization will be identified as the central player in the control of geometric reconstruction.

Physical characterization

There are three primary characterizations describing the microstructure evolution of polycrystalline materials during the manufacturing process: phase volume fraction, boundary condition and systemic energy. The summarized information is as follows:

- Volume fraction: the discrete indicator functions typically define the one-point probability function as

$$\begin{aligned} S_1^i(\boldsymbol{x}) &= \left\langle \boldsymbol{\chi}^i(\boldsymbol{x}) \right\rangle = P(\boldsymbol{\chi}^i(\boldsymbol{x}) = 1) \\ &\equiv \text{Probability density associated with phase } i \text{ found at position } \boldsymbol{x} \end{aligned} \tag{2.8}$$

  where $\langle\rangle$ is the ensemble average over all sample volume $(\boldsymbol{\Omega}_1, \boldsymbol{\Omega}_2, ..., \boldsymbol{\Omega}_m)$. It is possible to interpret the $S_1^i(\boldsymbol{x})$ as V^i (the volume fraction of phase i) for all $\boldsymbol{x}$ in the case of statistically homogeneous materials. Otherwise, it can be considered as a position-dependent volume fraction. The volume fraction as a prerequisite for physical reconstruction has been widely used to characterize the thermodynamic phases, twins, precipitates, voids, etc. (Table 2.1).

- Grain boundary character distributions (GBCD): grain boundaries play a critical role in the manufacturing process of polycrystals, including solidification, grain nucleation and growth, etc. The structure and properties of the grain boundaries depend on five-dimensional crystallographic parameters: the boundary plane orientation (two parameters) and misorientation between the two neighboring grains (three parameters) [12, 478]. Details are as follows:

  - Misorientation: the misorientation M_{AB} of a grain boundary between the two neighboring grains A and B is established as the active rotation operation neces-

sary to align grain A with grain B, expressed as

$$M_{AB} = O_A^{-1} O_B = M_{BA}^{-1} = (O_B^{-1} O_A)^{-1} \tag{2.9}$$

where O_A and O_B are the orientations of grain A and B, respectively [327]. For every misorientation M, there exist n^2 symmetrically equivalent descriptions, represented as $(S_c^i)^{-1} M (S_c^j)$, where S_c^i and S_c^j refer to crystal symmetry operators, and n is the order of the point group associated with the crystal system. Meanwhile, the same misorientation descriptions $M_{AB}(= M)$ and $M_{BA}(= M^{-1})$ are often known as grain exchange symmetry. Thus, the entire set of equivalence descriptions for a grain boundary misorientation is given as

$$M \sim M^{-1} \sim (S_c^i)^{-1} M (S_c^j) \sim (S_c^j)^{-1} M (S_c^i), \quad i, j = 1, 2, ..., N \tag{2.10}$$

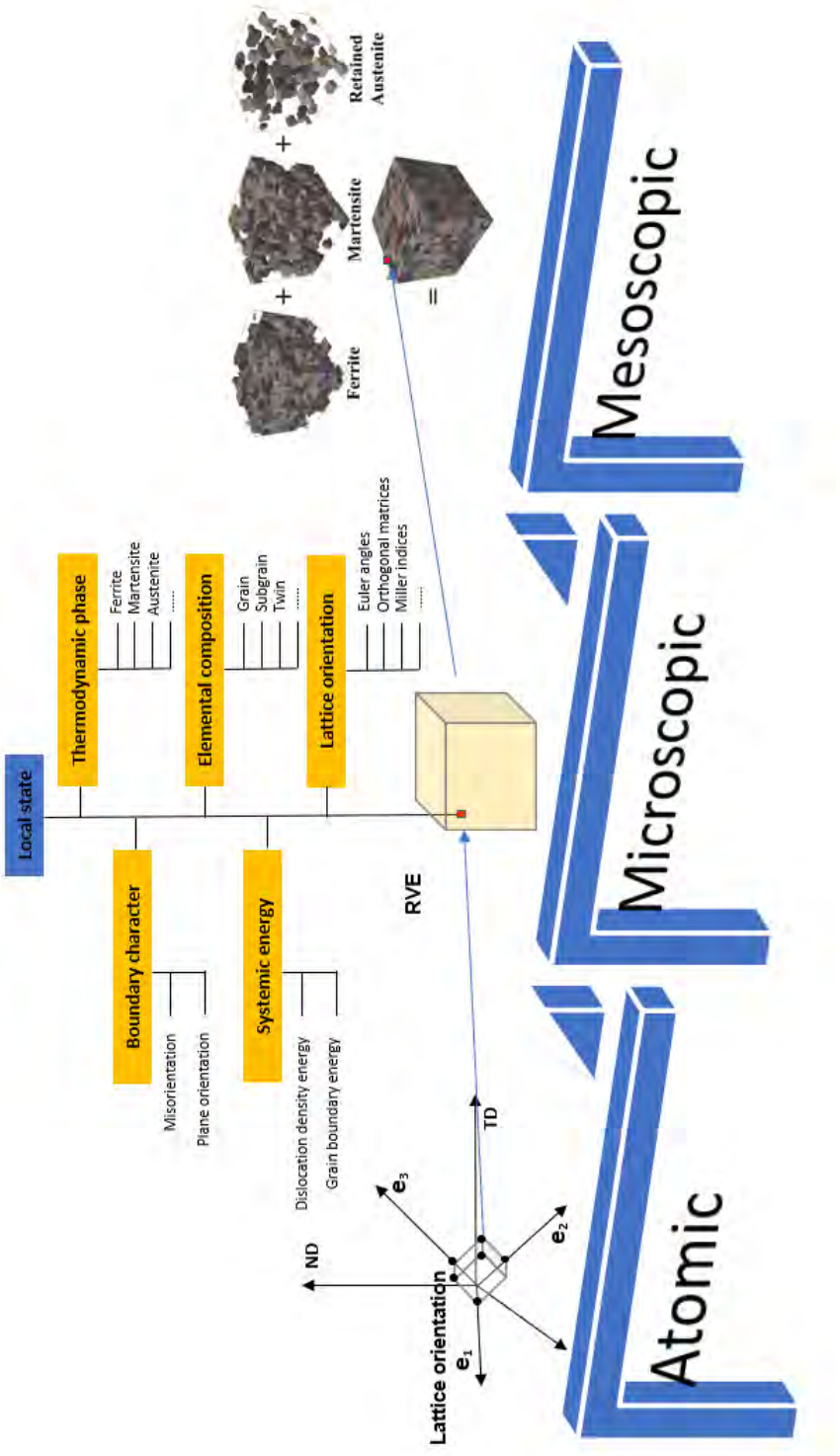

Fig. 2.5 Schematic illustration of the local state in polycrystalline materials.

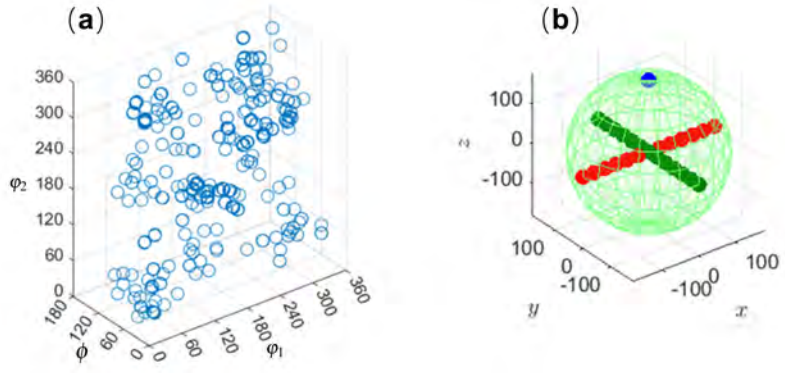

Fig. 2.6 Schematic illustration of the three-dimensional orientation space: (a) the Euler angles form, and (b) the axis-angle form. Generated from the open-source software MTEX [19].

Table 2.1 Illustrations of volume fraction in polycrystalline microstructure

Name	Application	Reference
Twin fraction	Additively manufactured metals	[302, 304]
Porosity fraction	Additively manufactured steels	[376]
Precipitate fraction	Al, Ti or Ni based superalloys	[431, 337, 336, 427]
Thermodynamic phase fraction	Advanced high strength steel, Mo-Si-B alloys	[55, 56, 268, 324, 71, 406]
Grain fraction	All polycrystalline materials	[136, 71]

Table 2.2 Characterization with polycrystalline microstructure

Order		Name	Space state	Reference
First	Physical	Volume fraction	Discrete	[302, 304, 376, 337, 336, 55, 56, 268]
		Boundary character	Continious (5D)	[12, 478, 21, 201]
		Boundary energy	Continious (5D)	[298, 368, 21, 201]
		Dislocation energy	Continious (1D)	[13, 161, 35, 121, 326]
	Geometric	Morphological	Volume	Continious (1D)	[190]
			Size	Continious (1D)	[110, 153, 470]
			Shape	Continious (1D)	[378, 238, 384, 52]
			Topology	Continious (1D)	[134]
			Orientation	Continious (3D)	[164, 83, 129, 290, 74]
		Crystallographic	Misorientation	Continious (3D)	[263, 475, 83]
			Texture	Continious (1D)	[88]
Second and higher		Two-point correlation	Discrete	[71, 431, 293]
		Chord length	Discrete	[223, 107]
		Two-point orientation correlation	Continious (3D)	[343, 122, 112, 357]
		Orientation autocorrelation	Continious (3D)	[112, 357]
		Two-point misorientation correlation	Continious (3D)	[32, 408]
		N-point orientation correlation	Continious (3D)	[160]

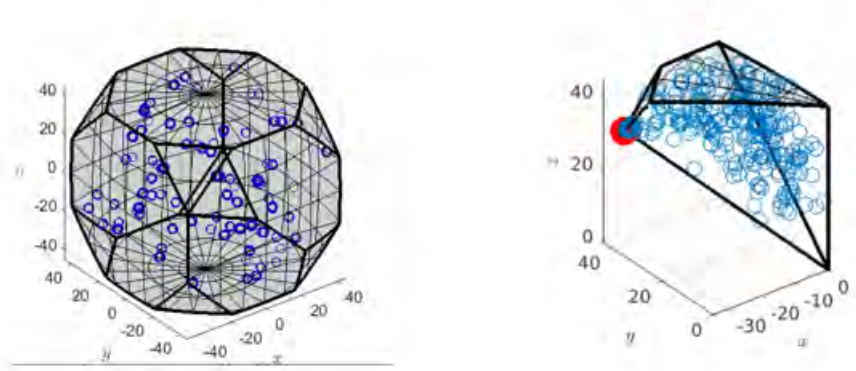

Fig. 2.7 Schematic illustration of the fundamental zone for the orientation and misorientation axis-angle spaces of point group $O(432)$. Generated from the open-source software MTEX [19].

With these equivalence relations, the rotation space can be divided into equivalence groups commonly referred to as the fundamental zone or the asymmetric domain. The misorientation is frequently described in terms of axis-angle parameterization (Table 4.1). Fig. 2.7 shows the fundamental zone for the orientation and misorientation axis-angle spaces of point group $O(432)$. For further details about the point group symmetries, we refer the reader to the following books and articles [148, 299, 104, 327]. The axis-angle parameterization of misorientation enables the distinction between low-angle and high-angle grain boundaries (LAGB and HAGB, respectively), which are connected to grains with different properties (Fig. 2.8). Coincident site lattices (CSL) [446, 368] have been one of the most central concepts in studying particular misorientations. [212] discovered that certain grain boundary misorientations frequently observed in copper after secondary recrystallization corresponded to lattice rotations that superimpose on a fraction of atomic sites. The inverse of the number of coinciding sites is used to name CSL misorientation. Taking the misorientation between parent and twin in fcc crystal structure as an example, one-third of the atomic sites are superimposed, so it is referred to $\Sigma 3$ $(60^0 < 110 >)$ boundary [179]. When two pre-existing twins interact during boundary migration, $\Sigma 9 = \Sigma 3 \times \Sigma 3$ $(38.9^0 < 110 >)$ boundaries are formed (second-order twin GB). Interaction between $\Sigma 3$ and $\Sigma 9$ GBs results

Fig. 2.8 Schematic illustration of low-angle and high-angle grain boundaries. Generated from the open-source software MTEX [19].

in $\Sigma 3$, $\Sigma 27a$ $(31.6^0 < 110 >)$ and $\Sigma 3$ $(35.4^0 < 210 >)$ boundaries (third-order twin GB) (Fig. 2.9) [267, 203].

– Plane orientation: the orientation of the grain boundary plane is determined by the normal vector $\boldsymbol{n}$ [197, 359], which is typically specified by the Miller indices, $[uvw]$, of the adjacent crystals' interface planes (Fig. 2.10). The plane normal is further described by two angles: the in-plane angle and the azimuthal angle [392]. After the experimental reconstruction in Section 2.2, either grid or vertex-edge-volume space discretization scheme has been utilized to quantify the plane normal. In the grid discretization, the boundary plane normals calculation derives directly from integer grid-based data. [158, 292, 202] obtained the normal vectors through fitting tangent planes to some specified grid points. [243] utilized first-order Cartesian moments of binary indicator functions to establish boundary plane normals from a grid-based microstructure image. In the vertex-edge-volume discretization, the boundary plane normals calculation is based on generating vertex-edge-surface from grid-based data. Three main types of methodology exist, namely, the line segment method, the stereological scheme, and the triangular surface mesh approach. The first step in the line segment method [94, 367] is to reconstruct the straight-line boundaries. This can be achieved by the OIM software [460]. The triple junctions are then acquired by specifying all sets of three segments that share the same coordinate of an endpoint. Finally, the cross product of two vectors on the boundary plane will identify the grain boundary normal. The stereological method [386, 392] was created as a statistical measure for deriving the grain boundary normal from observations on a two-dimensional

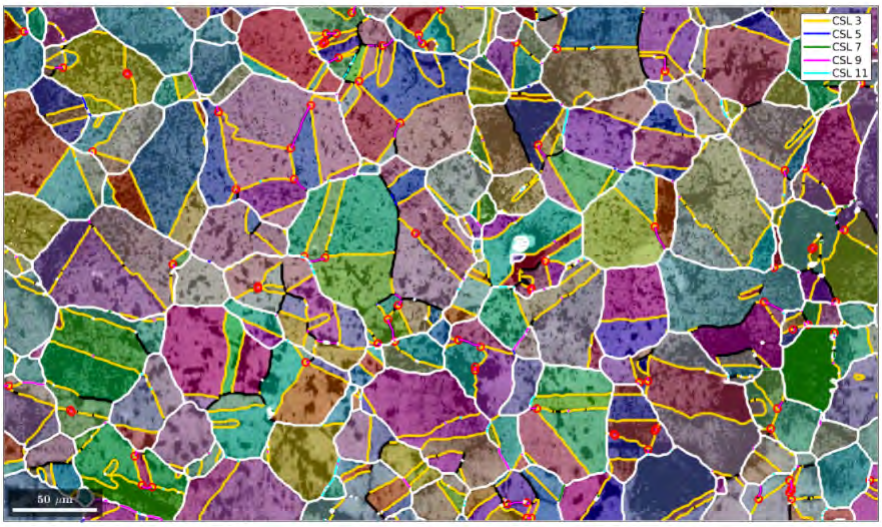

Fig. 2.9 Schematic illustration of the CSL boundaries. Generated from the open-source software MTEX [19].

data set. The normal of the grain boundary plane is a member of a set of planes that contain the boundary trace l_{ij} in the corresponding 2D section and satisfies the criteria $l_{ij} \cdot n_{ijk} = 0$, where n_{ijk} are a set of normals related to the possible grain boundary planes. As for the triangular surface mesh method [369, 93, 201, 21], the interfacial areas between two adjacent grains are segmented into triangular area sets using the marching cube algorithm described in Section 2.2. The plane normal is then computed independently for each triangle of this mesh.

- Systemic energy: the microstructure evolution in physical processing is an energy dissipation process. During processing, there are two main energy types: dislocation density energy and grain boundary energy. The two cases are summarized as follows:

  – Dislocation density: the dislocation density is caused, for example in AM materials, by the thermally induced stresses during fast solidification [204, 444, 245]. The TEM images show that the dislocation density presents a heterogeneous cellular block substructure [302, 304, 305]. Their boundaries having a high density of dislocations are identified as incidental dislocation boundaries (IDBs). In descriptions of boundaries, dislocations fall into two classes: geometrically-necessary dislocations (GNDs) and statistically-stored dislocations (SSDs). The SSDs arising from the random traping process during plastic deformation mainly comprise IDBs. In contrast, the GNDs evolving from strain gradient fields due to geometrical constraints of the crystal lattice principally makes up the subgrain

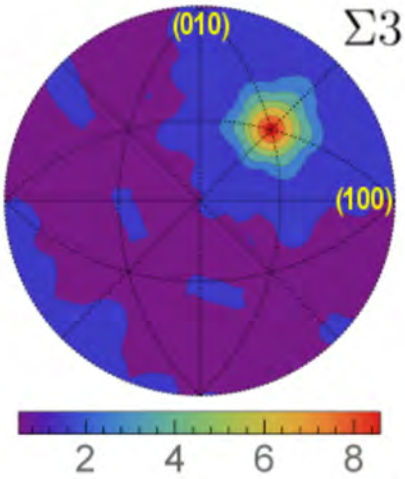

Fig. 2.10 Schematic illustration of the grain boundary plane distribution. Generated from the open-source software DREAM.3D [137].

or geometrically necessary boundaries (GNBs) [13, 161, 35]. The GNDs provide additional storage of dislocations required to handle the lattice curvature that results from non-uniform plastic deformation [121]. It can be resolved by conventional EBSD at each slip system through reduced-component curvature and dislocation density tensors (available in MTEX software) [326], defined as

$$\begin{aligned}
\rho_{\mathrm{GND}} &= \sum_{t'=1}^{M} \rho^{t'} = \min \sum_{t=1}^{N} \rho^{t} \\
\kappa_{ij} &= \sum_{t=1}^{N} \left(b_j^t l_i^t - \frac{1}{2} \delta_{ij} b_m^t l_m^t \right) \rho^t \equiv \sum_{t=1}^{N} \alpha_{ij}^{c,t} \rho^t \\
\alpha_{ij} &= \sum_{t=1}^{N} b_j^t l_i^t \rho^t
\end{aligned} \tag{2.11}$$

where N is the total number of dislocation types, M is a limited number of dislocation types, ρ_{GND} is the the total dislocation density, ρ^t are the individual dislocation densities, κ_{ij} are the components of curvature tensor, α_{ij} are the components of dislocation density tensor, b_j^t are the components of Burgers vector $\boldsymbol{b}^t$ and l_i^t are the components of line vector $\boldsymbol{l}^t$.

– Grain boundary energy: grain boundaries are imperfections with extra free energy per unit area. The grain boundary's extra energy acts as a stimulus for grain growth, roughly estimated as

$$\gamma = 2\gamma_s - B \tag{2.12}$$

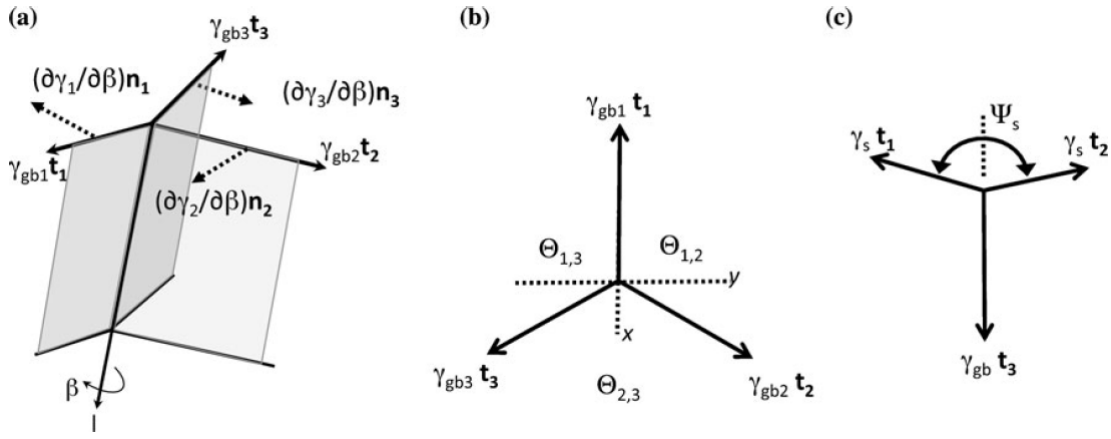

Fig. 2.11 Illustrations of the balance of interfacial energies at triple junctions. Reprinted from [368], with permission from Springer.

where r is the grain boundary energy, γ_s is the surface energy and B is the binding energy between the two surfaces [368]. [362] established the first successful model to present a reasonable explanation for grain boundaries energy with low misorientation angles [128]. In addition, it allows for the representation of any potential grain boundary as a group of dislocations [396]. Another eight fundamental polyhedra models have been developed to provide a simplified description of the local atomic packing at the boundary [449, 14, 130]. This has been demonstrated to be significant in interpreting the energy of tilt grain boundaries [130]. [456–458] were pioneers in computing grain boundary energy over a broad crystallographic domain using consistent methodologies. The findings indicated that grain boundary energy is highly dependent on the grain boundary plane. All measurements of grain boundary energy are implemented by assuming that the geometry of interface junctions exist in a thermodynamic equilibrium state. [150] defined the equilibrium of interfacial forces at a triple line in the form

$$\gamma_i \boldsymbol{t}_i + \frac{\partial \gamma_i}{\partial \beta} \boldsymbol{n}_i = 0 \tag{2.13}$$

where γ_i are the boundary energy of the ith interfaces, $\boldsymbol{t}_i$ and $\boldsymbol{n}_i$ are vectors tangential and normal to the interfaces, respectively and β is the rotation angle (Fig. 2.11.a). There are several ways to simplify the Herring equation. For example, if the differential terms are small enough to be neglected, the tangential

forces balance yields a simplified form

$$\frac{\gamma_1}{sin\varphi_1} = \frac{\gamma_2}{sin\varphi_2} = \frac{\gamma_3}{sin\varphi_3} \tag{2.14}$$

where φ_i are the equilibrium separation angles (Fig. 2.11.b) [146, 145, 385]. When a grain boundary comes into contact with a free surface, the equation can be simplified further by assuming that the surfaces have the same energy, described as

$$\frac{\gamma_3}{\gamma_s} = 2cos\left(\frac{\Psi}{2}\right) \tag{2.15}$$

where γ_s are the boundary energy of the free surface (Fig. 2.11.c) [306, 387]. The grain boundary energy can be calculated by conventional EBSD at triple junctions through the capillarity vector reconstruction method [298]. The capillarity vector reconstruction method employs the vector formulation of the Herring equation [155, 60], expressed as

$$(\boldsymbol{\xi}_1 + \boldsymbol{\xi}_2 + \boldsymbol{\xi}_3) \times \boldsymbol{l} = 0 \tag{2.16}$$

where $\boldsymbol{l}$ is the triple line vector, $\boldsymbol{\xi}_1$, $\boldsymbol{\xi}_2$ and $\boldsymbol{\xi}_3$ are the capillarity vectors correspond to three grain boundaries. Once the capillarity vector is obtained, the grain boundary is calculated from $\gamma = \boldsymbol{\xi}_i \cdot \boldsymbol{n}_i$, where $\boldsymbol{n}_i$ are vectors normal to grain boundaries.

The combined information of the grain boundary plane normal vector $\boldsymbol{n}$ and lattice misorientation M_{AB} provides specific descriptions of the boundary characterization. Examples are the tilt and twist boundaries, the grain boundary character distribution (GBCD), and the grain boundary energy distribution (GBED). The twist boundaries are those for which the axis of the lattice misorientation M_{AB} is parallel to the normal vector $\boldsymbol{n}$. The tilt grain boundary is the one for which the normal vector $\boldsymbol{n}$ is perpendicular to the axis of the lattice misorientation M_{AB}. The term symmetric tilt refers to the fact that the crystallographic planes surrounding the grains on each side of a boundary are identical. The remainder of the tilts are asymmetric. The grain boundary character distribution (GBCD) categorized based on grain boundary plane normal vector and lattice misorientation $\lambda(M_{AB}, \boldsymbol{n})$ is known as the relative areas of grain boundaries. Similarly, the grain boundary energy distribution (GBED) determined as a function of the grain boundary plane normal vector and lattice misorientation $\gamma(M_{AB}, \boldsymbol{n})$ is described as the relative energies of grain boundaries. Many researchers have performed correlation studies between GBCD and GBED [94, 237, 367, 34, 33]. One general conclusion is that GBCD is inversely correlated to GBED in microstructures formed by normal grain growth.

Geometric characterization

Geometric characterization can be classified into two broad categories: morphological and crystallographic. The following section aims to quantify a number of characteristics that determine the morphology and crystallography of polycrystalline materials. Additionally, the improvement and correlation of various characteristics are reviewed.

- Morphology: the morphological characterization provides necessary statistical information on the grain-level features, such as the distribution of grain volume, size, topology and neighbourhood. Summarized details are as follows.

  – Grain volume: the grain volume (grain area in 2D) is determined through the grid discretization in most cases. Each grid voxel is assigned to a grain during the grain reconstruction process based on its misorientation concerning its neighbours (Equation (2.10)). The grain volume V_{grain} is then defined by $V_{grain} = N_{voxel} \cdot V_{voxel}$, where V_{voxel} is the volume of a voxel and N_{voxel} is the number of voxels in the grain. The mean grain volume is calculated in the following

  $$\left\langle V_{grain} \right\rangle = \frac{\sum_{N_{grain}} V_{grain}}{N_{grain}} \tag{2.17}$$

  where N_{grain} is the number of grains. Next, one can define the grain volume distribution (GVD), $f(v)$, in a way that $f(v)dv$ is the number fraction of grains falling in a grain size of $v - \frac{dv}{2} \leq v < v + \frac{dv}{2}$. The full definition of grain volume distribution function between continuous variable interval is given by

  $$\int_0^{\infty} f(v)dv = \int_0^{v_{max}} f(v)dv = 1, \quad p(a \leq v \leq b) = \int_a^b f(v)dv \tag{2.18}$$

  where v_{max} is the volume of the largest grain. GVD is affected by the stereological strategies for determining the number of grains in a sample volume, such as the disector, selector, unbiased brick, center-of-mass, boundary inclusion and boundary exclusion. The study revealed that the disector, selector, unbiased brick and center-of-mass showed a good estimation of GVD while the boundary inclusion and boundary exclusion showed over- or underestimation of GVD [190].

– Grain size: the grain size R is specified by the equivalent sphere radius (ESR) (circle radius in 2D), computed as

$$R = ESR = \left(\frac{3}{4\pi} V_{grain}\right)^{\frac{1}{3}} \tag{2.19}$$

where V_{grain} is the grain volume. The mean grain size $\langle R \rangle$ [302] and grain size distribution (GSD), $f(r)$, are defined in the same way as in Equation (2.17) and Equation (2.18). Most of the time, the grain size distribution follows a log-normal pattern [110, 134, 435, 248], written as

$$f(r) = \frac{b}{\sqrt{\pi} r} e^{\left[-b^2\left\{ln(\frac{r}{r_m})\right\}^2\right]} \tag{2.20}$$

where r is a constant, and r_m is the median value in the log-normal distribution. In addition to log-normal fit, Hillert [153] proposed a grain size distribution function by merging the theory of Ostwald ripening with grain growth, established as

$$f(r) = A \frac{r}{(2-r)^{2+\beta}} exp\left(-\frac{2\beta}{2-r}\right) \tag{2.21}$$

where A is a constant, $\beta = 3$ for growth in 3D, $r = \frac{R}{R_{cr}}$ and R_{cr} is determined by $\langle R \rangle = 8\frac{R_{cr}}{9}$. Studies have found that the Hillert distribution significantly shifts the peak and shows a considerably shorter tail compared with the experimental dataset [134, 435]. Alternatively, Louat [254] developed a grain size distribution function by assuming the growth of boundaries as a diffusion-like process, given as

$$f(r) = Cr \cdot exp(-\alpha r^2) \tag{2.22}$$

where C and α are constants. The Louat distribution also deviates considerably from the experimental data by overestimating the smaller grains [134, 435].

– Grain topology: the grain topology is mainly decided using the vertex-edge-volume discretization scheme (Section 2.2). Correspondingly, characteristics investigating grain topology involve four types: the grain vertices, the grain edges, the grain faces and the grain shape (Table 2.3). The grain edges (triple lines) are formed where three neighboring grains are connected. Meanwhile, the grain vertices (quadruple points) occur where four mutually adjoining grains, four triple lines, and six-grain faces intersect at a single location (Fig. 2.12). Like the boundary plane normals calculation, the methodology for grain topology

characterization of vertices, edges and faces per grain falls into three categories: the line segment method, the stereological scheme, and the triangular surface mesh approach. The first step in the line segment method [248, 136] is to locate the special boundary point. The straight line segments connecting all the special points are then acquired using an error-per-unit-length algorithm. This can be achieved by the Micro-Imager software [136]. Finally, the grain faces (boundaries) are defined as the area enclosed between the line segments. The stereological method [142] was built as a statistical measure for characterizing a twin-dependent triple junction from a section plane. Concerning the triangular surface mesh method [436, 435], the iso-surface between two adjacent grains are rendered into triangular area sets using the marching cube algorithm [228]. The grain topology is then computed independently for each rendered surface. In addition to the aforementioned methods, the grain surface area distribution (grain perimeter in 2D) can also be estimated through equivalent sphere surface (equivalent circle perimeter in 2D), mean lineal intercept strategy [470, 82] pattern matching library approach [82] or the grid discretization scheme [134]. For the grid discretization scheme, the surface area per grain can be quantified by the number of voxels on all-grain faces. Another way to assess the surface area from grid data is to consider the fraction of voxels located on the grain's surface. This value represents the surface-to-volume ratio.

When it comes to grain shape types, the irregular shapes of grains in a polycrystalline microstructure make it hard to characterize grain shapes in general. Most shape descriptions can be based on combining groups of size factors to produce a unitless value [312]. One common practice is to generate ellipsoidal inclusions from voxel data from grid discretization data [134, 256]. The first step in this method is to calculate the zeroth-order moments (I_o), first-order moments (I_x, I_y, I_z) and second-order moments (I_{xx}, I_{yy}, I_{zz}) for each grain. Following that, the centroidal coordinates (x_c, y_c, z_c) of the best-fitting ellipsoid are determined using the zeroth- and first-order moments as

$$x_c = \frac{I_x}{I_o}, \quad y_c = \frac{I_y}{I_o}, \quad z_c = \frac{I_z}{I_o} \tag{2.23}$$

The principal axes orientation are determined by solving the eigenvalue problem for the moment of inertia tensor. Next, the major axis $(2a)$, minor axis $(2c)$ and

Table 2.3 Illustrations of grain topology in polycrystalline microstructure

Type	Name	Reference
Grain vertices	Number of vertices per grain	[435, 247, 248]
Grain edges	Number of edges per grain	[435, 142, 247, 248]
	Grain edge length distribution	[435]
Grain faces	Number of edges per face	[193, 435, 248]
	Number of faces per grain	[136, 435, 248, 87]
	Grain surface area distribution	[470, 136, 435, 134, 82, 248]
Grain shape	Aspect ratio	[134, 256, 302, 113]
	Principal axes orientation	[134, 256, 423, 302]
	Third moment invariant	[264, 256]

intermediate axis $(2b)$ of the ellipsoidal grain are solved in the following

$$a = \left[\frac{A^4}{B \cdot C}\right]^{\frac{1}{10}}, \quad b = \left[\frac{B^4}{A \cdot C}\right]^{\frac{1}{10}}, c = \left[\frac{C^4}{A \cdot B}\right]^{\frac{1}{10}} \tag{2.24}$$

where A, B and C are given by $A = \left(\frac{15}{4\pi}\right) \cdot \left(\frac{I_1+I_2-I_3}{2}\right)$, $B = \left(\frac{15}{4\pi}\right) \cdot \left(\frac{I_1+I_3-I_2}{2}\right)$, $C = \left(\frac{15}{4\pi}\right) \cdot \left(\frac{I_2+I_3-I_1}{2}\right)$. Finally, the aspect ratios $(\frac{b}{a}, \frac{c}{a})$ per grain are calculated. However, aspect ratios cannot distinguish grain shapes with different surface curvatures. Thus, the third moment invariant Ω_3 independent of translation, rotation, and isotropic scaling has been proposed to characterize the smoothness and complexity per grain [264], expressed as

$$\Omega_3 = \frac{V^5}{O_3}, \quad O_3 = \mu_{200}\mu_{020}\mu_{002} + 2\mu_{110}\mu_{101}\mu_{011} - \mu_{200}\mu_{011}^2 - \mu_{002}\mu_{110}^2 \tag{2.25}$$

where V is the volume per grain, and the μ_{pqr} terms represent the second-order moments.

– Grain neighborhood: neighbor grains are any grains that have at least one face in common with the grain under investigation [136, 134, 256]. Meanwhile, grains sharing a conjunct edge or corner are also considered as neighbors [247]. The mean number of neighbors $\langle N \rangle$ and number of neighboring grains distribution, $f(n)$, are defined in the same way as in Equation 2.17 and Equation 2.18.

The effects of voxel resolution on the grid-based characteristics like grain size, grain shape and grain neighborhood have been conducted [256]. The data analysis found that grain size and the number of neighbouring grains generally have insensitive resolution

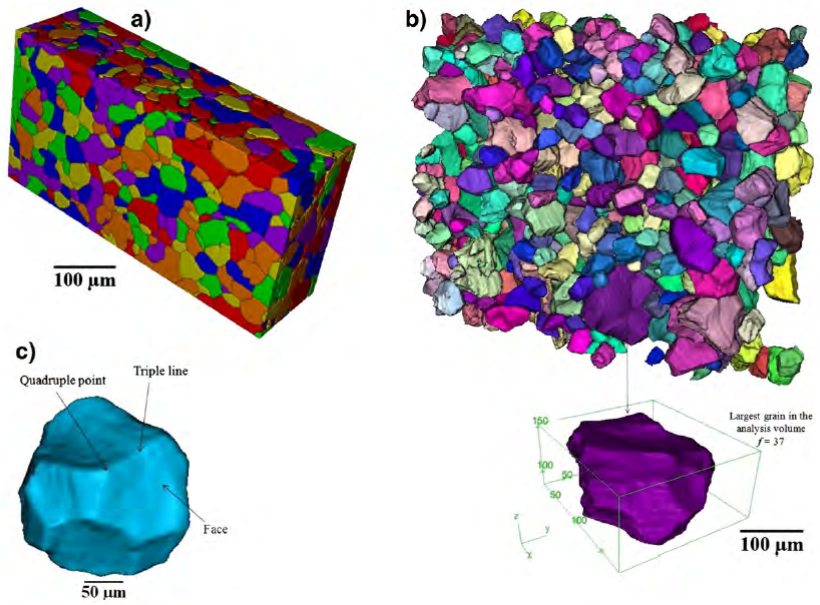

Fig. 2.12 Schematic illustration of the triple lines and quadruple points. Adapted from [435], Copyright (2014), with permission from Elsevier.

changes. In contrast, shape characteristics such as ellipsoid aspect ratios and the third moment invariant have more significant sensitivity. Simultaneously, correlations among morphological characteristics are also studied. The results revealed that the ellipsoid aspect ratios and the average neighbor diameter are unrelated to the grain size, whereas the number of grains and the surface-to-volume ratio are inversely correlated to grain size [134]. Moreover, the number of quadruple points, triple lines, faces, neighbours, the edge length and the surface area per grain is highly correlated with grain size [134, 435, 248]. Finally, considering the effects of nearest-neighbor grains, the relationship between grain size and grain face number, grain edge length and grain face number exhibit an excellent linear correlation [435].

- Crystallography: the morphological characterization of the grains can not examine the crystallographic nature. The orientation distribution function (ODF), misorientation distribution function (MODF) and micro-texture function (MTF) are presented in this part to describe the crystallography of the grains.

  – Orientation distribution function: the orientation g is a quantitative assessment of a material's macroscopic texture [104]. It represents the rotation relationship between the crystal axes of grains in a polycrystal and reference frame. The orientations can be equivalently described in different mathematical and

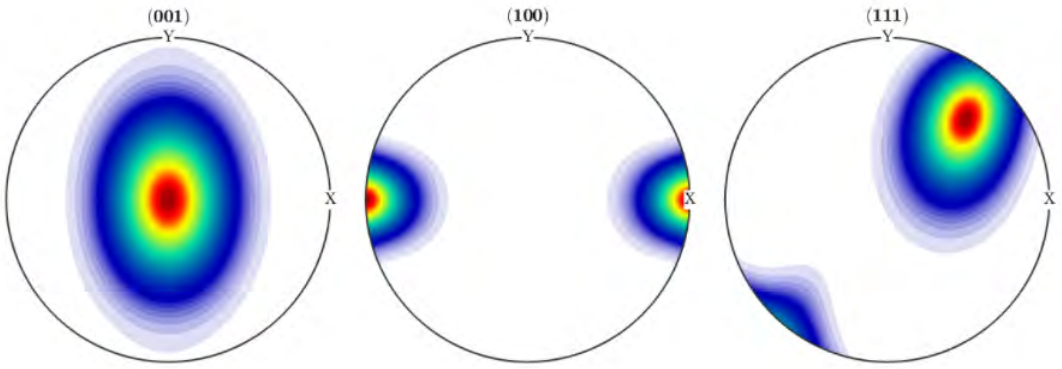

Fig. 2.13 Schematic illustration of the orientation distribution function. Generated from the open-source software MTEX [19].

non-mathematical parameterizations, each with three independent parameters (Table 4.1). The continuous orientation distribution function(ODF) is often used to quantify the preferred crystallographic orientation [116], expressed as

$$f(g)dg = \frac{V_{h\pm\frac{dh}{2}}}{V}, \quad \int_{g\in H} f(g)dg = 1 \tag{2.26}$$

where H is the orientation space, and $\frac{V_{h\pm\frac{dh}{2}}}{V}$ denotes the volume fraction associated with orientation g lying within an invariant measure dg. The ODF is commonly represented graphically through a stereographic projection for holding a particular crystallographic direction constant (Fig. 2.13).

– Misorientation distribution function: the misorientation distribution function (MDF) represents another texture related aspect of microstructural heterogeneity. The definition of MDF is the same way as the ODF, and it is typically described in axis-angle notation. A material's MDF is unquestionably linked to its ODF. When morphological characters are randomly distributed, the MDF completely depends on the ODF [304].

– Micro-texture function: the micro-texture function (MTF) quantifies the degree to which orientations and misorientations are clustered. It is similar to the MDF but provides data at a more local level. The MDF represents the total number of misorientations in the structure, whereas the MTF depicts how the lowest misorientations are spatially distributed relative to a specific grain [88, 134].

2.3.2 Second and higher order statistics

The higher-point statistics provide the distribution information both on the Cartesian and local state spaces. For instance, the two-point correlation $f(h,h'|\boldsymbol{r})$ is the volume probability density associated with finding the local state h' at the head of a random vector and the local state h at the tail [116, 329], defined as

$$f(h,h'|\boldsymbol{r}) = \frac{1}{vol(\boldsymbol{\Omega}|\boldsymbol{r})}\int_{\boldsymbol{x}\in\boldsymbol{\Omega}|\boldsymbol{r}} m(\boldsymbol{x},h)m(\boldsymbol{x}+\boldsymbol{r},h')\,d\boldsymbol{x} \tag{2.27}$$

where $\boldsymbol{\Omega}|\boldsymbol{r} = \{\boldsymbol{x}|\boldsymbol{x}\in\boldsymbol{\Omega},\boldsymbol{x}+\boldsymbol{r}\in\boldsymbol{\Omega}\}$ is the spatial region under the assumption of ergodicity and homogeneity and $m(\boldsymbol{x},h)$ is the microstructure function. Applications of the two-point correlation statistics could be the two-point orientation correlation function $f(g,g'|\boldsymbol{r})$ [343, 122, 112, 357], orientation autocorrelation function $\bar{p}_{\boldsymbol{r}}$ [112, 357], and two-point misorientation correlation function $f(\theta,D)$ [32, 408] (Equation (2.45)), described as

$$\begin{aligned} f(g,g'|\boldsymbol{r}) &= \frac{1}{vol(\boldsymbol{\Omega}|\boldsymbol{r})}\int_{\boldsymbol{x}\in\boldsymbol{\Omega}|\boldsymbol{r}} m(\boldsymbol{x},g)m(\boldsymbol{x}+\boldsymbol{r},g')\,d\boldsymbol{x} \\ \bar{p}_{\boldsymbol{r}} &= \frac{1}{V_{FZ}}\int_{FZ} f(g,g'|\boldsymbol{r})dg \\ \int_{\bar{\theta}}\int_{\bar{D}} f(\theta,D)d\theta dD &= \frac{N(\bar{\theta},\bar{D})}{N}, \quad \int_{\theta^*}\int_{D^*} f(\theta,D)d\theta dD = 1 \end{aligned} \tag{2.28}$$

Where V_{FZ} is the fundamental zone volume, θ represents the the misorientation angle, $D_{ij} = |\boldsymbol{r}_i - \boldsymbol{r}_j|$ denotes the distance between the centers for each pair of grains, $(\bar{\theta},\bar{D})$ indicates the intervals of length $(\Delta\theta,\Delta D)$ centered on the misorientation angle and distance values (θ,D), N is the total number of grains, $N(\bar{\theta},\bar{D})$ is the number of pairs encountered concurrently in these two intervals, and θ^* and D^* are the largest misorientation angle and distance interval.

For the same reasons as previously stated in Equation 2.7, a more practical, discretized form of the two-point correlation [185, 186, 196, 329, 330, 171, 132, 198, 271] can be expressed in an analogous manner as

$$\begin{aligned} f(h,h'|\boldsymbol{r})[\Delta h]^2 &\approx \sum_{p=1}^{N}\sum_{n=1}^{N}\sum_{\boldsymbol{t}} f_{\boldsymbol{t}}^{np}\chi_n(h)\chi_p(h')\chi_{\boldsymbol{t}}(\boldsymbol{r}) \\ f_{\boldsymbol{t}}^{np} &= \frac{1}{|\boldsymbol{S}_{\boldsymbol{t}}|}\sum_{\boldsymbol{s}=0}^{\boldsymbol{S}_{\boldsymbol{t}}-\boldsymbol{I}} m_{\boldsymbol{s}}^{n} m_{\boldsymbol{s}+\boldsymbol{t}}^{p} \end{aligned} \tag{2.29}$$

Where $f_{\boldsymbol{t}}^{np}$ represents the condensed form of the discrete two-point correlations reflecting the probability of finding local states located in the local state bins n and p at spatial bins whose centres are connected by the set of vectors indexed by $\boldsymbol{t}$, and $|\boldsymbol{S}_{\boldsymbol{t}}|$ represents the total number of spatial bins involved when $\boldsymbol{s}$ is utilized as a multidimensional array index.

Three-point and higher-order correlations can be defined in the same way as

$$\begin{aligned} &f(h_0,h_1,...,h_{n-1}|\boldsymbol{r}_1,\boldsymbol{r}_2,...,\boldsymbol{r}_{n-1}) \\ &= \frac{1}{vol(\boldsymbol{\Omega}|\boldsymbol{r}_1,\boldsymbol{r}_2,...,\boldsymbol{r}_{n-1})} \int_{\boldsymbol{x}\in\boldsymbol{\Omega}|\boldsymbol{r}_1,\boldsymbol{r}_2,...,\boldsymbol{r}_{n-1}} m(\boldsymbol{x},h_0),m(\boldsymbol{x}+\boldsymbol{r}_1,h_1),...,m(\boldsymbol{x}+\boldsymbol{r}_{n-1},h_{n-1})\,d\boldsymbol{x} \end{aligned} \tag{2.30}$$

where $\boldsymbol{\Omega}|\boldsymbol{r}_1,\boldsymbol{r}_2,...,\boldsymbol{r}_{n-1} = \cap_{i=1}^{n-1}\boldsymbol{\Omega}|\boldsymbol{r}_i$. One example is the n-point orientation correlation function (n-OCF) presented by [160]. Regarding the discrete local state definition, the two-point correlation is formally expressed as

$$S_2^{i,j}(\boldsymbol{x}_1,\boldsymbol{x}_2) = S_2^{i,j}(\boldsymbol{r}) = \left\langle \chi^i(\boldsymbol{x}_1)\chi^j(\boldsymbol{x}_2)\right\rangle \tag{2.31}$$

where $\langle\rangle$ is the ensemble average, $\chi^i(\boldsymbol{x}_1),\chi^j(\boldsymbol{x}_2)$ are the indicator functions and $\boldsymbol{r} = \boldsymbol{x}_2 - \boldsymbol{x}_1$. The discrete n-point probability function is expressed as

$$\begin{aligned} &S_n^{i,j,...,k}(\boldsymbol{x}_1,\boldsymbol{x}_2,...,\boldsymbol{x}_n) = S_n^{i,j,...,k}(\boldsymbol{r}_1,\boldsymbol{r}_2,...,\boldsymbol{r}_n) \\ &\equiv \text{Probability density associated with local state } i,j,...,k \text{ found in } n \text{ points at positions } \boldsymbol{x}_1,\boldsymbol{x}_2,...,\boldsymbol{x}_n \end{aligned} \tag{2.32}$$

where $\boldsymbol{r}_j = \boldsymbol{x}_{j+1} - \boldsymbol{x}_j$. The two-point correlation based on indicator functions has been widely utilized in the characterization and reconstruction of dual-phases [293] and precipitates [431] in polycrystals. In addition, [223] employed the chord length distribution to quantify and represent diverse polycrystalline microstructures. [107] developed an imaging method based on two-phase rotary chord length distributions to obtain the high-dimensional statistical information necessary for identifying the morphology and size characteristics of Ni-based superalloys.

2.3.3 Reduced-order representations

Besides the image processing techniques used in the experimental reconstruction, the microstructure characterization can also be precisely quantified through the machine learning (ML) [65] method. The ML method for autonomous microstructural characterization can be roughly classified into three primary steps, similar to the data collection and processing in the

experimental reconstruction. It starts with the distinction between polycrystalline structures and their boundaries via topological classifiers. The unsupervised ML algorithms, such as K-means, DBSCAN, mean-shift, and Gaussian mixture models, are then utilized to cluster the preconditioned voxels labelled by topological classifiers. Finally, a refinement step can further enhance the grain number and size of microstructures obtained by unsupervised ML. Since the high-dimensional explicit representations of the microstructure using the microstructure function make the PSPP linkage difficult [186, 51], the characterizations can also be implicitly extracted from the experimental images through some low-dimensional reduction techniques. For instance, principal component analysis [413, 414, 394] converts the high dimensional features of input images into latent vectors, and Karhunen–Loève expansion [242, 451] decomposes random polycrystalline microstructure into a few modes at the macroscale and mesoscale. Variational autoencoder (VAE) [63, 200, 461] and deep learning models have also been proposed to obtain a reduced dimensional representation of the polycrystalline microstructure images. Analogous to PCA, the VAE collects the input images' characteristics and turns them into latent vectors. Due to more profound encoder layers, VAE can manage far more complex features than PCA [200]. The deep learning (DL) models, including deep convolutional belief network (CDBN) [64], deep neural networks (DNN) [325] and convolutional neural networks (CNN) [206, 340], learn the microstructure characterization from image data and can provide a reduced-dimensional, parametric feature representation of the experimental images (embedding layers).

The microstructure characterizations can be used directly as input for the data-driven model to capture PSPP linkages [186]. For instance, the characterizations describing the morphology (grain size, shape, and topology) and crystallography (ODF, MDF) have been utilized to generate feature vectors for training a random forest learning algorithm that predicts the grain's stress hotspots [269, 270]. Similar characterizations have also been served as inputs for the Ridge regression and XGBoost models to predict microstructure-dependent mechanical properties in additively manufactured metals [151]. In addition, pole figure images and 3D orientation maps have also been explored as input data for the two- and three-dimensional convolutional neural network (CNN-2D and CNN-3D) to estimate biaxial stress-strain curves of sheet metals [463]. In recent years, [84] developed a graph neural network (GNN) model incorporating the grains' orientation, size, and number of neighbors to achieve an accurate and interpretable prediction of the properties of polycrystalline materials. [397] proposed a grain knowledge graph model capturing the node representation of grain size and orientation to realize the effective microstructure-property prediction. And [271] employed the two-point spatial correlations of the microstructure as the input to the robust CNN model for achieving the linkages between microstructures and properties and

building property closures in support of material design. Robust reduction techniques, including spectral methods (SM), principal component analysis (PCA), and representative aggregated microstructural parameters (RAMPs), have also been developed to transform the characterization spaces into lower-dimensional features. These reduction techniques, including spectral methods (SM), principal component analysis (PCA), and representative aggregated microstructural parameters (RAMPs), transform the characterization spaces into lower-dimensional features. These specified features are highly effective when used as inputs in the microstructure sensitive design (MSD), materials knowledge system (MKS), parametrically homogenized constitutive models (PHCMs), uncertainty quantification (UQ), and additive manufacturing (AM) (Table 2.4). Next, we focus on the three major reduced-order techniques.

Spectral methods

The spectral methods can reduce the infinite spaces to limited dimensions constituted with significantly compact and computationally efficient coefficients and bases, and thus increase the likelihood of formulating highly efficient PSPP relationships. Three techniques are mainly used in the spectral representation of varying complexity: the primitive basis, the discrete Fourier transform (DFT), and generalized spherical harmonic function (GSHF) [116, 186]. It should be noted that Equation 2.4 and Equation 2.29 are the spectral representations (the indicator functions are also termed as the primitive bases) of the microstructure function and two-point correlation that allows us to extract a discrete form of the continuous spaces. Furthermore, it might be more practical to utilise the DFT as the spectral representation of the discrete microstructure function m_s^n, stated as

$$\begin{aligned} M_{\boldsymbol{k}}^n &= \Im(m_{\boldsymbol{s}}^n) = \sum_{\boldsymbol{s}=0}^{\boldsymbol{S}-\boldsymbol{I}} m_{\boldsymbol{s}}^n e^{-\frac{2\pi i \boldsymbol{k}\boldsymbol{s}}{\boldsymbol{S}}} \\ m_{\boldsymbol{s}}^n &= \Im^{-1}(M_{\boldsymbol{k}}^n) = \frac{1}{|\boldsymbol{K}|} \sum_{\boldsymbol{k}=0}^{\boldsymbol{K}-\boldsymbol{I}} M_{\boldsymbol{k}}^n e^{\frac{2\pi i \boldsymbol{s}\boldsymbol{k}}{\boldsymbol{K}}} \end{aligned} \tag{2.33}$$

where $\Im$ and $\Im^{-1}$ represent the Fourier transform and the inverse Fourier transform. Meanwhile, the DFT representation of the ODF is defined as

$$f_b = \frac{1}{B} \sum_{k=0}^{B-1} F_k e^{\frac{2\pi i k b}{B}} \tag{2.34}$$

where $F_k = \Im(f_b)$, B denotes the number of individual bins in the orientation space indexed as b. The same DFT can be conducted on the discrete two-point correlations [117, 116, 186,

293], expressed as

$$F_{\boldsymbol{k}}^{np} = \Im(f_{\boldsymbol{t}}^{np}) = \frac{1}{|\boldsymbol{S_t}|}\sum_{\boldsymbol{s}=0}^{\boldsymbol{S_t}-\boldsymbol{I}}\sum_{\boldsymbol{t}=0}^{\boldsymbol{S_t}-\boldsymbol{I}} m_{\boldsymbol{s}}^{n} m_{\boldsymbol{s}+\boldsymbol{t}}^{p} e^{-\frac{2\pi i \boldsymbol{k}\boldsymbol{t}}{\boldsymbol{S_t}}} = \frac{1}{|\boldsymbol{S_t}|}\sum_{\boldsymbol{s}=0}^{\boldsymbol{S_t}-\boldsymbol{I}} m_{\boldsymbol{s}}^{n} \sum_{\boldsymbol{t}=0}^{\boldsymbol{S_t}-\boldsymbol{I}} m_{\boldsymbol{s}+\boldsymbol{t}}^{p} e^{-\frac{2\pi i \boldsymbol{k}\boldsymbol{t}}{\boldsymbol{S_t}}} \tag{2.35}$$

Let $\boldsymbol{s}+\boldsymbol{t}=\boldsymbol{z}$, then

$$F_{\boldsymbol{k}}^{np} = \frac{1}{|\boldsymbol{S_t}|}\sum_{\boldsymbol{s}=0}^{\boldsymbol{S_t}-\boldsymbol{I}} m_{\boldsymbol{s}}^{n} \sum_{\boldsymbol{z}=\boldsymbol{s}}^{\boldsymbol{S_t}-\boldsymbol{I}+\boldsymbol{s}} m_{\boldsymbol{z}}^{p} e^{-\frac{2\pi i \boldsymbol{k}(\boldsymbol{z}-\boldsymbol{s})}{\boldsymbol{S_t}}} = \frac{1}{|\boldsymbol{S_t}|}\sum_{\boldsymbol{s}=0}^{\boldsymbol{S_t}-\boldsymbol{I}} m_{\boldsymbol{s}}^{n} e^{-\frac{2\pi i \boldsymbol{k}(-\boldsymbol{s})}{\boldsymbol{S_t}}} \sum_{\boldsymbol{z}=\boldsymbol{s}}^{\boldsymbol{S_t}-\boldsymbol{I}+\boldsymbol{s}} m_{\boldsymbol{z}}^{p} e^{-\frac{2\pi i \boldsymbol{k}\boldsymbol{z}}{\boldsymbol{S_t}}} \tag{2.36}$$

Under the assumptions of periodic boundary conditions $m_{\boldsymbol{z}}^{p} = m_{\boldsymbol{z}+\boldsymbol{T}}^{p}$, we can get the following form:

$$F_{\boldsymbol{k}}^{np} = \frac{1}{|\boldsymbol{S_t}|}\sum_{\boldsymbol{s}=0}^{\boldsymbol{S_t}-\boldsymbol{I}} m_{\boldsymbol{s}}^{n} e^{-\frac{2\pi i \boldsymbol{k}(-\boldsymbol{s})}{\boldsymbol{S_t}}} \sum_{\boldsymbol{z}=0}^{\boldsymbol{S_t}-\boldsymbol{I}} m_{\boldsymbol{z}}^{p} e^{-\frac{2\pi i \boldsymbol{k}\boldsymbol{z}}{\boldsymbol{S_t}}} = \frac{1}{|\boldsymbol{S_t}|}(M_{\boldsymbol{k}}^{n})^{*} M_{\boldsymbol{k}}^{p} \tag{2.37}$$

where $*$ indicates the complex conjugate. When we take $n=p$, the autocorrelations can then be stated as

$$F_{\boldsymbol{k}}^{nn} = \frac{1}{|\boldsymbol{S_t}|}(M_{\boldsymbol{k}}^{n})^{*} M_{\boldsymbol{k}}^{n} = \frac{1}{|\boldsymbol{S_t}|}|M_{\boldsymbol{k}}^{n}|e^{i\theta_{k}^{n}}|M_{\boldsymbol{k}}^{n}|e^{-i\theta_{k}^{n}} = \frac{1}{|\boldsymbol{S_t}|}|M_{\boldsymbol{k}}^{n}|^{2} \tag{2.38}$$

where $|M_{\boldsymbol{k}}^{n}|$ represents the amplitude of the DFT and θ_{k}^{n} is the phase. Finally, a more efficient spectral representation of microstructure characterizations can be achieved through GSHF. For instance, the GSHF representation of the ODF [117, 116, 186] is defined as

$$\begin{aligned} f(g) &= \sum_{l=0}^{\infty}\sum_{m=-l}^{+l}\sum_{n=-l}^{+l} M_{l}^{mn} T_{l}^{mn}(g) \\ T_{l}^{mn}(g) &= T_{l}^{mn}(\varphi_1,\phi,\varphi_2) = e^{im\varphi_2} P_{l}^{mn}(cos\phi) e^{in\varphi_1} \end{aligned} \tag{2.39}$$

where P_{l}^{mn} are generalizations of associated Legendre functions, M_{l}^{mn} denotes the GSHF Fourier coefficients, and $T_{l}^{mn}(g)$ represents GSHF bases. It is critical to understand that the GSHF basis can be customized to reflect any desired crystal and sample symmetries by determining appropriate linear combinations of the unsymmetrized basis. For instance, symmetrized GSHF bases $\ddot{T}_{l}^{\mu n}(g)$ [186] for cubic-triclinic symmetry can be found as

$$\ddot{T}_{l}^{\mu n}(g) = \sum_{m=-l}^{+l} \ddot{A}_{l}^{m\mu}(g)\ddot{T}_{l}^{mn}(g) \tag{2.40}$$

where $\ddot{A}_l^{m\mu}(g)$ are the coefficients responsible for cubic crystal symmetry in GSHF. Another desired cubic-orthorhombic GSHF bases $\ddot{T}_l^{\mu n}(g)$ [86] are built as

$$\ddot{\ddot{T}}_l^{\mu n}(g) = \sum_{m=-l}^{+l} \sum_{m=-l}^{+l} \ddot{A}_l^{m\mu}(g) \dot{A}_l^{m\mu}(g) \ddot{T}_l^{mn}(g) \tag{2.41}$$

where $\dot{A}_l^{m\mu}(g)$ are the coefficients responsible for sample symmetry in GSHF. Then, the microstructure function with lattice orientation state [329] can be expressed as

$$\begin{aligned} m(\boldsymbol{x},g)dg &\approx \sum_{l,m,n} \sum_{\boldsymbol{s}=0}^{\boldsymbol{S}-\boldsymbol{I}} M_{l\boldsymbol{s}}^{mn} \ddot{T}_l^{mn}(g) \chi_{\boldsymbol{s}}(\boldsymbol{x}) dg \\ M_{l\boldsymbol{s}}^{mn} &= \frac{2l+1}{|\Delta \boldsymbol{x}|} \int_{FZ_g} \int_{\Omega_{\boldsymbol{x}}} m(\boldsymbol{x},g) \ddot{T}_l^{mn*}(g) \chi_{\boldsymbol{s}}(\boldsymbol{x}) d\boldsymbol{x} dg \end{aligned} \tag{2.42}$$

where $M_{l\boldsymbol{s}}^{mn}$ denotes the GSHF Fourier coefficients, $\ddot{T}_l^{mn}(g)$ represents symmetrized GSHF bases, $*$ indicates a complex conjugate, FZ is the fundamental zone, and $|\Delta \boldsymbol{x}|$ is the uniform volume of a spatial bin. In the particular case of a single crystal with lattice orientation g_o in a spatial bin $\boldsymbol{s}$, the appropriate GSHF Fourier coefficients are given by

$$M_{l\boldsymbol{s}}^{mn} = (2l+1) \ddot{T}_l^{mn*}(g_0) \tag{2.43}$$

When we replace the indicator functions with GSHF bases in Equation 2.29, the similar spectral representation of the two-point orientation correlation [329] by GSHF is defined as

$$\begin{aligned} f(g,g'|\boldsymbol{r})dgdg' &\approx \sum_K \sum_L \sum_{\boldsymbol{t}} F_{\boldsymbol{t}}^{LK} T_L(g) T_K(g') \chi_{\boldsymbol{t}}(\boldsymbol{r}) dgdg' \\ F_{\boldsymbol{t}}^{LK} &= \frac{1}{|\boldsymbol{S_t}|} \sum_{\boldsymbol{s}=0}^{\boldsymbol{S_t}-\boldsymbol{I}} M_{\boldsymbol{s}}^L M_{\boldsymbol{s}+\boldsymbol{t}}^K \end{aligned} \tag{2.44}$$

Where $T_L(g)$ and $M_{\boldsymbol{s}}^L$ are the abbreviated forms of T_l^{mn} and M_l^{mn}, respectively. Combining the GSHF representation of microstructure function in Equation (2.42), the definition in

Equation (2.45), the GSHF representation of autocorrelation [357, 112] may be derived as

$$\begin{aligned}
\bar{p}_{\boldsymbol{r}} &= \frac{1}{V_{FZ}} \int_{FZ} f(g,g'|\boldsymbol{r}) dg \\
&= \frac{1}{vol(\boldsymbol{\Omega}|\boldsymbol{r})} \frac{1}{V_{FZ}} \int_{g\in FZ} \int_{\boldsymbol{x}\in\boldsymbol{\Omega}|\boldsymbol{r}} m(\boldsymbol{x},g) m(\boldsymbol{x}+\boldsymbol{r},g') dg d\boldsymbol{x} \\
&= \frac{1}{vol(\boldsymbol{\Omega}|\boldsymbol{r})} \frac{1}{V_{FZ}} \int_{g\in FZ} \int_{\boldsymbol{x}\in\boldsymbol{\Omega}|\boldsymbol{r}} m(\boldsymbol{x},g) m^*(\boldsymbol{x}+\boldsymbol{r},g') dg d\boldsymbol{x} \\
&= \frac{1}{vol(\boldsymbol{\Omega}|\boldsymbol{r})} \frac{1}{V_{FZ}} \int_{g\in FZ} \int_{\boldsymbol{x}\in\boldsymbol{\Omega}|\boldsymbol{r}} \sum_{l,m,n} M_{l\boldsymbol{s}}^{mn} \ddot{T}_l^{mn}(g) \sum_{l,m,n} M_{l(\boldsymbol{x}+\boldsymbol{r})}^{mn*} \ddot{T}_l^{mn*}(g) dg d\boldsymbol{x} \\
&= \frac{1}{vol(\boldsymbol{\Omega}|\boldsymbol{r})} \frac{1}{V_{FZ}} \frac{1}{2l+1} \int_{\boldsymbol{x}\in\boldsymbol{\Omega}|\boldsymbol{r}} \sum_{l,m,n} M_{l\boldsymbol{s}}^{mn} M_{l(\boldsymbol{x}+\boldsymbol{r})}^{mn*} d\boldsymbol{x} \\
&= \frac{1}{|\boldsymbol{S_t}|} \frac{1}{V_{FZ}} \frac{1}{2l+1} \sum_{\boldsymbol{s}=0}^{\boldsymbol{S_t}-\boldsymbol{I}} \sum_{l,m,n} M_{l\boldsymbol{s}}^{mn} M_{l(\boldsymbol{x}+\boldsymbol{r})}^{mn*}
\end{aligned} \tag{2.45}$$

Where $m = m^*$ since m is a real value function, and $\int_{FZ} \ddot{T}_l^{mn}(g) \ddot{T}_{l'}^{m'n*'}(g) dg = \frac{1}{2l+1}$ if all the indices match else 0. The GSHF has been demonstrated to be more efficient for orientation and texture representation than DFT. In contrast, the DFT representation provides many computational advantages because of the fast Fourier transform (FFT) algorithms [116].

Principal component analysis

Principal component analysis (PCA) transforms high-dimensional data into a new orthogonal frame with axes sorted by observed variance. It is thus possible to derive an objective (data-driven) reduced-order representation of the original data using a truncated PCA representation [185]. For example, let $\{f_r|r = 1,2,...,R\}$ denote the truncated set of the independent two-point correlation. It is typically anticipated that PCA will identify a maximum of $(I-1)$ orthogonal directions in R-dimensional space ordered by decreasing degrees of variance in the provided ensemble of structures. Then the two-point correlation of the k-th microstructure in the ensemble can be mathematically expressed as

$$f_r^{(k)} = \sum_{i=1}^{min((I-1),R)} \alpha_i^{(k)} \varphi_{ir} + \bar{f}_r \tag{2.46}$$

where $k = 1,2,...,K$ indexes all microstructures in the ensemble, $\alpha_i^{(k)}$ (known as PC weights) represent an objective representation of the k-th structure in the new orthogonal reference frame identified by φ_{ir} (referred as PC bases). In contrast to other basis expansions (Fourier, Laplace, etc.), PC bases are not defined a priori and are instead determined based on the data.

In addition, maintaining the components correlated to the most significant inherent variance makes it frequently possible to generate an objective reduced-order representation of the two-point correlation with only a few parameters [171, 198, 293, 132], expressed as

$$f_r^{(k)} \approx \sum_{i=1}^{R^*} \alpha_i^{(k)} \varphi_{ir} + \bar{f}_r \tag{2.47}$$

where $R^* \ll min((I-1), R)$. The selection of R^* will rely on the particular qualities associated with the structure metrics.

The previous notions of PCA can be easily extended to other microstructure characterizations, including the orientation distribution function (ODF) [466], generalized Fourier series coefficients [330, 331], autocorrelation [112, 357], and chord length distribution [223, 107]. The PCA representations of the microstructure characterizations can perceive the inherent variance and perform quantitative analysis (regression, classification, etc.) in polycrystalline materials. This low-dimensional representation approach has been successfully used to extract high-fidelity PSPP linkages in terms of materials knowledge systems (MKS) [86, 430, 107, 198, 331, 422, 171, 330, 329], uncertainty quantification [112, 422], and surrogate crystal plasticity modeling [466, 293].

Representative aggregated microstructural parameters

Representative aggregated microstructural parameters (RAMPs) have been widely used in parametrically homogenized constitutive models (PHCMs) [322, 430, 447, 207, 323] and uncertainty quantification (UQ) [430, 322, 438] for accelerating PSPP linkage in the polycrystalline microstructure. The RAMPs provide a reduced representation of the crystallographic and morphological characterizations by a set $X_R = \left\{ \boldsymbol{I}^{tex}, \overline{OMA}_{\alpha\beta}, \bar{A}_{\theta_{mis},}, \bar{D}_g^{\mu}, \bar{D}_g^{\sigma} \right\}$, where $\boldsymbol{I}^{tex}$ denotes the second-order texture tensor, $\overline{OMA}_{\alpha\beta}$ indicates the lattice orientation with respect to material-symmetry axes, $A_{\theta_{mis}}$ represents the grain-pair misorientation parameter, $\bar{D}_g^{\mu}$ and $\bar{D}_g^{\sigma}$ are the mean and standard deviation of the grain size distribution. Detailed descriptions are itemized below:

- Texture intensity parameter and material-symmetry axes $(g_\alpha, \boldsymbol{v}_\alpha)$: The aggregated crystallographic c-axis orientation of hexagonal close-packed (HCP) crystals within a SERVE of the polycrystalline microstructure can be completely characterized by the symmetric, second-order texture tensor. It describes a weighted average of the c-axis poles, calculated as

$$\boldsymbol{I}^{tex} = \frac{1}{V} \sum_{k=1}^{n_{grains}} \hat{\boldsymbol{c}}^{(k)} \otimes \hat{\boldsymbol{c}}^{(k)} V^{(k)}, \quad I_{ij}^{tex} = \frac{1}{V} \sum_{k}^{n_{grains}} \hat{c}_i^{(k)} \hat{c}_j^{(k)} V^{(k)} \tag{2.48}$$

where $\hat{\boldsymbol{c}}^{(k)}$ and $V^{(k)}$ denotes the unit vector along the crystallographic c-axis and the volume of k-th grain in the microstructural SERVE of the total volume of V with the n_{grains} number of grains, The eigenvalues (g_α) and eigenvectors $(\boldsymbol{v}_\alpha)$ of $\boldsymbol{I}^{tex}$ reflect the respective RAMPs, also known as "texture intensity parameters" and "material-symmetry axe", respectively.

- Lattice orientation with respect to material-symmetry axes $(\overline{OMA}_{\alpha\beta})$: this RAMP quantifies the crystallographic slip system orientations in a reduced form by evaluating the density of the easy $< a >$ type slip systems relative to the material symmetry axes, defined as

$$\overline{OMA}_{\alpha\beta} = \frac{1}{V}\sum_{k=1}^{n_{grains}} Max\left\{\left|\boldsymbol{v}_\alpha \cdot \boldsymbol{S}^{(k)}_{0,basal} \cdot \boldsymbol{v}_\beta\right|, \left|\boldsymbol{v}_\alpha \cdot \boldsymbol{S}^{(k)}_{0,prism} \cdot \boldsymbol{v}_\beta\right|\right\} V^{(k)} \tag{2.49}$$

where $\boldsymbol{S}^{(k)}_{0,basal}$ and $\boldsymbol{S}^{(k)}_{0,prism}$ correspond to the Schmid tensors for basal-$< a >$ and prism-$< a >$ slip in the k-th grain.

- Grain-pair misorientation parameter $(\bar{A}_{\theta_{mis}})$: this RAMP quantifies the misorientation distribution by measuring the fraction of grain-pairs with less than 15° misorientation angle between their c-axes, defined as

$$\bar{A}_{\theta_{mis}} = \frac{\text{Grain boundary area with } \theta_{mis} < 15^\circ}{\text{Total grain boundary area in the polycrystalline SERVE}} \tag{2.50}$$

- Mean and standard deviation of the grain size distribution $(\bar{D}^{\mu}_{g}, \bar{D}^{\sigma}_{g})$: these RAMPs quantify the grain-size distribution by the mean $\bar{D}^{\mu}_{g}$ and standard deviation $\bar{D}^{\sigma}_{g}$ of a lognormal grain-size distribution.

The texture tensor $\boldsymbol{I}^{tex}$ can accurately capture individual micro-textures, so it is often selected as the basis for high-order characterization. This is exemplified by the two-point correlation function $S_2(\boldsymbol{r})$ [323], expressed as

$$\begin{aligned}
S^{EBSD}_{2,(p)}(\boldsymbol{r}) &= \frac{1}{A}\int_A \left[\hat{\boldsymbol{c}}(\boldsymbol{x}) \otimes \hat{\boldsymbol{c}}(\boldsymbol{x}) - \boldsymbol{I}^{tex}_{EBSD}\right] : \left[\hat{\boldsymbol{c}}(\boldsymbol{x}+\boldsymbol{r}) \otimes \hat{\boldsymbol{c}}(\boldsymbol{x}+\boldsymbol{r}) - \boldsymbol{I}^{tex}_{EBSD}\right] dA \\
\bar{S}^{EBSD}_{2,(p)}(\boldsymbol{r}) &= \frac{1}{A}\int_A \left[\boldsymbol{I}^{tex}(\boldsymbol{x}) - \boldsymbol{I}^{tex}_{EBSD}\right] : \left[\boldsymbol{I}^{tex}(\boldsymbol{x}+\boldsymbol{r}) - \boldsymbol{I}^{tex}_{EBSD}\right] dA \\
\bar{S}^{macro}_{2,(p)}(\boldsymbol{r}_k) &= \frac{1}{V}\sum_e \left[\boldsymbol{I}^{tex}(\boldsymbol{x}_e) - \boldsymbol{I}^{tex}_{EBSD}\right] : \left[\boldsymbol{I}^{tex}(\boldsymbol{x_e}+\boldsymbol{r_k}) - \boldsymbol{I}^{tex}_{EBSD}\right] V_e
\end{aligned} \tag{2.51}$$

Where $S^{EBSD}_{2,(p)}(\boldsymbol{r})$ is the two-point correlation function for microstructural EBSD scans on each of the orthogonal planes labeled with a subscript p, $\bar{S}^{EBSD}_{2,(p)}(\boldsymbol{r})$ is the generalized form

Table 2.4 Reduced-order algorithms for characterization representation in polycrystalline materials

Applications	Algorithms
Microstructure sensitive design (MSD)	Spectral methods (SM) [116, 8, 246, 438]
Materials knowledge system (MKS)	Spectral methods (SM) [363, 422, 331, 112, 171, 330, 329], Principal component analysis (PCA) [107, 198, 331, 422, 171, 330, 329]
Parametrically homogenized constitutive models (PHCMs)	Representative aggregated microstructural parameters (RAMPs) [322, 430, 447, 207, 323]
Uncertainty quantification (UQ)	Representative aggregated microstructural parameters (RAMPs) [430, 322, 438], Spectral methods (SM) [422], Principal component analysis (PCA) [112, 422]
Surrogate crystal plasticity modeling (SCPM)	Spectral methods (SM) [86], Principal component analysis (PCA) [466, 293], Representative aggregated microstructural parameters (RAMPs) [430, 447]
Additive manufacturing (AM)	Spectral methods (SM) [111, 357]

for macroscopic scale analysis, $\bar{S}^{macro}_{2,(p)}(\boldsymbol{r}_k)$ is the 3D case for macroscopic scale analysis, $\hat{\boldsymbol{c}}(\boldsymbol{x})$ denotes the unit vector along the crystallographic c-axis, $\boldsymbol{r}$ is a 2D vector separating two points $\boldsymbol{x}$ on the EBSD surface A, $\boldsymbol{I}^{tex}(\boldsymbol{x})$ centered at $\boldsymbol{x}$ is assessed over a sampling box in the EBSD image, $\boldsymbol{r}_k$ indicates a 2D separation vector between two elements on a given plane p, and V_e is the element volume such that $V = \sum_e V_e$.

Chapter 3

Literature review: physical and geometric reconstruction in polycrystalline materials

3.1 Introduction

Relying solely on imaging techniques to obtain the required microstructural data is insufficient. Firstly, getting high-quality microstructural images can be time-consuming and expensive. Secondly, capturing all random characteristics formed during processing is difficult, either because the experimental reconstruction lacks the required statistical homogeneity or because the parameter space is too vast to sample in an acceptable amount of time [215]. Synthetic microstructure (SM) models have recently become a reasonable alternative to experimental reconstruction for digital representation in polycrystalline materials. The SM models rely on a restricted number of parameters and allow for the reduction of stochastic errors in the underlying measurements. Generally, there are two types of SM models: physics-based and geometry-based [215, 28]. The physics-based models establish the PS linkages based on a physical description of the microstructure evolution that regulates the microstructure formation of polycrystalline materials during manufacturing processes. The cellular automata, Monte Carlo, vertex/front tracking, level set, machine learning, and phase field approaches are all used in the physics-based reconstruction of polycrystalline microstructures (Fig. 3.1). Meanwhile, geometry-based models generate an ensemble of statistically equivalent polycrystalline microstructures, often termed statistically equivalent representative volume elements (SERVEs) [316, 116, 276, 393], for the SPP linkages. The effective properties and statistical characterizations of the polycrystalline microstructure obtained by

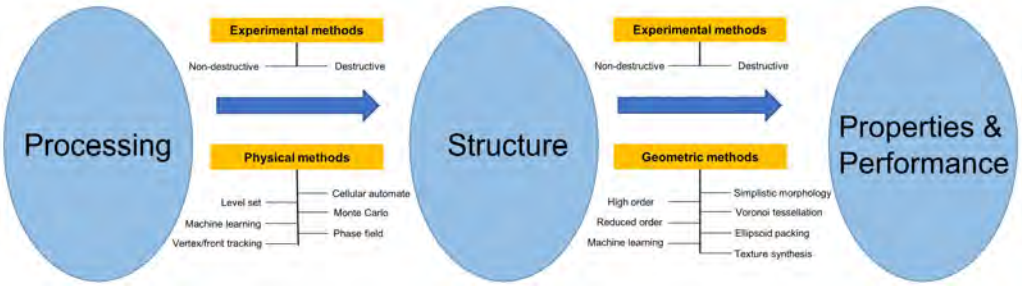

Fig. 3.1 Overview of digital reconstruction methods in mesoscopic polycrystalline materials for building PSPP linkages.

averaging the results from many geometric reconstructions are equivalent to those obtained from an RVE reconstruction [51, 393]. The simplistic morphology, Voronoi tessellation, ellipsoid packing, texture synthesis, high order, reduced order, and machine learning methods are all used in the geometric reconstruction of polycrystalline microstructures (Fig. 3.1).

This Chapter is a detailed description of physical and geometric reconstruction in polycrystalline materials. The steps, innovations, strengths and weaknesses in each reconstruction scheme will be elaborated on in detail.

3.2 Physical reconstruction

The energy is aggregated in polycrystalline microstructure during processing, and various evolutionary processes, such as solidification, grain coarsening, phase transformation and recrystallization, are activated to release the stored energy. One of the essentials for energy dissipation is grain nucleation and growth. Mechanisms of grain nucleation and growth are to some degree based on minimization of energy. Detailed descriptions are as follows:

- Grain nucleation: The classical Kolmogorov–Johnson–Mehl–Avrami model [205, 182, 16–18] introduces a variable X to establish the rate of grain nucleation, expressed as

$$X = 1 - exp\left(-Bt^{n_A}\right) \tag{3.1}$$

where t is the time, B and n_A are the Avrami coefficient and Avrami exponent, respectively. Drawbacks and improvements of the KJMA model could be found at [118, 428, 109]. Other models establish that there exists a critical dislocation density ρ_c for nucleation to take place [366, 333, 334, 375, 40]. The critical dislocation density

[366] is defined as

$$\rho_c = \left(\frac{20\gamma\dot{\varepsilon}^p_{eff}}{3blm\tau^2} \right)^{1/3} \tag{3.2}$$

where $\dot{\varepsilon}^p_{eff}$ is the rate of effective plastic strain, γ is the grain boundary energy, b is the Burgers vector, l is the dislocation mean free path, $\tau = \mu b^2/2$ is the dislocation line energy and μ is the shear modulus, A temperature-dependent Arrhenius relation can describe the grain boundary mobility m in the form

$$m = m_0 exp\left(-\frac{Q_m}{RT} \right) \tag{3.3}$$

where Q_m the activation energy for grain boundary migration, R is the universal gas constant, and T is the absolute temperature. The pre-exponential term m_0 can be considered as a function of temperature and crystallographic misorientation over the grain boundary [163]. The critical dislocation density is sometimes converted to a uniaxial, critical strain, and the strain can be further associated with the Zener-Hollomon parameter Z [165], written as

$$Z = \dot{\varepsilon}^p_{eff} exp\left(\frac{Q_d}{RT} \right) \tag{3.4}$$

where $\dot{\varepsilon}^p_{eff}$ is the rate of effective plastic strain, Q_d is the deformation activation energy, R is the universal gas constant, T is the absolute temperature. The rate of nucleation $\dot{n}$ corresponding to the proportional nucleation model [333, 334] takes into account a continuous nucleation process instead of the site-saturated nucleation, expressed as

$$\dot{n} = c\dot{\varepsilon}^p_{eff} exp\left(\frac{Q_n}{RT} \right) \tag{3.5}$$

where c is a constant, and Q_n is the activation energy for nucleation.

- Grain growth: after nucleation, the grains grow under a driving pressure p acting upon the grain boundaries. The velocity v at a grain boundary can be defined as

$$v = mp \tag{3.6}$$

where m is the boundary mobility [58, 133, 165]. The driving pressure p contains three components on the form

$$p = p_D + p_C + p_Z \tag{3.7}$$

where the component $p_C = -\frac{2\gamma}{r}$ is established on the grain boundary energy γ and the local grain boundary radius r. Additionally, the term $p_D = \tau[\rho]$ is related to the jump $[\rho]$ in dislocation density over the grain boundary. Finally, the term arising from the impurity particles drag through particle pinning is given by

$$p_Z = -z_1\gamma\frac{f_V^{z_2}}{r_p} \tag{3.8}$$

where the z_1 and z_2 are the z_i parameters [399, 255, 313, 167], γ is the grain boundary energy founded on the crystallographic misorientation angles [362, 455] and f_V is the volume fraction of particles with radius r_P.

For further elaboration on the mechanisms of grain nucleation and growth, readers may refer to the review papers [162, 98, 289, 139] and books [356, 174, 165]. Consequently, numerous models have been successfully developed to reconstruct the physical processing based on grain nucleation and growth. Illustrations of the range of techniques include the cellular automata, Monte Carlo approaches, vertex methods, level set and phase field models. The cellular automata and Monte Carlo approaches focus on the reconstruction of grain geometry through grid discretization. Moreover, the vertex methods, level set and phase field models focus on the generation of grain boundary via motion equation.

3.2.1 Cellular automata

The cellular automata [355, 356, 174, 139, 28] algorithm is founded on three basic principles: (a) grid discretization (discretizes the domain into cells allocated with various state features), (b) cell neighborhood (identifies its closest neighbors) (Table 1.1), and (c) transformation rules (update the changes in the cell states) aiming for the prediction of both spatial and temporal evolution in polycrystalline microstructures. Summarized steps are illuminated below:

- State generation: the analytical domain is first discretized into grids of sub-regions, namely the cells. The grid is regular in most cases, but random [173] and irregular [465] cases are feasible as well. The next step is to assign state variables (e.g., dislocation density or crystal orientation) to each cell. The initial state can be performed by random setting at suitable nucleation sites or collected through experimental data from physical samples.

- State update: after state generation, the discrete-time steps solutions are conducted to update the state variables of all cells according to the transformation rules. In each

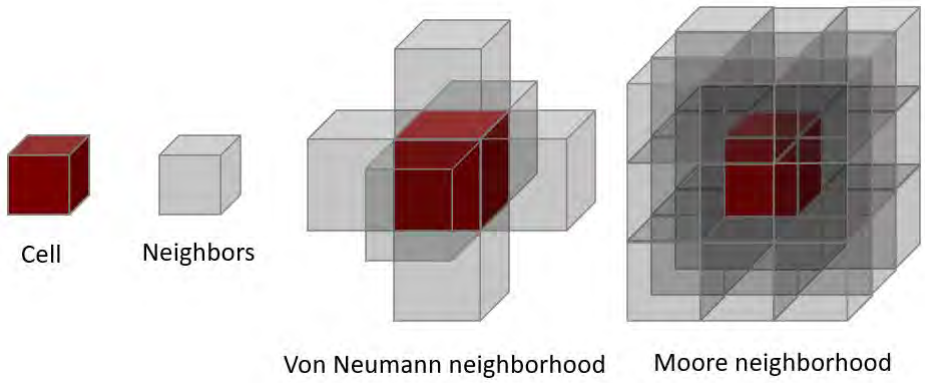

Fig. 3.2 Illustration of the 3D cellular automata with square cells. Two common types of neighborhood for a cell are illustrated: von Neumann neighborhood and Moore neighborhood

time step, the neighborhood of each cell is determined. Then the transformation rules are employed to identify the update state of each cell relying on its previous state and the previous state variables of its neighbors. Both deterministic [152] and probabilistic [353, 371, 140] switching rules are possible, and one of the probability criteria could be defined as

$$w_{switch} = \frac{v}{v_{max}} \tag{3.9}$$

where w_{switch} is the local switching probability, v is the local grain boundary velocity in Equation. 3.6 and v_{max} is the maximum velocity in the analytical domain for the previous time step. In each time step, a random number $\varepsilon \subset [0,1]$ is created. if $\varepsilon \leq w_{switch}$, the switch is approved, otherwise it is denied.

The cellular automata are efficient and relatively easy to perform once an appropriate transformation rule is selected. Therefore, it has been widely used to capture the microstructure evolution during processing in polycrystalline materials. Illustrations include solidification [81, 361, 403, 57, 479, 332, 442], recrystallization [152, 353, 95, 173, 213, 477, 465, 140, 49, 380, 476, 342, 214] and phase transformation [49, 476]. In addition, parallel computing is viable in cellular automata since each cell's state update is established on the data from a local neighborhood. Finally, grid discretization contributes to a convenient structure for automatic mesh generation, which makes cellular automata well combined with computational simulations. On the one hand, the simulation results can be assigned to the initial state generation [289, 381, 380, 342, 220]. In addition, the evolutional microstructure from cellular automata can be conveyed to the computational simulations for mechanical investigation [381, 380, 342]. Drawbacks of cellular automata lie mainly in the aliased representation of grain boundaries and the time and length scale explanation.

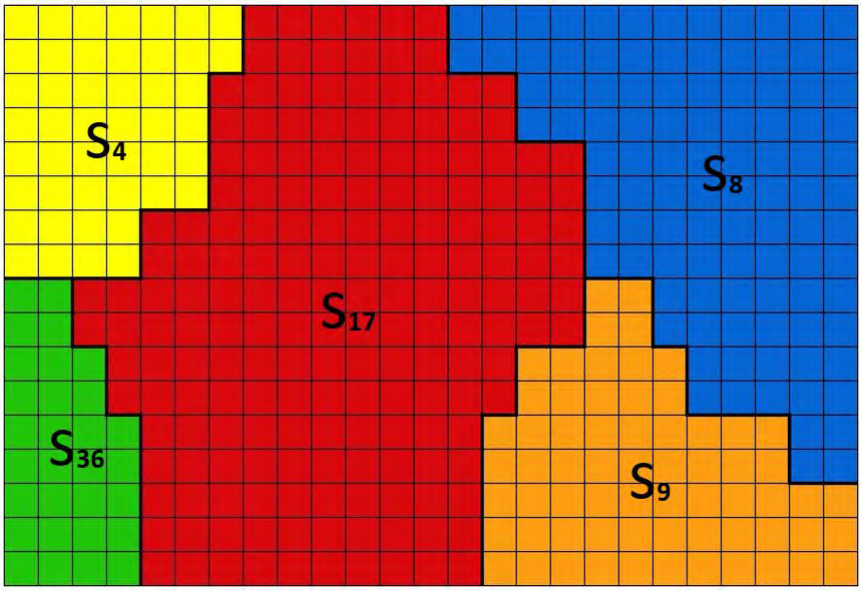

Fig. 3.3 Illustration of a 2D grain structure mapped onto a square lattice. All lattice sites belonging to a common grain share the same lattice index S_i. Grain boundaries are drawn with thicker lines.

3.2.2 Monte Carlo approaches

The key idea of the Monte Carlo method [370, 289, 356, 174, 139, 28] aims to perform a quantitative probabilistic analysis of practicable polycrystalline microstructure through repeated random sampling. Both grid discretization and discrete solution steps are implemented in the Monte Carlo approach. In each time step, a set of random states is proposed and validated until the expected grain distributions are met. Detailed information is presented as follows:

- State generation: similar to the cellular automata, the analytical domain is first discretized into grids of sub-regions, namely the lattices. The next step is to map the lattice structure into a polycrystalline structure with N lattice sites. Each lattice site s_i corresponding to the single grain is represented by a set of neighboring lattices with the same parameters (e.g., dislocation density or crystal orientation) (Fig. 3.3). The state parameters for each lattice site can be performed by random generation or collected through experimental data from physical samples. The total energy E of the analytical domain could be defined as

$$E = \sum_{i=1}^{N} \left(\sum_{j=1}^{n} \frac{1}{2} \gamma(s_i, s_j) + E_s(s_i) \right) \tag{3.10}$$

where n is the number of neighboring lattice sites for each individual lattice site s_i, the grain boundary energy $\gamma(s_i, s_j)$ as discussed in Equation (3.8) is a function of the lattice site s_i and its neighbors s_j, E_s the stored dislocation density energy at the lattice site s_i, and the grain boundary energy $\gamma(s_i, s_j)$ on lattice sites can be expressed as [474]

$$\gamma(s_i, s_j) = J \sum_{j=1}^{n} \left(1 - \delta_{O_{s_i} O_{s_j}}\right) \tag{3.11}$$

where J represents constant, δ means the Kronecker symbol, and O_{s_i} and O_{s_j} are orientations of the current lattice site s_i and its neighbor.

- State update: after state generation, Monte Carlo sampling of the analytical domain is performed to update the state parameters of lattice sites. This can be achieved by suggesting new state parameters for individual lattice site or switching state parameters between lattice sites in pairs. In each time step, the energy change ΔE from Equation (3.10) is calculated to determine the random sampling is accepted or rejected, and one of the probability criteria could be written as

$$w_{switch}(\Delta E) = \frac{1}{2} w_0 \left[1 - tanh\left(\frac{\Delta E}{2kT_s}\right)\right] \tag{3.12}$$

where w_{switch} is the switching probability, w_0 is the reduced mobility, k is the Boltzmann constant and T_s is the simulation temperature. For each sampling, a random number $\varepsilon \subset [0, 1]$ is created. if $\varepsilon \leq w_{switch}$, the switch is approved, otherwise it is denied.

Like the Cellular automata, the Monte Carlo approach is straightforward for implementation. Additionally, high computational efficiency can be realized via parallel computing. Therefore, it has been widely used not only to represent various physical processes [354, 172] but also to simulate the microstructure evolution under different processing conditions [156, 356]. In terms of reconstruction and simulation, software packages are available for public utilization, including the SPPARKS [338], PCLab [251] and MCMicro [265]. Limitations of Monte Carlo approaches lie mainly in the undesired derivation of grain boundaries and the physical length and time scales explanation.

3.2.3 Vertex methods

Vertex or front tracking methods [191, 311, 370, 452, 453, 289, 139, 28] simplify the complexity of polycrystalline microstructure during the evolution process since they only

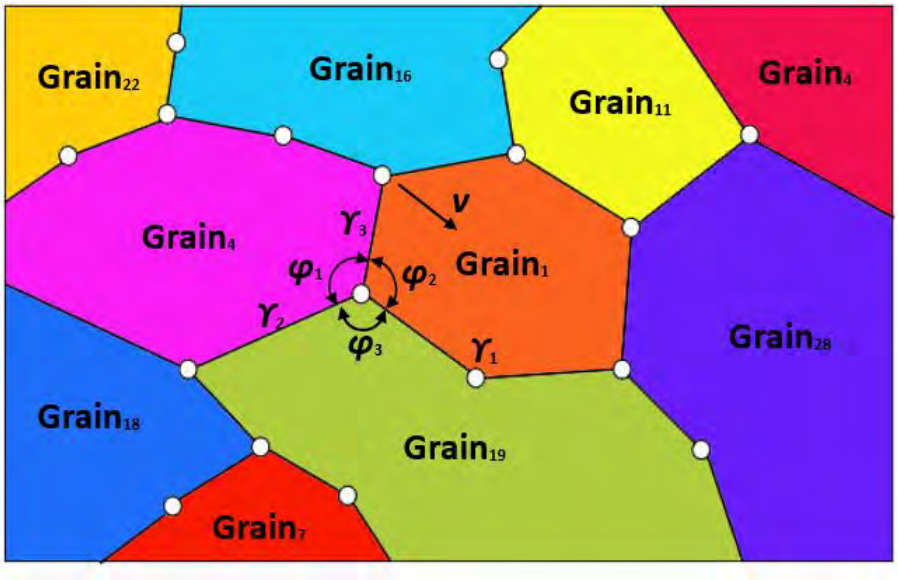

Fig. 3.4 Vertex model representation of polycrystalline microstructure. a triple junction between three boundaries have the interface energies $\gamma_{1,2,3}$ and the separation angles $\varphi_{1,2,3}$. The nodes are indicated by circles and the local velocity v of a node is shown.

concentrate on the movement of vertices rather than the curved grain boundaries. Details are elaborated below:

- Structure representation: the grain boundaries are represented by line segments connected at vertices or nodes (Fig. 3.4). The vertices could be located solely at triple (in 2D) or quadruple (in 3D) junctions [311, 162, 166] or possibly at additional intermediate positions along the grain boundaries [452]. The triple or quadruple junctions in vertex models are hypothetically subjected to an equilibrium state, represented as

$$\frac{\gamma_1}{sin\varphi_1} = \frac{\gamma_2}{sin\varphi_2} = \frac{\gamma_3}{sin\varphi_3} \tag{3.13}$$

  With the notation demonstrated in Fig. 3.5, where γ_i are the grain boundary energies and φ_i are the equilibrium separation angles.

- Motion equation: the evolution process of a line segment is modeled as completely dissipative. The grain boundary energy is defined as

$$C(\boldsymbol{x}) = \int_a \gamma da \tag{3.14}$$

and the dissipative function is given by

$$R(\boldsymbol{x},\boldsymbol{v}) = \int_a \frac{v^2}{m}\, da \tag{3.15}$$

where a is a segment length between two vertices, γ is the grain boundary energy discussed in Equation (3.8), v and m are the local grain boundary velocity and boundary mobility introduced in Equation (3.6). The total grain boundary energy and dissipation function are performed over all boundary segments, expressed as

$$\begin{aligned} C &= \frac{1}{2}\sum_{i=1}^{N}\sum_{j=1}^{(i)} \gamma_{ij}\left\|\boldsymbol{x}_{ij}\right\| \\ R &= \frac{1}{6}\sum_{i=1}^{N}\sum_{j=1}^{(i)} \frac{\left\|\boldsymbol{x}_{ij}\right\|}{m_{ij}}\left[(\boldsymbol{v}_i\boldsymbol{n}_{ij})^2 + (\boldsymbol{v}_j\boldsymbol{n}_{ij})^2 + (\boldsymbol{v}_i\boldsymbol{n}_{ij})(\boldsymbol{v}_j\boldsymbol{n}_{ij})\right] \end{aligned} \tag{3.16}$$

where N is the total number of vertices in the analytical domain, $\sum_{i=1}^{(i)}$ is the summation for all the segments j connected at vertex i, $\boldsymbol{x}_{ij}$ is a boundary segment between the points $\boldsymbol{x}_i$ and $\boldsymbol{x}_j$, γ_{ij}, m_{ij} and $\boldsymbol{n}_{ij}$ are the grain boundary energy, boundary mobility and normal vector related to the boundary segment between the points $\boldsymbol{x}_i$ and $\boldsymbol{x}_j$, $\boldsymbol{v}_i$ and $\boldsymbol{v}_j$ are the local grain boundary velocity at the points $\boldsymbol{x}_i$ and $\boldsymbol{x}_j$. The motion equation for a single vertex k can then be acquired from

$$\frac{\partial C}{\boldsymbol{x}_k} + \frac{\partial R}{\boldsymbol{v}_k} = 0, \quad i = 1,2,...,N \tag{3.17}$$

More details on the above derivations are reported in [311, 452].

- Discrete solution: discretizing the grain boundaries by triangular elements and the new locations of the vertices are calculated as

$$\boldsymbol{x}_k(t+\Delta t) = \boldsymbol{x}_k(t) + \boldsymbol{v}_k(t)\Delta t, \quad k = 1,2,...,N \tag{3.18}$$

where the velocities $\boldsymbol{v}_k$ are obtained from Equation (3.18), Δt is the time step. Topological difficulties can arise during the discrete solution, and corresponding treatment of vertices has to be established. Examples include, non-planar grain boundaries [115], biased small grains [452], detaching grains [454, 417] and quadruple junction mobility [297, 296].

The merits of vertex methods are reasonable physical time scale interpretation [452] and better representation of grain boundaries. However, the additional intermediate vertices

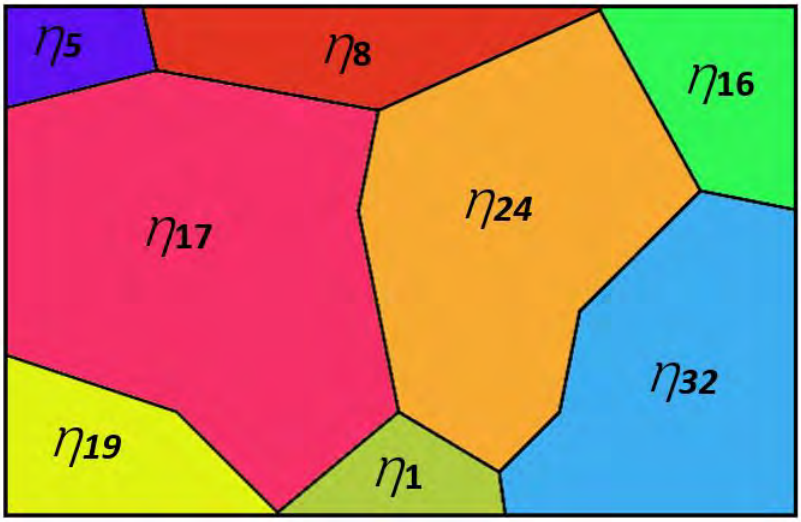

Fig. 3.5 Schematic representation of a grain microstructure using the orientation parameters η_k. Grain boundaries are indicated with solid lines.

for curved grain boundaries are more computationally demanding, and special numerical techniques concerning topological variations have to be employed. This makes it less widely used in physical reconstruction as compared to cellular automata and Monte Carlo approaches.

3.2.4 Phase field models

In phase field models [69, 356, 294, 409, 174, 350, 348, 139, 28], the polycrystalline microstructure is identified as phase field variables. Meanwhile, the grain boundaries are illustrated as diffuse transition interfaces where the value of phase field variables (ranging from 0 to 1) between adjacent grains changes continuously or sharply. Possible boundary evolutional conditions are described as partial differential equations, and phase field variables can be calculated from the motion equation through discrete solutions. The principal steps are described below:

- Structure representation: the phase field variables in polycrystalline microstructure are further subdivided into conserved and non-conserved variables. The conserved variables measure the local composition information and could represent a conserved concentration of solute atoms [106]. In contrast, the non-conserved variables include local structure information and could describe the crystallographic orientation [105]. Generally, there are two phase-field methods based upon non-conserved phase fields: a) the continuum phase field approach [211, 295] and b) multi-phase field approaches

[410, 199, 295]. In both methods, a large group of non-conserved phase field variables or order parameters η_k are utilized to describe the crystallographic orientations (Fig. 3.5). The main difference is the explanation of the phase field variables. In the continuum phase field approach, the phase field variables are independent, and the value of these variables vary monotonously between diffuse boundary interfaces without any restrictions. However, in the multi-phase field approach, the N coexisting phase field variables correspond to the volume fractions of each phase and are subject to the constraint

$$\sum_{k=1}^{N} \eta_k = 1, \quad where \quad \eta_k \geq 0, \quad \forall k \tag{3.19}$$

which has to be satisfied at each position in the analytical domain.

- Motion equation: the energy in the phase field models is defined as a function of the phase field variables and their gradients, written as

$$E = \int_V \left[f(c_i, \eta_k) + \sum_{i=1}^{n} \frac{\varepsilon}{2} (\bigtriangledown c_i)^2 + \sum_{k=1}^{N} \frac{\zeta_k}{2} (\bigtriangledown \eta_k)^2 \right] dV \tag{3.20}$$

where c_i and η_k are the conserved variables and non-conserved variables respectively, n and N are the corresponding number of conserved variables and non-conserved variables, V is the entire volume of the analytical domain, f is the local energy density function for each conserved variable c_i and non-conserved variable η_k, ε and ζ_k are the gradient energy coefficients related to the interface width and the interface energy controlling the diffuse translation of interfaces. After establishing the energy equation, the evolution laws for the conserved variables c_i and the orientation variables η_k are followed. This can be performed by utilizing the Cahn–Hilliard Equation [61] for the conserved variables c_i and the time-dependent Ginzburg–Landau or Allen–Cahn Equation [10] for the non-conserved variables η_k, expressed as

$$\begin{aligned} \dot{\eta}_k &= -L_k \frac{\delta E}{\delta \eta_k}, \quad k = 1, 2, ..., N \\ \dot{c}_i &= \bigtriangledown \left[D_i \bigtriangledown \left(\frac{\delta E}{\delta c_i} \right) \right], \quad i = 1, 2, ..., n \end{aligned} \tag{3.21}$$

where L_k and D_i are kinetic coefficients associated with the grain boundary mobilities and atomic diffusion, respectively.

- Discrete solution: The conserved and non-conserved variables in Equation (3.21) can be solved via numerical methods, such as finite differences, finite elements, or spectral

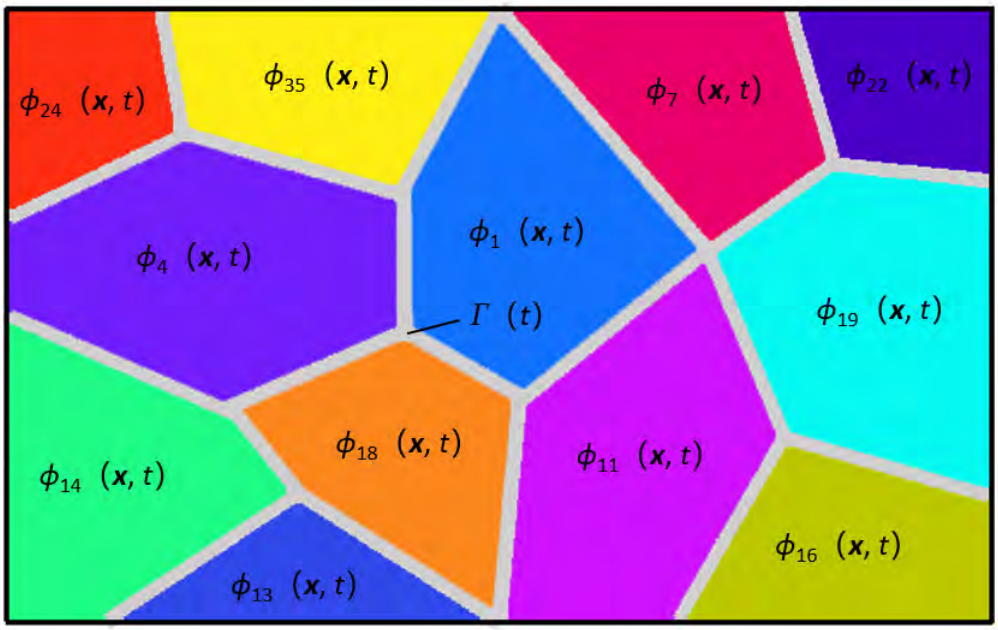

Fig. 3.6 Schematic representation of a grain microstructure using the level set function $\phi_i(\boldsymbol{x},t)$. Grain boundaries are indicated with white lines.

algorithms. In addition, grid adaptability is frequently performed to represent the diffuse transition interfaces better. Random small values are first assigned to the phase field variables. Then they are computed iteratively at every node of the discretized domain in each time step until the convergence criterion is met.

The diffuse transition treatment of grain boundaries can trace arbitrary interface geometries and generate complex and large grain morphologies. Thus, the phase field models can better reconstruct the grain boundaries than cellular automata and Monte Carlo approaches, which makes it successfully applied to simulate solidification [425, 47, 211, 445, 314, 199, 295], grain coarsening [426] and recrystallization [425, 211, 295, 199]. The disadvantages mainly reside in the high-intensity computation and less implementation for parallelization.

3.2.5 Level set models

The level set models [252, 37, 36, 39, 38, 139, 103, 102] are the relatively latest development compared to cellular automata and Monte Carlo approaches. Similar to the phase field models, the moving interfaces $\Gamma(t)$ represent the grain boundaries. Possible boundary evolutional conditions are described as continuous equations $\phi(\boldsymbol{x},t)$, and boundary location information can be calculated from the motion equation through discrete solutions. The core content is presented as follows:

- Structure representation: for polycrystalline microstructure containing N grain, an independent level set function $\phi_i(\boldsymbol{x},t)$ is assigned to each grain (Fig. 3.6). The zero set of the function then determines the boundary interfaces $\Gamma(t)$, expressed as

$$\phi_i(\boldsymbol{x},t) = d(\boldsymbol{x},\Gamma), \quad \Gamma = \{\boldsymbol{x} \in \Omega, \phi_i(\boldsymbol{x},t) = 0\} \quad \boldsymbol{x} \in \Omega, \quad i = 1,2,...,N \tag{3.22}$$

  where $\boldsymbol{x}$ is any point in the analytical domain Ω, and $d(\boldsymbol{x},\Gamma)$ is the Euclidean distance between any point $\boldsymbol{x}$ and boundary interfaces $\Gamma(t)$. Moreover, the level set function $\phi_i(\boldsymbol{x},t)$ is greater than zero inside grain G_i and less than zero outside grain G_i.

- Motion equation: the motion of the interfaces $\Gamma(t)$ is described as

$$\frac{\partial \phi}{\partial t} + \boldsymbol{v} \bigtriangledown \phi = 0, \quad i = 1,2,...,N \tag{3.23}$$

  where $\boldsymbol{v}$ is the interface velocity corresponding to the grain boundary velocity in Equation (3.6), and the location of the interface Γ_i of grain G_i is specified implicitly by the equation $\phi_i(\boldsymbol{x},t) = 0$. The initial value of the Equation (3.23) is often treated as a signed distance function. Meanwhile, the re-initialization techniques [39] are introduced and applied periodically to maintain the properties of a distance function during the numerical treatment.

- Discrete solution: the Equation (3.23) can be solved through the finite element method [252, 37, 36, 39, 38] or the finite difference scheme [103, 102]. Each level set function can evolve independently during each time step in the discrete solution. A correction or smoothing operation is utilized at the end of each time step to restore the topology aiming for avoiding overlapping domains or voids between interfaces [281]. Also, the sharp interfaces defining grain boundaries must be resolved for the adaptivity of the element mesh or solution grid [39].

As with the phase field models, the level set models avoid the complex problem of explicit tracing of interfaces as in the vertex methods. Also, they can provide a direct representation of interfaces and curvature, which is challenging to achieve in cellular automata and Monte Carlo approaches. Disadvantages reside in the expensive computational consumption and unpractical parallel computing.

3.3 Geometric reconstruction

Geometric reconstruction methods ignore the physical microstructural formation process and focus solely on polycrystalline materials' morphological and crystallographic information generation. Generally, geometric reconstructions are grouped into three major categories: shape-based reconstruction, texture synthesis, and others. Details of them will be elaborated on in the following section.

3.3.1 Shape-based reconstruction

In shape-based reconstruction, some simplified shapes like cubes [31], rhombic dodecahedrons [287, 286], truncated octahedrons [180], Voronoi polyhedrons [127], ellipsoids [384], have been used to represent the grain morphologies. A considerable amount of literature has been published on grain-based reconstruction, most of which is associated with Voronoi tessellation and ellipsoid packing. In light of this, the grain-based reconstruction could be divided into three groups: (a) simplistic regular morphologies (cubes, rhombic dodecahedrons, and truncated octahedrons); (b) Voronoi tesselation; and (c) ellipsoid packing. The next part sheds light on these three sections.

Simplistic regular morphologies

As pioneers in polycrystalline reconstruction, simplified grain morphologies have been widely used to establish a connection between microscopic structure and macroscopic properties. The regular microstructures (Fig. 3.7) facilitate numerical modeling and provide a novel mechanism to investigate the grain shape effects on grain interaction [382, 437], crystallographic texture evolution [383, 30], intergranular stress corrosion cracking [180] and aggregate response [365]. In [187], the grains were represented by 2D homogenized finite square elements to simulate the crystallographic texture evolution. In [31], the finite brick element has been used to represent a single averaged grain for the connection study between micro and macro variables in crystal plasticity deformation. Another regular morphology has been employed by [287, 286], who hypothesized the single fcc grain as a rhombic dodecahedral. They aims to investigate the crystal shape effect on the intergranular interaction. The main conclusion is that it is easier to study how grains interact with each other when they have better shapes and smaller gaps between them. The truncated octahedra-based grains have been proposed by [180] to check the stress corrosion cracking between grains. Moreover, it is concluded by [89] that the truncated octahedra grains can achieve a better crystallographic texture evolution prediction than the cubic grains. [365] represented grains

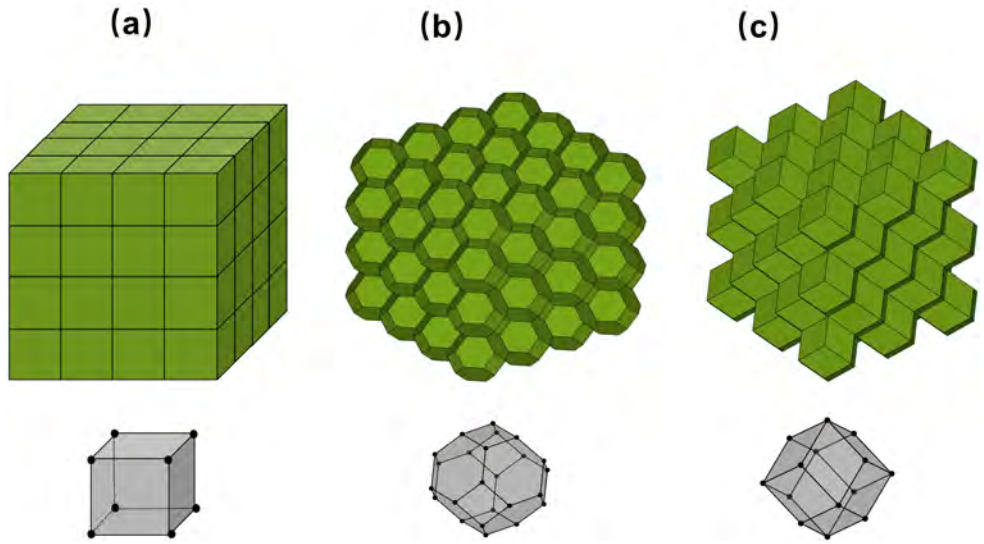

Fig. 3.7 Schematic presentation of the reconstructed polycrystalline microstructures with simplistic regular morphologies: (a) Cubes, (b) Truncated octahedrons, and (c) Rhombic dodecahedrons;

as the cubic, rhombic dodecahedral, and truncated octahedral morphologies simultaneously to examine the shape effect on grain aggregate mechanical response. They found that these simplified regular morphologies caused similar intergranular and intragranular stress distributions.

Voronoi tessellation

The Voronoi tessellation [127] originates from the Johnson and Mehl recrystallization model [182]. It divides the space into Voronoi polyhedrons, which form when random seeds start to grow and join together. The primary steps are summarized as follows:

- Seeds generation: defining a 3-D space $\boldsymbol{D} \in \boldsymbol{R}^3$ and allocating N seed points $\{S_i \in \boldsymbol{D} | i = 1,2,...,N\}$ to it. The coordinates of each seed could be random or achieved by the Poisson point process.

- Voronoi tesselation: each seed is associated with a Voronoi polyhedron $\boldsymbol{VP}(S_i)$, the space area of $\boldsymbol{VP}(S_i)$ is identified in Equation (3.24) with the set points $P(x,y,z)$.

$$\boldsymbol{VP}(S_i) = \{P(x,y,z) \in \boldsymbol{D} | d(P,S_i) < d(P,S_j), \quad \forall i \neq j \; i,j = 1,2,...,N\} \tag{3.24}$$

  where $d(P,S)$ is the Euclidean distance between the set point P and seed point S.

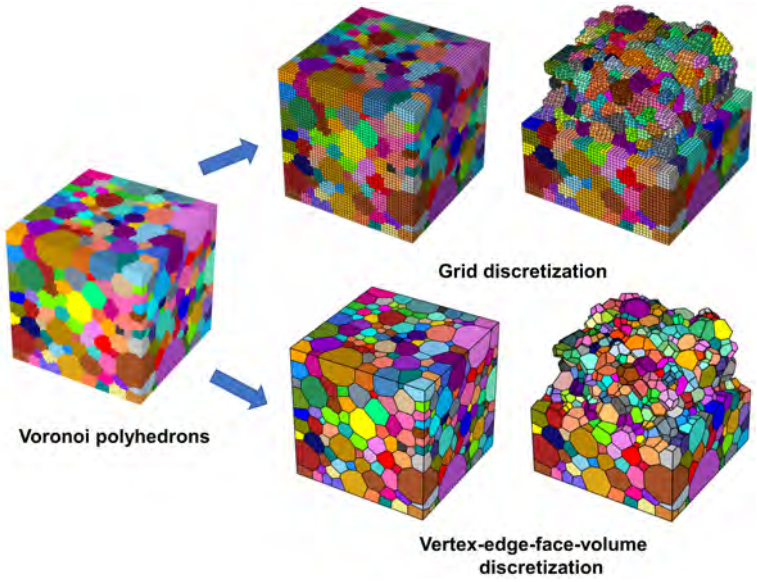

Fig. 3.8 Schematic presentation of the grid and vertex-edge-face-volume discretization for Voronoi polyhedral. Generated from the open-source software Neper [351].

- Space discretization: specifying the space area of each Voronoi polyhedron $\boldsymbol{VP}(S_i)$ by discretizing the whole domain.
- Orientation assignment: assigning crystallographic orientations to each Voronoi polyhedron $\boldsymbol{VP}(S_i)$.

For more efficient calculations, the hierarchical queue algorithm [358] has been used to implement the Euclidean distance function. The boundary recognition of the Voronoi polyhedron depends primarily on the distance to the corresponding seed. Alternatively, the relief immersion algorithm [284] derived from the watershed division has also been adopted to identify the boundary. The crystallographic orientation assignment could be based on a uniform distribution or a map extracted from an image reference [177]. Focusing on the space discretization, either grid [26, 319, 91] or vertex-edge-face-volume [217, 218, 91] method has been used in the Voronoi tessellation (Fig. 3.8). In the grid discretization, [468] generated 3D random Voronoi polyhedrons with a common constrained surface. They first produced the grains below the constrained surface through eroding or expanding neighbouring voxels and immediately implemented the Voronoi tessellation to fill the remaining space. In the vertex-edge-face-volume discretization, the level set method and Voronoi tessellation have been combined to model recrystallization [37]. [114] developed the grain edge splitting procedure for generating 3D periodic high-quality elements. To address the over-discretization refinement problem caused by the inevitable emergence of small Voronoi polyhedrons, [351]

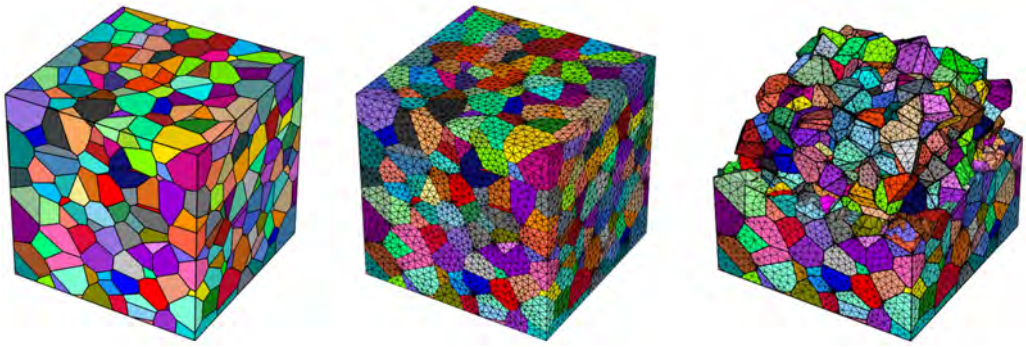

Fig. 3.9 Schematic presentation of the multi-meshing and re-meshing of 3D large-scale Voronoi polyhedrons. Generated from the open-source software Neper [351].

proposed a novel algorithm for the geometry regulation, multi-meshing, and re-meshing of 3D large-scale random polycrystals (Fig. 3.9).

[97] compared Voronoi tesselation with experimental reconstruction and highlighted that Voronoi tesselation overestimated the grain nearest neighbor distribution and underestimated the grain volume distribution. This is because the Voronoi tessellation, also known as the Poisson-Voronoi tessellation, randomly chooses the seed points following the Poisson-Voronoi distribution [29], which undoubtedly leads to a biased representation of the grain size distribution compared with experimental observations [215]. To obtain a more realistic grain size distribution, the controlled Poisson-Voronoi tessellation model involving a single control parameter has been developed to capture realistic grain morphologies [472, 473]. In [318], molecular dynamics and discrete element techniques have been combined to pack the particles with controlled grain size distributions. [395, 29, 416] utilized genetic algorithms to modify the Poisson-Voronoi tessellation to represent the size distribution more accurately, and [120] proposed a constraint Voronoi model to generate an approximate representation of the 3D polycrystalline microstructure for interpreting surface microstructural measurements. The power diagram (also known as the Laguerre diagram [15, 108, 352]) helps set the size of each Laguerre polyhedron $\boldsymbol{LP}(S_i)$ by adding a non-negative weight w_i:

$$\begin{aligned} \boldsymbol{LP}(S_i) &= \{P(x,y,z) \in \boldsymbol{D} | d_L(P,S_i) < d_L(P,S_j), \quad \forall i \neq j \; i,j = 1,2,...,N\} \\ d_L(P,S_\bullet) &= d_E(P,S_\bullet)^2 - w_\bullet \end{aligned} \tag{3.25}$$

where d_L is the power distance and d_E is the Euclidean distance. In recent years, Laguerre-Voronoi (LV) has been widely adopted as an alternative to Poisson-Voronoi (PV) [215, 143, 90, 352, 300]. It has been demonstrated that the LV diagram generates more accurate polycrystalline structures than the PV diagram. There are some open-source packages for Voronoi tessellation, such as Neper [351] (https://neper.info/) (Fig. 3.9), Voro++ [379]

(http://math.lbl.gov/voro++/), Qhull [27] (http://www.qhull.org/), and MicroStructPy [143] (https://docs.microstructpy.org/en/latest/).

3.3.2 Ellipsoid packing

Microstructural features generated by Voronoi tessellation could deviate directly from experimental observations. So, to make a polycrystalline structure whose morphological and crystallographic descriptions match the observed values, we need more precise geometric units and better statistical algorithms. Due to its good geometric properties, the ellipsoid seems to be one of the best choices. Initially, significant improvement was made by [384] where ellipsoids were used to represent grains for the reconstruction of the aluminium polycrystal. The details of the algorithm are given as follows:

- Ellipsoid generation: generating ellipsoids from the 2D experimental observations. Fig. 3.10 depicts the generation process. Fig. 3.10(a) presents the 2D EBSD scan perpendicular to the sample's normal direction. Fig. 3.10(b) shows that grains are fitted by ellipses. After that, distributions of ellipse semiaxes $f(a')$, and $f(b')$ can be accessed. Similarly, when selecting the 2D EBSD scan perpendicular to the sample's rolling direction, distributions of ellipse semiaxes $f(b')$, and $f(c')$ can be accessed as well. Here $\{a', b', c'\}$ are the semiaxes of the ellipse. What follows is an approximate calculation of the distribution of ellipsoid semiaxes,

$$< a' >= a\pi/4, a \approx 4a'/\pi; < b' >= b\pi/4, b \approx 4b'/\pi; < c' >= c\pi/4, c \approx 4c'/\pi \tag{3.26}$$

  where $\{a, b, c\}$ are the semiaxes of the ellipsoid (Fig. 3.10(c)). Moving on next is to quantify the joint probability distribution $f(a,b)$ or $f(c,b)$ and the conditional probability distribution $f(c|b)$ or $f(a|b)$. Finally, the true 3D ellipsoid distribution can be estimated by Equation (3.27) [384].

$$f(a,b,c) = f(a,b) \cdot f(c|b) = f(c,b) \cdot f(a|b) \tag{3.27}$$

- Ellipsoid packing: packing ellipsoids into a specified space. This is implemented by sampling a set of overlapping ellipsoids from the distribution $f(a,b,c)$ and randomly putting them into the specified space.

- Space discretization: specifying the space area of each ellipsoid without overlapping by discretizing the whole domain. The grid discretization is applied first to partition the entire domain into cubic lattices. Immediately after, the cellular automaton algorithm

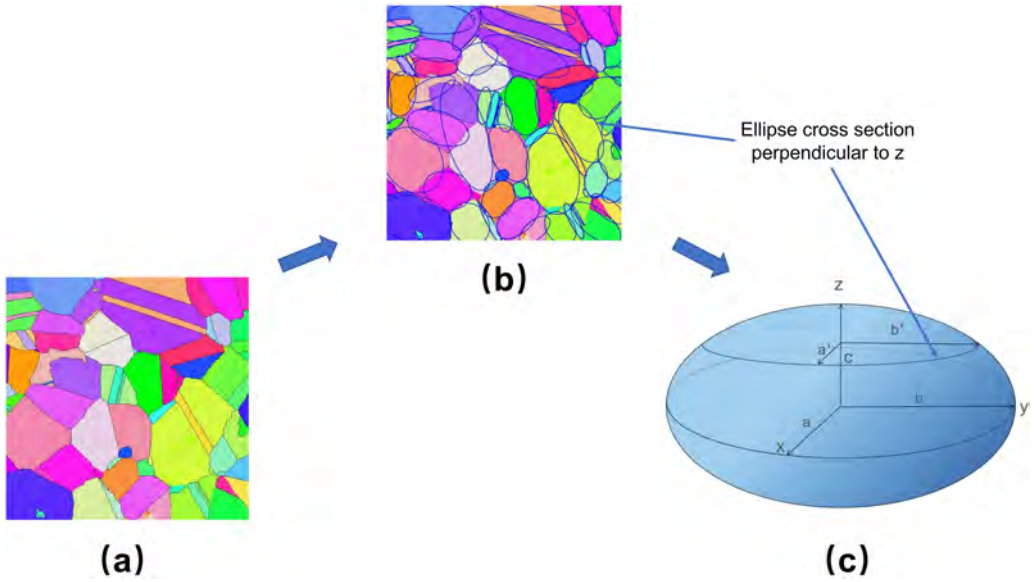

Fig. 3.10 Ellipsoid generation: (a) EBSD scan, (b) ellipse fitting, (c) ellipsoid projection.

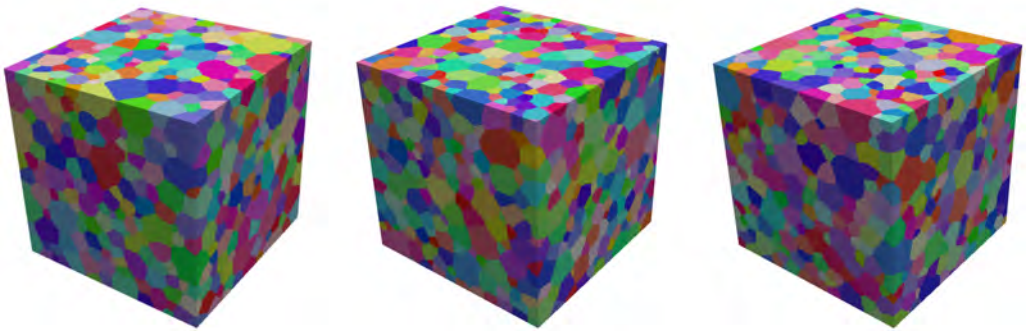

Fig. 3.11 Schematic presentation of the reconstructed polycrystalline microstructures through ellipsoid packing. Generated from the open-source software DREAM.3D [137].

fills the whole space with voxels where new ellipsoids are nucleated at the lattice centre of the initial ellipsoids and grow according to their original dimensions until they impinge other ellipsoids or the space boundaries.

- Orientation assignment: assigning crystallographic orientations to each new ellipsoid. This begins with assigning random orientations to the new ellipsoids in the reconstructed microstructure [288]. The simulated annealing algorithm can be then adopted to search for an optimum configuration of orientations and misorientations consistent with the experimental statistics. Fig. 3.11 presents some examples generated by the ellipsoid packing algorithm.

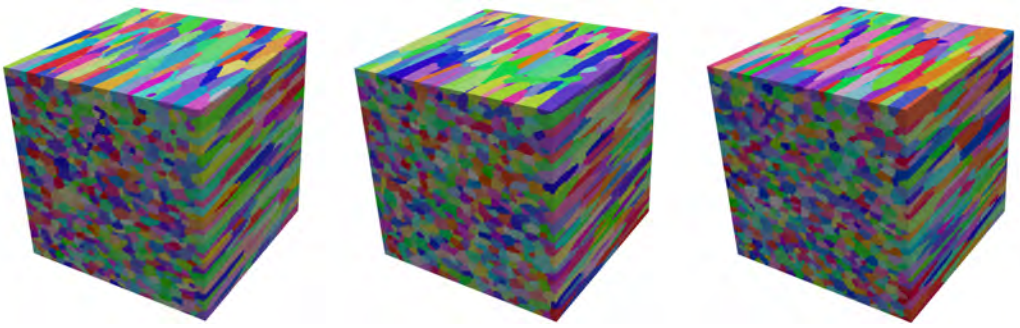

Fig. 3.12 Schematic presentation of the reconstructed polycrystalline microstructures with elongated grains. Generated from the open-source software DREAM.3D [137].

In the space discretization step, the grain boundaries made by the cellular automaton process are not natural and show a deviation from reality. To overcome this deficiency, the Monte Carlo grain growth method [373] has been adopted to relax the final grid-based structure and allow the grain boundaries to approximate the natural observations. The orthogonal EBSD scans-based method has been extended by [52] to reconstruct the commercial purity aluminium with elongated grains (Fig. 3.12). Instead of discretizing the space by grids, they implemented the vertex-edge-face-volume discretization to represent the grain boundaries through Voronoi tesselation. The Voronoi cells were then aggregated and scaled by an affine stretch to match the observed aspect ratios of grains. Another 2D scan-based method has been proposed by [407] to reconstruct 3D anisotropic polycrystalline microstructures with constrained surface ellipsoids. The above-mentioned 2D EBSD section methods can't accurately show how the grains are connected in 3D space. Additionally, other morphological descriptions, such as the grain neighbor and shape orientation distribution, can not be inferred from that work. To overcome such biases and limitations, [134, 135] reconstructed the polycrystalline structure directly from the 3D experimental data [136] (Fig. 3.13). In their ellipsoid generation step, each ellipsoidal grain's volume, aspect ratio, and shape orientation are created by sampling from their probability functions based on the 3D experimental data. In the ellipsoid packing step, besides the overlapping constraint, the placement of ellipsoids is also dominated by their neighbors' size and number. The most surface area criterion assigns the voxels, which are not included in any ellipsoids. The space discretization step resembles the way organized by [52], except that the generation of the Voronoi seed is guided by the boundary centroid between two grains instead of a random process. In the orientation assignment step, the orientation, misorientation, and microtexture are made and assigned using the probability assignment approach [88]. The DREAME.3D software [137] (http://dream3d.bluequartz.net/) contains most of the ellipsoid packing methods mentioned above.

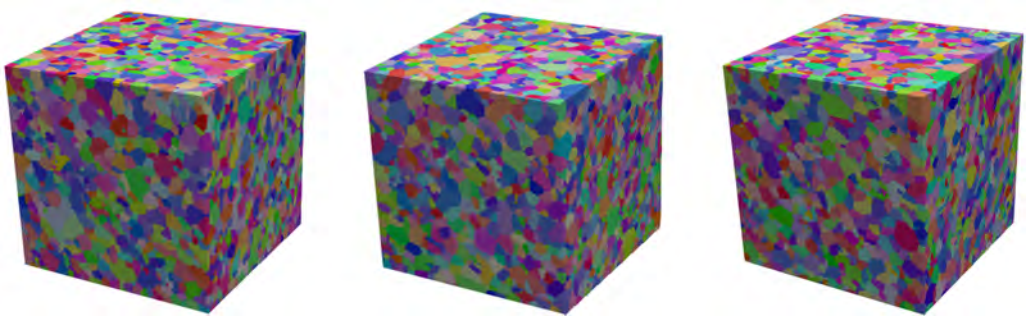

Fig. 3.13 Schematic presentation of the reconstructed polycrystalline microstructures from 3D experimental data. Generated from the open-source software DREAM.3D [137].

Recent research on ellipsoid packing has focused on improving the efficiency of ellipsoid packing algorithms, synthesizing polycrystalline microstructures with more than one phase, capturing more precise and accurate characterizations, making annealing twins and precipitates, and reconstructing polycrystalline microstructures through AM. In the optimized algorithms, [424] employed the ellipsoidal growth tessellations to replace the ellipsoid generation and ellipsoid packing steps. The reconstruction starts with the random field model with a marked point process for representing stochastic parameters. In terms of grains' aspect ratio, size, and nearest neighbor distributions, the results of the reconstruction are pretty close to what was observed in the experiments. [170] developed the advancing layer algorithm for dense ellipse packing. This method can achieve higher packing densities with low computational cost and simultaneously captures grains' shape, size, and spatial orientation distributions. The random sequential addition algorithm founded on grid discretization has been developed by [149] for efficient ellipsoid generation and packing. The proposed algorithm can successfully synthesize elongated grains and martensite bands. In the multiphase microstructures, the first-phase grain structure is created using the same procedure in [384]. The second and third phases are nucleated randomly on the first-phase grain boundaries and then grown until their volume fraction reaches an expected value. Illustrations of this algorithm can be found at [70, 406]. Beyond that, [71] inserted the second-phase particles into the synthetic polycrystalline microstructure in accordance with the pair-correlation function. [324] reconstructed the dual-phase titanium structure by employing the transformation phase insertion algorithm. [268] proposed a general framework for generating, validating and quantifying 3D anisotropic two-phase polycrystal materials. As for better characterization representation, the reconstructed polycrystalline microstructure generated by the log-normal size distribution can lead to unnatural large grains. [432] resolved the problem by applying truncated grain size distributions. Furthermore, the two-point correlation function [408, 71] has been employed to statistically characterize grain

morphology, orientation, and spatial distribution for highly heterogeneous polycrystalline reconstruction. Concerning the annealing twins reconstruction, [432] developed the twin insertion algorithm on the assumption that the twin grain does not inhabit the boundary of the parent grain and completely divides the parent grain. [22] reconstructed the twins on account of the parent grain size distribution, the conditional probability distributions of twin distance and thickness, and the joint probability of the number of twins. When it comes to the precipitate reconstruction, [337, 336] dispersed the precipitates into the reconstructed polycrystalline microstructure based on the precipitates' shape, size, volume, orientation, two-point correlation, 3D distance to surface, and random vector channel-width distributions. [431] utilized a genetic algorithm-based numerical algorithm for optimized selection of precipitate characterizations. Next, the precipitates with optimized descriptors were spatially inserted into the polycrystalline parent grain microstructure to construct 3D polyphase aluminum alloys. Finally, regarding polycrystalline microstructures involving AM, [423] proposed a universal material template for the standardized reconstruction of commonly used polycrystalline materials in AM processes. [113] introduced a new framework for reconstructing polycrystalline microstructures. The framework regenerates grain growth and allows for a specification of growth properties. This makes it easier to simulate and estimate materials with spatial differences, like those produced by AM.

Compared to Voronoi tessellations, the ellipsoid packing model generates polycrystalline microstructures closely matching the experimental observations. This is why the ellipsoid packing method is often used to investigate the SPP linkages in polycrystalline materials. For example, [302] investigated the effect of grain size and crystallographic polarity on stress hardening and anisotropic plasticity in additively manufactured metals generated by ellipsoid packing. [208] combined the ellipsoid packing algorithm with the uncertainty-quantified parametrically homogenized constitutive model to build a link between mechanical properties response and microstructural characterizations. [293] integrated machine learning with ellipsoid packing reconstruction to predict cyclic stress-strain responses. Additionally, ellipsoid packing has been applied in the microstructure sensitive study for optimized performance. Examples are the research carried out by [349, 462], who analyzed and designed the microstructure characterizations to quantify the probability of occurrence of the fatigue cracks; by [324], who created a database on the elasto-viscoplastic deformation in dual-phase titanium alloys; and by [430], who utilized the Bayesian regression machine learning model and data-consistent inversion to build the inverse linkage between the average grain size and average yield strength. In recent years, ellipsoid packing has been widely used in the ML-based surrogate model to predict the properties of polycrystalline materials. The microstructure data reconstructed by ellipsoid packing can be used directly as input for

the surrogate model. Then, DL networks, for instance, the convolutional neural network [340], the graph neural network [84] and the deep neural network [325], can be used to obtain low-dimensional microstructure embeddings (physical features) of the polycrystalline microstructure. Finally, the embeddings are connected to the target properties.

3.3.3 Texture synthesis

Texture synthesis [341, 85, 147, 480] has been a popular research topic in computer vision for filling in occlusions, compressing images and videos, removing the foreground, etc. The seminal and widely recognized work by [101, 448, 100] reframed the texture synthesis problem in an exemplar-based framework and provided more practical solutions. These works assume the original given image, $\boldsymbol{X}$, as a form of stationary Markov random field (MRF) with the following properties:

- Locality: $f(X_i|all\ particles\ except\ i) = f(X_i|neighbors\ of\ particle\ i)\ i = 1,2,...,N$, where N is the number of particles that correspond to the pixels or voxels in $\boldsymbol{X}$, X_i represents the local state in polycrystalline materials, like the orientation colormap, phases, etc., $f(X_i|all\ particles\ except\ i)$ and $f(X_i|neighbors\ of\ particle\ i)$ are the conditional probability density of X_i.

- Stationarity: $f(X_i|neighbors\ of\ particle\ i)$ does not depend on the location of X_i.

The texture synthesis model has been successfully applied to reconstruct polycrystalline materials [412, 216, 6, 176, 175]. Section 4.3 presents some examples generated by the texture synthesis model. The basic steps are summarized as follows:

- State generation: the synthesized domain, $\boldsymbol{Y}$, is first discretized into grids, namely pixels or voxels. The next step is establishing the $\boldsymbol{Y}$ as MRF. Pixels or voxels representing various local states are bonded to their neighbors. A pixel (voxel)'s neighborhood is determined by enclosing it in a area and connecting the pixel (voxel) to other pixels (voxels) inside the area. The initial state can be achieved by randomly allocating states to each grid in $\boldsymbol{Y}$ [412, 176, 175] or start from a small seed image taken randomly from the original given image, $\boldsymbol{X}$ [216, 6].

- State update: after state generation, the conditional probability density sampling from the original given image, $\boldsymbol{X}$, is performed to update the local state of the selected pixel (voxel) in the synthesized domain, $\boldsymbol{Y}$, based on the known states of its neighboring pixels (voxels). The update path could be implemented by random order [412, 176, 175], raster-scan order [448] or layer through layer form [101, 216, 6]. In each update

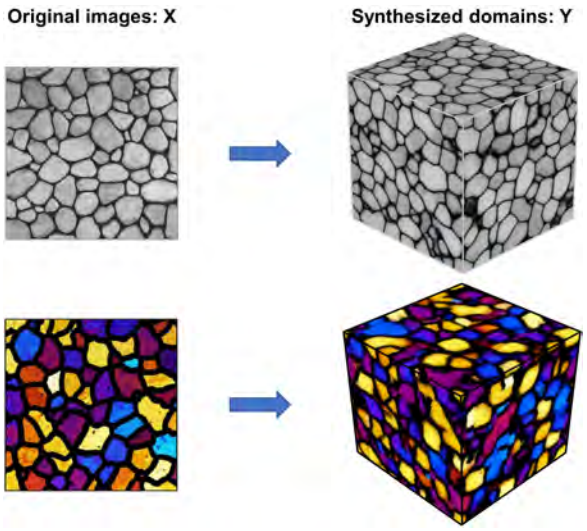

Fig. 3.14 Schematic presentation of the reconstructed 3D polycrystalline microstructures from experimental 2D polycrystalline microstructures through texture synthesis. Adapted from [176], Copyright (2020), with permission from Elsevier.

step, the conditional probability density $f(X_i|N^X)$ in $\boldsymbol{X}$ is assumed to be equal to the conditional probability density $f(Y_i|N^Y)$ in $\boldsymbol{Y}$. N^X and N^Y are the neighborhood of particle i in the $\boldsymbol{X}$ and $\boldsymbol{Y}$, respectively. The best matching of N_B^X is determined by solving the following minimization problem:

$$N_B^X = arg \min_{N_j^X} \sum_j \omega_j \left\| N_j^Y - N_j^X \right\|^2 \tag{3.28}$$

where j denotes the particles in N^X and N^Y, and ω is the Gaussian weighting function [176, 175]. Equation (4.13) is an exhaustive search for comparing all the N^X in $\boldsymbol{X}$ to the same corresponding size N^Y in $\boldsymbol{Y}$ and identifying N_B^X that results in the smallest squared distance.

The multiple-point simulations (MPS) method is analogous to texture synthesis in that the microstructure is considered as MRF and then reconstructed by searching for the conditional probability density $f(X_i|N^X)$ in the original image that best matches the conditional probability density $f(Y_i|N^Y)$ in the synthesized image [273, 51]. MPS has been widely used in geostatistical reconstruction [418, 419, 421, 464, 1, 23]. The main difference between MPS and texture synthesis is that MPS needs to integrate the conditioning constraint data representing geostatistical features. In addition to the global information from the original image, the synthesized image should be coherent with the local conditioning data and locally generate constraint values at constraint locations [273]. The exhaustive search and match

for similar neighborhoods in the original image, $\boldsymbol{X}$, make the texture synthesis method computationally prohibitive. Therefore, recent studies have focused on improving efficiency and accuracy. For example, the usage of patches instead of pixels for better computational implementation [100, 418–420] and the introduction of image quilting for better structural connectivity [100, 266, 3, 154]. Also, more advanced search methods have been proposed. Illustrations include random search [420, 464], adapted graph cuts [266, 240, 418, 420], and multi-scale search [464, 421, 308]. Meanwhile, pattern databases [464, 123], transform domains [3, 123, 421], edge features [1, 309, 2], and machine learning [23] have been utilized to accelerate template matching.

Polycrystalline microstructures generated by shape-based methods are largely idealized and fail to account for the complexities of real-world grain shapes [42]. Texture synthesis, especially the patch-based scheme, can be an attractive substitute for shape-based models due to its ability to capture complex features such as grain boundaries [418, 216]. Beyond that, texture synthesis can be used to reconstruct larger regions of microstructure (order of centimeters) required for engineering analysis by utilizing small-scale experimental data (order of microns) [6]. However, the quality of the reconstruction results in texture synthesis is unstable because it is easily affected by some specific parameters, including neighborhood size, overlap size, number of replicates, etc. As a result, sensitivity analysis should be conducted to optimize the parameters for the best quality [123, 24, 176]. Additionally, the reconstruction path frequently impacts the results, as spatial correlations may be lost [123, 51]. Finally, direct colormaps between orientation and color space are currently the most common techniques used for orientation coloring [327, 317, 176]. Due to the discontinuity and ambiguity issues inherent in representing the crystallographic features, texture synthesis has not been widely applied to the construction of SPP linkages.

3.3.4 Others

Other geometric reconstruction approaches have also been used to capture morphological and crystallographic features, such as high-order characterization models, reduced-order strategies, and machine learning. Fig. 3.15 presents some examples generated by these approaches. The reconstruction approaches mentioned above have not been widely applied in building SPP linkages compared to shape-based reconstruction models. Therefore, we briefly review each approach's concepts, strengths, and weaknesses. A detailed step-by-step description of each approach is beyond the scope of this review.

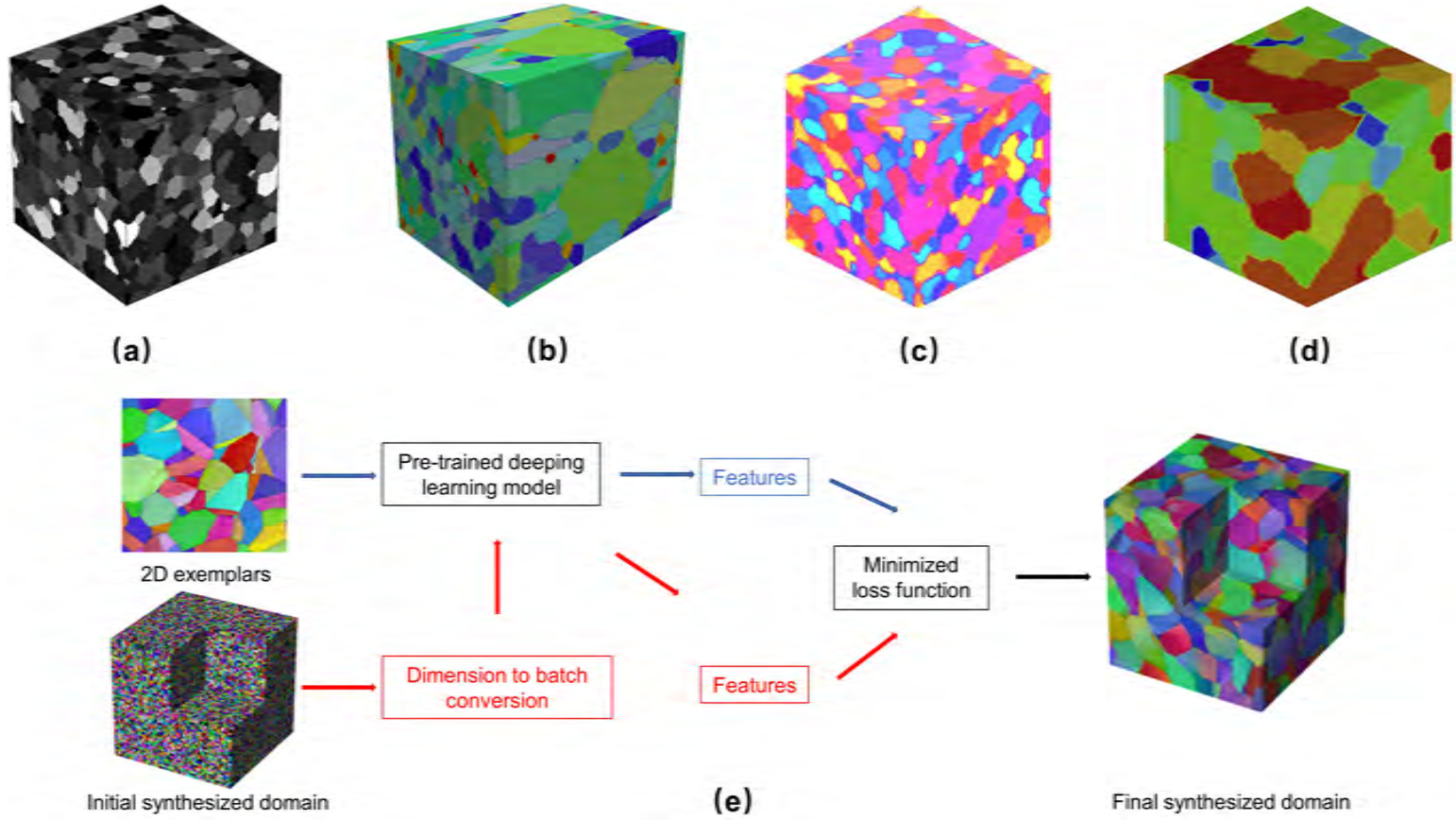

Fig. 3.15 Schematic presentation of the reconstructed 3D polycrystalline microstructures through phase recovery (a), simulated annealing (b), principal component analysis (c), nonlinear dimensionality reduction (d), and transfer learning (e). Adapted from [117, 126, 413, 242, 50], Copyright (2008,2016,2004,2010,2020,), with permission from Elsevier.

High-order characterization models

System energy, or objective function, is the difference in high-order correlation functions between the target and reconstructed images in high-order characterization models. The difference can be minimized until a threshold is reached using optimization methods such as simulated annealing [76, 178, 71] (Fig. 3.15(b)) and phase recovery [117] (Fig. 3.15(a)). The high-order characterization models are an effective tool for generating statically equivalent representative volume elements for the high-order characterization distributions. Nevertheless, the local material state in the high-order characterization models is restricted to a discrete, limited number of material phases. Further refinement of high-order characterization models might be necessary when more complex local states of the polycrystalline material (i.e., crystal lattice orientation) are investigated.

Reduced-order strategies

Similar to the reduced-order representations used in characterization extraction, low-dimensional reconstruction strategies have also been utilized for geometric reconstruction. One of the famous dimensionality reduction method is principal component analysis [413, 414] (Fig. 3.15(c)). The microstructures are initially represented by a class of eigen-microstructures using principal component analysis. A support vector machine is then utilized to classify eigen-microstructures according to their characteristics. After that, the eigen-microstructures will continue to evolve as new target microstructures are dynamically added to the database. Finally, a series of microstructures will be reconstructed by employing various fractions of eigen-microstructures. Other reduction tools, such as nonlinear dimensionality reduction (Fig. 3.15(d)), and multiscale approach [242, 451], have also been adopted to reconstruct polycrystalline materials initially with high dimensionality for texture. Reduced-order strategies demonstrate an advantage over high-order characterization models for computational efficiency and complex material state representations. Future research should concentrate on the model reduction of realistic microstructures instead of idealized stochastic characteristics.

Machine learning

Recently, machine learning-based methods have been applied to generate morphological and crystallographic information in polycrystalline materials. Unsupervised learning approaches based on convolutional deep belief network (CDBN) [64] and variational autoencoder (VAE) [63] have been developed to extract statistical features from the granular microstructures of alloys. The CDBN model, consisting of convolutional restricted Boltzmann machine layers, generates a reduced-dimensional, parametric representation of the granular polycrystalline

images. The stochastic reconstructions are derived from the final layer of the trained CDBN and inversely sample the previous layers via deconvolution. A VAE has an encoder that turns granular microstructure images into a set of statistical descriptions in the latent feature space and a decoder that uses the latent feature vector to reconstruct the granular polycrystalline images. Another machine learning-based method is deep transfer learning [50, 241] (Fig. 3.15(e)). Transfer learning is a mechanism for transferring information from pre-trained deep learning models to a new task. The pre-trained deep learning models can provide a reduced-dimensional feature representation of the granular microstructures. Stochastic microstructure reconstructions are generated using target microstructure feature values by adjusting the pixel/voxel values (gradient-based optimization) to minimize the loss function (gram-matrix differences). Machine learning-based methods can represent morphological information well. However, similar to texture synthesis, the disadvantage is that it is difficult to capture the crystallographic features due to discontinuity and ambiguity issues.

Chapter 4

Novel strategies for texture synthesis models applied to microstructure representation of polycrystalline materials

4.1 Introduction

As mentioned in the Chapter 2, the polycrystalline microstructures generated by shape-based methods are largely idealised and fail to account for the complexities of real-world microstructures [42]. Texture synthesis, especially the patch-based scheme, can be an attractive substitute for these models due to its ability to capture features such as grain boundaries [216, 176]. Beyond that, texture synthesis can be used to reconstruct larger regions of microstructure (order of centimeters) required for engineering analysis by utilising small-scale experimental data (order of microns) [6]. Given this, the texture synthesis model has been widely used in the microstructure representation of polycrystalline materials in recent years. For example, Liu and Shapiro [250] utilized the Markov Random Field (MRF) texture synthesis approach to reconstruct the granular polycrystalline images. Acar and Sundararaghavan [6] modeled the spatio-temporal evolution of polycrystalline microstructures using the MRF texture synthesis approach. Javaheri and Sundararaghavan [176] combined the MRF and histogram matching to reconstruct the 3D polycrystalline microstructures from 2D sections. Javaheri et al. [175] used the MRF texture synthesis approach to synthesize the large-scale metal additively manufactured polycrystalline microstructures.

However, in current practice, polycrystalline microstructure reconstruction using texture synthesis does have certain limitations [176]. For example, the orientation colormaps employed in polycrystalline microstructural visualization are often directly colored by Euler angles $(\varphi_1, \phi, \varphi_2)$ or Rodrigues-Frank vector (ρ_1, ρ_2, ρ_3) (Table 4.1) [360, 327, 317, 176]. This is easily achieved by assigning each of the three independent orientational parameters to one of the components in the RGB triplet. The apparent topological discrepancy between the unconnected orientation and connected color spaces will undoubtedly lead to color discontinuities. In the meantime, ignoring the crystal symmetry may cause color ambiguity, i.e., the same orientations can be represented by certainly diverse colors [327, 317]. In addition to the Euler angle colormaps, computational efficiency is also an issue. The exhaustive search and match for similar neighborhoods founded on the minimum weighted squared distance in the original image make the pixel-based texture synthesis method computationally prohibitive and morphologically deviant [176].

In this Chapter, the authors proposed to adapt the inverse pole figure (IPF) coloring algorithm to solve the discontinuities and ambiguity coloring problem. After that, the patch-based texture synthesis algorithms combined with image quilting techniques were utilized for better honoring the microstructural connectivity. Simultaneously, the raster path method and fast template matching schemes were adopted to improve the CPU performance. Moreover, the inverse orientation coloring algorithm was developed to derive the orientation dataset in the synthesized images through mapping orientations from the IPF coloring. Finally, the microstructure characterizations and comparison studies were presented.

4.2 Orientation coloring

4.2.1 Background

In polycrystalline materials, the lattice orientation $\boldsymbol{G}$ represents the rotation relationship between the crystal axes of single crystals and the reference frame. It can be equivalently described in different mathematical and non-mathematical parameterizations with three independent parameters (see Table 4.1) [327]. The lattice orientation coloring is the first consideration for microstructural visualization in polycrystalline materials because it plays a determining role in identifying grains. The two neighboring lattice points are located in the identical grain if the misorientation angle between them is under a specific value [135, 327, 317]. Therefore, the remarkable orientation changes defining grains or phase boundaries should preferably be visible through a significant color variation.

Table 4.1 Summary of parameterizations of orientation

Name	Parameters	Definition
Euler angles	$(\varphi_1, \phi, \varphi_2)$	$g_{ij} = \begin{pmatrix} cos\varphi_1 cos\varphi_2 - sin\varphi_1 sin\varphi_2 cos\phi & sin\varphi_1 cos\varphi_2 + cos\varphi_1 sin\varphi_2 cos\phi & sin\varphi_2 sin\phi \\ -cos\varphi_1 sin\varphi_2 - sin\varphi_1 cos\varphi_2 cos\phi & -sin\varphi_1 sin\varphi_2 + cos\varphi_1 cos\varphi_2 cos\phi & cos\varphi_2 sin\phi \\ sin\varphi_1 sin\phi & -cos\varphi_1 sin\phi & cos\phi \end{pmatrix}$
Miller indices	$(hkl)[uvw]$	$g_{ij} = \begin{pmatrix} \frac{u}{\sqrt{u^2+v^2+w^2}} & \frac{r}{\sqrt{r^2+s^2+t^2}} & \frac{h}{\sqrt{h^2+k^2+l^2}} \\ \frac{v}{\sqrt{u^2+v^2+w^2}} & \frac{s}{\sqrt{r^2+s^2+t^2}} & \frac{k}{\sqrt{h^2+k^2+l^2}} \\ \frac{w}{\sqrt{u^2+v^2+w^2}} & \frac{t}{\sqrt{r^2+s^2+t^2}} & \frac{l}{\sqrt{h^2+k^2+l^2}} \end{pmatrix}$
Matrix	a_{ij}	$g_{ij} = \begin{pmatrix} a_{11} & a_{12} & a_{13} \\ a_{21} & a_{22} & a_{23} \\ a_{31} & a_{32} & a_{33} \end{pmatrix}$
Axis-angle	$(\theta, \boldsymbol{n})$	$g_{ij} = \delta_{ij} cos\theta + n_i n_j (1 - cos\theta) + \sum_{k=1,3} \xi_{ijk} n_k sin\theta$
Rodrigues-Frank vector	(ρ_1, ρ_2, ρ_3)	$(\rho_1, \rho_2, \rho_3) = tan(\theta/2)\boldsymbol{n}$
Quaternion	$q = (q_1, q_2, q_3, q_4)$	$(\boldsymbol{q}, q_4) = (sin(\theta/2)\boldsymbol{n}, cos(\theta/2))$

Direct colormaps between the orientation and color space are currently the most common orientation coloring technique. However, some things should be improved with direct orientation-to-color mapping. One is the discontinuity issue induced by the apparent topological inconsistency between the orientation and color space. The color spaces, e.g., the hue-saturation-value (HSV), the hue-saturation-lightness (HSL), or the red-green-blue (RGB), are connected three-dimensional Euclidean ($\boldsymbol{R^3}$) spaces. Namely, it can deform or shrink any closed path within the color spaces indefinitely to a single point. In contrast, the orientation spaces are not inextricably linked and can not be incorporated into $\boldsymbol{R^3}$ [327]. Even though the three independent orientational parameters specify the three components in the RGB triplet, it has been accepted that $\boldsymbol{G}$ can not be continuously one-to-one mapped to any space lower than five dimensions [328]. In addition, ignoring the crystal symmetry may cause color ambiguity. For example, symmetrically equivalent orientations can be represented by divergent colors [317].

4.2.2 Perfectly colored orientations

Standard IPF coloring

To address the visualization issues in direct orientation-to-color mapping, the IPF coloring based on the Miller index has been proposed for improved orientation coloring (see Fig. 4.1).

The initial step in IPF coloring is to establish a direction vector $\boldsymbol{r}$ in the specimen coordinate system, e.g., parallel to the normal direction (**ND**) or rolling direction (**RD**)), and then transform it as the vector $\boldsymbol{h}$ in the crystal coordinate system through the following formula:

$$\boldsymbol{h} = \boldsymbol{G}^{-1}\boldsymbol{r} \tag{4.1}$$

where $\boldsymbol{G}$ is the lattice orientation (see Fig. 4.1.a). Each possible but crystallographically unequal vector $\boldsymbol{h}$ identifies the fundamental sector (FS) of a symmetry group $\boldsymbol{P}$ (see Fig. 4.1.b). Each point h in the FS corresponds to the unique vector $\boldsymbol{h}$. Two particular variables are introduced to define the location of h inside the FS: the polar angle θ and the azimuthal angle ρ. The θ is determined by the line distance (hp) between the point h and p (barycenter of the FS). The correspondence between the hp and the value of θ is built on the rule that the maximum distance span has the maximum polar angle of 90°. The polar angle θ ranges from 0° to 90° on the HSL colorization of the upper unit hemisphere and from 90° to 180° on the HSL colorization of the lower unit hemisphere. The angle between the pA and ph lines determines ρ. The value of ρ ranges from 0° to 360° (see Fig. 4.1.c). The asymmetric HSL distribution is then calculated through the polar and azimuthal angles to obtain the one-to-one coloring of h. Details of the HSL colormap are summarized as follows [317]:

- Customized hue gradient: the hue H, as the description of the azimuthal angle ρ, is expressed as

$$H = \int_0^{\omega} v(\rho)d\rho \tag{4.2}$$

where $v(\rho)$ is the the speed function. The speed function is customized to ensure a more even distribution of colors, defined as

$$v(\rho) = d(\rho)\left(0.5 + e^{-\frac{4}{7}[\rho]^2} + e^{-\frac{4}{7}\left[\rho-\frac{2\pi}{3}\right]^2} + e^{-\frac{4}{7}\left[\rho+\frac{2\pi}{3}\right]^2}\right) \tag{4.3}$$

where $d(\rho)$ is the distance between p and the boundary point b in FS (see Fig. 4.1.c). The barycenter and the three corners divide FS into three sections. The three interior angles ω_1, ω_2, ω_3 (see Fig. 4.1.c) of the three sections may be pretty dissimilar. In order to compensate for the angle differences, it is necessary to normalize the speed function in the following way

$$\int_0^{\omega_1} v(\rho)d\rho = \int_{\omega_1}^{\omega_1+\omega_2} v(\rho)d\rho = \int_{\omega_1+\omega_2}^{2\pi} v(\rho)d\rho = \frac{1}{3} \tag{4.4}$$

- Nonlinear lightness scaling: the nonlinear scaling map between the lightness L and polar angle θ has been introduced for a more balanced key, described as

$$L = \lambda_L \frac{\theta}{\pi} + (1 - \lambda_L) sin^2 \frac{\theta}{2} \tag{4.5}$$

  where the parameter λ_L allows adjusting the central white or black region size in the IPF key.

- Lightness dependent saturation: the disadvantage of the central white or black orientation coloring through nonlinear lightness scaling is that no remaining color can be utilized for annotations, drawing grain borders, and marking non-indexed pixels. To overcome this limitation, the lightness dependent saturation has been proposed to color the central region with bright or dark gray, expressed as

$$S = 1 - 2\lambda_S |L - 0.5| \tag{4.6}$$

  where the parameter λ_S specifies the degree to which the center is grayish.

There are several inherent advantages to using the $\boldsymbol{P}$-specific IPF-color key: Firstly, the FS of the symmetry group $\boldsymbol{P}$ can ensure that similar orientations correspond to similar colors. Secondly, the asymmetric HSL distribution makes it possible to correlate the color difference between two orientations with the size of the misorientation angle. Finally, and most importantly, discontinuous-free color distributions can be achieved as long as each boundary in the FS is a crystallographic mirror plane. Specifically, suppose R is defined as the main rotation axis. In that case, all symmetry groups satisfying the conditions (a) $2 \perp R$ and (b) $2 \perp \bar{2}$ can present smooth color transitions at the boundary of the FS through the standard asymmetric HSL distribution. Table 4.2 shows the symmetry point groups that meet this condition in the column “standard". Examples of standard symmetry groups are $m\bar{3}m$, $\bar{4}3m$, $6/mmm$, $\bar{6}2m$, $\bar{6}m2$, $6mm$, $3m1$, $4/mmm$, $4mm$, mmm, $mm2$, $m2m$, $2mm$, and $1m1$.

Extended IPF coloring

Table 4.2 also distinguishes the symmetry groups by the order k and lattice types. The order k of all symmetry groups specifies the FS’s equivalent size (but not shape). For a certain symmetry group $\boldsymbol{P}$ listed in the column “extended" of Table 4.2, the order is half the value of the matching super symmetry group $\boldsymbol{P}_+$ in the column “standard". Consequently, the diversity of $\boldsymbol{P}$ is precisely twice that of $\boldsymbol{P}_+$. The FS of $\boldsymbol{P}$ in the column "extended" is not entirely enclosed by mirror planes. Applying the standard asymmetric HSL distribution directly to it

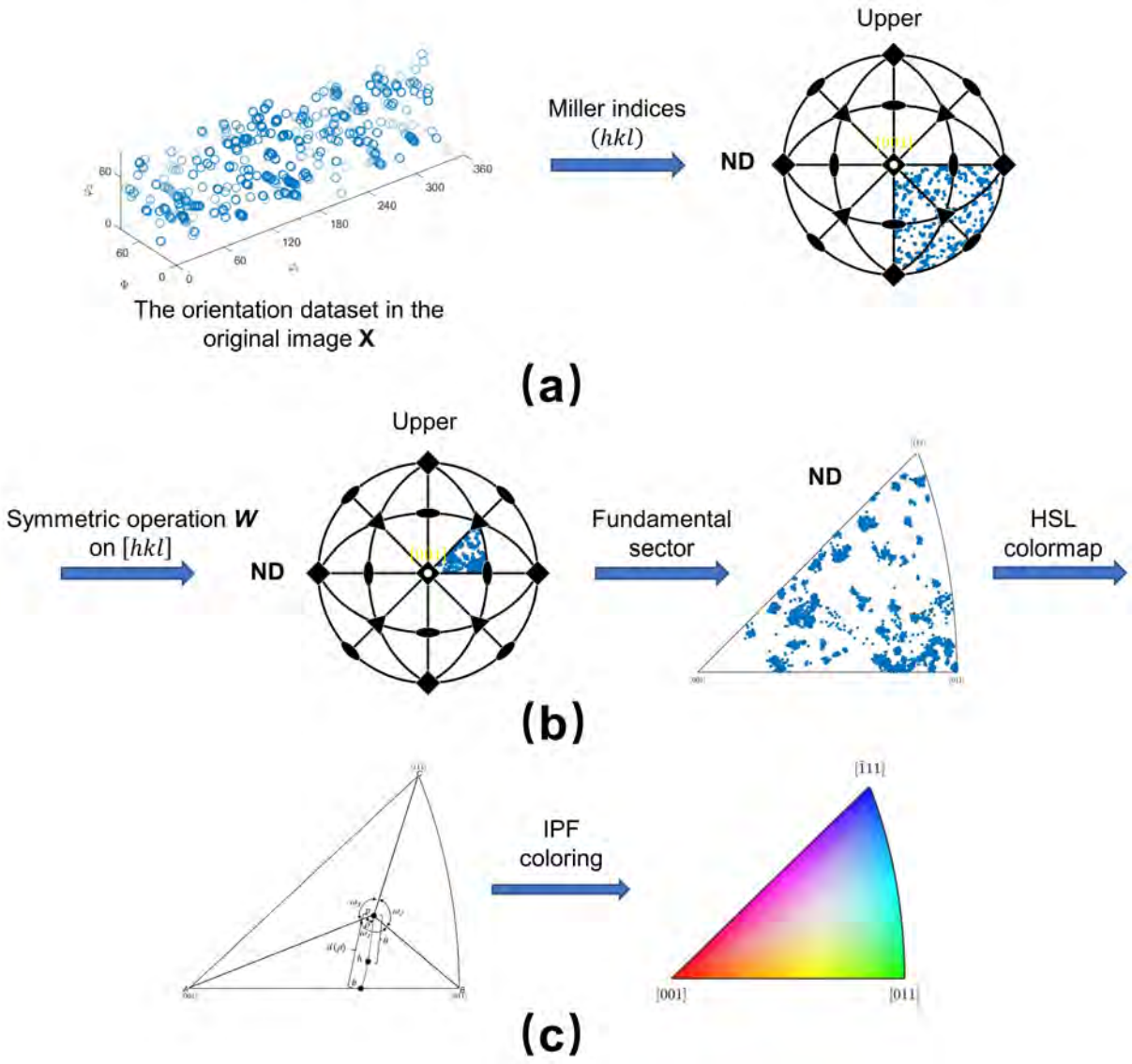

Fig. 4.1 Flowchart of the standard IPF (e.g., the normal direction) coloring for the $m\bar{3}m$ symmetry group.

Table 4.2 Point groups are distinguished by lattice type, standard or extended color distribution. k specifies the relative order of the various groups. Neither the standard nor the extended color distribution is appropriate for $\bar{3}, \bar{4}$ and $\bar{1}$.

lattice type	k	standard	k	extended				no
cubic	48	$m\bar{3}m$	24	432	$m\bar{3}$			
	24	$\bar{4}3m$	12	23				
hexagonal, trigonal	24	$6/mmm$	12	622	$6/m$	$\bar{3}m1$	$\bar{3}1m$	
	12	$\bar{6}2m$, $\bar{6}m2$	6	$\bar{6}$	321	312		
	12	$6mm$	6	6				
	6	$3m1$	6	3				
tetragonal	16	$4/mmm$	8	422	$\bar{4}2m$	$\bar{4}m2$	$4/m$	$\bar{4}$
	8	$4mm$	4	4				
orthorhombic, monoclinic	8	mmm	4	222	$112/m$	$12/m1$		$\bar{1}$
	4	$mm2$	2	112				
	4	$m2m$, $2mm$	2	121				
triclinic	2	$1m1$	1	1				no

will undoubtedly result in color discontinuities. To address this potential issue, the extended asymmetric HSL distribution has been proposed as a means of defining discontinuity-free keys for all symmetry groups $\boldsymbol{P}$ in the column "extended" [317]. The implementation is achieved by coloring half of the FS of $\boldsymbol{P}$ consistent with the FS of $\boldsymbol{P}_+$ with a bright center through the standard asymmetric HSL distribution from the unit upper hemisphere. The remaining half will be colored with a dark center using the standard asymmetric HSL distribution from the unit lower hemisphere. The general process for orientation coloring through the extended asymmetric HSL distribution is defined as

- Calculate the crystal direction h via Equation (4.1) and transform it into the FS of the symmetry group $\boldsymbol{P}$ through the symmetric operation $\boldsymbol{W} \in \boldsymbol{P}$.
- Transform h into the FS of the super symmetry group $\boldsymbol{P}_+$ via the symmetric operation $\boldsymbol{W}_+ \in \boldsymbol{P}_+$ and identify the polar angle θ and the azimuthal angle ρ for $\boldsymbol{W}_+ h$.
- Verify whether $\boldsymbol{W}h$ and $\boldsymbol{W}_+ h$ are identical. If not, mirror the polar angle θ and the azimuthal angle ρ to the lower hemisphere.
- Allocate a color to the polar angle θ and the azimuthal angle ρ using the HSL colormap mentioned before.

Fig. 4.2, Fig. 4.3, Fig. 4.4 and Fig. 4.5 depict the $\boldsymbol{P}$-specific IPF-color key, stereo diagrams for symmetry elements, upper spherical surface projection, and lower spherical

surface projection for different symmetry groups distinguished by lattice types, standard or extended color distributions. For symmetry groups, $\bar{3}$, $\bar{4}$ and $\bar{1}$, no images are displayed because no discontinuous-free color distributions are available. As previously stated in Section 4.2, the parameter λ_L adjusts the central white or black region size in the IPF key, and the parameter λ_S specifies the degree to which the center is grayish. We take $\lambda_L = 0.25$ and $\lambda_S = 0.25$ in the flowing $\boldsymbol{P}$-specific IPF-color keys for a more balanced orientation coloring.

4.3 Texture synthesis

As discussed in Section 4.2, the direct colormaps between the orientation and color space inevitably lead to discontinuity and ambiguity. Therefore, in the following section, we first employ the $\boldsymbol{P}$-specific IPF-color key for improved visualization of the original image $\boldsymbol{X}$. After that, the patch-based texture synthesis (PTS) method with the raster-scan order is proposed for the stochastic geometric reconstruction of $\boldsymbol{Y}$, followed immediately by utilizing the fast template matching and image quilting techniques to avoid exhaustive search, preserve better microstructural continuity, and reduce required computational cost. Finally, we map orientations from the $\boldsymbol{P}$-specific IPF-color key for the applications of microstructure characterizations and structure-properties-performance linkages.

4.3.1 Patch-based texture synthesis

Algorithm 1 An algorithm for patch-based texture synthesis

procedure PTS ($\boldsymbol{X}$, $size_{\boldsymbol{T}}$, $size_{\boldsymbol{OL}}$, n_{can}, n_{de}) ▷ n_{can} is the number of candidates
  for $i = 1 : n_{de}$ **do** ▷ n_{de} is the number of data events
    $\boldsymbol{T} \leftarrow randomize\ (size_{\boldsymbol{T}}, \boldsymbol{X})$
    $\boldsymbol{path} \leftarrow randomize\_raster\ (path\ origin,\ path\ direction)$
    for *each location* $\boldsymbol{u}$ *along* $\boldsymbol{path}$ **do**
      $\boldsymbol{OL_u} \leftarrow extract\_current\_overlap\ (\boldsymbol{u}, \boldsymbol{T}, size_{\boldsymbol{OL}})$
      $\boldsymbol{OL_c} \leftarrow template\ matching\ (\boldsymbol{X}, \boldsymbol{OL_u})$ ▷ $\boldsymbol{OL_c}$ are candidate overlap regions
      $\boldsymbol{cand\_loc} \leftarrow extract\_candidate\_locations\ (\boldsymbol{OL_c}, n_{can})$
      $\boldsymbol{loc} \leftarrow randomize\ (\boldsymbol{cand\_loc})$ ▷ $\boldsymbol{cand\_loc}$ are candidate locations in $\boldsymbol{X}$
      $\boldsymbol{D_T(u)} \leftarrow assign\ (\boldsymbol{loc}, \boldsymbol{X}, size_{\boldsymbol{T}})$
    end for
  end for
  return all data events $\boldsymbol{D_T(u)}$
end procedure

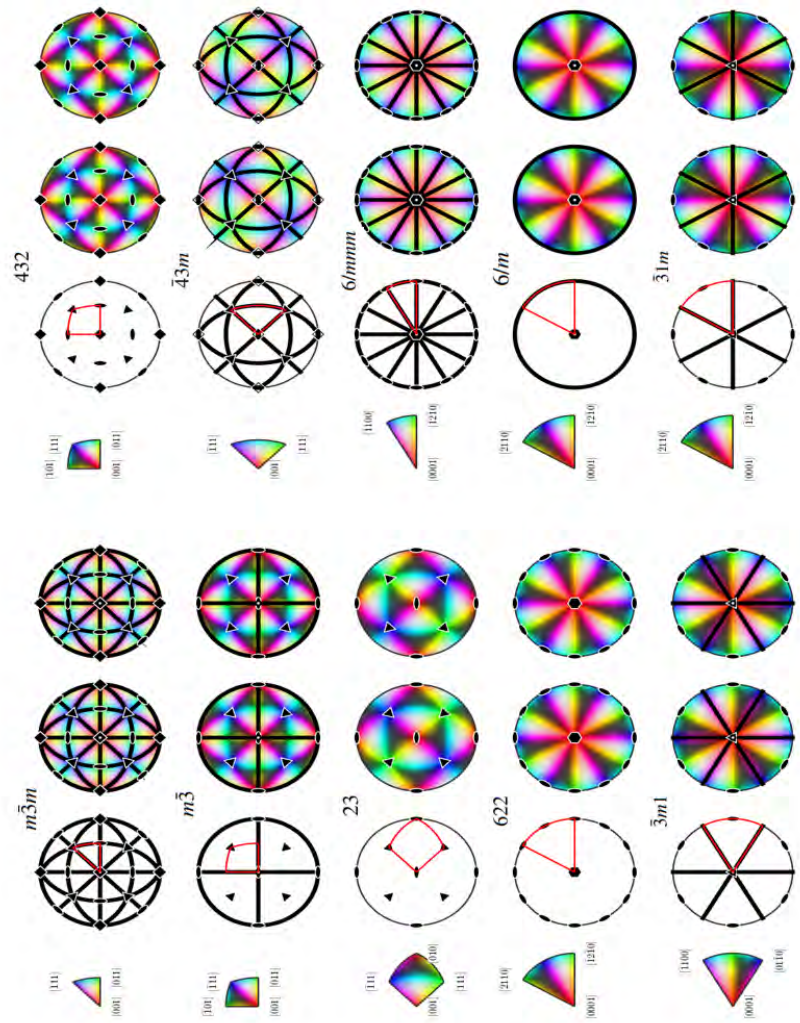

Fig. 4.2 Illustrations of the IPF color key considering the point groups.

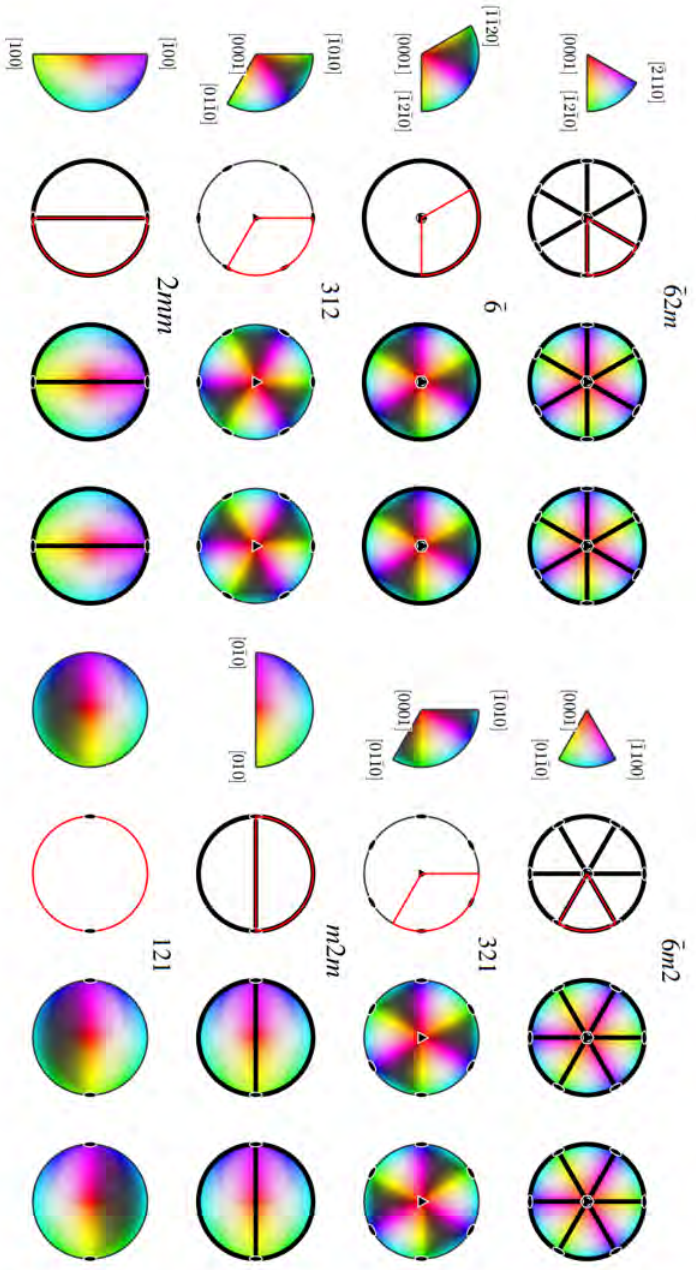

Fig. 4.3 Illustrations of the IPF color key considering the point groups.

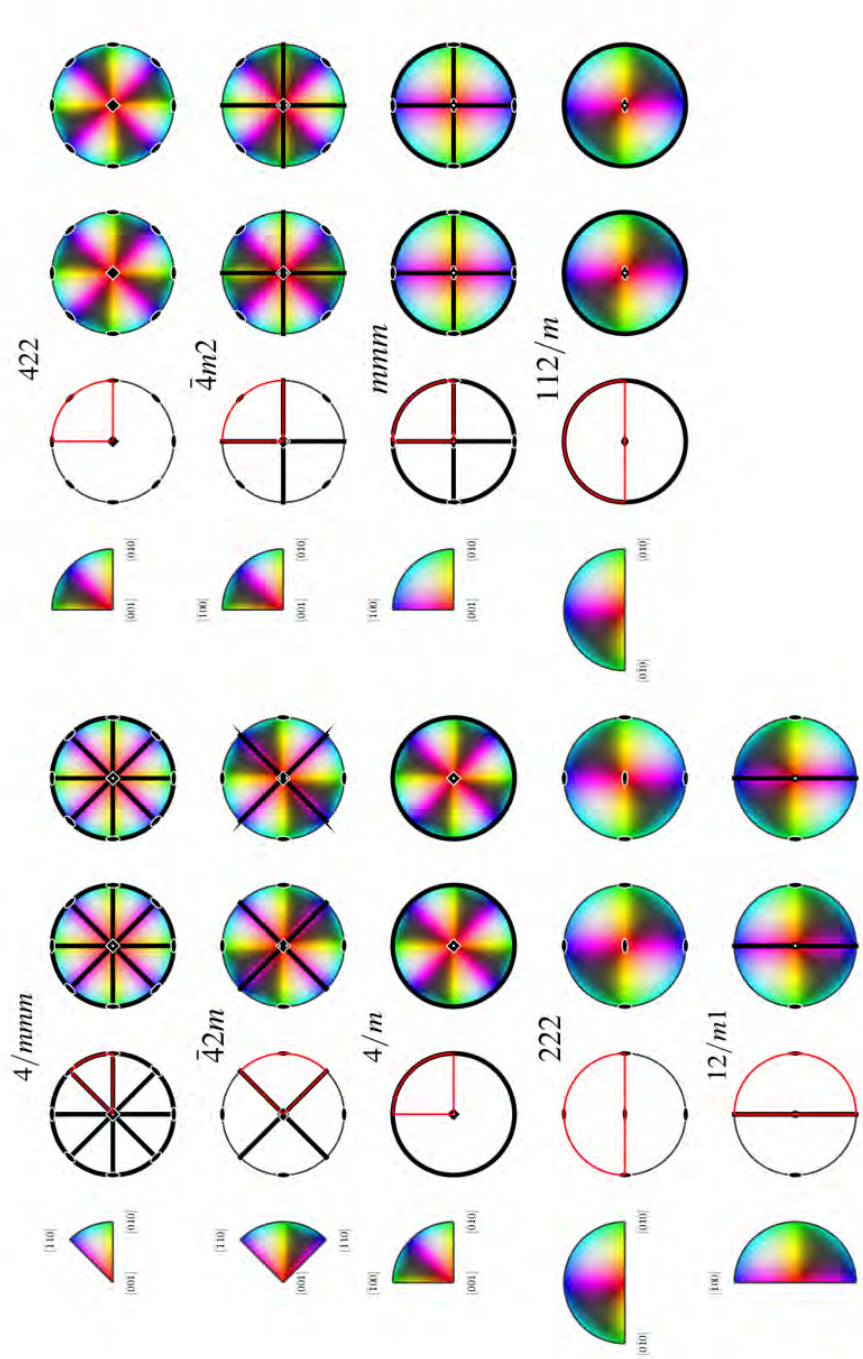

Fig. 4.4 Illustrations of the IPF color key considering the point groups.

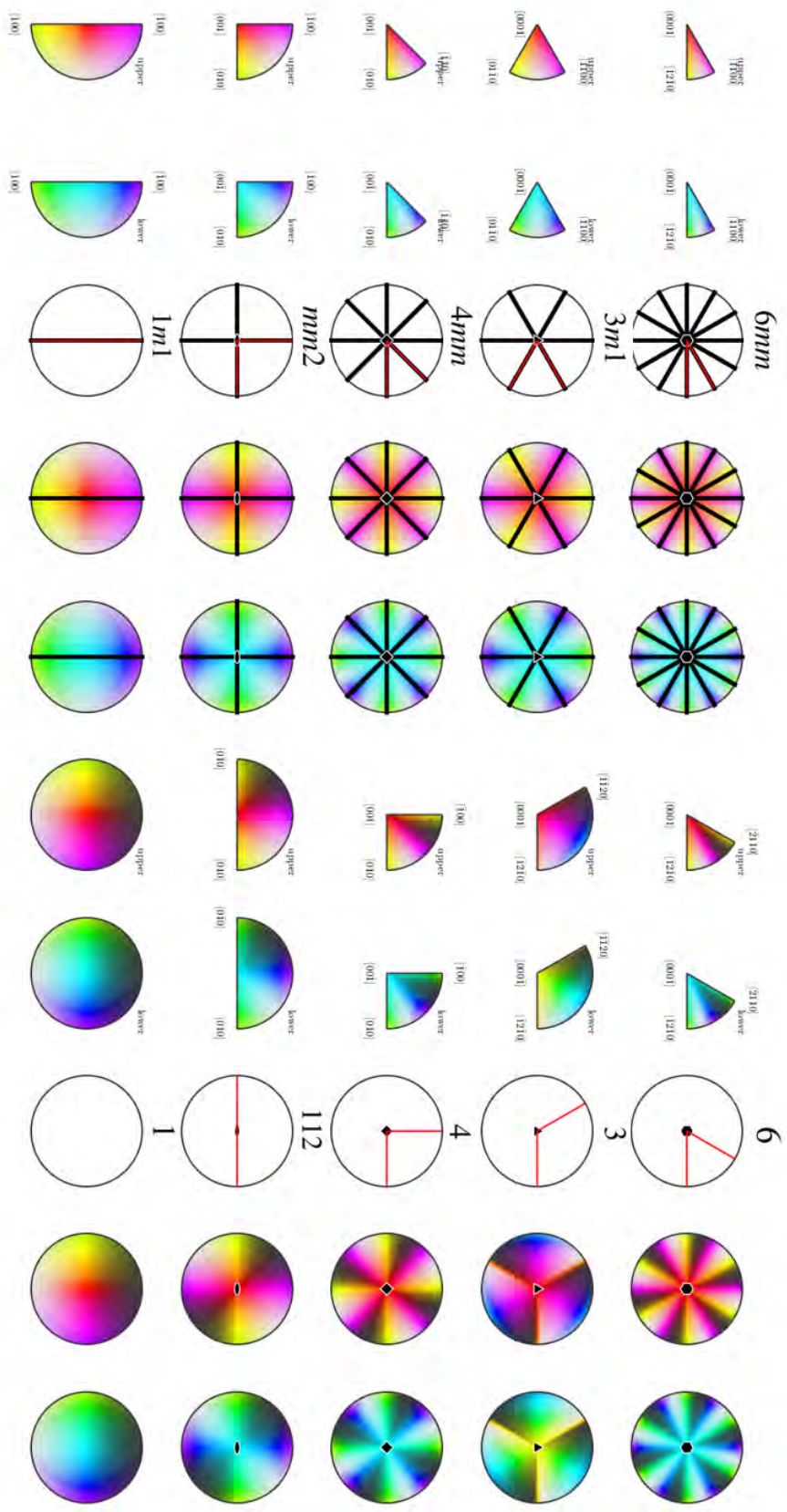

Fig. 4.5 Illustrations of the IPF color key considering the point groups.

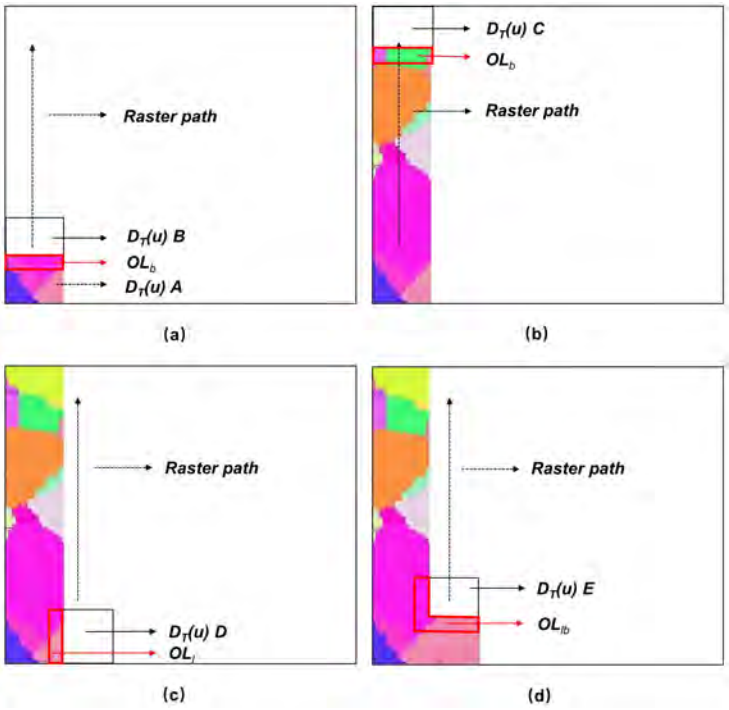

Fig. 4.6 Illustration of the patch-based texture synthesis (PTS) algorithm with the raster-scan order.

Fig. 4.6 summarizes the central concepts of the PTS algorithm with the raster-scan order. It begins at the origin of the raster path in the synthesized domain $\boldsymbol{Y}$, accompanied by the data event $\boldsymbol{D_T(u)}$ $\boldsymbol{A}$. A patch $\boldsymbol{T}$ is chosen randomly from the initial given image, and inserted into $\boldsymbol{D_T(u)}$ $\boldsymbol{A}$ at the location $\boldsymbol{u}(x,y)$. Then, a small bottom overlap area $\boldsymbol{OL}_b$ is specified (Fig. 4.6a). The original image $\boldsymbol{X}$ is scanned for a patch that best matches the overlap area $\boldsymbol{OL}_b$ based on the similarity measures. If multiple patches share the same similarity, one is randomly chosen and superimposed into $\boldsymbol{D_T(u)}$ $\boldsymbol{B}$ alongside the raster path. This procedure is repeated until the $\boldsymbol{D_T(u)}$ $\boldsymbol{C}$ at the end of the first raster path are inserted into the patch matched from $\boldsymbol{X}$ (Fig. 4.6b). The PTS algorithm then proceeds upward, selecting another raster path adjacent to the previous one. The first patch inserted into the $\boldsymbol{D_T(u)}$ $\boldsymbol{D}$ must match the left overlap area $\boldsymbol{OL}_l$ (Fig. 4.6c) and the second patch inserted into the data event($\boldsymbol{D_T(u)}$ $\boldsymbol{E}$ must match the overlap areas $\boldsymbol{OL}_{lb}$ on the left and bottom sides (Fig. 4.6d). The pseudo-code for the PTS model is given in Algorithm 1. The initial image $\boldsymbol{X}$, the size of the patch $\boldsymbol{T}$, and the size of the overlap region $\boldsymbol{OL}$ are all required inputs for the PTS algorithm. The random raster path origin, raster path direction, patch location in $\boldsymbol{X}$, and patch size ensure sufficient stochastic realizations (lines 3-4 in Algorithm 1). Only the information of the overlap region $\boldsymbol{OL}$ from each data event $\boldsymbol{D_T(u)}$ along the raster path is used for calculating the template matching function, which measures the similarity between

the overlap region $\boldsymbol{OL}$ and the initial image $\boldsymbol{X}$ (lines 6-7 in Algorithm 1). The three RGB channels could be performed synchronously in the template matching algorithm (line 7 in Algorithm 1) to generate a unifying matching location in $\boldsymbol{X}$. Implementing template matching using the grey-scale channel is a simple and effective way. The candidate locations $\boldsymbol{cand\_loc}$, corresponding to the overlap candidate regions $\boldsymbol{OL_c}$, are then extracted from $\boldsymbol{X}$ (line 8 in Algorithm 1). A random location is selected, and the patch at that location is assigned to the data event $\boldsymbol{D_T(u)}$ at location $\boldsymbol{u}(x,y)$ (lines 9-10 in Algorithm 1). For example, the three RGB channels are allocated synchronously to the current data event based on a unifying matching location in $\boldsymbol{X}$. The algorithm then proceeds along the raster paths, repeating the processes until all the data events $\boldsymbol{D_T(u)}$ are allocated with the patches (line 11 in Algorithm 1).

Fast template matching

Various template match methods have been successfully applied in the PTS model. One of the most standard implementations is the sum of squared differences method for accurate target detection [123, 3, 176, 175]. [418] discovered that the cross-correlation method could significantly improve the simulation speed and patch reproduction. Given that the cross-correlation calculation serves as a filtering template through convolution, the computational performance can be further improved by calculating the cross-correlations using the convolution theorem [421], written as

$$\boldsymbol{X} \otimes \boldsymbol{OL} = \Im^{-1}\left[\Im(\boldsymbol{X}) * \Im(\boldsymbol{OL})\right] \tag{4.7}$$

where $\otimes$ indicates the convolution between $\boldsymbol{X}$ and $\boldsymbol{OL}$, $*$ denotes the pointwise product operation, $\Im$ and $\Im^{-1}$ represent the Fourier transform, and the inverse Fourier transform, respectively. In brief, the Fourier transform of the convolution between $\boldsymbol{X}$ and $\boldsymbol{OL}$ equals the pointwise product of the Fourier transforms of $\boldsymbol{X}$ and $\boldsymbol{OL}$. Thus, the improved template match algorithm entails converting the $\boldsymbol{X}$ and $\boldsymbol{OL}$ to the frequency domain via the fast Fourier transform (FFT), expressed as

$$\Im\left[f(x,y)\right] = F(u,v) = \sum_{x=0}^{I-1}\sum_{y=0}^{J-1} exp\left[-2\pi i(ux/I + vy/J)\right] \tag{4.8}$$

where $f(x,y)$, for $x = 0,1,2,...,I-1$, and $y = 0,1,2,...,J-1$, indicates an $I \times J$ image in the spatial domain. After that, the pointwise product of the Fourier transforms of $\boldsymbol{X}$ and $\boldsymbol{OL}$ is calculated, and then the inverse Fourier transform converts the pointwise product result

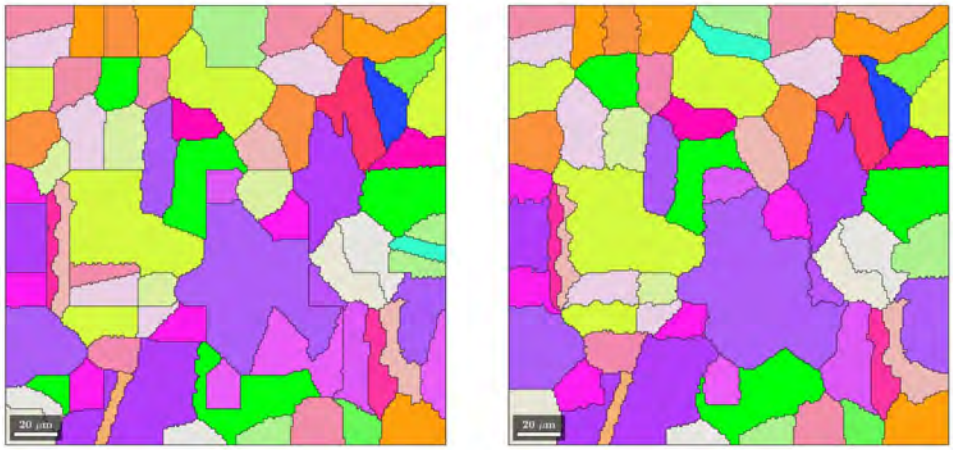

Fig. 4.7 Illustration of the imaging quilting (IQ) algorithm: (a) patch-based texture synthesis without imaging quitting; (b) patch-based texture synthesis with imaging quitting.

into the spatial domain, described as

$$f(x,y) = \frac{1}{I \times J} \sum_{u=0}^{I-1} \sum_{v=0}^{J-1} F(u,v) exp\left[2\pi i(ux/I + vy/J)\right] \tag{4.9}$$

Image quilting

Algorithm 2 An algorithm for image quilting

procedure PTS ($\boldsymbol{T}_1$, $\boldsymbol{T}_2$, $\boldsymbol{OL}_1$, $\boldsymbol{OL}_2$)
  $\boldsymbol{e} \leftarrow (\boldsymbol{OL}_1 - \boldsymbol{OL}_1)^2$
  for $i = 1 : m$ **do** ▷ m is the row number in $\boldsymbol{e}$
    for $j = 1 : n$ **do** ▷ n is the column number in $\boldsymbol{e}$
      $\boldsymbol{E}_{i,j} \leftarrow \boldsymbol{e}_{i,j} + min\ (\boldsymbol{E}_{i-1,j-1},\ \boldsymbol{E}_{i-1,j},\ \boldsymbol{E}_{i-1,j+1});\ if\ j = 2,...,n-1$
      $\boldsymbol{E}_{i,j} \leftarrow \boldsymbol{e}_{i,j} + min\ (\boldsymbol{E}_{i-1,j},\ \boldsymbol{E}_{i-1,j+1});\ if\ j = 1$
      $\boldsymbol{E}_{i,j} \leftarrow \boldsymbol{e}_{i,j} + min\ (\boldsymbol{E}_{i-1,j-1},\ \boldsymbol{E}_{i-1,j});\ if\ j = n$
    end for
  end for
  $k \leftarrow min\ (\boldsymbol{E}_{m,j});\ j = 1,...,n$ ▷ k denotes the arrival point of MCP on the last row of $\boldsymbol{E}$
  $MCP \leftarrow min\ (\boldsymbol{E}_{i,k-1},\ \boldsymbol{E}_{i,k},\ \boldsymbol{E}_{i,k+1});\ i = n-1,...,1$
end procedure

Fig. 4.7 shows the synthesized results using the PTS method. It is apparent that the vertical and horizontal incompatibilities appear at the edges of overlapping patches (see

Fig. 4.7.a). The noticeable seam in the overlap areas can disorder the grain boundary structures and further affect the properties and performance. The inconsistencies are due to the considerable overlap error caused by the suboptimal patch chosen. To address this issue, the imaging quilting (IQ) algorithm [100, 266, 3, 154, 24] is introduced into the PTS model. The IQ algorithm examines the overlap error between the selected patch in $\boldsymbol{X}$ and the patch in $\boldsymbol{D_T(u)}$. A minimum cost path (MCP) then defines the new boundaries in the overlap areas. Fig. 4.7.b shows the IQ algorithm's results. It can be seen that the IQ algorithm can significantly improve patch continuity and better capture boundary features in polycrystalline materials.

The pseudocode in the Algorithm 2 computes the MCP for a vertical overlap area. The input parameters are the two overlapping patches $\boldsymbol{T}_1$ and $\boldsymbol{T}_2$ with overlapping areas $\boldsymbol{OL}_1$ and $\boldsymbol{OL}_2$. It starts with identifying the surface error $\boldsymbol{e}$ through the smallest squared distance between $\boldsymbol{OL}_1$ and $\boldsymbol{OL}_2$ (line 2 in Algorithm 2). Then, the cumulative minimum error $\boldsymbol{E}$ is calculated along the vertical direction (lines 3-9 in Algorithm 2). In the end, the smallest value of the last row in $\boldsymbol{E}$ will indicate the final arrival point k of MCP, and one can trace back the arrival point k for each row i $(i = n-1, ..., 1)$ as $min\ (\boldsymbol{E}_{i,k-1},\ \boldsymbol{E}_{i,k},\ \boldsymbol{E}_{i,k+1})$ and find the MCP (lines 10-11 in Algorithm 2). The same principle applies to the computation of MCP for a horizontal overlap area.

4.3.2 Mapping orientations from the IPF coloring

The microstructure generated by the IPF-color-based PTS model can not specify the crystallographic characterizations due to few studies investigating the inverse mapping from the IPF coloring to the $\boldsymbol{G}$. Since the properties and performance in polycrystalline materials are highly dependent on the crystallographic characterizations [302, 55, 301], it is critical to establish the orientation information in the synthesized polycrystalline microstructure. In this section, we develop the new methods pioneered in mapping orientations from the $\boldsymbol{P}$-specific IPF-color key. They are composed of two parts: the inverse IPF-color key for transforming the RGB triple into the azimuthal angle ρ and the polar angle θ and the orientation probability assignment for quantifying the azimuthal angle φ.

Inverse IPF-color key

The colormap in the standard or extended $\boldsymbol{P}$-specific IPF-color key represents the one-to-one mapping between the RGB triplet and the vector $\boldsymbol{h}$ in the crystal coordinate system (see Equation (4.1)). Therefore, the first step in mapping orientations from the $\boldsymbol{P}$-specific IPF-color key is to convert each RGB triplet into the crystal direction $\boldsymbol{h}$, stated as

- Transform the RGB triplet into the HSL triplet.
- Convert the hue H into the azimuthal angle ρ based on Equation (4.2). Similarly, calculate the polar angle θ from Equation (4.5) and Equation (4.6) based on the lightness L and the saturation S (see Fig. 4.8).
- Determine the symmetrically equivalent crystal direction $\boldsymbol{h}$ based on the polar angle θ and the azimuthal angle ρ (see Fig. 4.9).

It may take a long time to solve the azimuthal angle ρ and polar angle θ from the nonlinear Equation (4.2), Equation (4.5) and Equation (4.6). Recognizing that the relationships between H and ρ in Equation (4.2), S and L in Equation (4.6), and L and θ in Equation (4.5) are monotonic, it is possible to precompute the function curves to avoid the time-consuming and expensive procedure of solving Equation (4.2), Equation (4.5) and Equation (4.6). Fig. 4.8 illustrates these precomputed curves between H and ρ, S and L and L and θ. The derivation from the polar angle θ and the azimuthal angle ρ to the crystal direction $\boldsymbol{h}$ is expressed as (see Fig. 4.9)

- Calculate the vector $\boldsymbol{N}_\rho$ through the conditions (a) $\boldsymbol{N}_\rho \perp \boldsymbol{p}$ and (b) $\boldsymbol{N}_\rho \perp \boldsymbol{b}$.
- Calculate the vector $\boldsymbol{h}$ via Equation (4.10).

$$\begin{aligned} \boldsymbol{h} \cdot \boldsymbol{N}_\rho &= 0 \\ \boldsymbol{h} \cdot \boldsymbol{p} &= cos(\theta) \\ \boldsymbol{h} \cdot \boldsymbol{b} &= cos(\theta_{\rho b}) \end{aligned} \tag{4.10}$$

where $\cdot$ is the dot product of two vectors, $\boldsymbol{N}_\rho$ is the normal vector perpendicular to the plane P_ρ, and $\theta_{\rho b}$ is the angle between the vector $\boldsymbol{h}$ and $\boldsymbol{p}$ in the plane P_ρ.

Orientation probability assignment

One crystal direction can not determine the lattice orientation $\boldsymbol{G}$ in polycrystalline materials. For instance, the Miller indices $(hkl)[uvw]$ for orientation parameterization are specified by the rotation relationship between the two crystal directions $[001]$ and $[100]$ in the crystal coordinate system and the normal direction $\boldsymbol{ND}$ and rolling direction $\boldsymbol{RD}$ in the specimen coordinate system. With one crystal direction $[hkl]$, e.g., the $\boldsymbol{ND}$ in the crystal coordinate system, solved via the inverse $\boldsymbol{P}$-specific IPF-color key, the other crystal direction $[uvw]$, e.g., the $\boldsymbol{RD}$ in the crystal coordinate system, can be established through the proposed azimuthal angle φ illustrated in Fig. 4.10.a. The φ is the angle between the vector $\boldsymbol{R_1}$ and $\boldsymbol{RD}$ in the plane P_φ perpendicular to the vector $\boldsymbol{ND}$. The vector $\boldsymbol{R_1}$ is the intersection line between

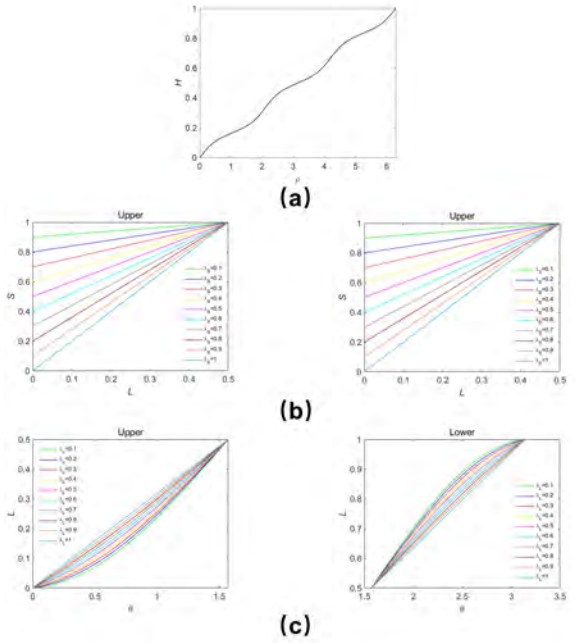

Fig. 4.8 Precomputed curves: (a) the $H-\rho$, (b) the $S-L$, and (c) the $L-\theta$.

the plane (010) and the plane P_{φ}. The derivation from the azimuthal angle φ to the crystal direction $[uvw]$ is expressed as (see Fig. 4.10.b)

- Calculate the vector $\boldsymbol{R_2}$ through the conditions (a) $\boldsymbol{R_2} \perp \boldsymbol{ND}$ and (b) $\boldsymbol{R_2} \perp \boldsymbol{R_1}$.
- Calculate the vector $\boldsymbol{RD}$ via Equation (4.11).

$$\begin{aligned} \boldsymbol{RD} \cdot \boldsymbol{ND} &= 0 \\ \boldsymbol{RD} \cdot \boldsymbol{R_1} &= cos(\varphi) \\ \boldsymbol{RD} \cdot \boldsymbol{R_2} &= cos(\varphi_1) \end{aligned} \tag{4.11}$$

where φ_1 is the angle between the vector $\boldsymbol{R_2}$ and $\boldsymbol{RD}$ in the plane P_{φ}, the relationship between φ_1 and φ is expressed as

$$\varphi_1 = \begin{cases} \pi/2 - \varphi & 0 \leq \varphi < \pi/2 \\ \varphi - \pi/2 & \pi/2 \leq \varphi < \pi \\ \varphi - \pi/2 & \pi \leq \varphi < 3\pi/2 \\ 2\pi - \varphi & 3\pi/2 \leq \varphi < 2\pi \end{cases} \tag{4.12}$$

After establishing the relationship between φ and $[uvw]$, the next step is utilizing the orientation probability assignment (OPA) method to randomly sample the φ from the conditional

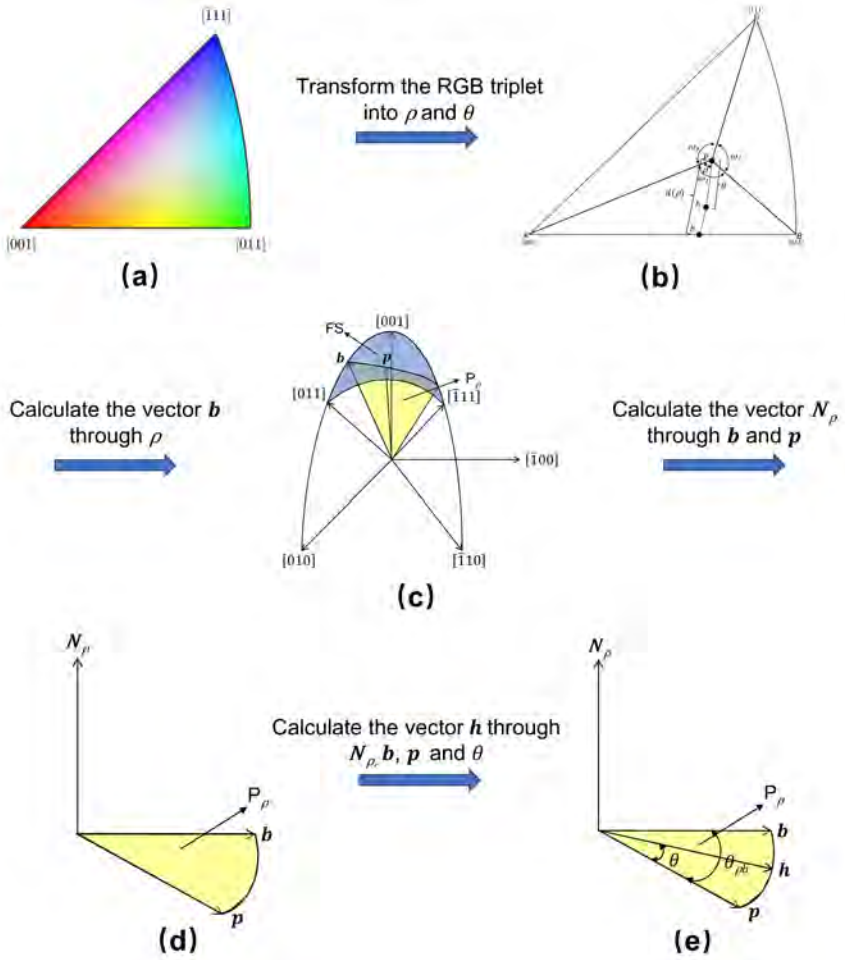

Fig. 4.9 Flowchart of converting the RGB triplet into the symmetrically equivalent crystal direction $\boldsymbol{h}$.

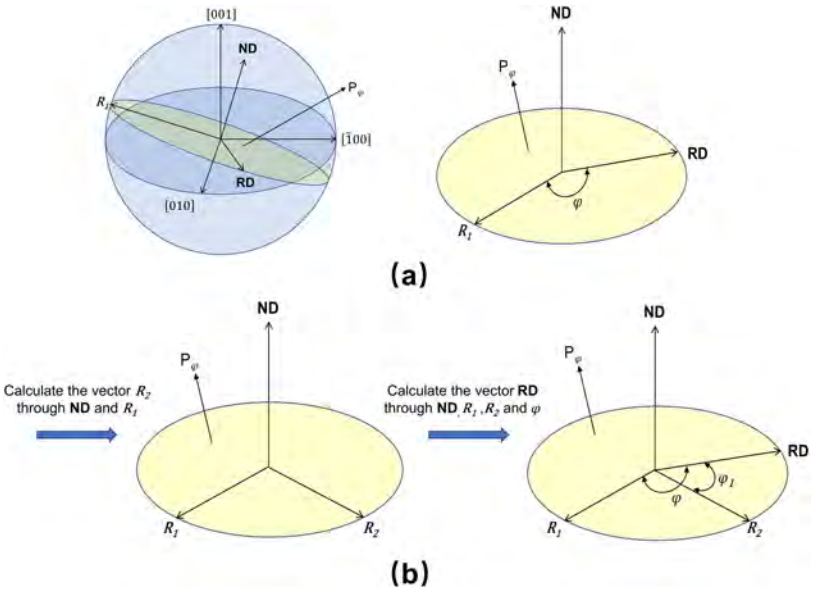

Fig. 4.10 Illustration of the proposed azimuthal angle φ defined by the ***RD*** and ***ND*** in the crystal coordinate system.

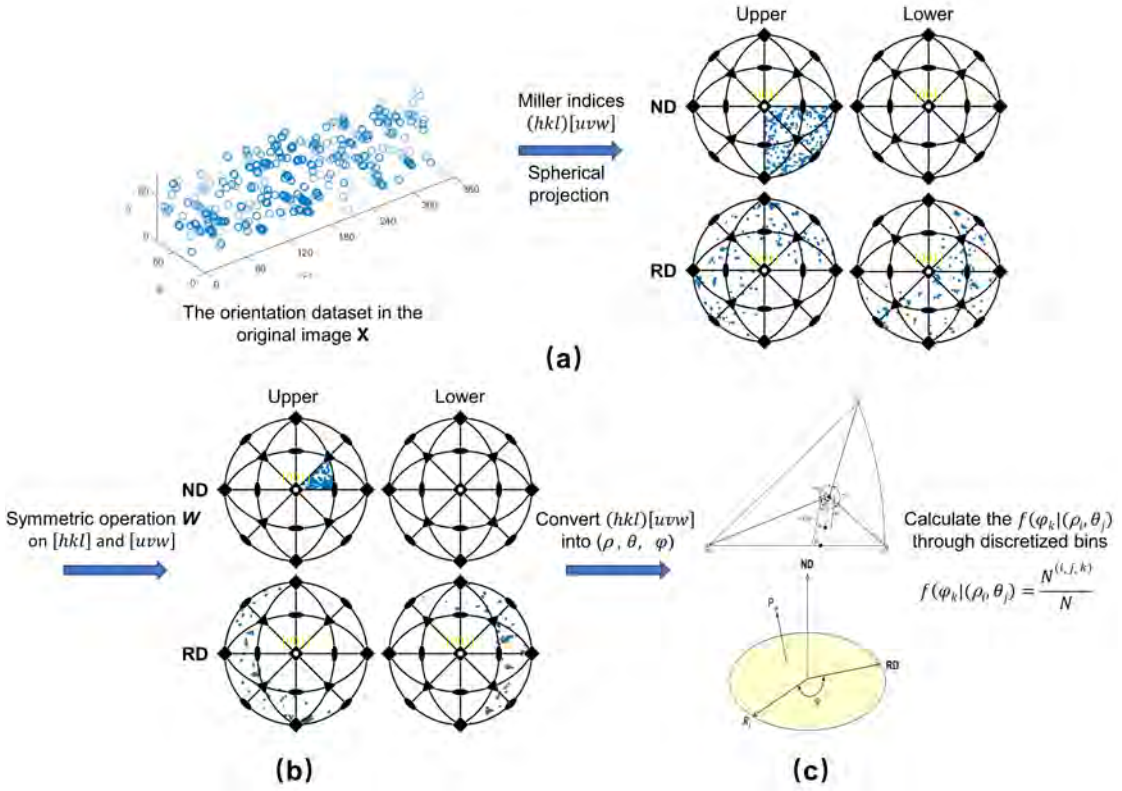

Fig. 4.11 Illustration of the flowchart for calculating the $f(\varphi_k|(\rho_i,\ \theta_j))$, using the $m\bar{3}m$ symmetry group as an example.

probability density $f(\varphi_k|(\rho_i,\ \theta_j))$ $(k = 1,2,...,K)$ calculated from the orientation dataset in the original image $\boldsymbol{X}$. The steps for calculating the $f(\varphi_k|(\rho_i,\ \theta_j))$ are summarized as

- Convert the orientation dataset in the original image $\boldsymbol{X}$ into the Miller indices $(hkl)[uvw]$ (see Fig. 4.11.a).
- Project $[hkl]$ to the FS via the symmetric operation $\boldsymbol{W}$ and simultaneously perform the same symmetric operation on $[uvw]$ (see Fig. 4.11.b).
- Transform the crystal direction $[hkl]$ into the polar angle θ and the azimuthal angle ρ. Meanwhile, describe the crystal direction $[uvw]$ through the azimuthal angle φ (see Fig. 4.11.c).
- Discretize the polar angle θ, the azimuthal angle ρ, and the azimuthal angle φ into bins. For example, the azimuthal angle ρ ranging from 0° to 360° degrees is discretized into I bins ρ_i $(i = 1,2,...,I)$ of dimension $2\pi/I$; The polar angle θ ranging from 0° to 180° degrees is discretized into J bins θ_j $(j = 1,2,...,J)$ of dimension π/J; The proposed azimuthal angle φ ranging from 0° to 360° degrees is discretized into K bins φ_k $(k = 1,2,...,K)$ of dimension $2\pi/K$;
- Calculate the $f(\varphi_k|(\rho_i,\ \theta_j))$ $(k = 1,2,...,K)$ by dividing the number of orientations $N^{(i,\ j,\ k)}$ in the $(\rho_i,\ \theta_j,\ \varphi_k)$ element over the total number of orientations N in the orientation space elements ranging from $(\rho_i,\ \theta_j,\ \varphi_1)$ to $(\rho_i,\ \theta_j,\ \varphi_K)$, expressed as $\frac{N^{(i,\ j,\ k)}}{N}$ (see Fig. 4.11.c).

Once the polar angle θ, the azimuthal angle ρ, and the azimuthal angle φ are determined (see Fig. 4.12.a), we can obtain the orientation dataset in the synthesized images $\boldsymbol{Y}$ by transforming the polar angle θ and the azimuthal angle ρ into the crystal direction $[hkl]$ and derivating the crystal direction $[uvw]$ from the azimuthal angle φ (see Fig. 4.12.b-Fig. 4.12.d). Fig. 4.13 shows the results of the orientation dataset in some synthesized images. It can be concluded that the orientation datasets in the synthesized images are statistically equivalent to the orientation dataset in the original image.

4.4 Applications

4.4.1 Microstructure characterizations

As mentioned in Section 3.3, the geometry-based reconstruction aims to synthesize the SERVEs whose microstructure characterizations are statistically equivalent to those of the

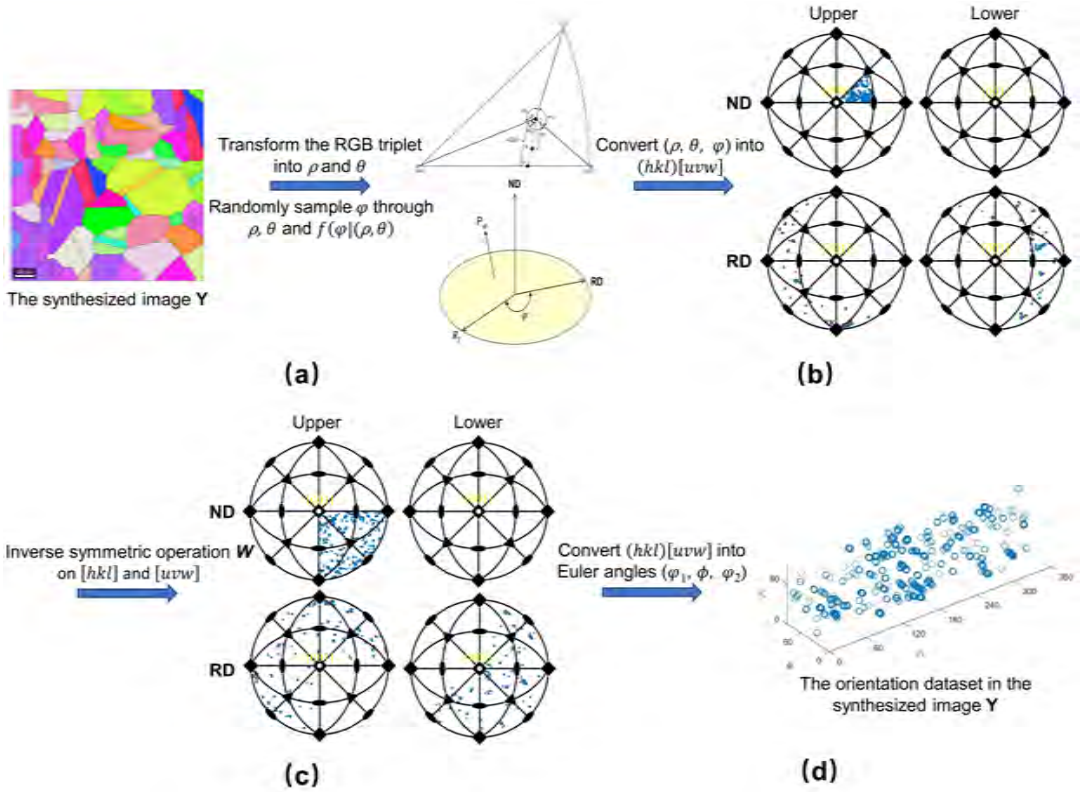

Fig. 4.12 Illustrations of converting the RGB triplets into the orientation dataset in the synthesized images $\boldsymbol{Y}$.

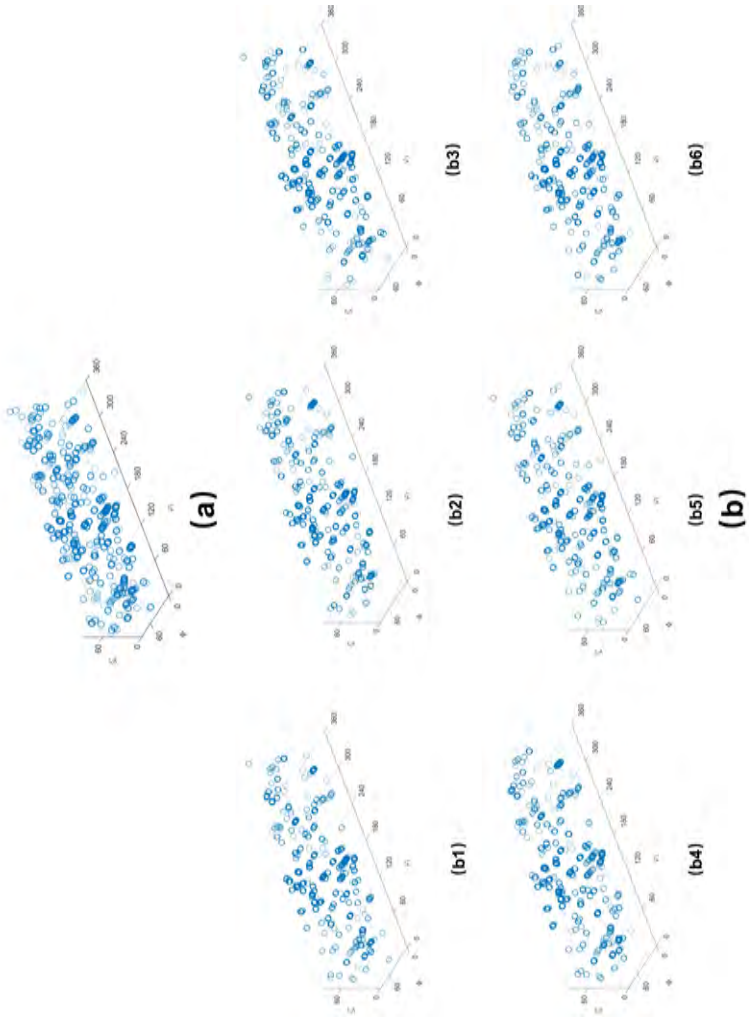

Fig. 4.13 Illustration of the orientation dataset in the original image (a) and synthesized domains (b).

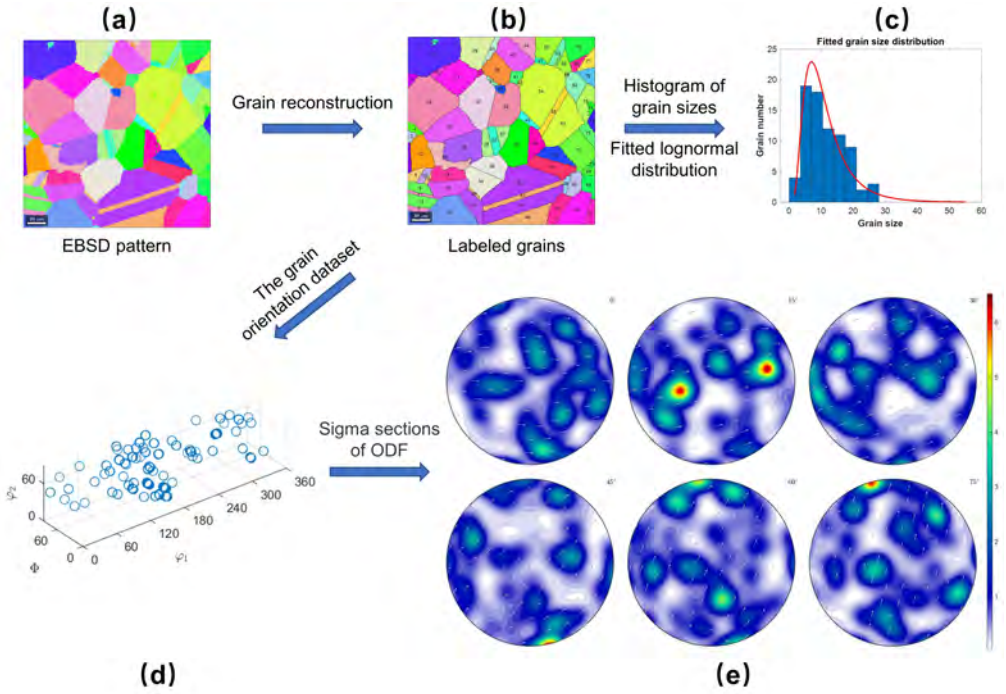

Fig. 4.14 The microstructure characterizations of the original orientation dataset for an FCC nickel-based Inconel 718 superalloy.

corresponding RVE. This part will validate the reconstruction results generated by the enhanced PTS algorithm in terms of morphological and crystallographic characterizations. The sample of interest is a face-centered cubic (FCC) nickel-based Inconel 718 superalloy. It was prepared through a grinding and polishing machine. An electron backscatter diffraction (EBSD) map was then acquired to characterize the microstructural lattice orientation information using a scanning electron microscope (SEM) equipped with an EDAX DigiView EBSD camera. Fig. 4.14.a illustrates the EBSD pattern in which the crystallographic orientation is represented with the $m\bar{3}m$ IPF coloring. Fig. 4.14.b depicts the labeled grains reconstructed as the set of pixels whose misorientation angle is under a certain threshold.

Section 2.3 has revealed that the grain size distribution (GSD) correlates strongly with the grain size, volume, topology, and neighborhood distributions. Therefore, the GSD is utilized to validate the SERVEs generated by the enhanced PTS algorithm. Fig. 4.14.c shows the grain size histogram and fitted lognormal distribution in the original EBSD pattern (RVE). Crystallographic characterizations of polycrystalline materials can not be quantified by the GSD. Frequently, the orientation distribution function (ODF) is often used to characterize the preferred crystallographic orientation of grains. Fig. 4.14.e depicts the ODF of reconstructed grains in terms of sigma sections [19]. Fig. 4.15.c presents the reconstructed grains generated from the synthesized images $\boldsymbol{Y}$. It is clear that incompatible small grains appear in the

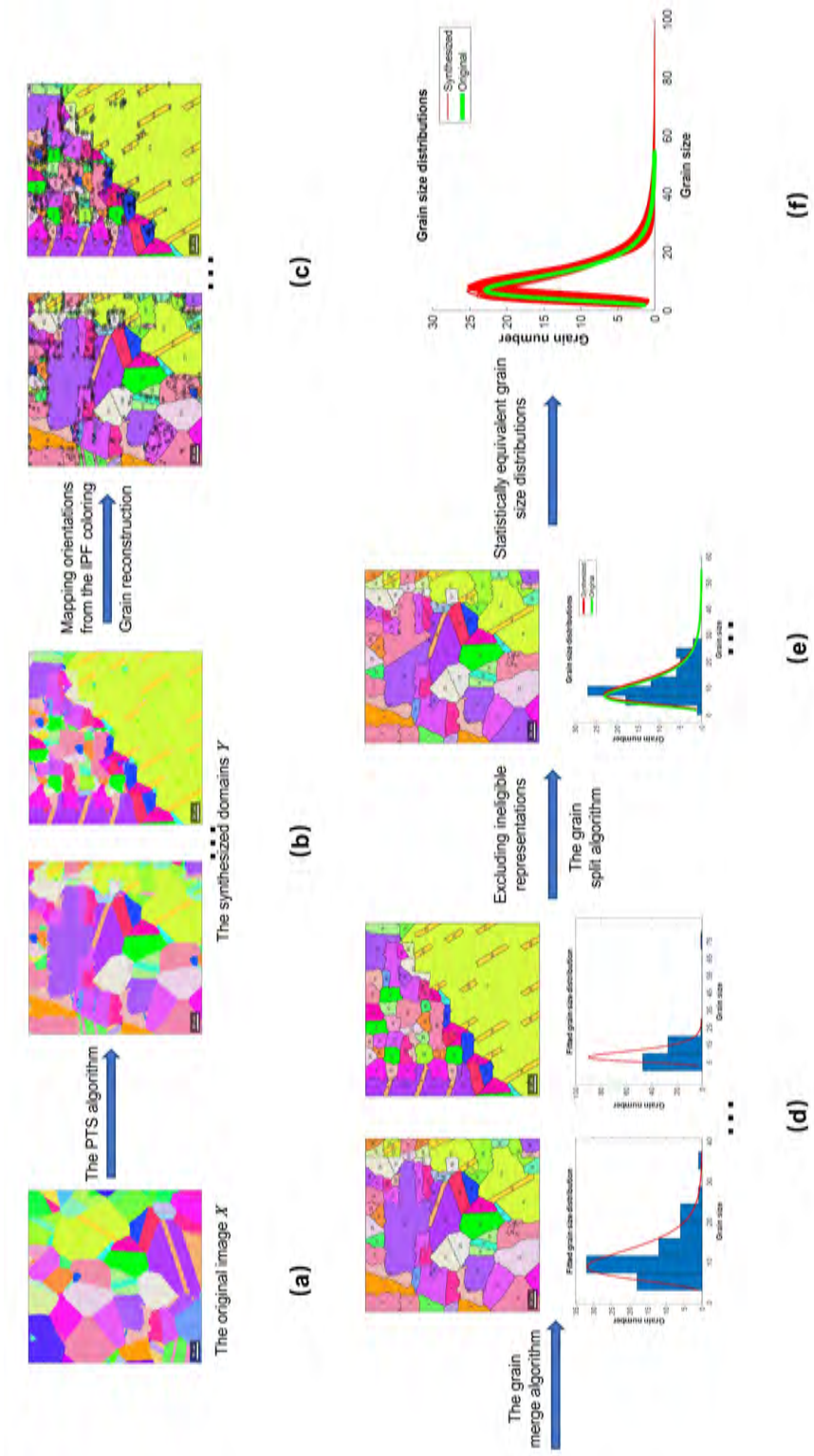

Fig. 4.15 The flowchart of grain size distributions for the synthesized orientation dataset.

Algorithm 3 An algorithm for merging grains

1: Generate the synthesized images $\boldsymbol{Y}$
2: Mapping orientations from the IPF coloring
3: Grain reconstruction
4: **repeat**
5: Initialize S_c
6: Eliminate small grains
7: Fill in the voids
8: Grain reconstruction
9: **until** stopping criterion is met

intragranular and intergranular regions. The inconsistencies are caused by experimental measurements and overlap errors. To address this issue, the grain merge algorithm (see Algorithm 3) is proposed by assigning the small grains to the surrounding big grains. It begins by initializing a critical value of the grain area (S_c) in order to identify small grains (line 5, Fig. 4.16.a2). The small grains, or errors, are then chosen and eliminated (line 6, Fig. 4.16.a3). Following that, the deleted regions are filled using the spline filter (line 7, Fig. 4.16.a4). Finally, the algorithm repeats the process until the required grain size is reached. An additional crucial function of the grain merge algorithm is to eliminate ineligible representations (see Fig. 4.15.d-Fig. 4.15.e). The qualified synthetic images are identified by satisfying the following criteria:

$$\|GSD_{\boldsymbol{X}} - GSD_{\boldsymbol{Y}}\|^2 \leq \varepsilon \tag{4.13}$$

where ε is the threshold value, $GSD_{\boldsymbol{X}}$ and $GSD_{\boldsymbol{Y}}$ are the distributions of grain size in the original and synthetic images, respectively. Due to the absence of small grains, the grain merge algorithm will invariably overestimate the GSD of synthetic images. The grain split algorithm (see Algorithm 4) has been suggested as a solution for this issue (see Fig. 4.15.e). The first step of the algorithm for grain splitting is the random selection of a grain (line 3, Fig. 4.16.b2). The grain's triple points are then determined by identifying the grain's boundary points shared with two adjacent grains (line 4, Fig. 4.16.b3). Following that, the split line between the triple point and centroid will divide the selected grain in half (lines 5-7, Fig. 4.16.b4). Fig. 4.15.f and Fig. 4.17 show the GSD and the corresponding GOD for the synthesized polycrystalline structure. Lastly, the algorithm repeats the process until the required GSD threshold value (see Equation (4.13)) is reached. It can be concluded that the microstructure characterizations of the synthesized polycrystalline structure are statistically equivalent to the counterpart of the original RVE.

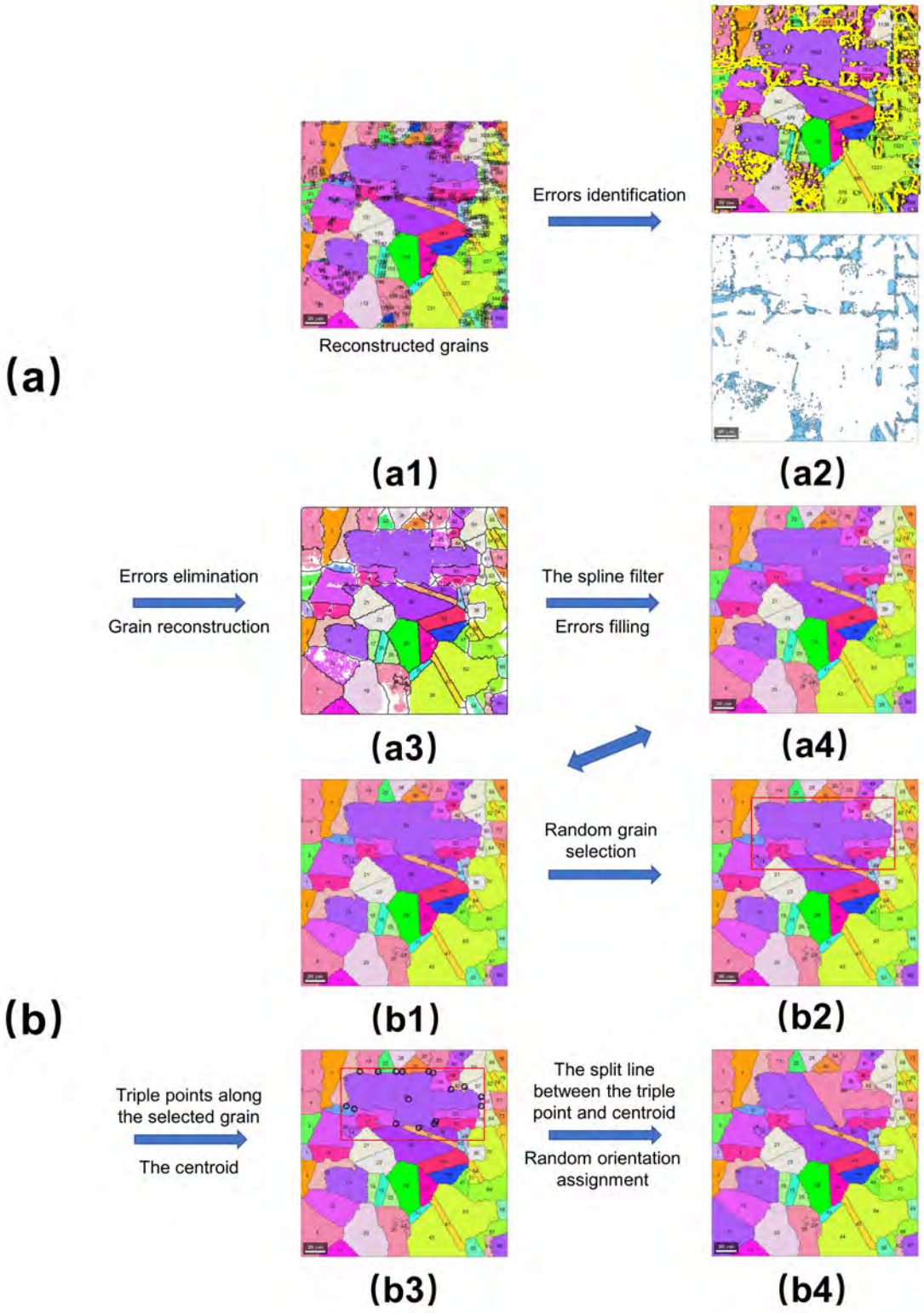

Fig. 4.16 The merge-and-split rules in grain size characterizations: (a) the grain merge algorithm for error elimination, (b) the grain split algorithm for bias correction.

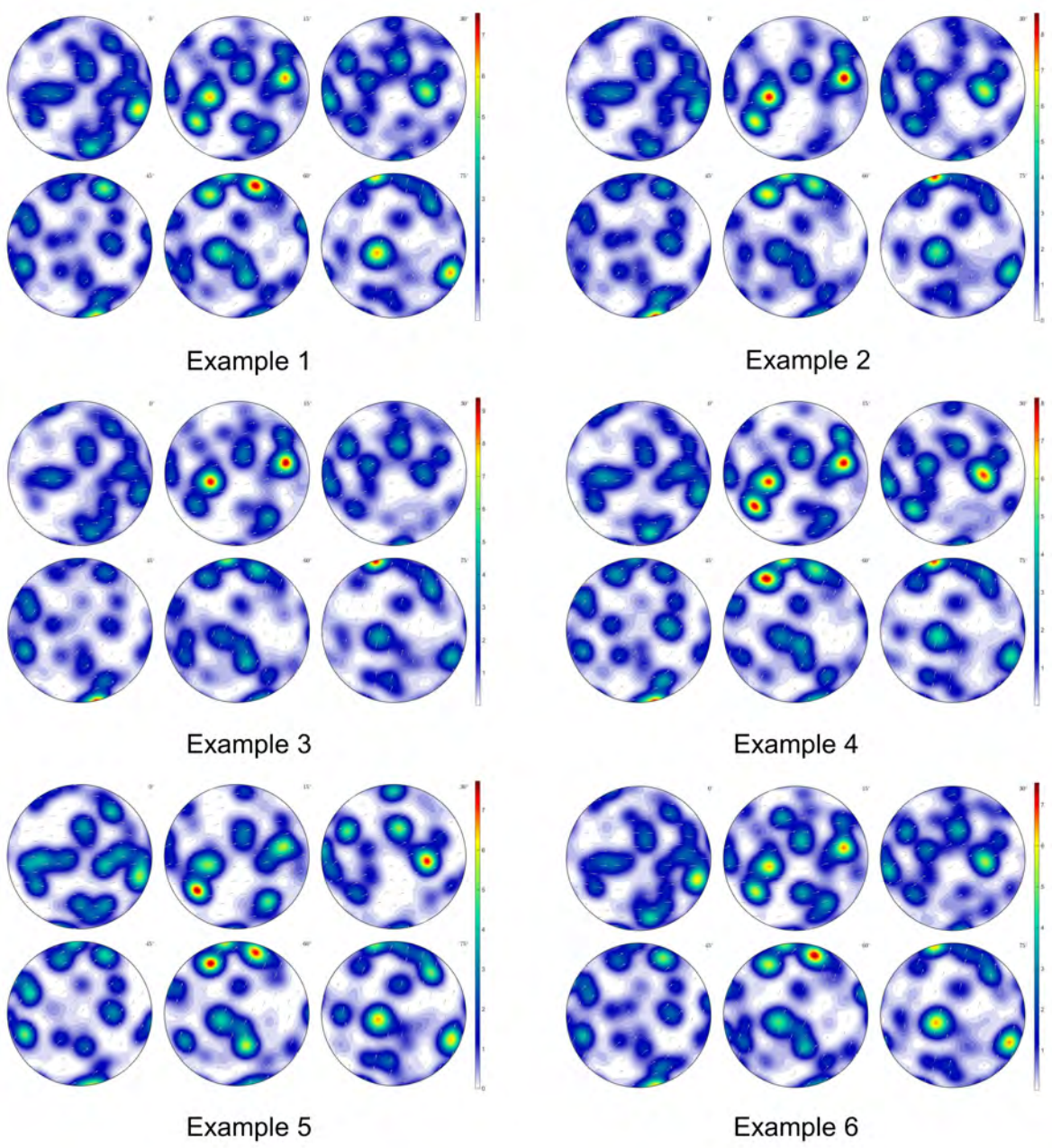

Fig. 4.17 Illustration of the grain orientation distributions for the synthesized grain orientation dataset.

Algorithm 4 An algorithm for splitting grains

1: Initialize the merged grains
2: **repeat**
3: Random grain selection
4: Specify the triple point
5: Bisect the selected grain
6: Orientation assignment
7: Grain reconstruction
8: **until** stopping criterion is met

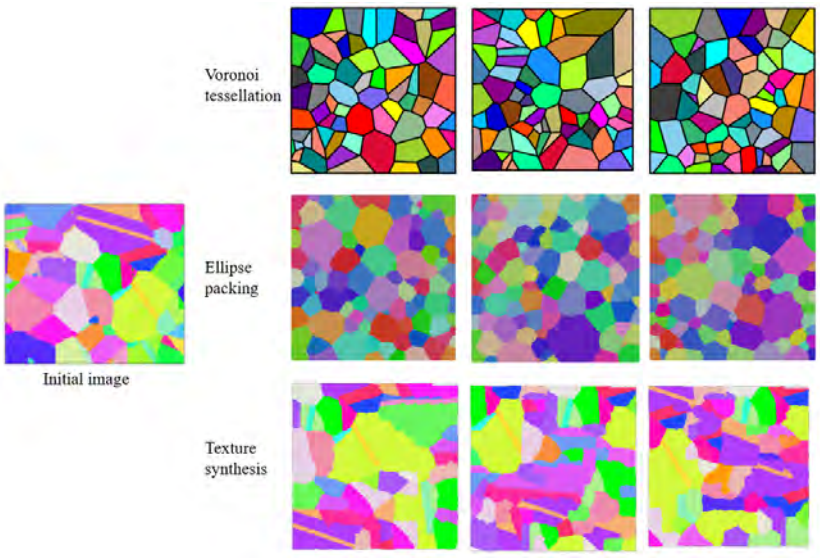

Fig. 4.18 Comparisons of microstructural reconstruction and characterization using Voronoi tesselation, ellipse packing, and improved PTS schemes.

4.4.2 Comparison studies

We further validate the improved PTS method in this section by comparing it to the Voronoi tesselation and ellipse packing methods. The synthetic images, grain size distributions, and boundary conditions generated by the Voronoi tesselation, ellipse packing, and improved PTS methods are shown in Fig. 4.18. The Voronoi tesselation and ellipse packing methods clearly underestimate the grain size distribution, whereas the improved PTS method perfectly matches the grain size distribution in the original image. In the meantime, the improved PTS method is superior to Voronoi tesselation and ellipse packing in grain boundary representation, especially for twin boundaries.

4.5 Conclusions

This Chapter presents some novel strategies for texture synthesis models applied to the microstructural reconstruction and characterization of polycrystalline materials, such as perfect orientation coloring, patch-based texture synthesis, fast template matching, image quilting, inverse IPF coloring, and grain merge-split rules. The main conclusions are:

- The IPF coloring scheme resolves flawlessly the discontinuity issue caused by the apparent topological inconsistency between the orientation and color space, as well as the ambiguity issue caused by crystal symmetry. Meanwhile, the inverse IPF coloring can generate orientation datasets in synthesized polycrystalline microstructures that are statistically equivalent to the counterpart in the original RVE.

- The grain size and orientation distributions generated by the improved PTS models correspond perfectly to the experimental observations. Furthermore, the improved PTS models outperform the Voronoi tesselation and ellipse packing methods in grain boundary representation, particularly for twin boundaries.

Chapter 5

Explicit characterization algorithms for texture synthesis models applied to microstructure representation of polycrystalline materials.

5.1 Introduction

Besides the discontinuity and ambiguity coloring issues solved in Chapter 2, the characterizations generated by texture synthesis models are implicit and do not explicitly quantify the microstructural features [51]. Therefore, this Chapter explicitly proposes some algorithms to quantify the microstructural characterizations of polycrystalline materials. Fig. 5.1 provides a flowchart of the explicit characteriszation algorithms with their governing principles, objectives, and input requirements. They consist of three primary algorithms to provide a comprehensive description and representation of grain-level microstructures: grain nucleation and growth, constrained grain orientation generation, and constrained grain boundary generation. Details of each algorithm are presented below.

5.2 Algorithm A: Grain nucleation and growth

In the physical reconstruction of polycrystalline materials, the Monte Carlo (MC) model is built using a probabilistic method based on the reorientation of lattice sites. This makes the model very effective for problems with multiple length and time scales. Besides, the MC model offers attractive benefits for grain growth reconstruction because it is simple and easy

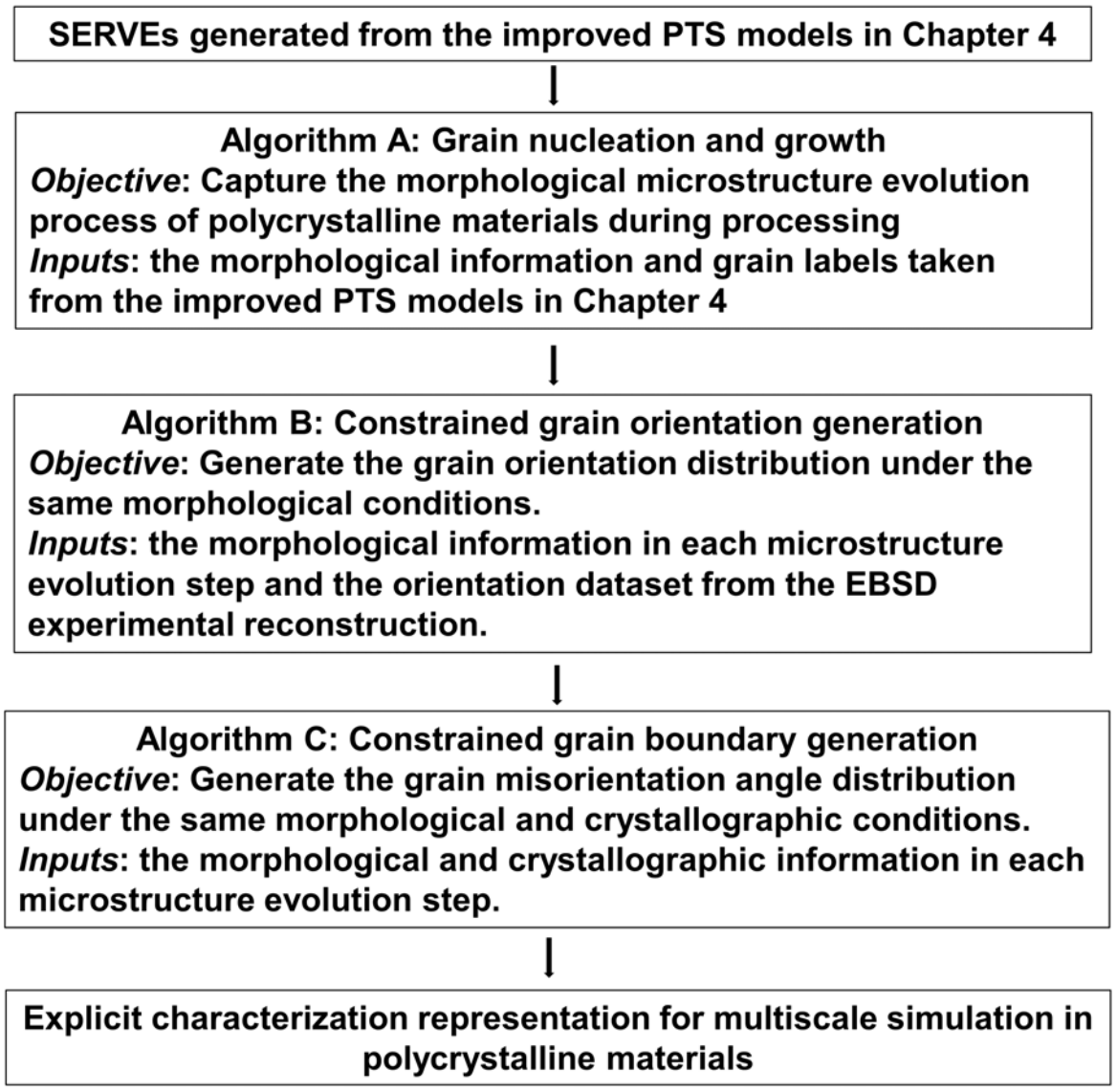

Fig. 5.1 Flowchart of the explicit characterization algorithms procedure. Each algorithm's governing principles, objectives, and required inputs are enumerated.

to implement. Furthermore, the model has minimum computational requirements, especially considering the algorithm's extreme suitability for parallelization. Thus, we use the MC model to simulate the grain growth of polycrystalline materials during processing.

During each MC time step, grain nucleation is accomplished by introducing new grains at random points along grain boundaries. Each embryonic grain comprises a small collection of adjacent lattices with a new orientation and zero stored energy. Meanwhile, grain growth is achieved by changing the orientation of a randomly selected lattice site to one of its nearest neighbor orientations. After the activation of nucleation and growth, the lattice states and sites are updatated, and the energy change ΔE from Equation (3.10) is calculated to determine whether the grain nucleation and growth are accepted or rejected. The probability criterion can be stated as [474]

$$P = \begin{cases} 1, & \Delta E \leq 0 \\ exp\left(\frac{-\Delta E}{kT_s}\right), & \Delta E \geq 0 \end{cases} \tag{5.1}$$

Grain nucleation and growth are accepted when ΔE decreases. When ΔE increases, grain nucleation and growth are accepted with Boltzmann probability.

Fig. 5.2 shows the grain nucleation and growth results through the MC model. The input data is the morphological information and grain labels taken from the improved PTS models in Chapter 4 (Fig. 5.2.a), and the output data is the morphological microstructure evolution process of polycrystalline materials during processing (Fig. 5.2.b1-Fig. 5.2.b6). Fig. 5.3 quantifies the morphological microstructure changes in terms of the fitted grain size distribution.

5.3 Algorithm B: Constrained grain orientation generation

Fig. 5.4 shows the flowchart of the constrained grain orientation generation algorithm (CGOG). The input data is the orientation dataset from the EBSD experimental reconstruction and the morphological information in each microstructure evolution step (Fig. 5.4.a). The target of the CGOG algorithm is to explicitly and stochastically generate the grain orientation distributions (Fig. 5.5.a1-a6) under the same morphological conditions (Fig. 5.5.b1-b6). The pseudo-code for the CGOG model is given in Algorithm 5. The initial morphological information ($\boldsymbol{MI}$) and the orientation dataset from the EBSD reconstruction ($EBSD_{\boldsymbol{G}}$) are all required inputs for the CGOG algorithm (line 1 in Algorithm 5). It begins with the grain reconstruction based on the orientation dataset from the EBSD reconstruction (Section 2.2) (line 2 in Algorithm 5). After that, we merge the grain orientation to its neighbors when their misorientation angle is under a certain threshold (line 3 in Algorithm 5). The probability of

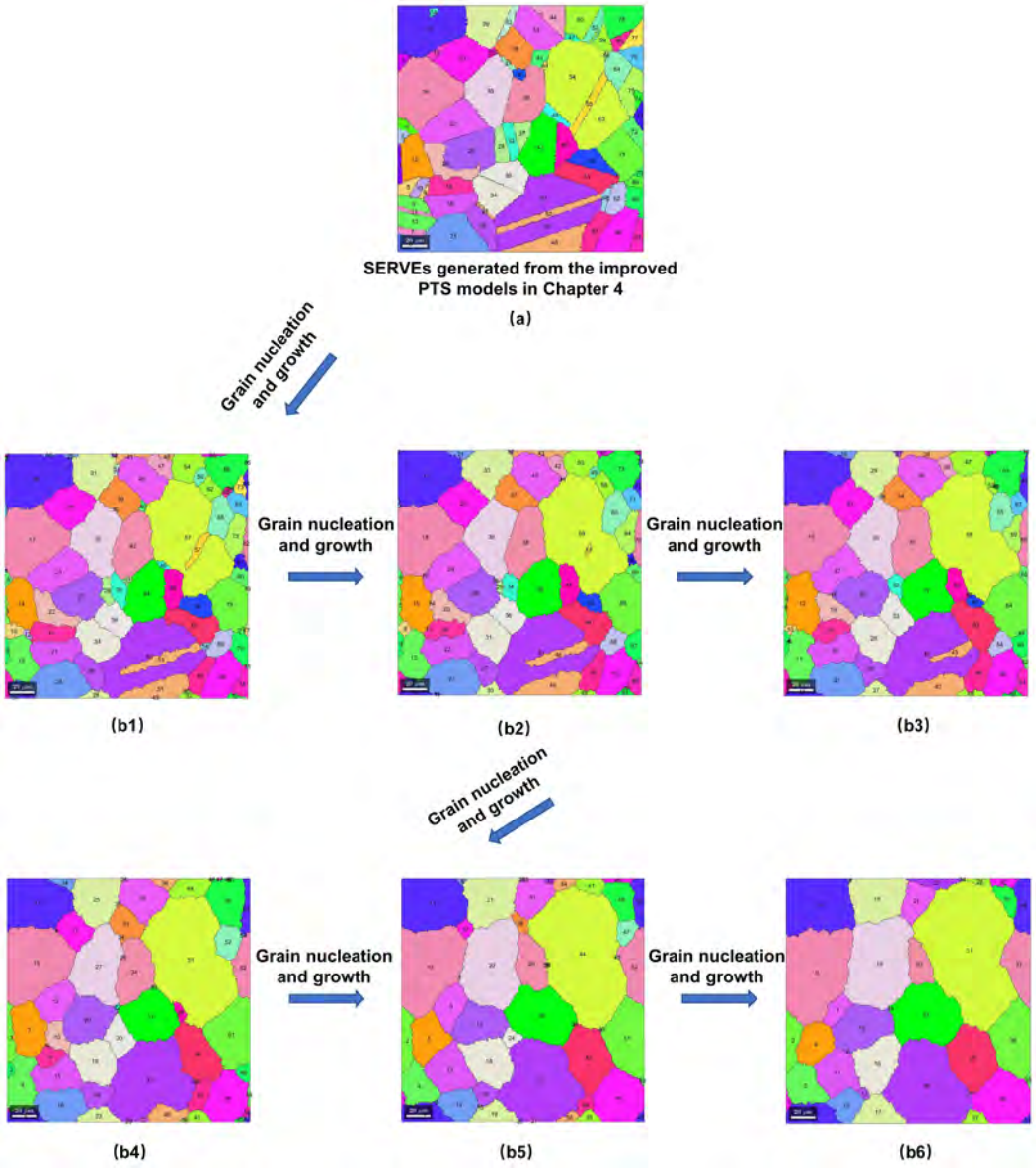

Fig. 5.2 Flowchart of the grain nucleation and growth algorithm.

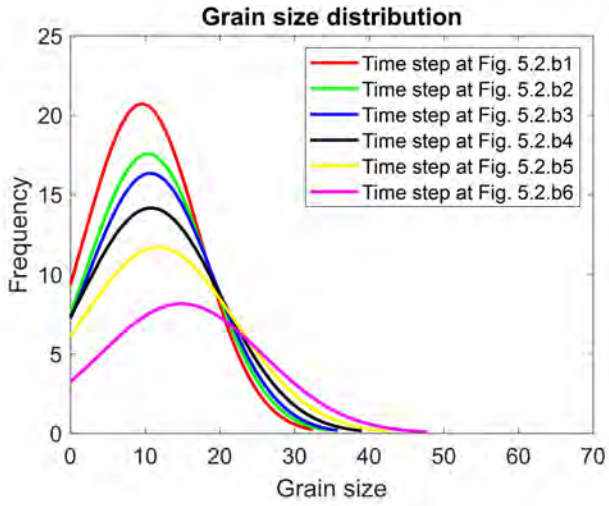

Fig. 5.3 The grain size distributions at different evolutionary time steps.

Algorithm 5 An algorithm for constrained grain orientation generation

procedure CGOG($\boldsymbol{MI}$, $EBSD_{\boldsymbol{G}}$)
  $Grain_{\boldsymbol{G}} \leftarrow Grain\_reconstruction\ (EBSD_{\boldsymbol{G}})$
  $Grain\_merge_{\boldsymbol{G}} \leftarrow Grain\_merge\ (Grain_{\boldsymbol{G}})$
  $f_{\boldsymbol{G}_{all}} \leftarrow Probability\_calculation\ (Grain\_merge_{\boldsymbol{G}})$
  while existing unassigned grain in $\boldsymbol{MI}$ **do**
    $Grain_{selection} \leftarrow Random\_selection\ (unassigned\ grains)$
    if all the neighboring grains of $Grain_{selection}$ is unassigned **then**
      $\boldsymbol{G}_{selection} \leftarrow Discrete\_sample\ (f_{\boldsymbol{G}_{all}})$
      $Grain_{selection} \leftarrow Orientation\_assignment\ (\boldsymbol{G}_{selection})$
    else
      $f_{\boldsymbol{G}_{left}} \leftarrow Probability\_calculation\ (Grain\_left_{\boldsymbol{G}})$
      $\boldsymbol{G}_{selection} \leftarrow Discrete\_sample\ (f_{\boldsymbol{G}_{left}})$
      $Grain_{selection} \leftarrow Orientation\_assignment\ (\boldsymbol{G}_{selection})$
    end if
  end while
end procedure

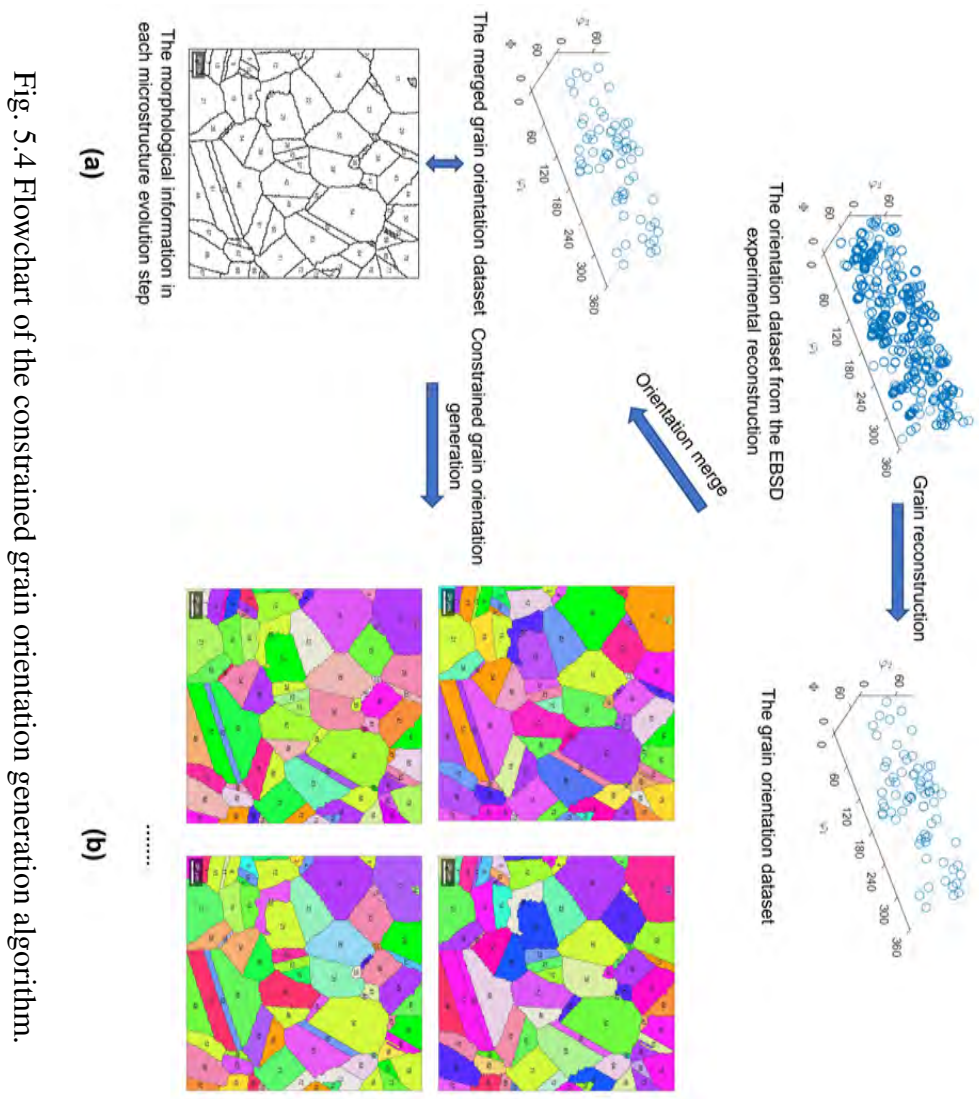

Fig. 5.4 Flowchart of the constrained grain orientation generation algorithm.

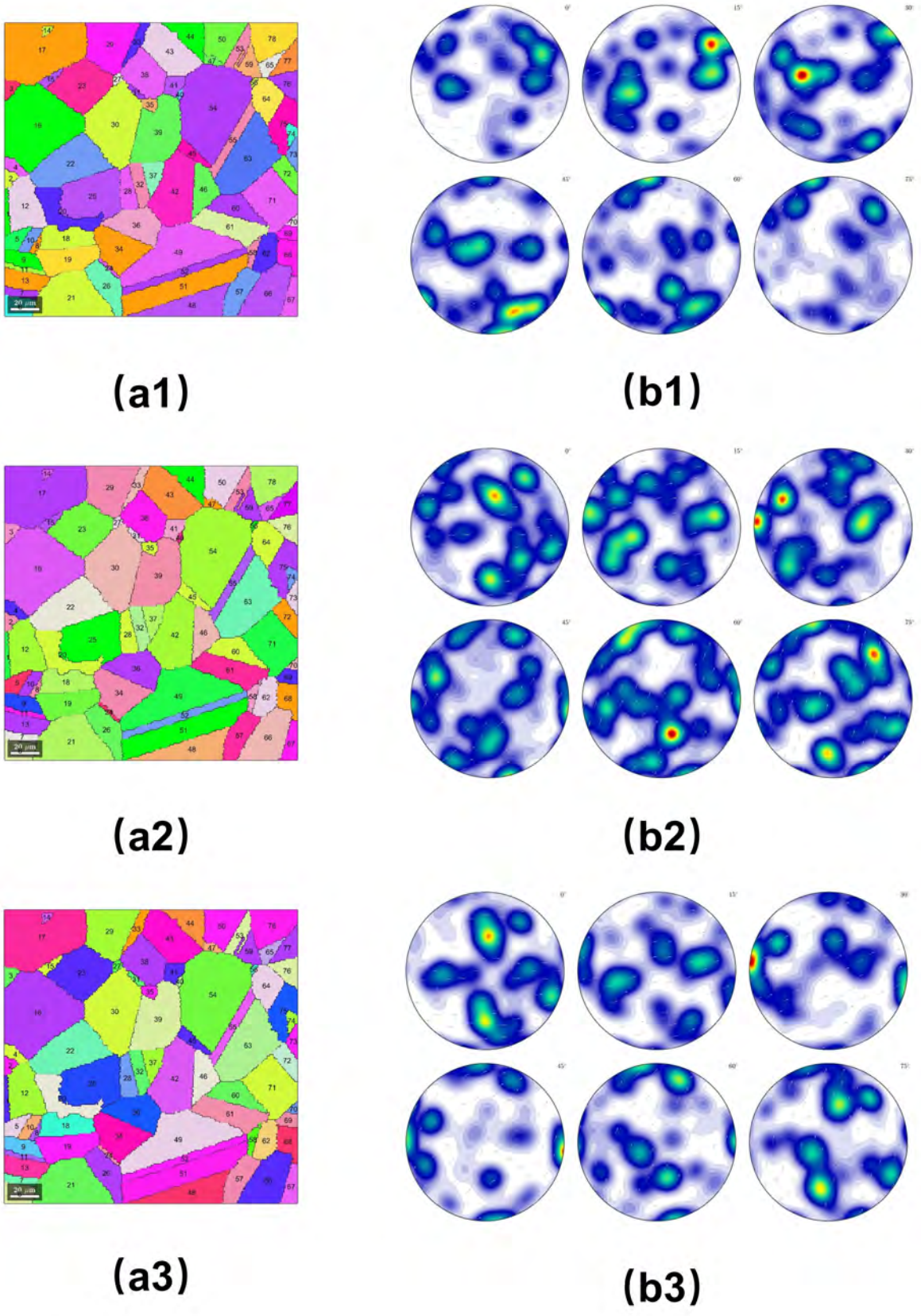

Fig. 5.5 Illustrations of the grain orientation distributions under the same morphological conditions in each microstructure evolution step: (a1-a3) the morphological conditions, (b1-b3) the grain orientation distributions.

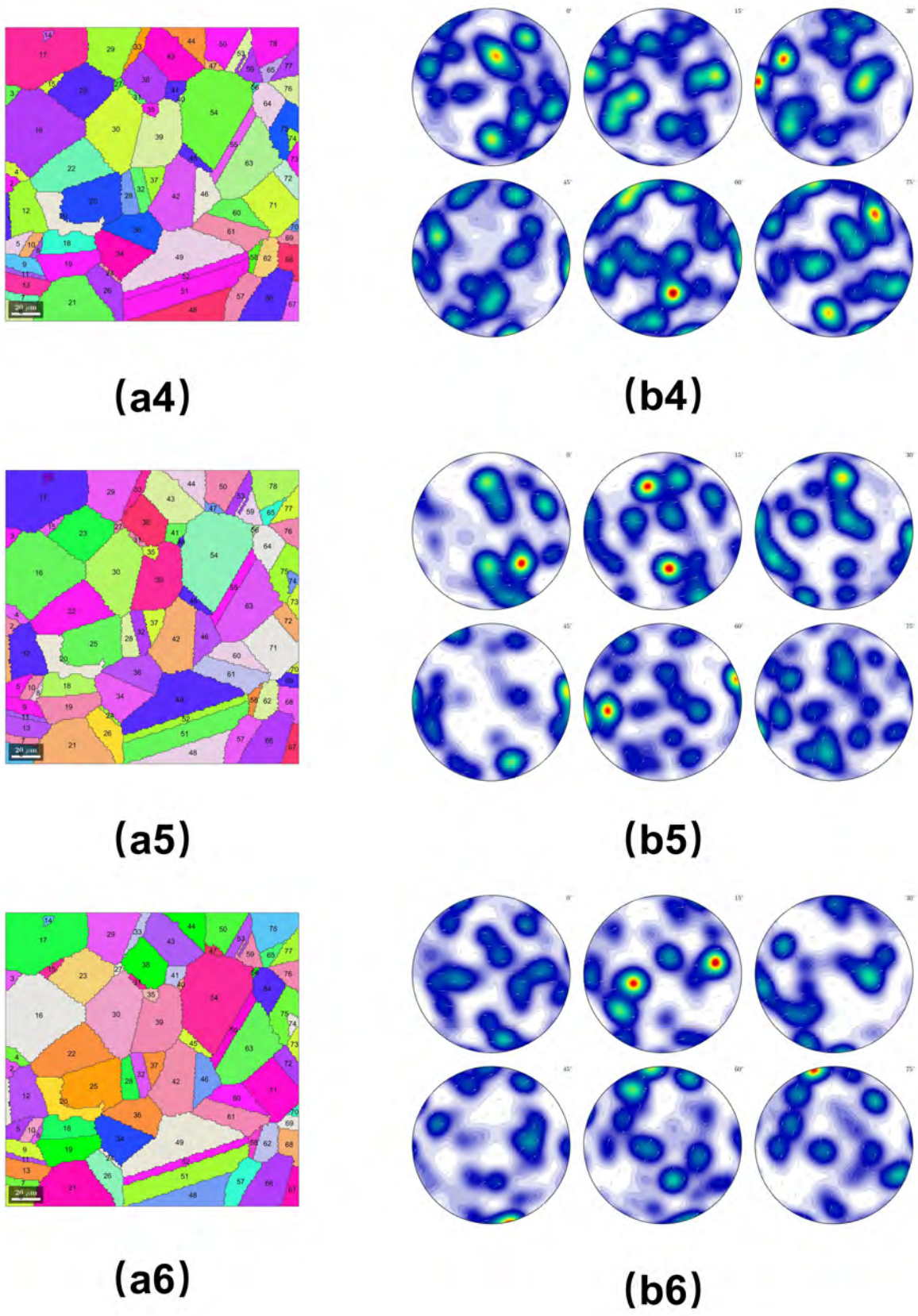

Fig. 5.5 Illustrations of the grain orientation distributions under the same morphological conditions in each microstructure evolution step: (a4-a6) the morphological conditions, (b4-b6) the grain orientation distributions.

Algorithm 6 An algorithm for constrained grain boundary generation

procedure CGBG($\boldsymbol{MI}_{original}, \boldsymbol{CI}_{original}$)
  $GSBs \leftarrow Morphological\_characterization\ (\boldsymbol{MI}_{original})$
  $N_{original} \leftarrow Morphological\_characterization\ (\boldsymbol{MI}_{original})$
  $GBD_{original} \leftarrow Morphological\_characterization\ (\boldsymbol{MI}_{original})$
  $f_{GSBs} \leftarrow Probability\_calculation\ (GSBs)$
  Initialize $GBD_{updated} = 0$
  while $\left\|GBD_{original} - GBD_{updated}\right\|^2 > \varepsilon$ **do**
    $Bin_{selection} \leftarrow Random\_selection\ (f_{GSBs})$
    $Grain\_pair_{selection} \leftarrow Random\_selection\ (grains\ belonging\ to\ the\ Bin_{selection})$
    $\boldsymbol{CI}_{updated} \leftarrow Orientation\_exchange\ (\boldsymbol{CI}_{original}, Grain\_pair_{selection})$
    $\boldsymbol{MI}_{updated} \leftarrow Grain\_reconstruction\ (\boldsymbol{CI}_{updated})$
    $GN_{updated} \leftarrow Morphological\_characterization\ (\boldsymbol{MI}_{updated})$
    if $N_{updated} = N_{original}$ **then**
      Exchange accepted
      $\boldsymbol{CI}_{updated} = \boldsymbol{CI}_{original}$
    else
      Exchange rejected
      $\boldsymbol{CI}_{original} = \boldsymbol{CI}_{updated}$
    end if
    $GBD_{updated} \leftarrow Morphological\_characterization\ (\boldsymbol{MI}_{updated})$
  end while
end procedure

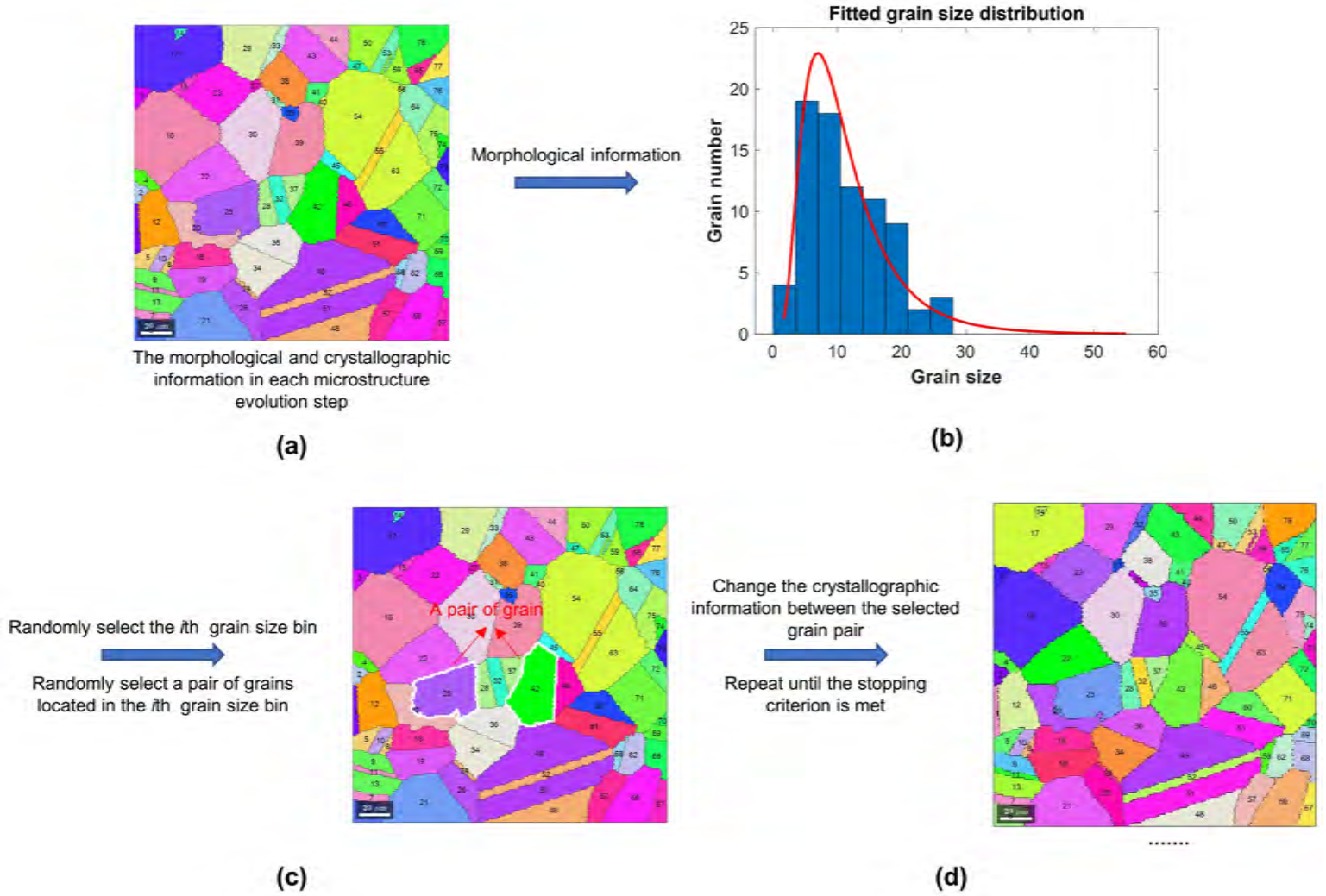

Fig. 5.6 Flowchart of the constrained grain boundary generation algorithm.

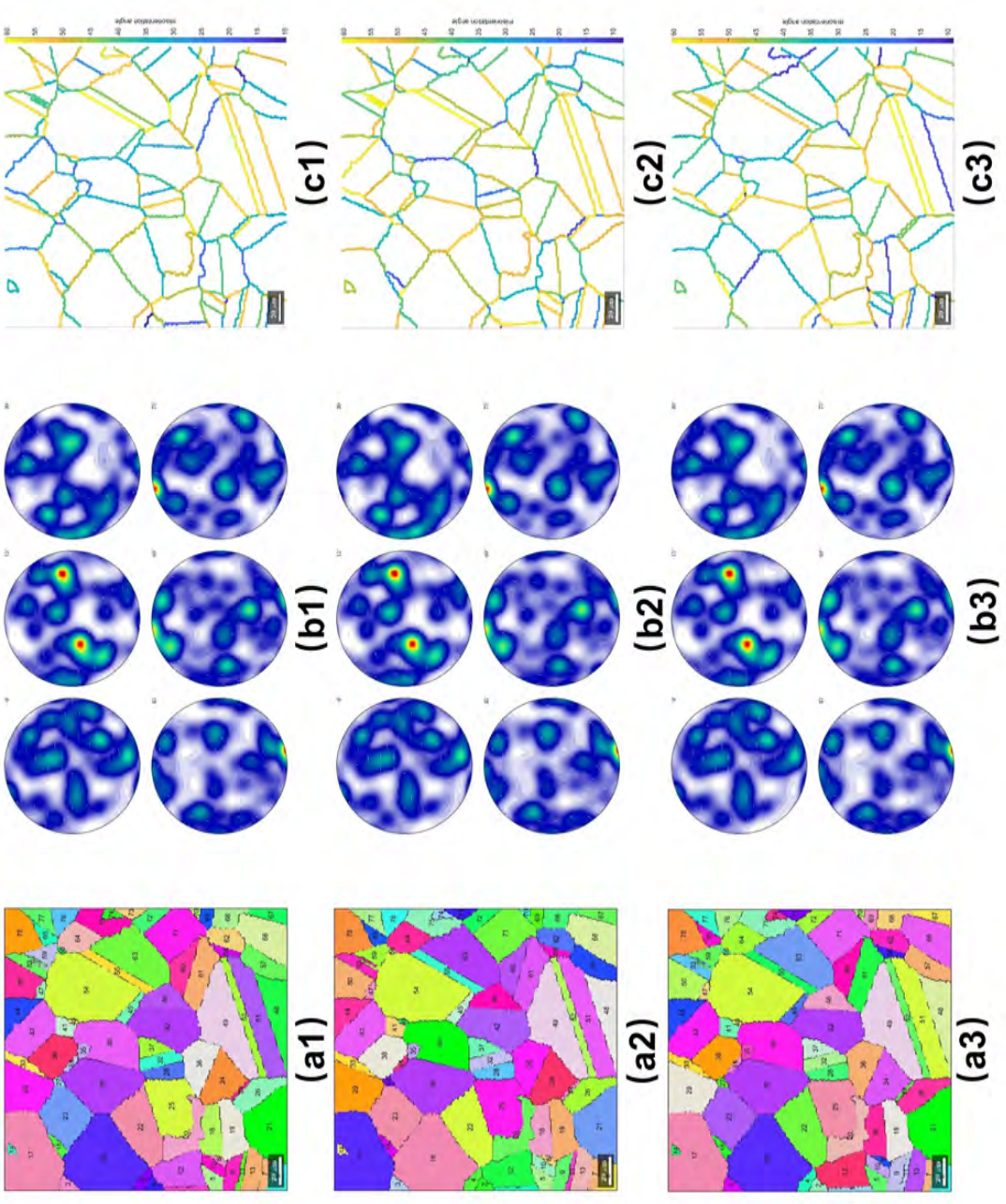

Fig. 5.7 Illustrations of the grain boundary conditions under the same morphological and crystallographic information in each microstructure evolution step: (a1-a3) the morphological conditions; (b1-b3) the grain orientation distributions; (c1-c3) the grain boundary distributions.

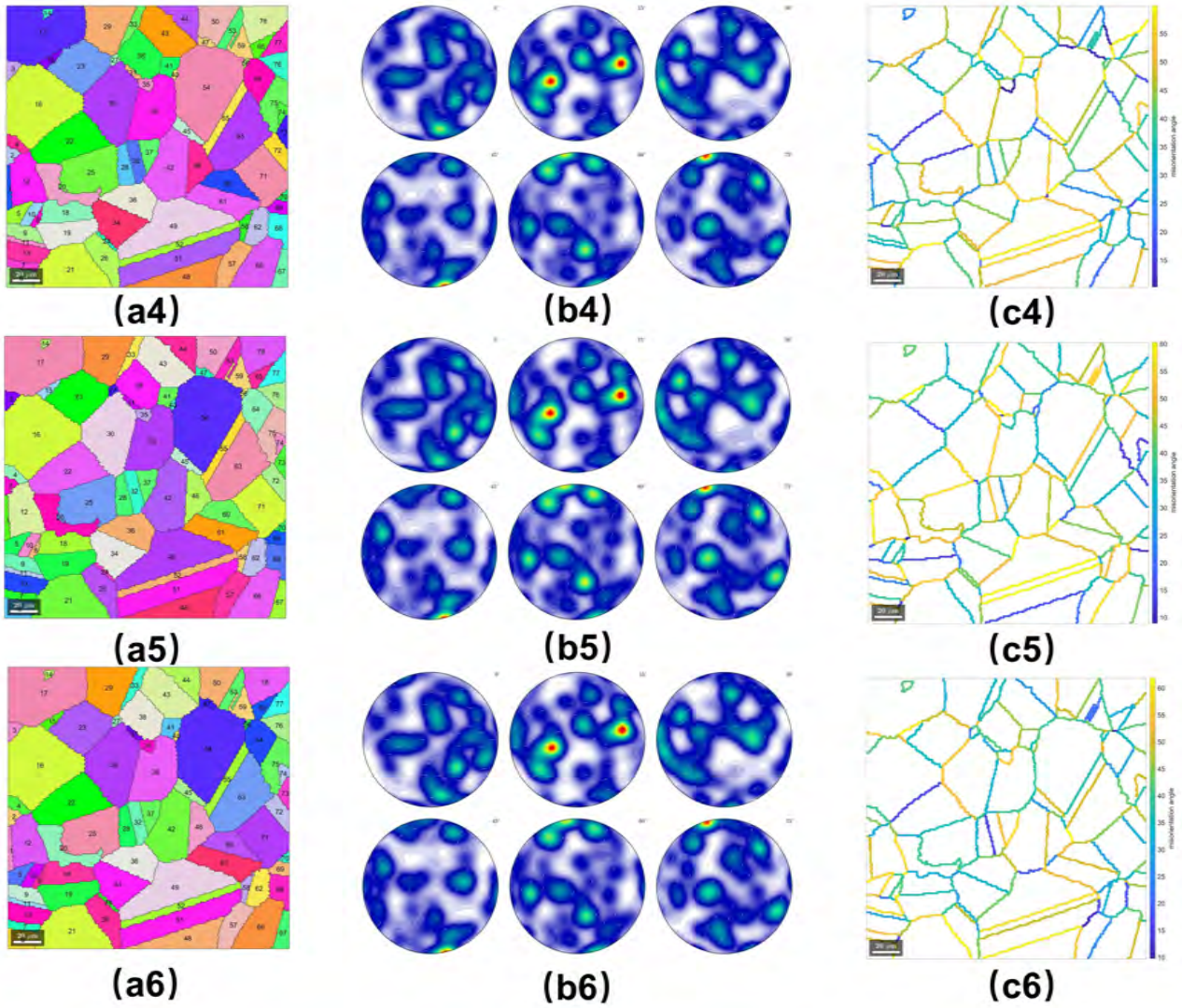

Fig. 5.7 Illustrations of the grain boundary conditions under the same morphological and crystallographic information in each microstructure evolution step: (a1-a3) the morphological conditions; (b1-b3) the grain orientation distributions; (c1-c3) the grain boundary distributions.

the *i*th merge grain orientation ($Grain\_merge_{\boldsymbol{G}}$) (line 4 in Algorithm 5) is then calculated as

$$f_{\boldsymbol{G}_i} = \frac{V(\boldsymbol{G}_i)}{V(\boldsymbol{G}_{all})} \quad i = 1,2,...,N \tag{5.2}$$

where N is the total grain number, $\boldsymbol{G}_i$ is the *i*th grain orientation, $V(\boldsymbol{G}_{all})$ is the total grain volume or area, and $V(\boldsymbol{G}_i)$ is the *i*th grain volume or area whose grain orientation is equal to $\boldsymbol{G}_i$. Next, we randomly select a grain, sample a grain orientation from the grain orientation probability ($f_{\boldsymbol{G}_{all}}$) and assign the sampled orientation to the selected grain. If the neighbors of the selected grain have been assigned, the calculation of the grain orientation probability should not include the orientation of the neighboring grains (lines 5-13 in Algorithm 5). This procedure is repeated until all grains are assigned.

5.4 Algorithm C: Constrained grain boundary generation

Fig. 5.6 shows the flowchart of the constrained grain boundary generation algorithm (CGBG). The input data is the orientation dataset from the EBSD experimental reconstruction and the morphological information in each microstructure evolution step (Fig. 5.6.a). The target of the CGBG algorithm is to explicitly and stochastically generate the grain boundary distributions (Fig. 5.7.c1-c6) under the same morphological (Fig. 5.7.a1-a6) and crystallographic conditions (Fig. 5.7.b1-b6). The pseudo-code for the CGBG model is given in Algorithm 6. The original morphological information ($\boldsymbol{MI}_{original}$) and the original crystallographic information $\boldsymbol{CI}_{original}$ are all required inputs for the CGOG algorithm (line 1 in Algorithm 6). It begins with the microstructure characterization of grain size bins (*GSBs*) (line 2 in Algorithm 6), grain number ($N_{original}$) (line 3 in Algorithm 6), and grain boundary distribution ($GBD_{original}$) (line 4 in Algorithm 6) (Section 2.3). The probability of the *i*th grain size bin (line 5 in Algorithm 6) is then calculated as

$$f_{GSBs_i} = \frac{(N_{GSBs_i})}{N_{all}} \quad i = 1,2,...,N \tag{5.3}$$

where N_{GSBs_i} is the number of grains whose grain size is located in the *i*th grain size bin ($GSBs_i$) (Fig. 5.6.b). Next, we sample a grain size bin from the grain size bin probability and randomly select a grain pair located in the chosen grain size bin (lines 8-10 in Algorithm 6). We exchange the orientation information of the grain pair can calculate the updated grain number. The exchange is accepted if the original grain number is equal to the updated grain number. Otherwise, it is rejected (lines 11-20 in Algorithm 6). This procedure is repeated until the GBD convergence criteria are met.

5.5 Conclusions

This Chapter presents some explicit characterization algorithms for texture synthesis models applied to the microstructural reconstruction and characterization of polycrystalline materials, such as grain nucleation and growth, constrained grain orientation generation, and constrained grain boundary generation. The main conclusions are:

- The grain nucleation and growth algorithm can capture the morphological evolution of the SERVEs generated from the improved PTS models in Chapter 4. The constrained grain orientation generation algorithm can stochastically characterize the grain orientation variations based on the orientation dataset generated from the EBSD reconstruction under the same morphological conditions. The constrained grain boundary generation algorithm can stochastically describe the grain boundary variations under the same morphological and crystallographic conditions.

- This research represents the first endeavor to develop a fully automated method for generating accurate and quantitative characterizations in texture synthesis models. The output of this synthetic microstructure generator can be readily interfaced with micromechanical models to construct PSPP linkages in polycrystalline materials.

Chapter 6

Micromechanical simulation in nickel-based superalloys

6.1 Introduction

Grain structure and continuum material deformation can be explicitly illustrated using multi-scale full-field homogenization of polycrystal models based on the finite element method, and grain interactions can also be considered carefully to produce the collective response of a polycrystal aggregate [393]. When subjected to macroscopic loadings, each grain is susceptible to substantially localized deformations due to the deformation incompatibility with neighboring grains. These finite local deformations can cause significant lattice distortion, altering grain orientation distributions (texture development) and the subsequent mechanical response (e.g., ductile failure) [234].

As discussed in Section 4.4, the sample of interest is a face-centered cubic (FCC) nickel-based Inconel 718 superalloy. The characteristics of nickel-based superalloys are high strength, exceptional welding and hot working properties, excellent fatigue resistance and fracture toughness. They are commonly used for turbine blades in aerospace engines (Fig. 1.1). The following Chapter will briefly introduce the micromechanical simulation in nickel-based Inconel 718 superalloy. We will begin with the single crystal model based on the finite element method, compare it to micropillar compression experiments, calibrate the material parameters from the experimental results, and then conduct polycrystalline micromechanical simulations using the calibrated material parameters.

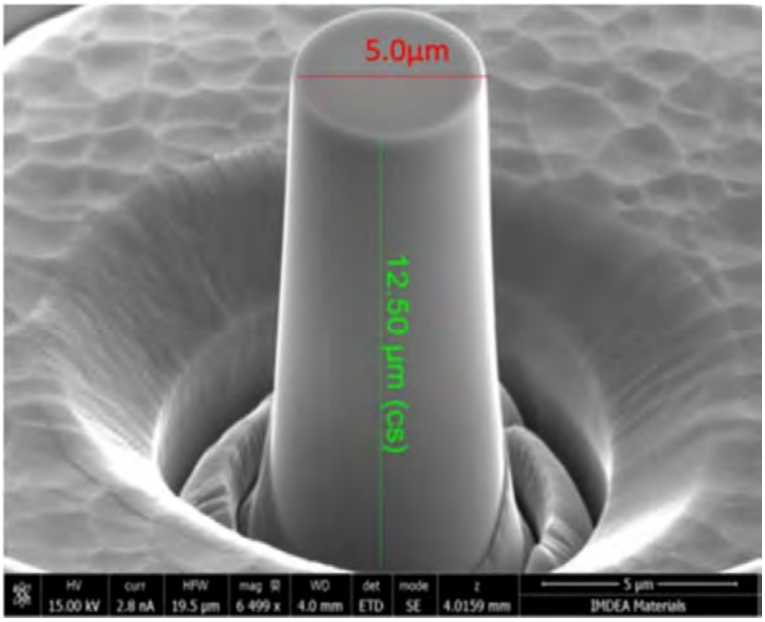

Fig. 6.1 Illustration of the single crystal micropillar in the unconfined compression testing.

6.2 Micromechanical simulation of the single crystal model

6.2.1 Micropillar compression test

The micropillar compression test is a novel technique for investigating the mechanical properties of materials at micro and nano length scales. To minimize the surface damage caused by FIB, the micropillars chosen for this experiment were prepared using the ring milling technique in the center of the selected grains, followed by a polishing step using the current of 230 pA. As shown in Fig. 6.1, the geometric diameter of the micropillar is 5 μm, the angle of the lateral slope of the circular table is 1.5°, and the length-to-width ratio of the micropillar is 2.5.

Fig. 6.2 shows the original and calibrated stress-strain curves in the unconfined micropillar compression testing with the $10^{-4}s^{-1}$ strain rate and <235> loading direction. It is well known that the difficult alignment between the flat punch and the micropillar head strongly influences the initial loading slope in micropillar experiments. This misalignment at the initial contacts of the micropillar and flat punch head leads to late material yielding and a significant reduction in the initial loading stiffness. Therefore, it is necessary to calibrate the original stress-strain curve using Equation (6.1) [219] to get an early material yielding, expressed as

$$\varepsilon_{calibrated}(\sigma) = \varepsilon_{original}(\sigma) - \frac{\sigma_{unloaded}}{S_{unloaded}} \tag{6.1}$$

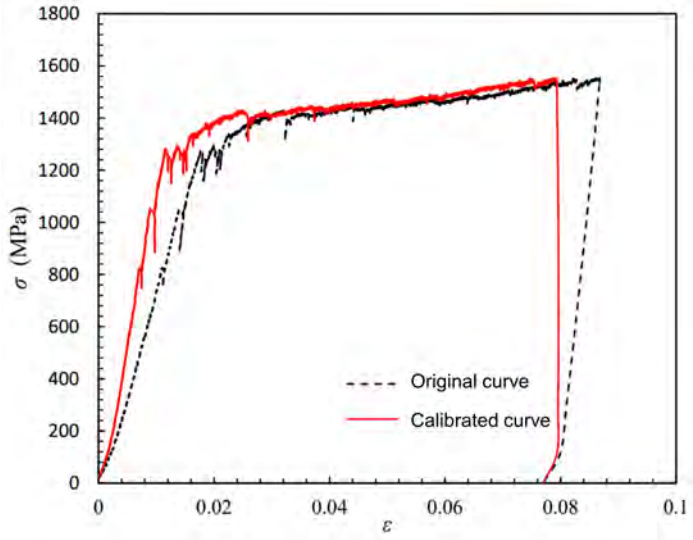

Fig. 6.2 The original and calibrated stress-strain curves in the unconfined micropillar compression testing.

where $\varepsilon_{original}(\sigma)$ is the unloaded stress, and $S_{unloaded}$ is the unloaded stress-strain slope.

6.2.2 Single crystal plasticity constitutive model

Crystal plasticity (CP) models have been extensively developed and utilized to study the slip-controlled deformation of crystalline materials. To describe how the microscopic deformations in nickel-based superalloys respond to the loads imposed by their environment (simplification by neglecting thermal expansion), the Cauchy stress $\boldsymbol{\sigma}$ in conventional continuous theory must be characterized by a constitutive law based on the history of the deformation gradient $\boldsymbol{F}$. A flow rule is then required to describe the evolutionary slip in response to the resolved shear stress to generate a closed-form constitutive equation for polycrystalline materials.

Kinematic equations

Most CP models start with the multiplicative decomposition of $\boldsymbol{F}$ into its elastic ($\boldsymbol{F}^e$) and plastic ($\boldsymbol{F}^p$) parts [226], expressed as

$$\boldsymbol{F} = \boldsymbol{F}^e \boldsymbol{F}^p \tag{6.2}$$

where $\boldsymbol{F}^e$ indicates the elastic deformation gradient in the deformed configuration concerning the relaxed or intermediate configuration, and $\boldsymbol{F}^p$ denotes the plastic deformation gradient

concerning an initial configuration. As a means of representing the plastic flow [48], [226] proposed the plastic velocity gradient of a single crystal depends linearly on crystallographic slip rate as follows:

$$\boldsymbol{L}^p = \dot{\boldsymbol{F}}^p (\boldsymbol{F}^p)^{-1} = \sum_{\alpha=1}^{N} \dot{\gamma}^\alpha \boldsymbol{m}^\alpha \otimes \boldsymbol{n}^\alpha \tag{6.3}$$

where the dot over a variable shows the absolute difference relative to time t, N indicates the total number of slip systems, $\dot{\gamma}^\alpha$, $\boldsymbol{m}^\alpha$ and $\boldsymbol{n}^\alpha$ are the slip rate, slip direction, and slip plane normal of the slip system α respectively, and $\otimes$ refers to the dyadic product. Next, continuum mechanics defines the work rate per unit reference volume $\dot{W}$ [48] as

$$\begin{aligned} \dot{W} &= J\boldsymbol{\sigma} : \boldsymbol{L} \\ &= J\boldsymbol{\sigma} : \left[\dot{\boldsymbol{F}}^e (\boldsymbol{F}^e)^{-1} + \boldsymbol{F}^e \boldsymbol{L}^p (\boldsymbol{F}^e)^{-1}\right] \\ &= (\boldsymbol{F}^e)^{-1} J\boldsymbol{\sigma} (\boldsymbol{F}^e)^{-T} : \dot{\boldsymbol{E}}^e + \sum_{\alpha=1}^{N} (\boldsymbol{F}^e)^T J\boldsymbol{\sigma} (\boldsymbol{F}^e)^{-T} : \boldsymbol{m}^\alpha \otimes \boldsymbol{n}^\alpha \dot{\gamma}^\alpha \end{aligned} \tag{6.4}$$

where : represents a double tensor contraction, N indicates the total number of slip systems, $J = det(\boldsymbol{F})$, $\boldsymbol{L} = \dot{\boldsymbol{F}}(\boldsymbol{F})^{-1}$ and $\boldsymbol{E}^e = \frac{1}{2}\left[(\boldsymbol{F}^e)^T \boldsymbol{F}^e - \boldsymbol{I}\right]$ refer to relative volume change (Jacobian), velocity gradient, and the elastic Green strain, respectively, $J\boldsymbol{\sigma}$ and $\boldsymbol{L}$ are a work-conjugate pair. For dissipative metals, it is assumed that the stress work rate per unit volume can be split into elastic and plastic portions [234] as

$$\dot{W} = \boldsymbol{T}^* : \dot{\boldsymbol{E}}^e + \sum_{\alpha=1}^{N} \tau^\alpha \dot{\gamma}^\alpha \tag{6.5}$$

where $\boldsymbol{T}^*$ indicates the second Piola-Kirchhoff stress elastically work-conjugate to the elastic Green strain, and τ^α refers to the resolved shear stress plastically work-conjugate to the slip rate. When Equation (6.4) and Equation (6.5) are compared, the expressions for the second Piola-Kirchhoff stress $\boldsymbol{T}^*$ and the resolved shear stress τ^α are obtained as

$$\begin{aligned} \boldsymbol{T}^* &= (\boldsymbol{F}^e)^{-1} J\boldsymbol{\sigma} (\boldsymbol{F}^e)^{-T} \\ \tau^\alpha &= (\boldsymbol{F}^e)^T \boldsymbol{F}^e \boldsymbol{T}^* : (\boldsymbol{m}^\alpha \otimes \boldsymbol{n}^\alpha) \end{aligned} \tag{6.6}$$

Here, $\boldsymbol{T}^*$ is commonly assumed to be linearly dependent on the elastic Green strain for metals, expressed as

$$\boldsymbol{T}^* = \mathfrak{I} : \boldsymbol{E}^e \tag{6.7}$$

where $\mathfrak{I}$ represents the fourth-order elastic stiffness tensor reliant on three independent elastic constants for cubic crystals [236].

Flow rule

The Orowan equation [321, 234] related to dislocation kinetics initially describes the flow rule of crystalline materials as

$$\dot{\gamma}^{\alpha} = \rho_m b v^{\alpha} \tag{6.8}$$

where ρ_m indicates the density of mobile dislocations, b denotes the length of Burgers vector, and v^{α} represents the average dislocation velocity in the direction of a slip system α. Depending on the response of dislocation density and velocity to applied stress, the slip rate can then be written in the flow function form [374] as

$$\dot{\gamma}^{\alpha} = f(\tau^{\alpha}, S^{\alpha}) \tag{6.9}$$

where f refers to a flow function independent of slip system type, and S^{α} represents the slip resistance (scalar or tensorial) variable related to the dislocation density in the slip system α. In [279], an explicit connection has been defined between S^{α} and the dislocation density. In this article, the thermally activated flow rule proposed by [59] has been employed to simulate the ductile failure in the nickel-base single crystal superalloys, stated as

$$\dot{\gamma}^{\alpha} = f(\tau^{\alpha}, S^{\alpha}) = \dot{\gamma}_0 exp\left(-\frac{F_0}{KT}\left\langle 1 - \left\langle \frac{|\tau^{\alpha} - B^{\alpha}| - S^{\alpha}\mu/\mu_0}{\tau_0 \mu/\mu_0} \right\rangle^{p} \right\rangle^{q}\right) sgn(\tau^{\alpha} - B^{\alpha}) \tag{6.10}$$

where $\dot{\gamma}_0$, p, q are the exponents and pre-exponential constants, F_0 indicates the total free energy required to overcome the lattice resistance, K represents the Boltzmann constant, B^{α} signifies effective back stress, T denotes the absolute temperature, τ_0 refers to the lattice friction stress at $0K$, μ and μ_0 mean shear moduli at temperature T and $0K$, respectively. The brackets $\langle\rangle$ define a function that gives $\langle x\rangle \equiv x$ for $x > 0$, and $\langle x\rangle \equiv 0$ for $x \leq 0$. The evolution of slip resistance S^{α} is governed by

$$\dot{S}^{\alpha} = \sum_{\beta=1}^{N} h^{\alpha\beta}\left(\frac{S_{sat} - S^{\beta}}{S_{sat} - S_0}\right)\left|\dot{\gamma}^{\beta}\right| \tag{6.11}$$

where $h^{\alpha\beta}$ is the hardening matrix, and S_{sat} is the saturated slip resistance from the initial value S_0. The hardening matrix $h^{\alpha\beta}$ is further defined as

$$h^{\alpha\beta} = h_s\left[w_0 + (1 - w_1)\delta_{\alpha\beta}\right] \tag{6.12}$$

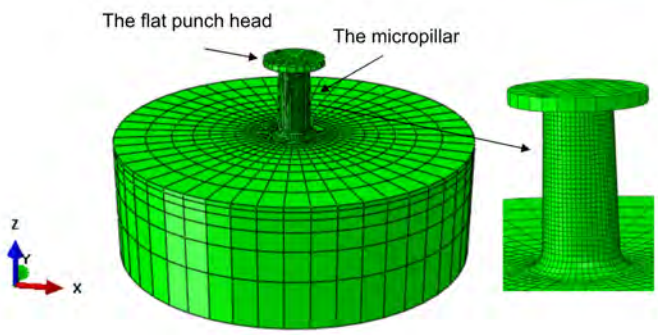

Fig. 6.3 The CPFEM model for the single crystal micropillar structure.

where $h^{\alpha\beta}$ is the hardening matrix, and S_{sat} is the saturated slip resistance from the initial value S_0. h_s is a material constant, $\delta_{\alpha\beta}$ is the Kronecker delta, and the values of w_0 and w_1 represent the hardening behaviour of the material.

6.2.3 Finite element implementation of the single crystal plasticity constitutive model

Fig. 6.3 shows the CPFEM model for the single-crystal micropillar structure. The geometry of the micropillar in the CPFEM model is the same as the single crystal micropillar in the unconfined compression testing. The analytical domain was discretized with eight-node brick elements. The flat punch head was modeled as a rigid body. The contact surface between the flat punch and micropillar head was modeled using the Coulomb friction model with a coefficient of friction of 0.1. The base of the micropillar was entirely confined, whereas the flat punch head was subjected to a vertical load with the constant velocity.

The accumulated equivalent plastic strain ε_{eq} in the ductile failure model is numerically updated by solving a nonlinear equation system using the time discretization approach. To accomplish this, it is necessary to calculate the consistent tangent (Jacobian) to obtain a solution to the global Newton-Raphson iteration at each time step. In general, the consistent tangent $\mathbb{C}$ of a rate-form constitutive law is defined as

$$\mathbb{C} = \frac{1}{J}\frac{\partial \Delta \boldsymbol{\tau}}{\partial \Delta \boldsymbol{\varepsilon}} \tag{6.13}$$

where $\boldsymbol{\tau}$ denotes the Kirchhoff stress, $\Delta\boldsymbol{\tau}$ stands for the co-rotational Kirchhoff stress increment, and $\Delta\boldsymbol{\varepsilon}$ refers to the the strain increment. The derivation of the consistent tangent for a particular constitutive model depends on how to characterize the co-rotational Kirchhoff stress increment in terms of strain increment. [279] used the Jaumann rate of Cauchy stress

rather than the incremental-form formulation in Equation (6.13) to define the global material Jacobian. In this work, a more efficient consistent tangent proposed by [234] is utilized to achieve an improved convergence rate. The proposed co-rotational Kirchhoff stress increment is established as

$$\begin{aligned} \Delta\boldsymbol{\tau} &= \hat{\boldsymbol{\tau}}\Delta t \\ &= (\dot{\boldsymbol{\tau}} - \boldsymbol{\Omega}\boldsymbol{\tau} + \boldsymbol{\tau}\boldsymbol{\Omega})\Delta t \end{aligned} \tag{6.14}$$

where $\hat{\boldsymbol{\tau}}$ indicates the Jaumann rate of Kirchhoff stress [67] at the end of the increment, and $\boldsymbol{\Omega} = \frac{1}{2}(\boldsymbol{L} - \boldsymbol{L}^T)$ represents the spin rate [48] in terms of the skew part of the velocity gradient $\boldsymbol{L}$. Following Equation (6.6), the time rate of Kirchhoff stress can be represented as

$$\begin{aligned} \dot{\boldsymbol{\tau}} &= \dot{\boldsymbol{F}}^e(\boldsymbol{F}^e)^{-1}\boldsymbol{\tau} + \boldsymbol{\tau}(\boldsymbol{F}^e)^{-T}(\dot{\boldsymbol{F}}^e)^T + \boldsymbol{F}^e\dot{\boldsymbol{T}}^*(\boldsymbol{F}^e)^T \\ &= (\boldsymbol{D} + \boldsymbol{\Omega} - \boldsymbol{L}^{p*})\boldsymbol{\tau} + \boldsymbol{\tau}(\boldsymbol{D} - \boldsymbol{\Omega} - (\boldsymbol{L}^{p*})^T) + \boldsymbol{F}^e\dot{\boldsymbol{T}}^*(\boldsymbol{F}^e)^T \end{aligned} \tag{6.15}$$

where

$$\begin{aligned} \boldsymbol{L} &= \boldsymbol{D} + \boldsymbol{\Omega} \\ &= \dot{\boldsymbol{F}}(\boldsymbol{F})^{-1} \\ &= \dot{\boldsymbol{F}}^e(\boldsymbol{F}^e)^{-1} + \boldsymbol{F}^e\dot{\boldsymbol{F}}^p(\boldsymbol{F}^p)^{-1}(\boldsymbol{F}^e)^{-1} \\ &= \dot{\boldsymbol{F}}^e(\boldsymbol{F}^e)^{-1} + \boldsymbol{F}^e\boldsymbol{L}^p(\boldsymbol{F}^e)^{-1} \\ &= \boldsymbol{L}^e + \boldsymbol{L}^{p*} \end{aligned} \tag{6.16}$$

Here $\boldsymbol{D} = \frac{1}{2}(\boldsymbol{L} + \boldsymbol{L}^T)$ represents the strain rate [48] in terms of the symmetric part of the velocity gradient $\boldsymbol{L}$. Substituting Equation (6.15) into Equation (6.14) gives

$$\Delta\boldsymbol{\tau} = \left((\boldsymbol{D} - \boldsymbol{L}^{p*})\boldsymbol{\tau} + \boldsymbol{\tau}(\boldsymbol{D} - (\boldsymbol{L}^{p*})^T) + \boldsymbol{F}^e\dot{\boldsymbol{T}}^*(\boldsymbol{F}^e)^T\right)\Delta t \tag{6.17}$$

Following Equation (6.7), the time rate of the second Piola-Kirchhoff stress can be stated as

$$\begin{aligned}
\dot{\boldsymbol{T}}^* &= \mathfrak{J} : \dot{\boldsymbol{E}}^e \\
&= \mathfrak{J} : \frac{1}{2}\left[(\dot{\boldsymbol{F}}^e)^T \boldsymbol{F}^e + (\boldsymbol{F}^e)^T \dot{\boldsymbol{F}}^e\right] \\
&= \mathfrak{J} : \frac{1}{2}\left[(\boldsymbol{F}^e)^T (\dot{\boldsymbol{F}}^e (\boldsymbol{F}^e)^{-1})^T \boldsymbol{F}^e + (\boldsymbol{F}^e)^T \dot{\boldsymbol{F}}^e (\boldsymbol{F}^e)^{-1} \boldsymbol{F}^e\right] \\
&= \mathfrak{J} : \frac{1}{2}\left[(\boldsymbol{F}^e)^T (\boldsymbol{L}^e)^T \boldsymbol{F}^e + (\boldsymbol{F}^e)^T \boldsymbol{L}^e \boldsymbol{F}^e\right] \\
&= \mathfrak{J} : (\boldsymbol{F}^e)^T \frac{1}{2}\left[(\boldsymbol{L}^e)^T + \boldsymbol{L}^e\right] \boldsymbol{F}^e \\
&= \mathfrak{J} : (\boldsymbol{F}^e)^T \frac{1}{2}\left[\boldsymbol{L} - \boldsymbol{L}^{p*} + \boldsymbol{L}^T - (\boldsymbol{L}^{p*})^T\right] \boldsymbol{F}^e \\
&= \mathfrak{J} : (\boldsymbol{F}^e)^T \left[\boldsymbol{D} - \frac{1}{2}(\boldsymbol{L}^{p*} + (\boldsymbol{L}^{p*})^T)\right] \boldsymbol{F}^e
\end{aligned} \tag{6.18}$$

Substituting Equation (6.18) into Equation (6.17) gives

$$\begin{aligned}
\Delta\boldsymbol{\tau} &= \left((\boldsymbol{D} - \boldsymbol{L}^{p*})\boldsymbol{\tau} + \boldsymbol{\tau}(\boldsymbol{D} - (\boldsymbol{L}^{p*})^T) + \boldsymbol{F}^e \dot{\boldsymbol{T}}^* (\boldsymbol{F}^e)^T\right) \Delta t \\
&= \left((\boldsymbol{D} - \boldsymbol{L}^{p*})\boldsymbol{\tau} + \boldsymbol{\tau}(\boldsymbol{D} - (\boldsymbol{L}^{p*})^T) + \boldsymbol{F}^e (\mathfrak{J} : (\boldsymbol{F}^e)^T \left[\boldsymbol{D} - \frac{1}{2}(\boldsymbol{L}^{p*} + (\boldsymbol{L}^{p*})^T)\right] \boldsymbol{F}^e)(\boldsymbol{F}^e)^T\right) \Delta t \\
&= \left((\boldsymbol{D} - \boldsymbol{L}^{p*})\boldsymbol{\tau} + \boldsymbol{\tau}(\boldsymbol{D} - (\boldsymbol{L}^{p*})^T) + \boldsymbol{F}^e \left[\mathfrak{J} : (\boldsymbol{F}^e)^T \left[\boldsymbol{D} - \frac{1}{2}(\boldsymbol{L}^{p*} + (\boldsymbol{L}^{p*})^T)\right] \boldsymbol{F}^e\right] (\boldsymbol{F}^e)^T\right) \Delta t \\
&= \left((\boldsymbol{D} - \boldsymbol{L}^{p*})\boldsymbol{\tau} + \boldsymbol{\tau}(\boldsymbol{D} - (\boldsymbol{L}^{p*})^T) + \mathfrak{J}^* : \left[\boldsymbol{D} - \frac{1}{2}(\boldsymbol{L}^{p*} + (\boldsymbol{L}^{p*})^T)\right]\right) \Delta t
\end{aligned} \tag{6.19}$$

Here $\mathfrak{J}^* = (\mathfrak{J})_{ijkl} \boldsymbol{F}^e \boldsymbol{E}_i \otimes \boldsymbol{F}^e \boldsymbol{E}_j \otimes \boldsymbol{F}^e \boldsymbol{E}_k \otimes \boldsymbol{F}^e \boldsymbol{E}_l$, and $(\mathfrak{J})_{ijkl}$ indicates the tensorial components of $\boldsymbol{L}$ connected to the orthogonal Cartesian basis $(\boldsymbol{E}_1, \boldsymbol{E}_2, \boldsymbol{E}_3)$ at the initial configuration. All variables without further indications are defined at the end of the increment, and Euler backward time discretization is implemented. Note that

$$\begin{aligned}
\boldsymbol{D}\Delta t &= \Delta\boldsymbol{\varepsilon} \\
\boldsymbol{L}^{p*}\Delta t &= \sum_{\alpha=1}^{N} \Delta\gamma^\alpha \boldsymbol{F}^e \boldsymbol{m}^\alpha \otimes \boldsymbol{n}^\alpha (\boldsymbol{F}^e)^{-1}
\end{aligned} \tag{6.20}$$

Substituting Equation (6.20) into Equation (6.19) yields

$$\begin{aligned}\Delta\boldsymbol{\tau} =& \left((\boldsymbol{D}-\boldsymbol{L}^{p*})\boldsymbol{\tau} + \boldsymbol{\tau}(\boldsymbol{D}-(\boldsymbol{L}^{p*})^T) + \mathfrak{J}^* : \left[\boldsymbol{D} - \frac{1}{2}(\boldsymbol{L}^{p*}+(\boldsymbol{L}^{p*})^T)\right]\right)\Delta t \\ =& \Delta\boldsymbol{\varepsilon}\boldsymbol{\tau} + \boldsymbol{\tau}\Delta\boldsymbol{\varepsilon} + \mathfrak{J}^* : \Delta\boldsymbol{\varepsilon} - \boldsymbol{L}^{p*}\Delta t\,\boldsymbol{\tau} - \boldsymbol{\tau}(\boldsymbol{L}^{p*})^T\Delta t - \mathfrak{J}^* : \frac{1}{2}(\boldsymbol{L}^{p*}\Delta t + (\boldsymbol{L}^{p*})^T\Delta t) \\ =& \Delta\boldsymbol{\varepsilon}\boldsymbol{\tau} + \boldsymbol{\tau}\Delta\boldsymbol{\varepsilon} + \mathfrak{J}^* : \Delta\boldsymbol{\varepsilon} - \sum_{\alpha=1}^{N}\Delta\gamma^\alpha\left[\boldsymbol{F}^e\boldsymbol{m}^\alpha\otimes\boldsymbol{n}^\alpha(\boldsymbol{F}^e)^{-1}\boldsymbol{\tau} + \boldsymbol{\tau}\boldsymbol{n}^\alpha(\boldsymbol{F}^e)^{-1}\otimes\boldsymbol{F}^e\boldsymbol{m}^\alpha\right] \\ & - \sum_{\alpha=1}^{N}\frac{\Delta\gamma^\alpha}{2}\mathfrak{J}^* : \left[\boldsymbol{F}^e\boldsymbol{m}^\alpha\otimes\boldsymbol{n}^\alpha(\boldsymbol{F}^e)^{-1} + \boldsymbol{n}^\alpha(\boldsymbol{F}^e)^{-1}\otimes\boldsymbol{F}^e\boldsymbol{m}^\alpha\right]\end{aligned} \tag{6.21}$$

Equation (6.21) demonstrates that the Kirchhoff stress increment $\Delta\boldsymbol{\tau}$ is exclusively dependent on the strain increment $\Delta\boldsymbol{\varepsilon}$ and the slip increment $\Delta\gamma^\alpha$ of active slip systems. The primary point of the consistent Jacobian is thus to establish the link between $\Delta\boldsymbol{\varepsilon}$ and $\Delta\gamma^\alpha$. Following Equation (6.9), the slip rate of a slip system can be obtained as

$$\dot{\gamma}^\alpha = \frac{\Delta\gamma^\alpha}{\Delta t} = f(\tau^\alpha, S^\alpha) = \dot{\gamma}_n^\alpha + \dot{\dot{\gamma}}_n^\alpha\Delta t = f(\tau_n^\alpha, S_n^\alpha) + \frac{\partial f}{\partial\tau_n^\alpha}\dot{\tau}_n^\alpha\Delta t + \frac{\partial f}{\partial S_n^\alpha}\dot{S}_n^\alpha\Delta t \tag{6.22}$$

where $\dot{\gamma}_n^\alpha$, τ_n^α and S_n^α stands for the slip rate, resolved shear stress and slip resistance variable of the slip system α at the start of the increment n, respectively. Next, we concentrate on the two rate terms in Equation (6.22), namely $\dot{\tau}_n^\alpha\Delta t$ and $\dot{S}_n^\alpha\Delta t$, to derive the link between $\Delta\boldsymbol{\varepsilon}$ and $\Delta\gamma^\alpha$. Taking the time rate of the resolved shear stress of a slip system on Equation (6.6) and applying Equation (6.16), and Equation (6.18) give

$$\begin{aligned}\dot{\tau}^\alpha &= \left[(\dot{\boldsymbol{F}}^e)^T\boldsymbol{F}^e\boldsymbol{T}^* + (\boldsymbol{F}^e)^T\dot{\boldsymbol{F}}^e\boldsymbol{T}^* + (\boldsymbol{F}^e)^T\boldsymbol{F}^e\dot{\boldsymbol{T}}^*\right] : (\boldsymbol{m}^\alpha\otimes\boldsymbol{n}^\alpha) \\ &= \left[(\boldsymbol{F}^e)^T(\dot{\boldsymbol{F}}^e(\boldsymbol{F}^e)^{-1})^T\boldsymbol{F}^e\boldsymbol{T}^* + (\boldsymbol{F}^e)^T\dot{\boldsymbol{F}}^e(\boldsymbol{F}^e)^{-1}\boldsymbol{F}^e\boldsymbol{T}^* + (\boldsymbol{F}^e)^T\boldsymbol{F}^e\dot{\boldsymbol{T}}^*\right] : (\boldsymbol{m}^\alpha\otimes\boldsymbol{n}^\alpha) \\ &= (\boldsymbol{F}^e)^T\left[(\dot{\boldsymbol{F}}^e(\boldsymbol{F}^e)^{-1})^T\boldsymbol{\tau} + \dot{\boldsymbol{F}}^e(\boldsymbol{F}^e)^{-1}\boldsymbol{\tau} + \boldsymbol{F}^e\dot{\boldsymbol{T}}^*(\boldsymbol{F}^e)^T\right](\boldsymbol{F}^e)^{-T} : (\boldsymbol{m}^\alpha\otimes\boldsymbol{n}^\alpha) \\ &= (\boldsymbol{F}^e)^T\left[(\boldsymbol{L}-\boldsymbol{L}^{p*})^T\boldsymbol{\tau} + (\boldsymbol{L}-\boldsymbol{L}^{p*})\boldsymbol{\tau} + \boldsymbol{F}^e\dot{\boldsymbol{T}}^*(\boldsymbol{F}^e)^T\right](\boldsymbol{F}^e)^{-T} : (\boldsymbol{m}^\alpha\otimes\boldsymbol{n}^\alpha) \\ &= \left[(\boldsymbol{L}-\boldsymbol{L}^{p*})^T\boldsymbol{\tau} + (\boldsymbol{L}-\boldsymbol{L}^{p*})\boldsymbol{\tau} + \boldsymbol{F}^e\dot{\boldsymbol{T}}^*(\boldsymbol{F}^e)^T\right] : (\boldsymbol{F}^e\boldsymbol{m}^\alpha\otimes\boldsymbol{n}^\alpha(\boldsymbol{F}^e)^{-1}) \\ &= \left[(2\boldsymbol{D}-(\boldsymbol{L}^{p*})^T-\boldsymbol{L}^{p*})\boldsymbol{\tau} + (\boldsymbol{L}-\boldsymbol{L}^{p*})\boldsymbol{\tau} + \mathfrak{J}^* : \left[\boldsymbol{D} - \frac{1}{2}(\boldsymbol{L}^{p*}+(\boldsymbol{L}^{p*})^T)\right]\right] : (\boldsymbol{F}^e\boldsymbol{m}^\alpha\otimes\boldsymbol{n}^\alpha(\boldsymbol{F}^e)^{-1})\end{aligned} \tag{6.23}$$

Multiplying Equation (6.23) by Δt on both sides and applying Equation (6.20) result in

$$\begin{aligned}\dot{\tau}^{\alpha}\Delta t =& \left[(2\boldsymbol{D}-(\boldsymbol{L}^{p*})^{T}-\boldsymbol{L}^{p*})\boldsymbol{\tau}+(\boldsymbol{L}-\boldsymbol{L}^{p*})\boldsymbol{\tau}+\mathfrak{J}^{*}\colon\left[\boldsymbol{D}-\frac{1}{2}(\boldsymbol{L}^{p*}+(\boldsymbol{L}^{p*})^{T})\right]\right]\Delta t\colon(\boldsymbol{F}^{e}\boldsymbol{m}^{\alpha}\otimes\boldsymbol{n}^{\alpha}(\boldsymbol{F}^{e})^{-1})\\ =&(2\Delta\boldsymbol{\varepsilon}\boldsymbol{\tau}+\mathfrak{J}^{*}\colon\Delta\boldsymbol{\varepsilon})\colon(\boldsymbol{F}^{e}\boldsymbol{m}^{\alpha}\otimes\boldsymbol{n}^{\alpha}(\boldsymbol{F}^{e})^{-1})\\ &-\sum_{\beta=1}^{N}\Delta\gamma^{\beta}\left[\boldsymbol{F}^{e}\boldsymbol{m}^{\beta}\otimes\boldsymbol{n}^{\beta}(\boldsymbol{F}^{e})^{-1}+\boldsymbol{n}^{\beta}(\boldsymbol{F}^{e})^{-1}\otimes\boldsymbol{F}^{e}\boldsymbol{m}^{\beta}\right]J\boldsymbol{\sigma}\colon(\boldsymbol{F}^{e}\boldsymbol{m}^{\alpha}\otimes\boldsymbol{n}^{\alpha}(\boldsymbol{F}^{e})^{-1})\\ &-\sum_{\beta=1}^{N}\frac{\Delta\gamma^{\beta}}{2}(\boldsymbol{F}^{e}\boldsymbol{m}^{\alpha}\otimes\boldsymbol{n}^{\alpha}(\boldsymbol{F}^{e})^{-1})\colon\mathfrak{J}^{*}\colon\left[\boldsymbol{F}^{e}\boldsymbol{m}^{\beta}\otimes\boldsymbol{n}^{\beta}(\boldsymbol{F}^{e})^{-1}+\boldsymbol{n}^{\beta}(\boldsymbol{F}^{e})^{-1}\otimes\boldsymbol{F}^{e}\boldsymbol{m}^{\beta}\right]\end{aligned} \tag{6.24}$$

The term $\dot{S}^{\alpha}\Delta t$ in Equation (6.22) depends on a particular evolutionary law for internal variables. For efficiency, it is assumed that applying the evolutionary law for internal variables results in a linear relationship between $\dot{S}^{\alpha}\Delta t$ and the slip increments of all slip systems, stated as

$$\dot{S}^{\alpha}\Delta t=\sum_{\beta=1}^{N}g^{\alpha\beta}\Delta\gamma^{\beta} \tag{6.25}$$

where $g^{\alpha\beta}$ indicates the cross coefficient between the slip systems α and β. Generally, $g^{\alpha\beta}$ is dependent on all state variables. Further, substituting Equation (6.25) and Equation (6.24) into Equation (6.22) gives

$$\frac{\Delta\gamma^{\alpha}}{\Delta t}+\sum_{\beta=1}^{N}\Delta\gamma^{\beta}(C_{1}^{\alpha\beta}+C_{2}^{\alpha\beta}+C_{3}^{\alpha\beta})=C_{0}^{\alpha}+\boldsymbol{C}^{\alpha}\colon\Delta\boldsymbol{\varepsilon} \tag{6.26}$$

where

$$\begin{aligned}C_{0}^{\alpha}=&f(\tau_{n}^{\alpha},S_{n}^{\alpha})\\ C_{1}^{\alpha\beta}=&\frac{\partial f}{\partial\tau_{n}^{\alpha}}\left[\boldsymbol{F}^{e}\boldsymbol{m}^{\beta}\otimes\boldsymbol{n}^{\beta}(\boldsymbol{F}^{e})^{-1}+\boldsymbol{n}^{\beta}(\boldsymbol{F}^{e})^{-1}\otimes\boldsymbol{F}^{e}\boldsymbol{m}^{\beta}\right]\boldsymbol{\tau}\colon(\boldsymbol{F}^{e}\boldsymbol{m}^{\alpha}\otimes\boldsymbol{n}^{\alpha}(\boldsymbol{F}^{e})^{-1})\\ C_{2}^{\alpha\beta}=&\frac{\partial f}{\partial\tau_{n}^{\alpha}}(\boldsymbol{F}^{e}\boldsymbol{m}^{\alpha}\otimes\boldsymbol{n}^{\alpha}(\boldsymbol{F}^{e})^{-1})\colon\frac{\mathfrak{J}^{*}}{2}\colon\left[\boldsymbol{F}^{e}\boldsymbol{m}^{\beta}\otimes\boldsymbol{n}^{\beta}(\boldsymbol{F}^{e})^{-1}+\boldsymbol{n}^{\beta}(\boldsymbol{F}^{e})^{-1}\otimes\boldsymbol{F}^{e}\boldsymbol{m}^{\beta}\right]\\ C_{3}^{\alpha\beta}=&-\frac{\partial f}{\partial S_{n}^{\alpha}}g^{\alpha\beta}\\ \boldsymbol{C}^{\alpha}=&\frac{\partial f}{\partial\tau_{n}^{\alpha}}\left[2(\boldsymbol{F}^{e}\boldsymbol{m}^{\alpha}\otimes\boldsymbol{n}^{\alpha}(\boldsymbol{F}^{e})^{-1})\boldsymbol{\tau}+(\boldsymbol{F}^{e}\boldsymbol{m}^{\alpha}\otimes\boldsymbol{n}^{\alpha}(\boldsymbol{F}^{e})^{-1})\colon\mathfrak{J}^{*}\right]\end{aligned} \tag{6.27}$$

Overall, there are three steps involved in determining the Jacobian matrix. First, the plastic slip increase can be obtained as a linear function of the strain increment by using Equation (6.26). This result is then substituted into Equation (6.21) to establish a linear relationship between the Kirchhoff stress increment and the strain increment. Finally, the consistent tangent can be determined based on its definition in Equation (4.7).

6.3 Calibration of the single crystal plasticity constitutive model parameters

Table 6.1 presents the simulation's material parameters regarding elastic constants and flow properties. Here, the elastic parameter set, E, G, and ν, denote the cubic plane modulus, shear modulus, and Poisson ratio respectively. They are calculated from the alternative elastic stiffness constants (C_{11}, C_{12}, C_{44}) taken from [274] for a nickel-based superalloy, described as

$$\begin{aligned}
\mathfrak{I} &= \begin{bmatrix} C_{11} & C_{12} & C_{12} & 0 & 0 & 0 \\ C_{12} & C_{11} & C_{12} & 0 & 0 & 0 \\ C_{12} & C_{12} & C_{11} & 0 & 0 & 0 \\ 0 & 0 & 0 & C_{44} & 0 & 0 \\ 0 & 0 & 0 & 0 & C_{44} & 0 \\ 0 & 0 & 0 & 0 & 0 & C_{44} \end{bmatrix} \\
E &= \frac{(C_{11}+2C_{12})(C_{11}-C_{12})}{C_{11}+C_{12}} \\
\nu &= \frac{C_{12}}{C_{11}+C_{12}} \\
G &= C_{44}
\end{aligned} \tag{6.28}$$

The flow parameters are set to optimally accommodate the measured stress-strain data in the unconfined micropillar compression testing. The current framework takes $w_0 = 1$ and $w_1 = 1$ for the case of Taylor latent hardening [234] but does not consider the back stress in line with the method described in the references [131, 471, 53]. The material's plastic hardening and yield strength are controlled mainly by changing S_{sat}, S_0, and h_s during calibration. Fig. 6.4 presents single crystal micropillars' measured and simulated unconfined compression testing results under the $10^{-4}s^{-1}$ strain rate and <235> loading direction. The solid red line is the calibrated stress-strain curve from the unconfined micropillar compression test, and the dashed black line is the simulated stress-strain curve from the finite element implementation

Table 6.1 Material properties of nickel-based Inconel 718 superalloy used in simulations

Parameter	Dimension	Value
E	GPa	113.494
G	GPa	109.6
ν	-	0.408
$\dot{\gamma}_0$	s^{-1}	450
F_0	kJ mol^{-1}	286
p	-	1.0
q	-	1.9
μ	GPa	138.6
μ_0	GPa	150.4
τ_0	MPa	781.3
S_0	MPa	2.04
S_{sat}	MPa	5529.95
h_s	MPa	330.0
w_0	-	1
w_1	-	1

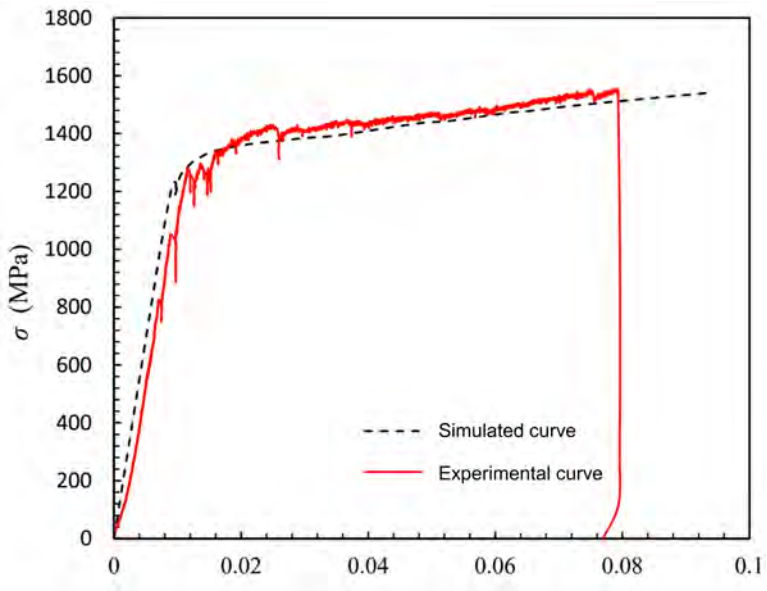

Fig. 6.4 Calibration of the single crystal plasticity constitutive model parameters for the nickel-based Inconel 718 superalloy.

of the single crystal plasticity constitutive model. It can be concluded that the simulated and experimental stress-strain curves are in good agreement.

6.4 Verification of the single crystal plasticity constitutive model

This Section further verifies the calibrated parameters for the single crystal plasticity constitutive model through comparison studies between the simulation and experiment of the unconfined compression test. Fig. 6.4 presents three unconfined compression tests with different strain rates ($10^{-4}s^{-1}$, $10^{-3}s^{-1}$, $10^{-2}s^{-1}$) and loading directions ($< 235 >$, $< 235 >$, $< 213 >$). It can be concluded that the simulated stress-strain curves from the finite element implementation of the single crystal plasticity constitutive model are very close to the experimental results. Meanwhile, the single crystal plasticity finite element model can accurately capture the deformed micropillar's shape and the slip bands' location. Therefore, the predictive capability of the single crystal plasticity model for nickel-based Inconel 718 superalloy is verified.

6.5 Micromechanical simulation of the RVE model

This Section applies the single crystal plasticity constitutive model to simulate polycrystalline nickel-based Inconel 718 superalloy. It starts from the manual EBSD reconstruction of the RVE for polycrystalline nickel-based Inconel 718 superalloy (Fig. 2.3). Fig. 6.5 shows the reconstructed polycrystalline nickel-based Inconel 718 superalloy with different RVE sizes. Fig. 6.6 shows the simulated stress-strain curves with different RVE sizes under the uniaxial tension condition. As described in Fig. 6.5, the stress-strain curves of the four different RVE sizes under the uniaxial tension condition are relatively close in both the elastic and plastic stages. Therefore, the 3D RVE is representative in simulating polycrystalline nickel-based Inconel 718 superalloy under the uniaxial tension condition. However, to better describe the micromechanical response of the nickel-based Inconel 718 superalloy, the RVE4 with the largest size is used here for the micromechanical analysis of the polycrystalline nickel-based Inconel 718 superalloy. Fig. 6.5 shows the compared stress-strain curves between the RVE polycrystalline simulation and the uniaxial tension experiment. The solid red line is the macroscopic experimental curve under the uniaxial tension condition [282], and the dashed black line is the simulated stress-strain curve under the uniaxial tension condition from the finite element implementation of the RVE4 microstructure. It can be concluded that

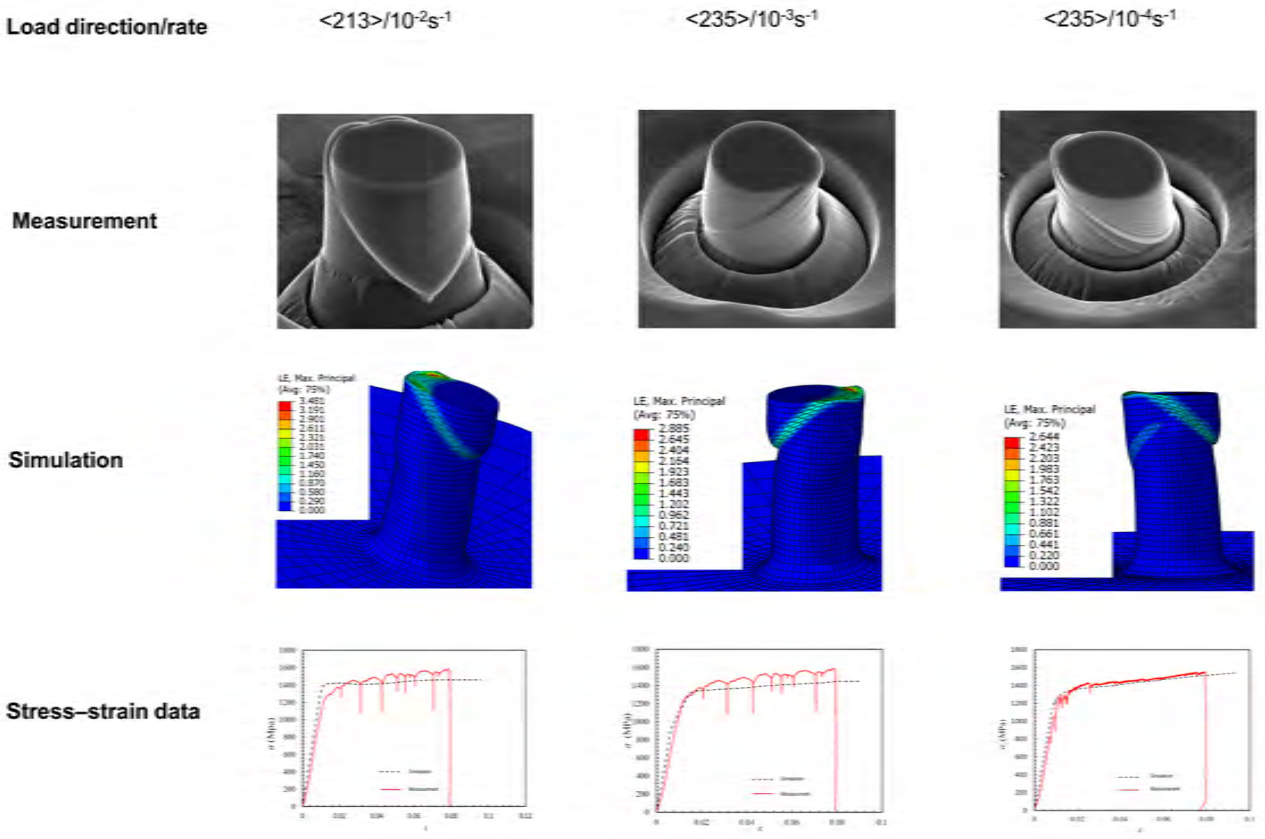

Fig. 6.4 Stress-strain data from measurements and simulations of unconfined compression tests from single crystal micropillars.

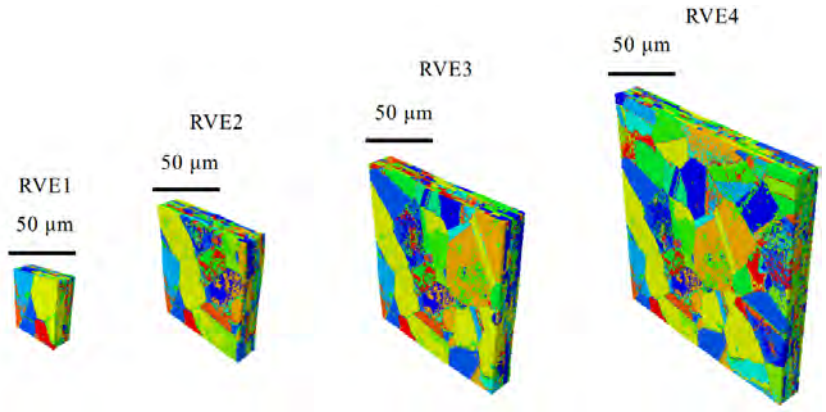

Fig. 6.5 The reconstructed polycrystalline nickel-based Inconel 718 superalloy with different RVE sizes.

the simulated and experimental stress-strain curves are in good agreement. Therefore, the predictive capability of the single crystal plasticity constitutive model for the polycrystalline nickel-based Inconel 718 superalloy is verified.

6.6 Conclusions

This Chapter established a single crystal plasticity constitutive model to analyze the micromechanical behavior of nickel-based Inconel 718 superalloy. Meanwhile, we utilized it to predict the micromechanical behavior of the single crystal and polycrystalline microstructure. The main conclusions are:

- The single crystal plasticity finite element model can accurately capture the stress-strain curve, the deformed shape, and the slip bands' location in the single crystal micropillar microstructure. Therefore, the predictive capability of the single crystal plasticity constitutive model for the single crystal nickel-based Inconel 718 superalloy is verified.
- The single crystal plasticity finite element model can accurately capture the stress-strain curve of the polycrystalline microstructure. Therefore, the predictive capability of the single crystal plasticity constitutive model for the polycrystalline nickel-based Inconel 718 superalloy is verified.

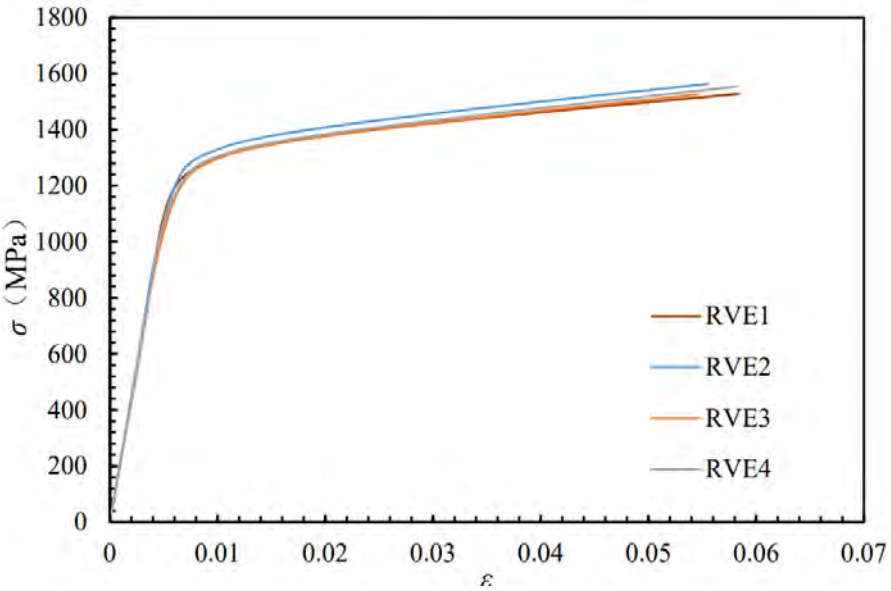

Fig. 6.6 The simulated stress-strain curves with different RVE sizes under the uniaxial tension condition.

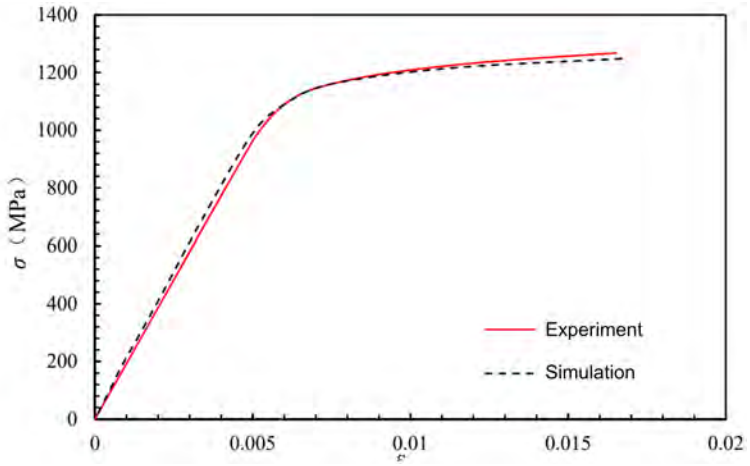

Fig. 6.7 The compared stress-strain curves between the RVE polycrystalline simulation and the uniaxial tension experiment.

Chapter 7

Processing-structure-properties-performance linkages in nickel-based superalloys

7.1 Introduction

As discussed in Chapter 1, the nucleation and growth phenomenon occurs during the evolutionary processes of polycrystalline materials, leading to random morphological and crystallographic microstructure characteristics (e.g., grain size, grain orientation, grain boundaries, etc.). Undoubtedly, the random characteristics formed during processing are responsible for the anisotropic behavior of polycrystalline microstructures and determine their macroscopic properties and performance. This Chapter focuses on building the processing-structure-properties-performance linkages in nickel-based superalloys. The novel reconstruction strategies developed in Chapter 4 and the explicit characterization algorithms proposed in Chapter 5 are coupled with the crystal plasticity constitutive model built in Chapter 5 to study the ductile failure in nickel-based Inconel 718 superalloy under the uniaxial tension condition. This Chapter comprises three parts: the ductile failure mechanism in nickel-based superalloys, the correlation study between the microstructure characterizations and the ductile failure, and the ductile failure sets. Their details are discussed below.

7.2 Micromechanical simulation of the ductile failure

7.2.1 Ductile failure mechanism

Ductile failure as a phenomenon is often observed in polycrystalline materials. Damage initiation and propagation in ductile metals are closely linked to the accumulated equivalent plastic strain ε_{eq} [235, 233]. ε_{eq} serves as a representation for localised deformation, defined as

$$\varepsilon_{eq} = \int_0^t \left(\frac{2}{3} \boldsymbol{D}^p : \boldsymbol{D}^p \right)^{\frac{1}{2}} dt \tag{7.1}$$

where t indicates the current time, and the symmetric part of the plastic velocity gradient gives the plastic strain rate $\boldsymbol{D}^p$ as

$$\begin{aligned} \boldsymbol{D}^p &= \frac{1}{2}(\boldsymbol{L}^{p*} + (\boldsymbol{L}^{p*})^T) \\ &= \frac{1}{2}(\boldsymbol{F}^e \boldsymbol{L}^p (\boldsymbol{F}^e)^{-1} + (\boldsymbol{F}^e)^{-T} (\boldsymbol{L}^p)^T (\boldsymbol{F}^e)^T) \\ &= \frac{1}{2} \sum_{\alpha=1}^{N} \dot{\gamma}^\alpha \left[\boldsymbol{F}^e \boldsymbol{m}^\alpha \otimes \boldsymbol{n}^\alpha (\boldsymbol{F}^e)^{-1} + (\boldsymbol{F}^e)^{-T} \boldsymbol{n}^\alpha \otimes \boldsymbol{m}^\alpha (\boldsymbol{F}^e)^T \right] \end{aligned} \tag{7.2}$$

where $\boldsymbol{L}^{p*} = \boldsymbol{F}^e \boldsymbol{L}^p (\boldsymbol{F}^e)^{-1}$ stands for the plastic velocity gradient in the final configuration, and $\boldsymbol{L}^p$ refers to the plastic velocity gradient in the intermediate configuration. A strain-controlled variable ω for accounting for damage is introduced such that material damage occurs when a threshold plastic strain ε_c is achieved. The variable ω takes 0 for no damage and 1 for total damage. Thus, the damage criterion is expressed as

$$\omega = \begin{cases} 0, & if\ \varepsilon_{eq} < \varepsilon_c \\ \\ 1, & otherwise \end{cases} \tag{7.3}$$

A modified local elastic stiffness tensor $\mathfrak{I}^*$ is utilised to interpret the reduced load carrying ability due to the existence of damage, given as

$$\mathfrak{I}^* = \mathfrak{I}(1-\omega) \tag{7.4}$$

An abrupt change in the value of ω in a FE model might result in substantial fluctuations in the local stress state and, as a result, make it difficult to achieve equilibrium. Thus, the modified Cauchy-Lorentz cumulative distribution function is proposed to present a

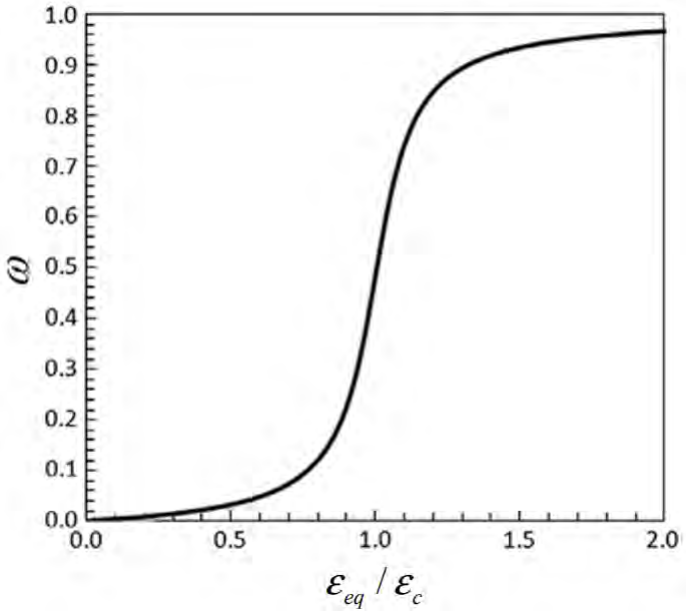

Fig. 7.1 Illustration of damage evolution with $d = 0.1$.

continuously varying ω as

$$\omega = 1 + \left[\frac{1}{2} + \frac{1}{\pi} arctan(\frac{\varepsilon_c}{d})\right]^{-1} \left[\frac{1}{\pi} arctan(\frac{\varepsilon_{eq} - \varepsilon_c}{d}) - \frac{1}{2}\right] \tag{7.5}$$

A nonzero value of d allows for a smooth transition from $\omega = 0$ to $\omega = 1$. In this work, we take d as 0.1 (Fig. 7.1).

7.2.2 Finite element implementation of the ductile failure

Fig. 7.2 shows the CPFEM model of the ductile failure simulation for the 2D polycrystalline RVE of the Inconel 718 superalloy. The input polycrystalline microstructure is the 2D RVE of the Inconel 718 superalloy mentioned in Chapter 6 (Fig. 7.2.a). The base of the 2D polycrystalline microstructure is entirely confined, whereas the top of the 2D polycrystalline microstructure is subjected to the vertical tensile stress (Fig. 7.2.c). After the grain reconstruction in Fig. 7.2.b, the orientation points in the individual grain are discretized with eight-node brick elements. A particular color represents each brick element sharing the same lattice orientation characterization (Fig. 7.2.d).

We incorporated the verified constitutive parameters (Table 6.1) and the ductile failure model into the CPFEM implementation to simulate the damage initiation and propagation at different time steps (Fig. 7.3). The yellow area at each time step represents the most prominent accumulated equivalent plastic strain. Consistent with physical observations,

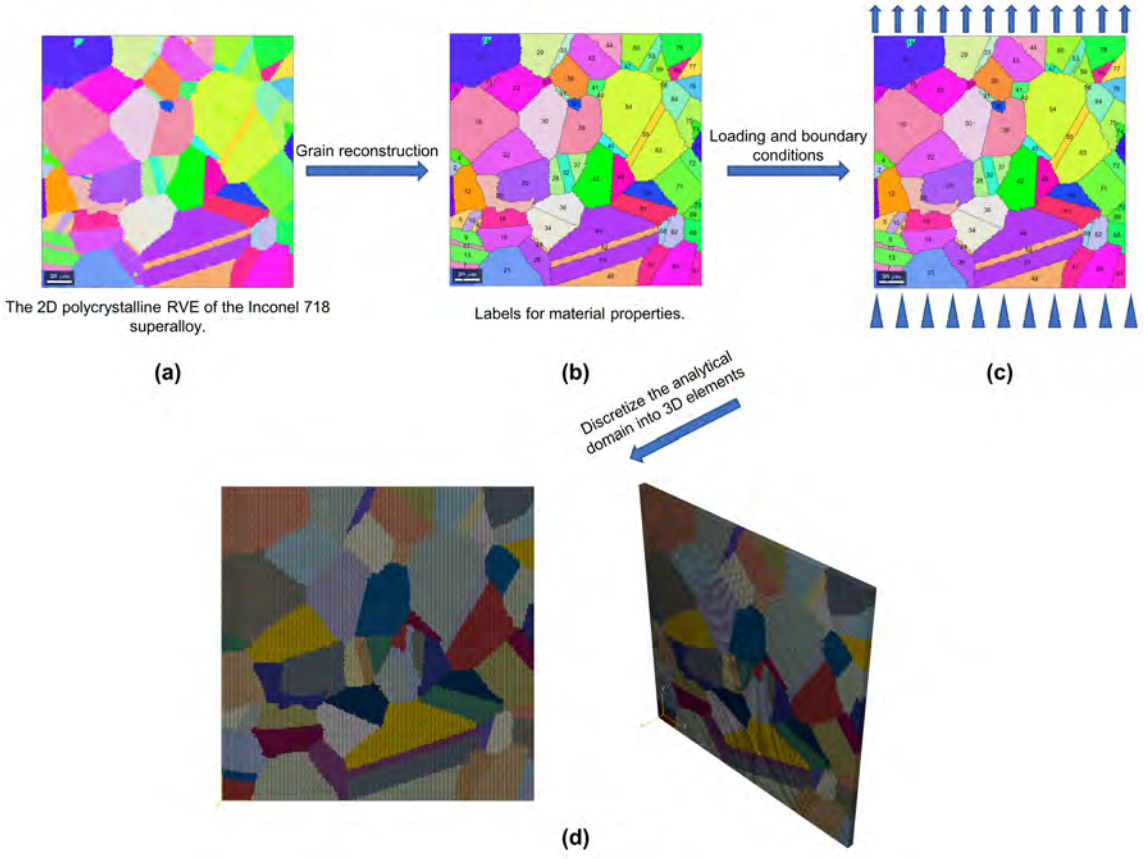

Fig. 7.2 The CPFEM model of the ductile failure simulation for the 2D polycrystalline RVE of the Inconel 718 superalloy.

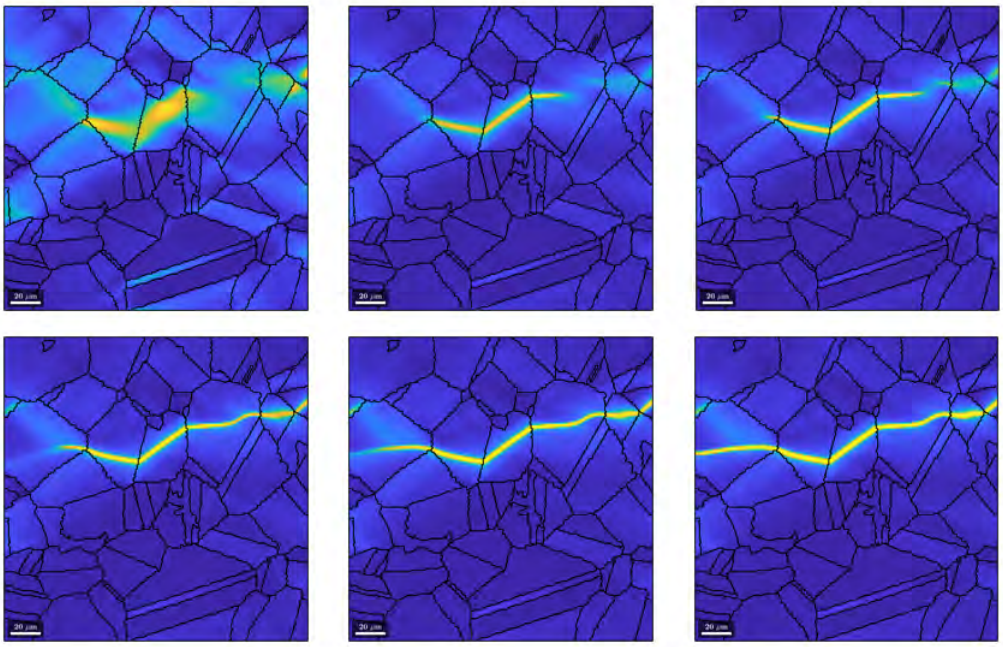

Fig. 7.3 Prediction of damage initiation and propagation controlled by accumulated equivalent plastic strain.

it is concluded that ductile failure initiates around triple junctions due to highly localized plastic deformation and extends along grain boundaries. Some transgranular damage may be observable in Fig. 7.3, but intergranular damage dominates the failure response.

7.3 Correlation study between the microstructure characterizations and the ductile failure

Fig. 7.4 demonstrates the flowchart of the microstructure characterization influences on ductile failure. The novel reconstruction strategies in Chapter 4 and the explicit characterization algorithms in Chapter 5 are applied to the 2D polycrystalline RVE of the Inconel 718 superalloy to generate stochastic microstructure characterizations regarding grain size, orientation, and boundary. The stochastic microstructure characterizations then serve as input to the CPFEM model to investigate their corresponding properties and performance.

7.3.1 Grain size

We take the nine illustrations of explicit characterization algorithms with grain size decrease in Fig. 7.5 as input for the established CPFEM ductile failure model. Fig. 7.6 exhibits the

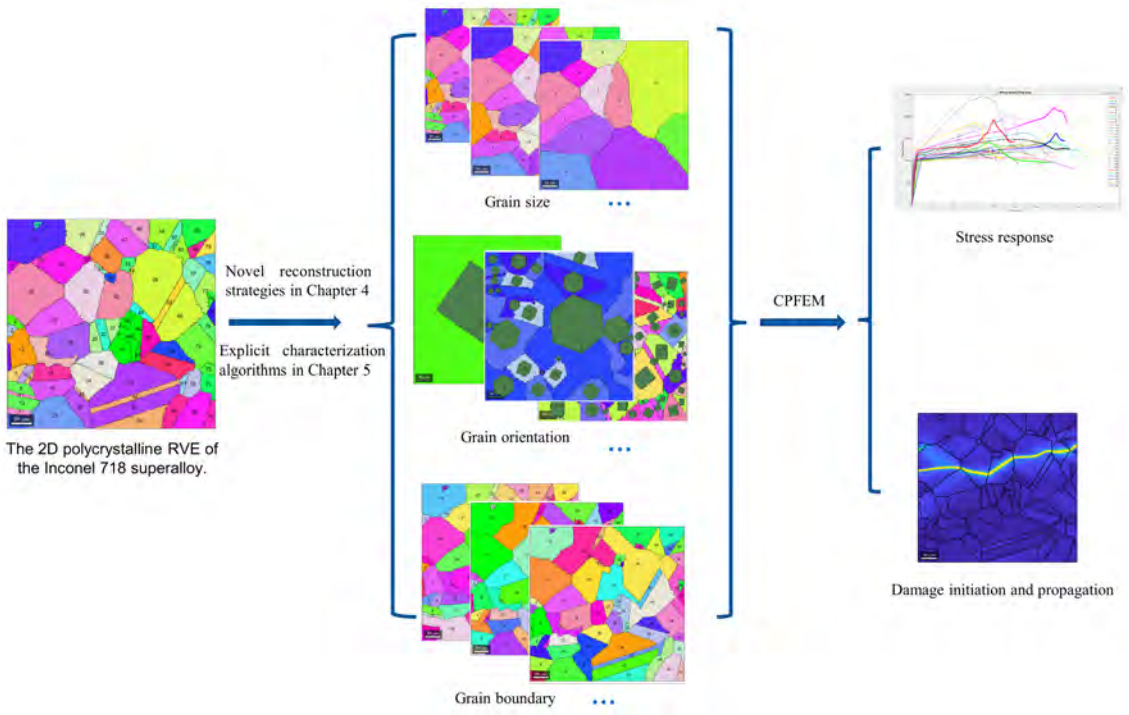

Fig. 7.4 Flowchart of the microstructure characterization influences on ductile failure.

grain size distribution of the nine illustrations. Fig. 7.7 reveals the Von Mises stress-time step curves. Fig. 7.8 presents the ductile failure localizations.

7.3.2 Grain orientation

We randomly select four illustrations of explicit characterization algorithms with grain orientation as input for the established CPFEM model. Fig. 7.9 exhibits the grain orientation distribution (inverse pole figure in x ([100]), y ([010]), and z ([001]) direction). Fig. 7.10 reveals the Von Mises stress-time step curves. Fig. 7.11 presents the ductile failure localizations.

7.3.3 Grain boundary

We take the twelve illustrations of explicit characterization algorithms with varying grain boundary conditions in Fig. 7.12 as input for the established CPFEM model. Fig. 7.13 exhibits the grain size distribution of the twelve illustrations. Fig. 7.14 reveals the Von Mises stress-time step curves. Fig. 7.15 presents the ductile failure localizations.

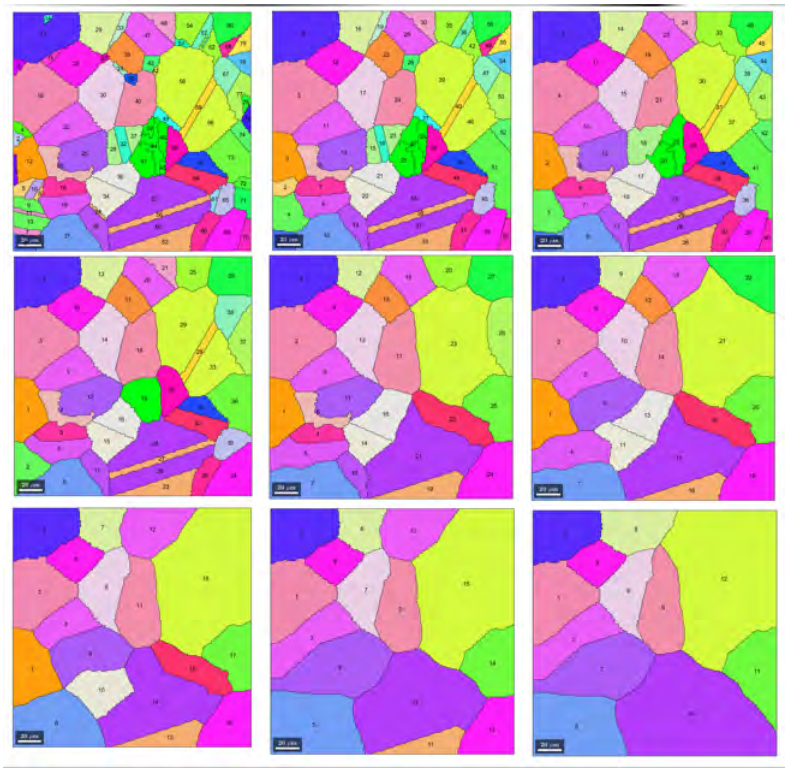

Fig. 7.5 Illustrations of explicit characterization algorithms with increased grain sizes.

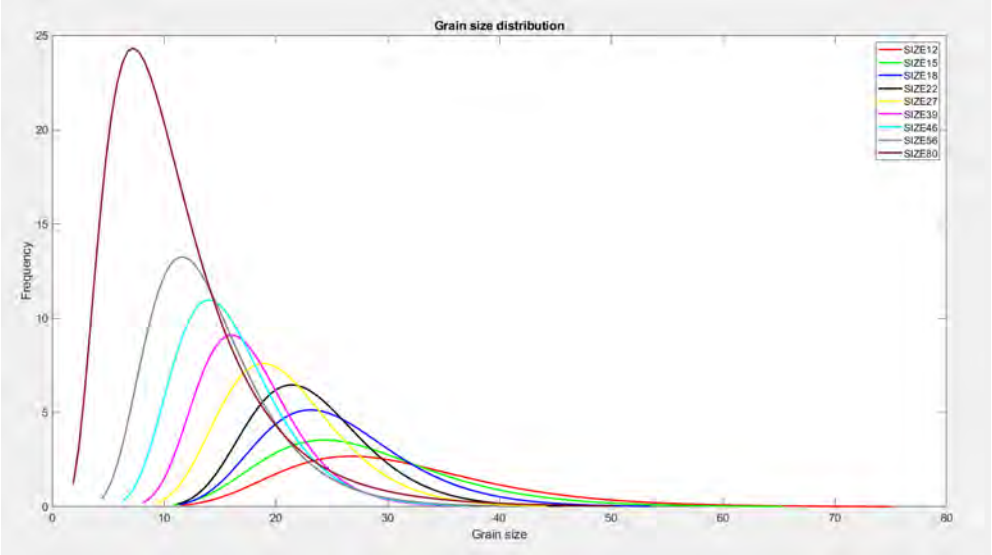

Fig. 7.6 Illustrations of the grain size distributions with increased grain sizes.

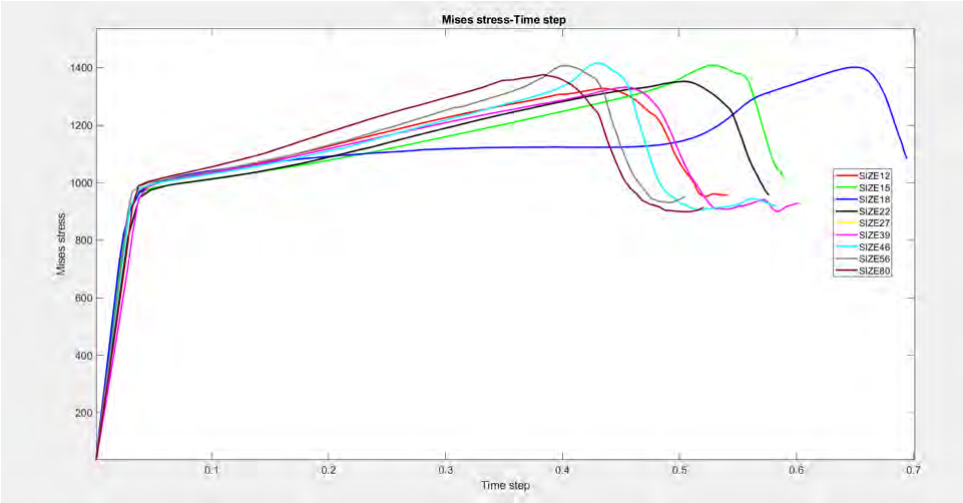

Fig. 7.7 Illustrations of the Von Mises stress-time step curves with increased grain sizes.

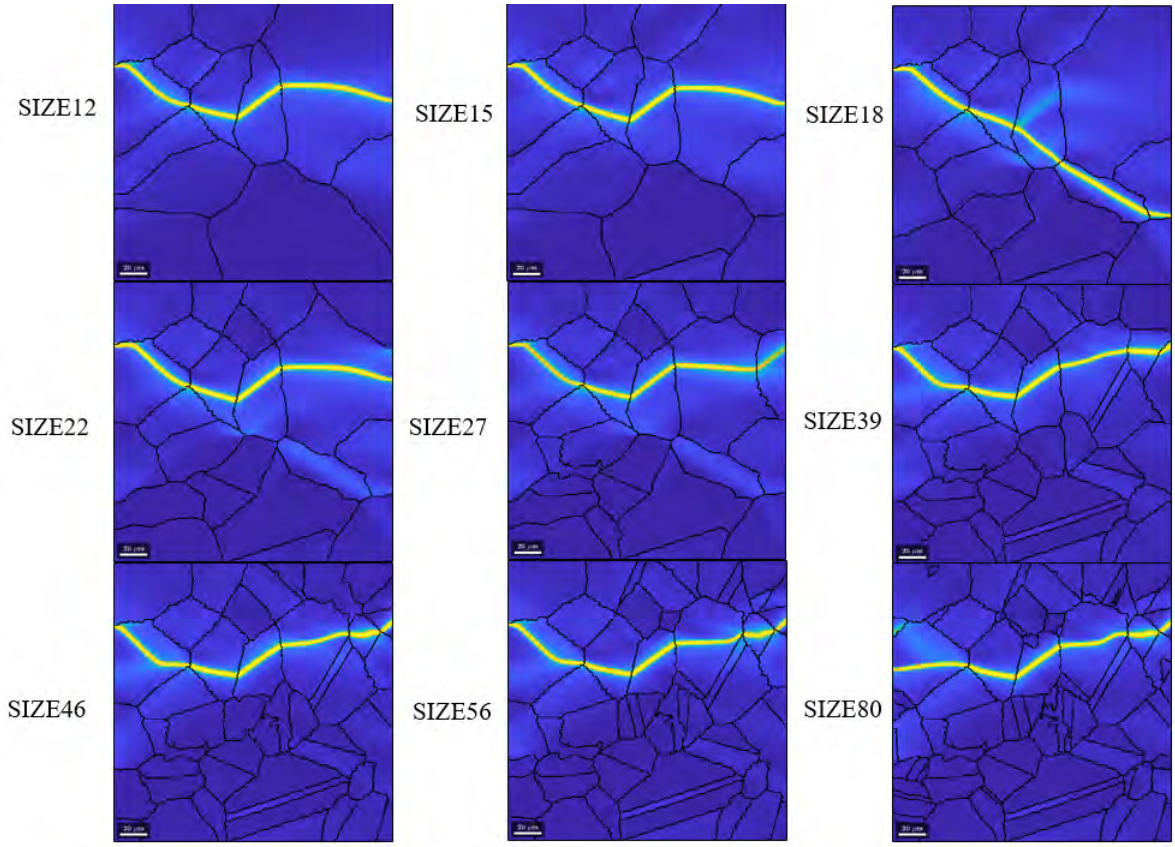

Fig. 7.8 Illustrations of the ductile failure localizations with increased grain sizes.

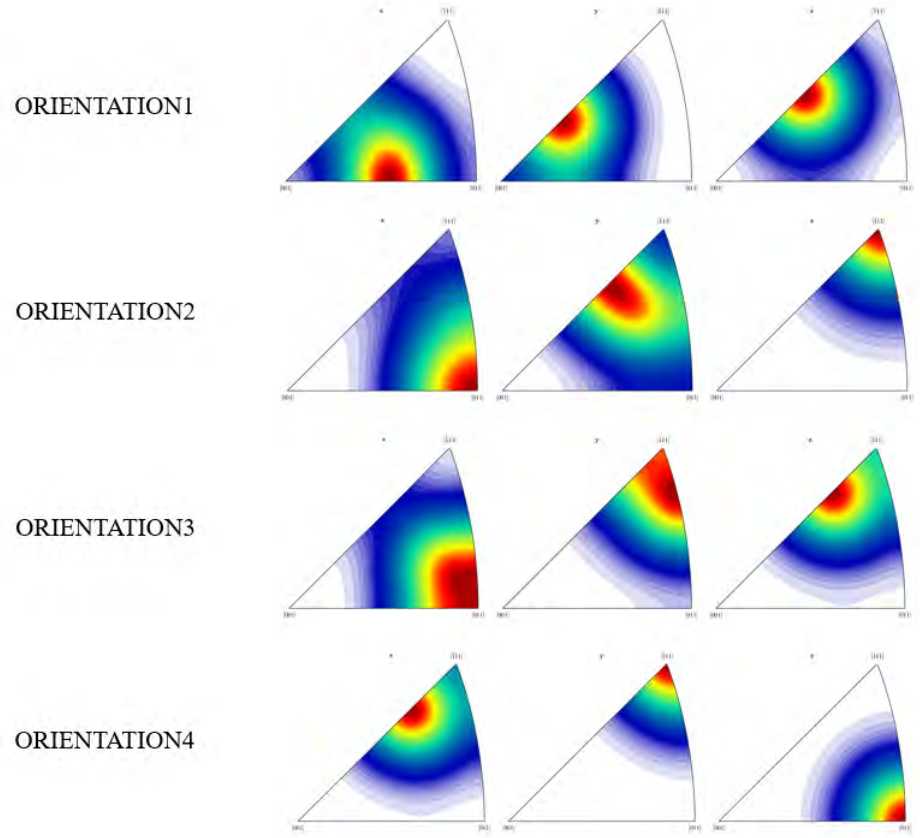

Fig. 7.9 Illustrations of explicit characterization algorithms with varying grain orientations.

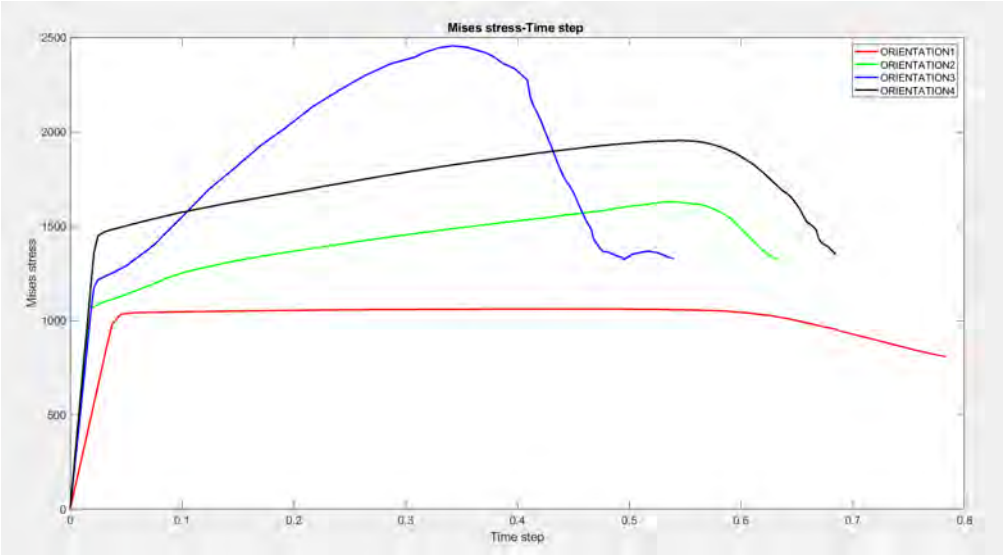

Fig. 7.10 Illustrations of the Von Mises stress-time step curves with varying grain orientations.

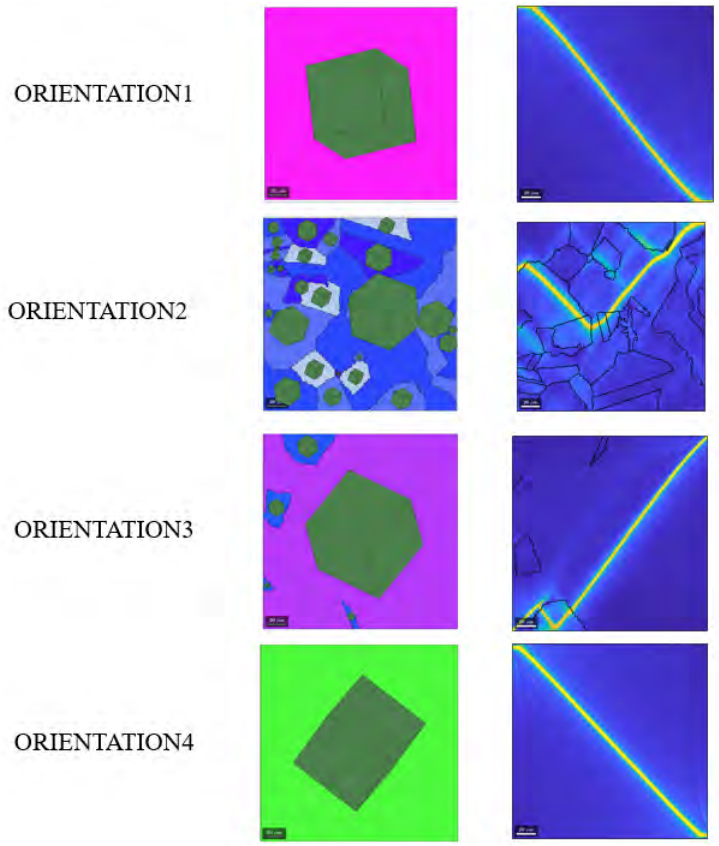

Fig. 7.11 Illustrations of the ductile failure localizations with varying grain orientations.

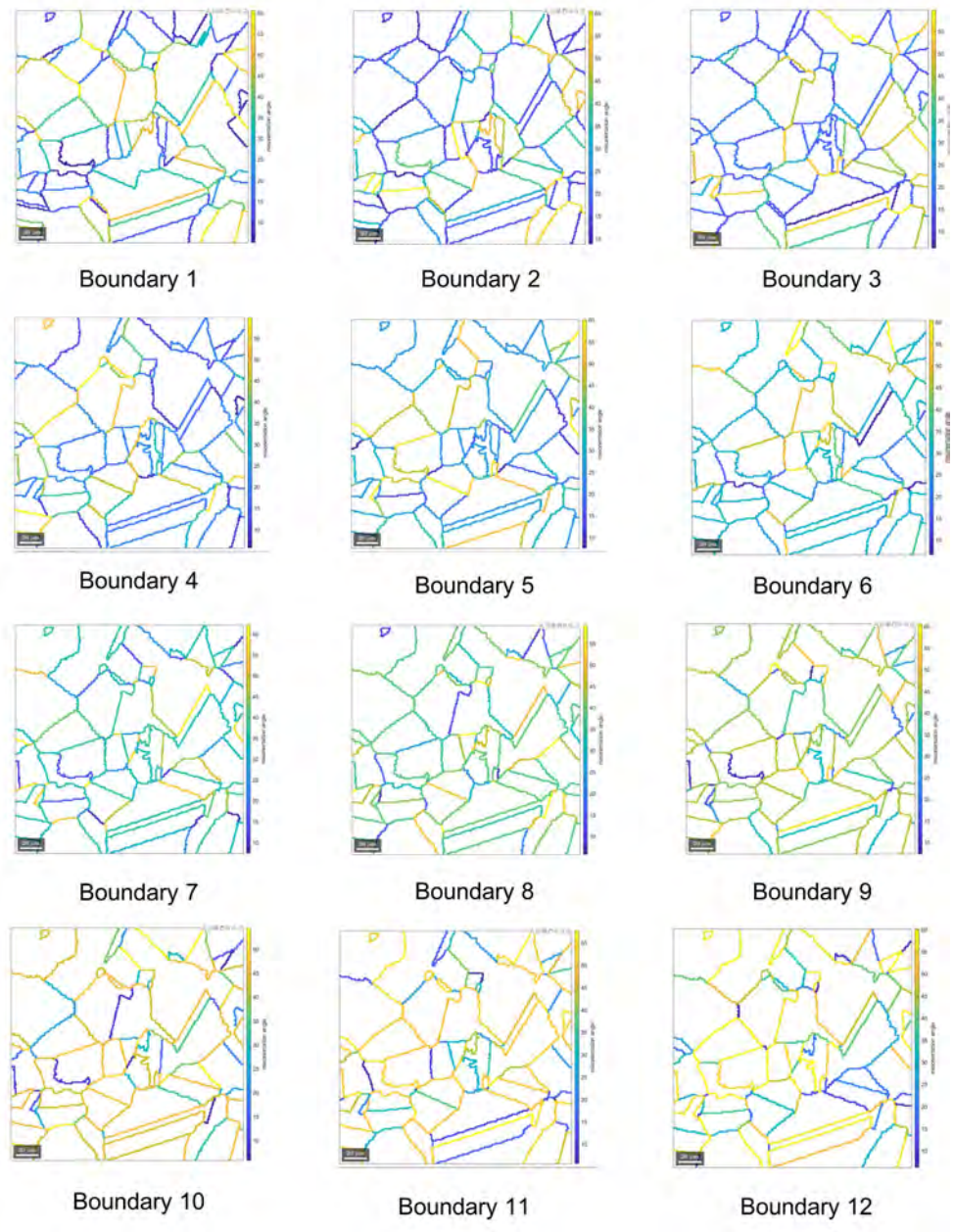

Fig. 7.12 Illustrations of the explicit characterization algorithms with varying grain boundary conditions.

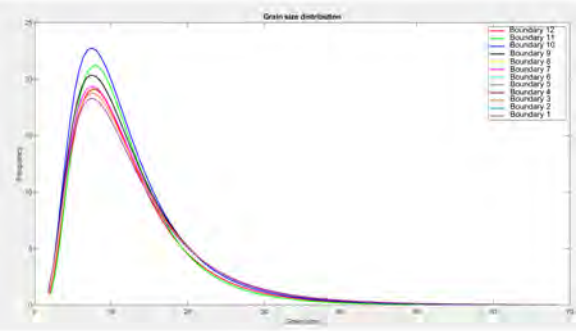

Fig. 7.13 Illustrations of the grain size distributions with varying grain boundary conditions.

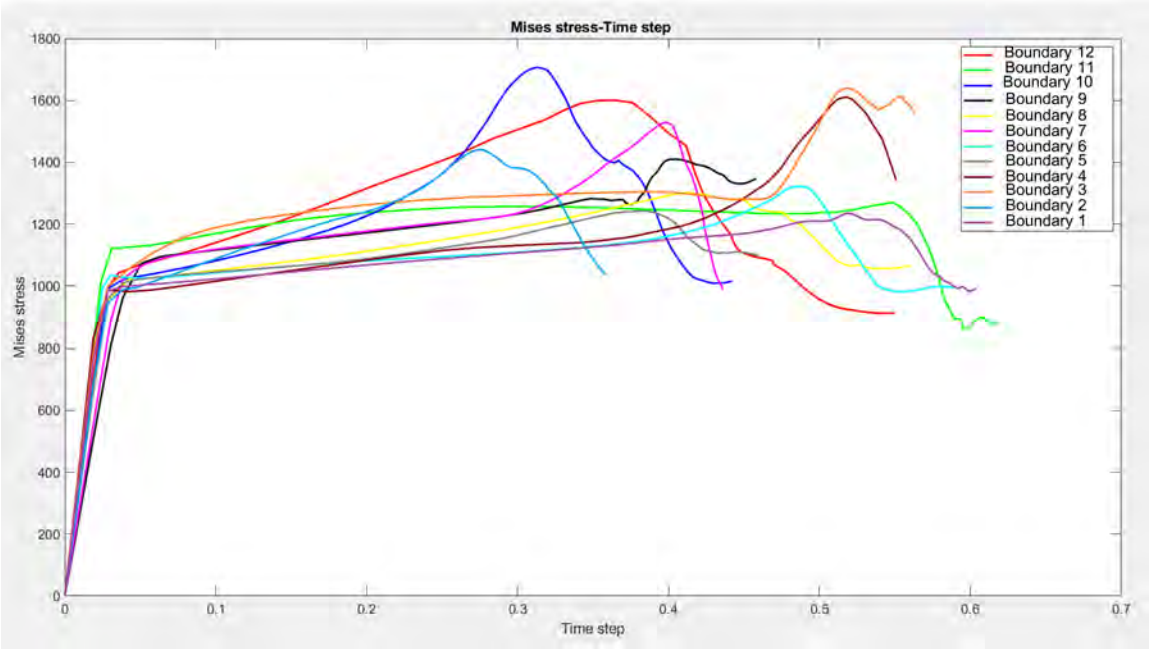

Fig. 7.14 Illustrations of the Von Mises stress-time step curves with varying grain boundary conditions.

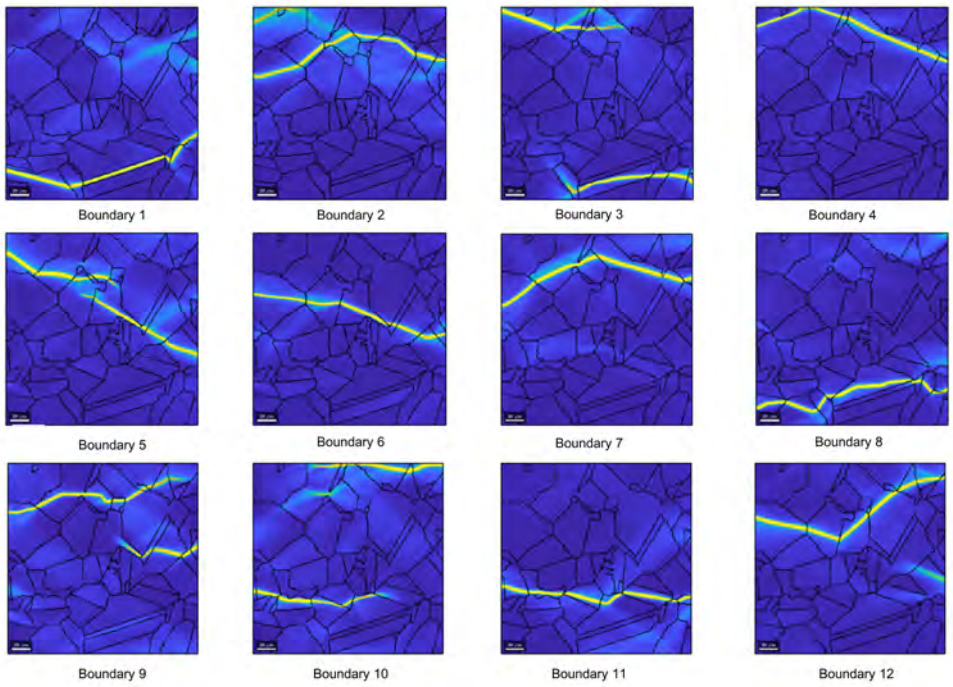

Fig. 7.15 Illustrations of the ductile failure localizations with varying boundary conditions.

7.4 Ductile failure sets of statistical microstructure characterizations

Based on Fig. 7.7, Fig. 7.10, and Fig. 7.14, we can observe that the properties, such as the ultimate tensile stress and Von Mises stress, are sensitive to grain size and orientation characterizations, especially for the grain orientation characterization. The ultimate tensile stress changes from 1000 Mpa to 2500 Mpa in Fig. 7.10. Meanwhile, the different failure locations in Fig. 7.8, Fig. 7.11, and Fig. 7.15 verify that ductile failure performance (failure initiation and propagation) is strongly sensitive to boundary conditions. Therefore, two ductile failure subsets can be built: the properties subset for grain orientations and the performance subset for grain boundaries. The SERVEs-based texture synthesis algorithms (Chapter 4) can be utilized first to generate all possible statistical microstructure characterizations from experimental observation. After that, explicit characterization algorithms with grain nucleation and growth can be employed to expand or shrink the grain size to a particular range (Fig. 7.16). Finally, generated samples through explicit characterization algorithms with grain orientation serve as input for the established CPFEM model to build the properties subset. Or, generated samples through explicit characterization algorithms with grain boundary serve as input for

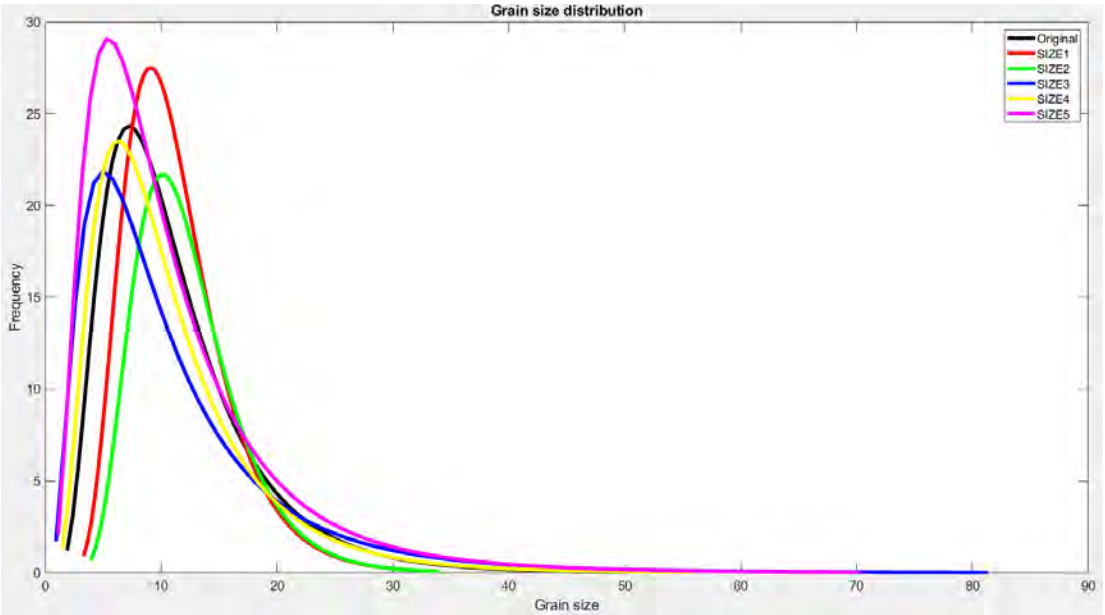

Fig. 7.16 Illustration of expanding or shrinking the grain size distribution.

the established CPFEM model to construct the performance subset. By doing so, complete and closed ductile failure sets can be established. Fig. 7.17 shows the flowchart of ductile failure properties subset related to grain orientation. Fig. 7.18 shows the flowchart of ductile failure performance subset related to the grain boundary. Reduction techniques, including spectral methods (SM), principal component analysis (PCA), and representative aggregated microstructural parameters (RAMPs), can be applied to the ductile failure sets to improve efficiency (Subsection 2.3.3).

7.5 Conclusions

This Chapter established the ductile failure model to analyze the damage initiation and propagation of nickel-based Inconel 718 superalloy. Meanwhile, the correlation study between the microstructure characterizations and ductile failure has been conducted, and the PSPP linkages have been built. The main conclusions are:

- The properties, such as the ultimate tensile stress and Von Mises stress, are sensitive to grain size and orientation characterizations, especially for the grain orientation characterization. The ductile failure performance (failure initiation and propagation) is strongly sensitive to boundary conditions. Therefore, two ductile failure subsets can be built: the properties subset for grain orientations and the performance subset for grain boundaries.

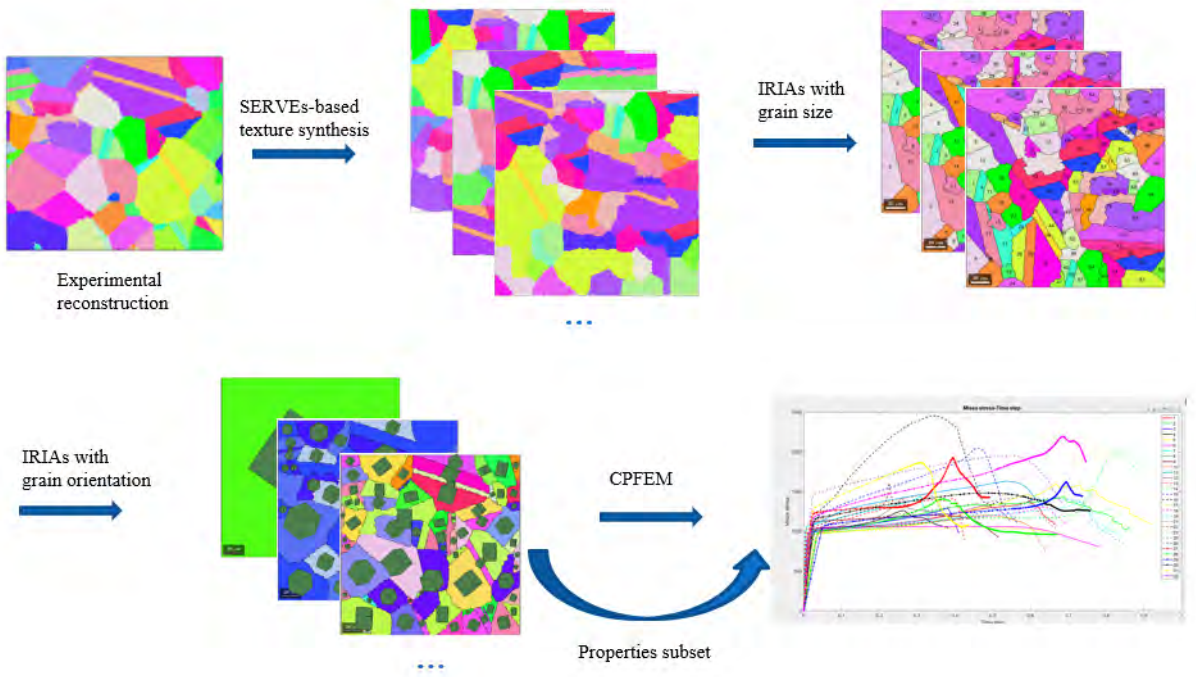

Fig. 7.17 Flowchart of ductile failure properties subset related to grain orientation.

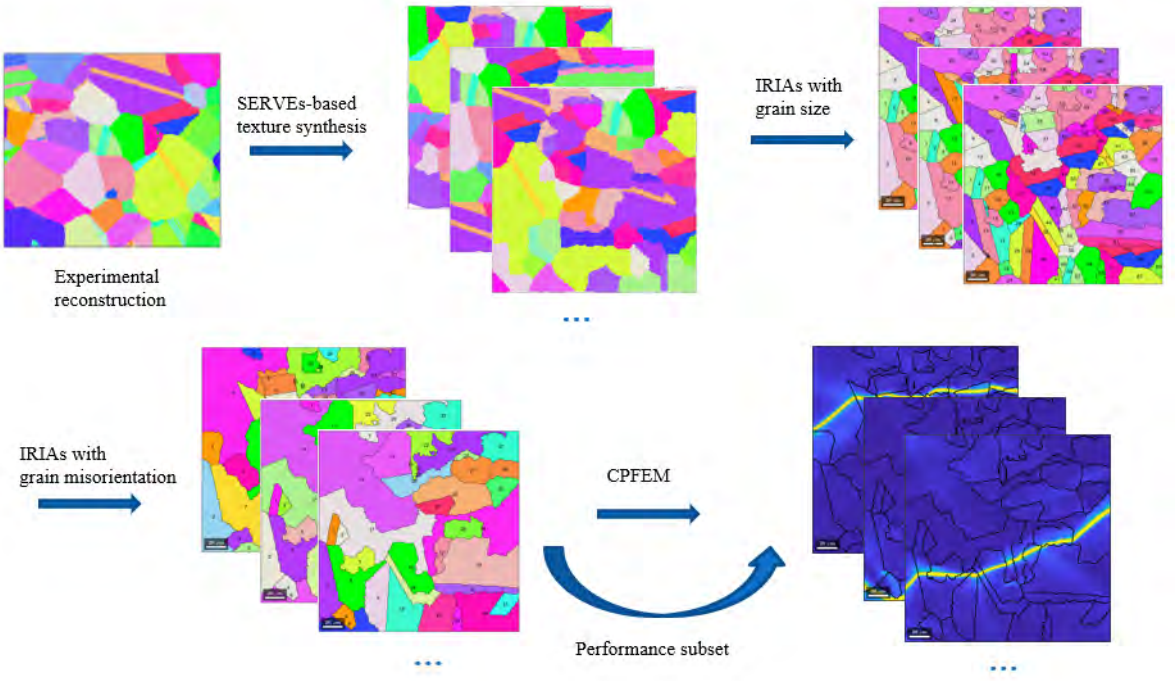

Fig. 7.18 Flowchart of ductile failure performance subset related to grain boundary.

Chapter 8

Conclusions

8.1 Conclusions

The main innovation of this thesis is to propose some reconstruction and characterization algorithms in texture synthesis models applied to the microstructure representation of polycrystalline materials. Besides, the micromechanism of the nickel-based superalloys has been simulated, and the linkages between processing-structure-properties-performance have been established. The main conclusions of the thesis can be summarized as follows:

- Microstructure reconstruction in polycrystalline materials is generally classified into experimental, physical, and geometrical reconstruction. The experimental reconstruction aims at reconstruction through experimental measurement of realistic microstructure, such as serial sectioning and non-destructive reconstruction. The physical reconstruction focuses on the processing simulation of grain nucleation and growth responsible for the microstructure formation under specific constraints, including the cellular automate, Monte Carlo approaches, vertex methods, level set and phase field models. The geometrical reconstruction ignores the physical microstructural formation process and targets the morphological and crystallographic information generation in polycrystalline materials, for example, the Voronoi tessellation, ellipsoid packing, and texture synthesis.

- Microstructure characterization in polycrystalline materials can be classified into first-order and higher-order descriptions. The first-order statistics provide information about the likelihood of finding a specific local state at a single point sampled from the material. According to the different emphasis of local state h, the one-point statistics are further subdivided into two large groups: physical and geometric. Three primary characterizations describe the microstructure evolution of polycrystalline materials

during the manufacturing process: phase volume fraction, boundary condition and systemic energy. Geometric characterization can be classified into two broad categories: morphological and crystallographic. The morphological characterization provides necessary statistical information on the grain-level features, such as the distribution of grain volume, size, topology and neighbourhood. The crystallographic characterization examines the crystallography of the grains, including the orientation distribution function, misorientation distribution function and micro-texture function. The higher-point statistics provide the distribution information on the Cartesian and local state spaces. For instance, the two-point correlation, chord length, two-point orientation correlation, orientation autocorrelation, two-point misorientation correlation, and n-point orientation correlation.

- Robust reduction techniques can transform the characterization spaces into lower-dimensional features, including spectral methods, principal component analysis, and representative aggregated microstructural parameters. These lower-dimensional features are highly effective when used as inputs in the microstructure sensitive design, materials knowledge system, parametrically homogenized constitutive models, uncertainty quantification, and additive manufacturing in polycrystalline materials.

- The patch-based texture synthesis reconstruction algorithm can perfectly capture the statistical microstructure characterizations from experimental observation. It can be served as an alternative geometric reconstruction for Voronoi tessellation and ellipsoid packing.

- The single crystal plasticity finite element model can accurately capture the stress-strain curve, the deformed shape, and the slip bands' location in the single crystal micropillar microstructure. Therefore, the predictive capability of the single crystal plasticity constitutive model for the single crystal nickel-based Inconel 718 superalloy is verified. The single crystal plasticity finite element model can accurately capture the stress-strain curve of the polycrystalline microstructure. Therefore, the predictive capability of the single crystal plasticity constitutive model for the polycrystalline nickel-based Inconel 718 superalloy is verified.

- The grain nucleation and growth algorithm can capture the morphological evolution of the SERVEs generated from the improved PTS models in Chapter 4. The constrained grain orientation generation algorithm can stochastically characterize the grain orientation variations based on the orientation dataset generated from the EBSD reconstruction under the same morphological conditions. The constrained grain boundary generation

algorithm can stochastically describe the grain boundary variations under the same morphological and crystallographic conditions.

- Correlation studies between microstructure characterization and macroscopic ductile failure in nickel-based superalloy reveal that the properties, such as the ultimate tensile stress and Von Mises stress, are sensitive to grain size and orientation characterizations, especially for the grain orientation characterization. The ductile failure performance (failure initiation and propagation) is strongly sensitive to boundary conditions. Therefore, two ductile failure subsets can be built: the properties subset for grain orientations and the performance subset for grain boundaries.

8.2 Perspectives

The main task of this thesis is to solve the reconstruction and characterization problems in texture synthesis models applied to the microstructure representation of polycrystalline materials. This thesis has effectively accomplished its intended purpose. However, more interesting concerns come out. They are beyond the scope of this thesis due to the time constraints of my Ph.D. but will be the subject of my future research. The future works of this thesis can be summarized as follows:

- The 3D characterizations, e.g., the grain size, shape, and neighbor distributions affected by spatial connectivity, cannot be precisely quantified from the 2D reconstructions. Therefore, future work should be focused on applying the improved patch-based texture synthesis model to the 3D reconstruction of polycrystalline materials.

- The morphological and crystallographic characterizations (e.g., grain size, grain orientation, etc.) that are correlated with materials processing parameters (e.g., deformation, thermal history, etc.) as well as specific materials properties and performance (e.g., stress and strain responses, stress and strain field, ductile failure, brittle fracture, fatigue failure, etc.). This enables us to construct the forward and inverse PSPP linkages in data-driven modeling to optimize manufacturing processes (cause-effect design) or create new polycrystalline materials (goals-driven design).

- The ductile failure sets using the most sensible microstructural parameters, such as grain orientation distributions and boundary characters, can facilitate the selection of material structure and processing for suitable specific engineering requirements. It can be excellent guidance for microstructure sensitive design, materials knowledge system,

uncertainty quantification, and surrogate crystal plasticity modeling in polycrystalline materials.

References

[1] Abdollahifard, M. J., Baharvand, M., and Mariéthoz, G. (2019a). Efficient training image selection for multiple-point geostatistics via analysis of contours. *Computers & Geosciences*, 128:41–50.

[2] Abdollahifard, M. J., Mariéthoz, G., and Ghavim, M. (2019b). Quantitative evaluation of multiple-point simulations using image segmentation and texture descriptors. *Computational Geosciences*, 23(6):1349–1368.

[3] Abdollahifard, M. J. and Nasiri, B. (2017). Exploiting transformation-domain sparsity for fast query in multiple-point geostatistics. *Computational Geosciences*, 21(2):289–299.

[4] Abid, N. H., Al-Rub, R. K. A., and Palazotto, A. N. (2017). Micromechanical finite element analysis of the effects of martensite morphology on the overall mechanical behavior of dual phase steel. *International Journal of Solids and Structures*, 104:8–24.

[5] Acar, P. (2021). Recent progress of uncertainty quantification in small-scale materials science. *Progress in Materials Science*, 117:100723.

[6] Acar, P. and Sundararaghavan, V. (2016). A markov random field approach for modeling spatio-temporal evolution of microstructures. *Modelling and Simulation in Materials Science and Engineering*, 24(7):075005.

[7] Acar, P. and Sundararaghavan, V. (2019). Stochastic design optimization of microstructural features using linear programming for robust design. *AIAA Journal*, 57(1):448–455.

[8] Adams, B. L., Kalidindi, S., and Fullwood, D. T. (2012). *Microstructure sensitive design for performance optimization*. Butterworth-Heinemann.

[9] Alkemper, J. and Voorhees, P. (2001). Quantitative serial sectioning analysis. *Journal of Microscopy*, 201(3):388–394.

[10] Allen, S. M. and Cahn, J. W. (1979). A microscopic theory for antiphase boundary motion and its application to antiphase domain coarsening. *Acta Metallurgica*, 27(6):1085–1095.

[11] Alveen, P., Carolan, D., McNamara, D., Murphy, N., and Ivanković, A. (2013). Micromechanical modelling of ceramic based composites with statistically representative synthetic microstructures. *Computational Materials Science*, 79:960–970.

[12] An, D., Griffiths, T., Konijnenberg, P., Mandal, S., Wang, Z., and Zaefferer, S. (2018). Correlating the five parameter grain boundary character distribution and the intergranular corrosion behaviour of a stainless steel using 3d orientation microscopy based on mechanical polishing serial sectioning. *Acta Materialia*, 156:297–309.

[13] Arsenlis, A. and Parks, D. (1999). Crystallographic aspects of geometrically-necessary and statistically-stored dislocation density. *Acta Materialia*, 47(5):1597–1611.

[14] Ashby, M., Spaepen, F., and Williams, S. (1978). The structure of grain boundaries described as a packing of polyhedra. *Acta Metallurgica*, 26(11):1647–1663.

[15] Aurenhammer, F. (1987). Power diagrams: properties, algorithms and applications. *SIAM Journal on Computing*, 16(1):78–96.

[16] Avrami, M. (1939). Kinetics of phase change. i general theory. *The Journal of Chemical Physics*, 7(12):1103–1112.

[17] Avrami, M. (1940). Transformation-time relations for random distribution of nuclei kinetics of phase change, ii. *Journal of Chemical Physics*, 8:212.

[18] Avrami, M. (1941). Kinetics of phase change. iii: Granulation, phase change and microstructure. *Journal of Chemical Physics*, 9:177–184.

[19] Bachmann, F., Hielscher, R., and Schaeben, H. (2010). Texture analysis with mtex–free and open source software toolbox. In *Solid State Phenomena*, volume 160, pages 63–68. Trans Tech Publ.

[20] Bacon, G. E. (2013). *X-Ray and Neutron Diffraction: The Commonwealth and International Library: Selected Readings in Physics*. Elsevier.

[21] Bagri, A., Hanson, J. P., Lind, J., Kenesei, P., Suter, R. M., Gradečak, S., and Demkowicz, M. J. (2017). Measuring grain boundary character distributions in ni-base alloy 725 using high-energy diffraction microscopy. *Metallurgical and Materials Transactions A*, 48(1):354–361.

[22] Bagri, A., Weber, G., Stinville, J.-C., Lenthe, W., Pollock, T., Woodward, C., and Ghosh, S. (2018). Microstructure and property-based statistically equivalent representative volume elements for polycrystalline ni-based superalloys containing annealing twins. *Metallurgical and Materials Transactions A*, 49(11):5727–5744.

[23] Bai, T. and Tahmasebi, P. (2020). Hybrid geological modeling: Combining machine learning and multiple-point statistics. *Computers & Geosciences*, 142:104519.

[24] Baninajar, E., Sharghi, Y., and Mariethoz, G. (2019). Mps-apo: a rapid and automatic parameter optimizer for multiple-point geostatistics. *Stochastic Environmental Research and Risk Assessment*, 33(11):1969–1989.

[25] Bansal, R., Kubis, A., Hull, R., and Fitz-Gerald, J. (2006). High-resolution three-dimensional reconstruction: A combined scanning electron microscope and focused ion-beam approach. *Journal of Vacuum Science & Technology B: Microelectronics and Nanometer Structures Processing, Measurement, and Phenomena*, 24(2):554–561.

[26] Barbe, F., Decker, L., Jeulin, D., and Cailletaud, G. (2001). Intergranular and intragranular behavior of polycrystalline aggregates. part 1: Fe model. *International Journal of Plasticity*, 17(4):513–536.

[27] Barber, C. B., Dobkin, D. P., and Huhdanpaa, H. (1996). The quickhull algorithm for convex hulls. *ACM Transactions on Mathematical Software (TOMS)*, 22(4):469–483.

[28] Bargmann, S., Klusemann, B., Markmann, J., Schnabel, J. E., Schneider, K., Soyarslan, C., and Wilmers, J. (2018). Generation of 3d representative volume elements for heterogeneous materials: A review. *Progress in Materials Science*, 96:322–384.

[29] Barker, J., Bollerhey, G., and Hamaekers, J. (2016). A multilevel approach to the evolutionary generation of polycrystalline structures. *Computational Materials Science*, 114:54–63.

[30] Bate, P. and da Fonseca, J. Q. (2004). Texture development in the cold rolling of if steel. *Materials Science and Engineering: A*, 380(1-2):365–377.

[31] Beaudoin, A., Dawson, P., Mathur, K., and Kocks, U. (1995). A hybrid finite element formulation for polycrystal plasticity with consideration of macrostructural and microstructural linking. *International Journal of Plasticity*, 11(5):501–521.

[32] Beausir, B., Fressengeas, C., Gurao, N. P., Toth, L. S., and Suwas, S. (2009). Spatial correlation in grain misorientation distribution. *Acta Materialia*, 57(18):5382–5395.

[33] Beladi, H., Nuhfer, N. T., and Rohrer, G. S. (2014). The five-parameter grain boundary character and energy distributions of a fully austenitic high-manganese steel using three dimensional data. *Acta Materialia*, 70:281–289.

[34] Beladi, H. and Rohrer, G. S. (2013). The relative grain boundary area and energy distributions in a ferritic steel determined from three-dimensional electron backscatter diffraction maps. *Acta Materialia*, 61(4):1404–1412.

[35] Belyakov, A., Kimura, Y., Adachi, Y., and Tsuzaki, K. (2004). Microstructure evolution in ferritic stainless steels during large strain deformation. *Materials Transactions*, 45(9):2812–2821.

[36] Bernacki, M., Chastel, Y., Coupez, T., and Logé, R. E. (2008). Level set framework for the numerical modelling of primary recrystallization in polycrystalline materials. *Scripta Materialia*, 58(12):1129–1132.

[37] Bernacki, M., Digonnet, H., Resk, H., Coupez, T., and Loge, R. (2007). Development of numerical tools for the multiscale modelling of recrystallization in metals, based on a digital material framework. In *AIP Conference Proceedings*, volume 908, pages 375–380. American Institute of Physics.

[38] Bernacki, M., Logé, R. E., and Coupez, T. (2011). Level set framework for the finite-element modelling of recrystallization and grain growth in polycrystalline materials. *Scripta Materialia*, 64(6):525–528.

[39] Bernacki, M., Resk, H., Coupez, T., and Logé, R. E. (2009). Finite element model of primary recrystallization in polycrystalline aggregates using a level set framework. *Modelling and Simulation in Materials Science and Engineering*, 17(6):064006.

[40] Bernard, P., Bag, S., Huang, K., and Logé, R. E. (2011). A two-site mean field model of discontinuous dynamic recrystallization. *Materials Science and Engineering: A*, 528(24):7357–7367.

[41] Bernier, J. V., Barton, N. R., Lienert, U., and Miller, M. P. (2011). Far-field high-energy diffraction microscopy: a tool for intergranular orientation and strain analysis. *The Journal of Strain Analysis for Engineering Design*, 46(7):527–547.

[42] Bertolino, G., Bilger, N., and Crepin, J. (2007). Modeling microstructures and microstructural effects on macroscopic and intragranular mechanical behavior. *Computational Materials Science*, 40(3):408–416.

[43] Bhandari, Y., Sarkar, S., Groeber, M., Uchic, M., Dimiduk, D., and Ghosh, S. (2007). 3d polycrystalline microstructure reconstruction from fib generated serial sections for fe analysis. *Computational Materials Science*, 41(2):222–235.

[44] Biswas, A., Prasad, M. R., Vajragupta, N., Kostka, A., Niendorf, T., and Hartmaier, A. (2020). Effect of grain statistics on micromechanical modeling: The example of additively manufactured materials examined by electron backscatter diffraction. *Advanced Engineering Materials*, 22(5):1901416.

[45] Błachnio, J., Spychała, J., and Zasada, D. (2021). Analysis of structural changes in a gas turbine blade as a result of high temperature and stress. *Engineering Failure Analysis*, 127:105554.

[46] Bodelot, L. (2019). Investigation of the relationship between microstructural features and strain localization in polycrystalline 316 l. *Experimental Mechanics*, 59(5):691–702.

[47] Boettinger, W. J., Warren, J. A., Beckermann, C., and Karma, A. (2002). Phase-field simulation of solidification. *Annual Review of Materials Research*, 32(1):163–194.

[48] Bonet, J., Gil, A. J., and Wood, R. D. (2016). *Nonlinear solid mechanics for finite element analysis: statics*. Cambridge University Press.

[49] Bos, C., Mecozzi, M., and Sietsma, J. (2010). A microstructure model for recrystallisation and phase transformation during the dual-phase steel annealing cycle. *Computational Materials Science*, 48(3):692–699.

[50] Bostanabad, R. (2020). Reconstruction of 3d microstructures from 2d images via transfer learning. *Computer-Aided Design*, 128:102906.

[51] Bostanabad, R., Zhang, Y., Li, X., Kearney, T., Brinson, L. C., Apley, D. W., Liu, W. K., and Chen, W. (2018). Computational microstructure characterization and reconstruction: Review of the state-of-the-art techniques. *Progress in Materials Science*, 95:1–41.

[52] Brahme, A., Alvi, M., Saylor, D., Fridy, J., and Rollett, A. (2006). 3d reconstruction of microstructure in a commercial purity aluminum. *Scripta Materialia*, 55(1):75–80.

[53] Bridier, F., McDowell, D. L., Villechaise, P., and Mendez, J. (2009). Crystal plasticity modeling of slip activity in ti–6al–4v under high cycle fatigue loading. *International Journal of Plasticity*, 25(6):1066–1082.

[54] Briffod, F., Bleuset, A., Shiraiwa, T., and Enoki, M. (2019). Effect of crystallographic orientation and geometrical compatibility on fatigue crack initiation and propagation in rolled ti-6al-4v alloy. *Acta Materialia*, 177:56–67.

[55] Briffod, F., Shiraiwa, T., and Enoki, M. (2021). Micromechanical investigation of the effect of the crystal orientation on the local deformation path and ductile void nucleation in dual-phase steels. *Materials Science and Engineering: A*, 826:141933.

[56] Brindley, K. A., Priddy, M. W., and Neu, R. W. (2019). Integrative materials design of three-phase mo-si-b alloys. *Integrating Materials and Manufacturing Innovation*, 8(1):1–16.

[57] Brown, S. and Bruce, N. (1995). Three-dimensional cellular automaton models of microstructural evolution during solidification. *Journal of Materials Science*, 30(5):1144–1150.

[58] Burke, J. and Turnbull, D. (1952). Recrystallization and grain growth. *Progress in Metal Physics*, 3:220–292.

[59] Busso, E. P. and McClintock, F. A. (1996). A dislocation mechanics-based crystallographic model of a b2-type intermetallic alloy. *International Journal of Plasticity*, 12(1):1–28.

[60] Cahn, J. and Hoffman, D. (1974). A vector thermodlnamics for anisotropic surfaces—ii. curved and faceted surfaces. *Acta Metallurgica*, 22(10):1205–1214.

[61] Cahn, J. W. (1961). On spinodal decomposition. *Acta Metallurgica*, 9(9):795–801.

[62] Cai, W., Sun, C., Wang, C., Qian, L., Li, Y., and Fu, M. (2022). Modelling of the intergranular fracture of twip steels working at high temperature by using czm–cpfe method. *International Journal of Plasticity*, 156:103366.

[63] Cang, R., Li, H., Yao, H., Jiao, Y., and Ren, Y. (2018). Improving direct physical properties prediction of heterogeneous materials from imaging data via convolutional neural network and a morphology-aware generative model. *Computational Materials Science*, 150:212–221.

[64] Cang, R., Xu, Y., Chen, S., Liu, Y., Jiao, Y., and Yi Ren, M. (2017). Microstructure representation and reconstruction of heterogeneous materials via deep belief network for computational material design. *Journal of Mechanical Design*, 139(7):071404.

[65] Chan, H., Cherukara, M., Loeffler, T. D., Narayanan, B., and Sankaranarayanan, S. K. (2020). Machine learning enabled autonomous microstructural characterization in 3d samples. *npj Computational Materials*, 6(1):1–9.

[66] Chapman, D., Thomlinson, W., Johnston, R., Washburn, D., Pisano, E., Gmür, N., Zhong, Z., Menk, R., Arfelli, F., and Sayers, D. (1997). Diffraction enhanced x-ray imaging. *Physics in Medicine & Biology*, 42(11):2015.

[67] Chaves, E. W. (2013). *Notes on continuum mechanics*. Springer Science & Business Media.

[68] Chen, J., Gao, H., Hu, X., Yang, L., Ke, D., Liu, X., Yan, S., Lu, R., and Misra, R. (2020). The significant size effect on nucleation and propagation of crack during tensile deformation of copper foil: Free surface roughening and crystallography study. *Materials Science and Engineering: A*, 790:139678.

[69] Chen, L.-Q. (2002). Phase-field models for microstructure evolution. *Annual Review of Materials Research*, 32(1):113–140.

[70] Chen, P., Ghassemi-Armaki, H., Kumar, S., Bower, A., Bhat, S., and Sadagopan, S. (2014). Microscale-calibrated modeling of the deformation response of dual-phase steels. *Acta Materialia*, 65:133–149.

[71] Chen, S., Kirubanandham, A., Chawla, N., and Jiao, Y. (2016). Stochastic multi-scale reconstruction of 3d microstructure consisting of polycrystalline grains and second-phase particles from 2d micrographs. *Metallurgical and Materials Transactions A*, 47(3):1440–1450.

[72] Chen, T., Sakidja, R., Ching, W.-Y., and Zhou, C. (2019). Crystal plasticity modeling of void growth on grain boundaries in ni-based superalloys. *JOM*, 71(11):3859–3868.

[73] Choi, S.-H., Kim, E.-Y., Woo, W., Han, S., and Kwak, J. (2013). The effect of crystallographic orientation on the micromechanical deformation and failure behaviors of dp980 steel during uniaxial tension. *International Journal of Plasticity*, 45:85–102.

[74] Chowdhury, S. G., Datta, S., Kumar, B. R., De, P., and Ghosh, R. (2007). Randomization of texture during recrystallization of austenite in a cold rolled metastable austenitic stainless steel. *Materials Science and Engineering: A*, 443(1-2):114–119.

[75] Christodoulou, P. G., Dancette, S., Lebensohn, R. A., Maire, E., and Beyerlein, I. J. (2021). Role of crystallographic orientation on intragranular void growth in polycrystalline fcc materials. *International Journal of Plasticity*, 147:103104.

[76] Chung, S.-Y. and Han, T.-S. (2010). Reconstruction of random two-phase polycrystalline solids using low-order probability functions and evaluation of mechanical behavior. *Computational Materials Science*, 49(4):705–719.

[77] Cloetens, P., Barrett, R., Baruchel, J., Guigay, J.-P., and Schlenker, M. (1996). Phase objects in synchrotron radiation hard x-ray imaging. *Journal of Physics D: Applied Physics*, 29(1):133.

[78] Cloetens, P., Ludwig, W., Baruchel, J., Van Dyck, D., Van Landuyt, J., Guigay, J., and Schlenker, M. (1999). Holotomography: Quantitative phase tomography with micrometer resolution using hard synchrotron radiation x rays. *Applied Physics Letters*, 75(19):2912–2914.

[79] Cloetens, P., Pateyron-Salomé, M., Buffiere, J., Peix, G., Baruchel, J., Peyrin, F., and Schlenker, M. (1997). Observation of microstructure and damage in materials by phase sensitive radiography and tomography. *Journal of Applied Physics*, 81(9):5878–5886.

[80] Cordero, N., Forest, S., Busso, E. P., Berbenni, S., and Cherkaoui, M. (2012). Grain size effects on plastic strain and dislocation density tensor fields in metal polycrystals. *Computational Materials Science*, 52(1):7–13.

[81] Cortie, M. (1993). Simulation of metal solidification using a cellular automaton. *Metallurgical Transactions B*, 24(6):1045–1053.

[82] Coutinho, Y., Rooney, S., and Payton, E. (2017). Analysis of ebsd grain size measurements using microstructure simulations and a customizable pattern matching library for grain perimeter estimation. *Metallurgical and Materials Transactions A*, 48(5):2375–2395.

[83] Cullity, B. and Stock, S. (2001). Elements of x-ray diffraction third edition. *Prenrice hall, New Jersey*.

[84] Dai, M., Demirel, M. F., Liang, Y., and Hu, J.-M. (2021). Graph neural networks for an accurate and interpretable prediction of the properties of polycrystalline materials. *npj Computational Materials*, 7(1):1–9.

[85] De Bonet, J. S. (1997). Multiresolution sampling procedure for analysis and synthesis of texture images. In *Proceedings of the 24th annual conference on Computer graphics and interactive techniques*, pages 361–368.

[86] de Oca Zapiain, D. M., Lim, H., Park, T., and Pourboghrat, F. (2022). Predicting plastic anisotropy using crystal plasticity and bayesian neural network surrogate models. *Materials Science and Engineering: A*, 833:142472.

[87] DeHoff, R. T. and Patterson, B. R. (2020). Topological event rates and the evolution of the grain face distribution in grain growth. *Acta Materialia*, 201:403–411.

[88] Deka, D., Joseph, D. S., Ghosh, S., and Mills, M. J. (2006). Crystal plasticity modeling of deformation and creep in polycrystalline ti-6242. *Metallurgical and Materials Transactions A*, 37(5):1371–1388.

[89] Delannay, L., Jacques, P. J., and Kalidindi, S. R. (2006). Finite element modeling of crystal plasticity with grains shaped as truncated octahedrons. *International Journal of Plasticity*, 22(10):1879–1898.

[90] Depriester, D. and Kubler, R. (2019). Radical voronoï tessellation from random pack of polydisperse spheres: Prediction of the cells' size distribution. *Computer-Aided Design*, 107:37–49.

[91] Diard, O., Leclercq, S., Rousselier, G., and Cailletaud, G. (2005). Evaluation of finite element based analysis of 3d multicrystalline aggregates plasticity: Application to crystal plasticity model identification and the study of stress and strain fields near grain boundaries. *International Journal of Plasticity*, 21(4):691–722.

[92] Diehl, M., Niehuesbernd, J., and Bruder, E. (2019). Quantifying the contribution of crystallographic texture and grain morphology on the elastic and plastic anisotropy of bcc steel. *Metals*, 9(12):1252.

[93] Dillon, S. J., Lee, S., Rollett, A. D., and Rohrer, G. S. (2008). Measuring the five parameter grain boundary character distribution from three-dimensional orientation maps. *Microscopy and Microanalysis*, 14(S2):978–979.

[94] Dillon, S. J. and Rohrer, G. S. (2009). Characterization of the grain-boundary character and energy distributions of yttria using automated serial sectioning and ebsd in the fib. *Journal of the American Ceramic Society*, 92(7):1580–1585.

[95] Ding, R. and Guo, Z. X. (2002). Microstructural modelling of dynamic recrystallisation using an extended cellular automaton approach. *Computational Materials Science*, 23(1-4):209–218.

[96] Dingreville, R., Karnesky, R. A., Puel, G., and Schmitt, J.-H. (2016). Review of the synergies between computational modeling and experimental characterization of materials across length scales. *Journal of Materials Science*, 51(3):1178–1203.

[97] Döbrich, K., Rau, C., and Krill, C. (2004). Quantitative characterization of the three-dimensional microstructure of polycrystalline al-sn using x-ray microtomography. *Metallurgical and Materials Transactions A*, 35(7):1953–1961.

[98] Doherty, R., Hughes, D., Humphreys, F., Jonas, J. J., Jensen, D. J., Kassner, M., King, W., McNelley, T., McQueen, H., and Rollett, A. (1997). Current issues in recrystallization: a review. *Materials Science and Engineering: A*, 238(2):219–274.

[99] Dunn, D. and Hull, R. (1999). Reconstruction of three-dimensional chemistry and geometry using focused ion beam microscopy. *Applied Physics Letters*, 75(21):3414–3416.

[100] Efros, A. A. and Freeman, W. T. (2001). Image quilting for texture synthesis and transfer. In *Proceedings of the 28th annual conference on Computer graphics and interactive techniques*, pages 341–346.

[101] Efros, A. A. and Leung, T. K. (1999). Texture synthesis by non-parametric sampling. In *Proceedings of the seventh IEEE international conference on computer vision*, volume 2, pages 1033–1038. IEEE.

[102] Elsey, M., Esedo [gbar] lu, S., and Smereka, P. (2011). Large-scale simulations and parameter study for a simple recrystallization model. *Philosophical Magazine*, 91(11):1607–1642.

[103] Elsey, M., Esedog, S., Smereka, P., et al. (2009). Diffusion generated motion for grain growth in two and three dimensions. *Journal of Computational Physics*, 228(21):8015–8033.

[104] Engler, O. and Randle, V. (2009). *Introduction to texture analysis: macrotexture, microtexture, and orientation mapping*. CRC press.

[105] Fan, D. and Chen, L.-Q. (1997). Computer simulation of grain growth using a continuum field model. *Acta Materialia*, 45(2):611–622.

[106] Fan, D., Chen, S., and Chen, L.-Q. (1999). Computer simulation of grain growth kinetics with solute drag. *Journal of Materials Research*, 14(3):1113–1123.

[107] Fan, Y., Yang, X., Shi, D., Tan, L., and Huang, W. (2021). Quantitative mapping of service process-microstructural degradation-property deterioration for a ni-based superalloy based on chord length distribution imaging process. *Materials & Design*, 203:109561.

[108] Fan, Z., Wu, Y., Zhao, X., and Lu, Y. (2004). Simulation of polycrystalline structure with voronoi diagram in laguerre geometry based on random closed packing of spheres. *Computational Materials Science*, 29(3):301–308.

[109] Farjas, J. and Roura, P. (2006). Modification of the kolmogorov–johnson–mehl–avrami rate equation for non-isothermal experiments and its analytical solution. *Acta Materialia*, 54(20):5573–5579.

[110] Feltham, P. (1957). Grain growth in metals. *Acta Metallurgica*, 5(2):97–105.

[111] Fernandez-Zelaia, P., Kirka, M. M., Rossy, A. M., Lee, Y., and Dryepondt, S. N. (2021). Nickel-based superalloy single crystals fabricated via electron beam melting. *Acta Materialia*, 216:117133.

[112] Fernandez-Zelaia, P. and Melkote, S. N. (2019). Process-structure-property modeling for severe plastic deformation processes using orientation imaging microscopy and data-driven techniques. *Integrating Materials and Manufacturing Innovation*, 8(1):17–36.

[113] Foster, R. C., Vander Wiel, S., Anghel, V., and Bronkhorst, C. (2021). Towards random generation of microstructures of spatially varying materials from orthogonal sections. *Computational Materials Science*, 192:110313.

[114] Fritzen, F., Böhlke, T., and Schnack, E. (2009). Periodic three-dimensional mesh generation for crystalline aggregates based on voronoi tessellations. *Computational Mechanics*, 43(5):701–713.

[115] Fuchizaki, K., Kusaba, T., and Kawasaki, K. (1995). Computer modelling of three-dimensional cellular pattern growth. *Philosophical Magazine B*, 71(3):333–357.

[116] Fullwood, D. T., Niezgoda, S. R., Adams, B. L., and Kalidindi, S. R. (2010). Microstructure sensitive design for performance optimization. *Progress in Materials Science*, 55(6):477–562.

[117] Fullwood, D. T., Niezgoda, S. R., and Kalidindi, S. R. (2008). Microstructure reconstructions from 2-point statistics using phase-recovery algorithms. *Acta Materialia*, 56(5):942–948.

[118] Furu, T., Marthinsen, K., and Nes, E. (1990). Modelling recrystallisation. *Materials Science and Technology*, 6(11):1093–1102.

[119] Galán-López, J. and Hidalgo, J. (2020). Use of the correlation between grain size and crystallographic orientation in crystal plasticity simulations: Application to aisi 420 stainless steel. *Crystals*, 10(9):819.

[120] Ganesan, S., Javaheri, I., and Sundararaghavan, V. (2021). Constrained voronoi models for interpreting surface microstructural measurements. *Mechanics of Materials*, 159:103892.

[121] Gao, H. and Huang, Y. (2003). Geometrically necessary dislocation and size-dependent plasticity. *Scripta Materialia*, 48(2):113–118.

[122] Gao, X., Przybyla, C., and Adams, B. (2006). Methodology for recovering and analyzing two-point pair correlation functions in polycrystalline materials. *Metallurgical and Materials Transactions A*, 37(8):2379–2387.

[123] Gardet, C., Le Ravalec, M., and Gloaguen, E. (2016). Pattern-based conditional simulation with a raster path: a few techniques to make it more efficient. *Stochastic Environmental Research and Risk Assessment*, 30(2):429–446.

[124] Ghosh, S., Bhandari, Y., and Groeber, M. (2008). Cad-based reconstruction of 3d polycrystalline alloy microstructures from fib generated serial sections. *Computer-Aided Design*, 40(3):293–310.

[125] Ghosh, S. and Dimiduk, D. (2011). *Computational methods for microstructure-property relationships*, volume 1. Springer.

[126] Ghosh, S., Weber, G., and Keshavarz, S. (2016). Multiscale modeling of polycrystalline nickel-based superalloys accounting for subgrain microstructures. *Mechanics Research Communications*, 78:34–46.

[127] Gilbert, E. (1962). Random subdivisions of space into crystals. *The Annals of Mathematical Statistics*, 33(3):958–972.

[128] Gjostein, N. A. and Rhines, F. (1959). Absolute interfacial energies of [001] tilt and twist grain boundaries in copper. *Acta Metallurgica*, 7(5):319–330.

[129] Glavicic, M. and Semiatin, S. (2006). X-ray line-broadening investigation of deformation during hot rolling of ti–6al–4v with a colony-alpha microstructure. *Acta Materialia*, 54(20):5337–5347.

[130] Gleiter, H. (1983). On the structure of grain boundaries in metals. *Atomistics of Fracture*, pages 433–464.

[131] Goh, C.-H., Wallace, J., Neu, R., and McDowell, D. (2001). Polycrystal plasticity simulations of fretting fatigue. *International Journal of Fatigue*, 23:423–435.

[132] Gorgannejad, S., Gahrooei, M. R., Paynabar, K., and Neu, R. (2019). Quantitative prediction of the aged state of ni-base superalloys using pca and tensor regression. *Acta Materialia*, 165:259–269.

[133] Gottstein, G. and Shvindlerman, L. S. (2009). *Grain boundary migration in metals: thermodynamics, kinetics, applications*. CRC press.

[134] Groeber, M., Ghosh, S., Uchic, M. D., and Dimiduk, D. M. (2008a). A framework for automated analysis and simulation of 3d polycrystalline microstructures.: Part 1: Statistical characterization. *Acta Materialia*, 56(6):1257–1273.

[135] Groeber, M., Ghosh, S., Uchic, M. D., and Dimiduk, D. M. (2008b). A framework for automated analysis and simulation of 3d polycrystalline microstructures. part 2: Synthetic structure generation. *Acta Materialia*, 56(6):1274–12872.

[136] Groeber, M. A., Haley, B., Uchic, M. D., Dimiduk, D. M., and Ghosh, S. (2006). 3d reconstruction and characterization of polycrystalline microstructures using a fib–sem system. *Materials Characterization*, 57(4-5):259–273.

[137] Groeber, M. A. and Jackson, M. A. (2014). Dream. 3d: a digital representation environment for the analysis of microstructure in 3d. *Integrating Materials and Manufacturing Innovation*, 3(1):56–72.

[138] Gulsoy, E., Simmons, J., and De Graef, M. (2009). Application of joint histogram and mutual information to registration and data fusion problems in serial sectioning microstructure studies. *Scripta Materialia*, 60(6):381–384.

[139] Hallberg, H. (2011). Approaches to modeling of recrystallization. *Metals*, 1(1):16–48.

[140] Hallberg, H., Wallin, M., and Ristinmaa, M. (2010). Simulation of discontinuous dynamic recrystallization in pure cu using a probabilistic cellular automaton. *Computational Materials Science*, 49(1):25–34.

[141] Han, Z., Zhang, L., Azzam, R., Zhou, J., and Wang, S. (2021). A statistical index indicating the degree and mechanical effects of grain size heterogeneity in rocks. *Engineering Geology*, 293:106292.

[142] Hardy, G. B. and Field, D. P. (2016). Reliability of twin-dependent triple junction distributions measured from a section plane. *Acta Materialia*, 103:809–822.

[143] Hart, K. A. and Rimoli, J. J. (2020). Microstructpy: A statistical microstructure mesh generator in python. *SoftwareX*, 12:100595.

[144] Hasan, M. and Acar, P. (2022). Uncertainty quantification of metallic microstructures with analytical and machine learning based approaches. *AIAA Journal*, 60(1):461–472.

[145] Hasson, G., Boos, J.-Y., Herbeuval, I., Biscondi, M., and Goux, C. (1972). Theoretical and experimental determinations of grain boundary structures and energies: Correlation with various experimental results. *Surface Science*, 31:115–137.

[146] Hasson, G. and Goux, C. (1971). Interfacial energies of tilt boundaries in aluminium. experimental and theoretical determination. *Scripta Metallurgica*, 5(10):889–894.

[147] Heeger, D. J. and Bergen, J. R. (1995). Pyramid-based texture analysis/synthesis. In *Proceedings of the 22nd annual conference on Computer graphics and interactive techniques*, pages 229–238.

[148] Heinz, A. and Neumann, P. (1991). Representation of orientation and disorientation data for cubic, hexagonal, tetragonal and orthorhombic crystals. *Acta Crystallographica Section A: Foundations of Crystallography*, 47(6):780–789.

[149] Henrich, M., Pütz, F., and Münstermann, S. (2020). A novel approach to discrete representative volume element automation and generation-dragen. *Materials*, 13(8):1887.

[150] Herring, C. and Kingston, W. (1951). The physics of powder metallurgy. *WE Kingston, Edition: McGraw Hill, New York*.

[151] Herriott, C. and Spear, A. D. (2020). Predicting microstructure-dependent mechanical properties in additively manufactured metals with machine-and deep-learning methods. *Computational Materials Science*, 175:109599.

[152] Hesselbarth, H. W. and Göbel, I. (1991). Simulation of recrystallization by cellular automata. *Acta Metallurgica et Materialia*, 39(9):2135–2143.

[153] Hillert, M. (1965). On the theory of normal and abnormal grain growth. *Acta Metallurgica*, 13(3):227–238.

[154] Hoffimann, J., Scheidt, C., Barfod, A., and Caers, J. (2017). Stochastic simulation by image quilting of process-based geological models. *Computers & Geosciences*, 106:18–32.

[155] Hoffman, D. W. and Cahn, J. W. (1972). A vector thermodynamics for anisotropic surfaces: I. fundamentals and application to plane surface junctions. *Surface Science*, 31:368–388.

[156] Holm, E. A. and Battaile, C. C. (2001). The computer simulation of microstructural evolution. *Jom*, 53(9):20–23.

[157] Holzer, L., Muench, B., Wegmann, M., Gasser, P., and Flatt, R. J. (2006). Fib-nanotomography of particulate systems—part i: Particle shape and topology of interfaces. *Journal of the American Ceramic Society*, 89(8):2577–2585.

[158] Hoppe, H., DeRose, T., Duchamp, T., McDonald, J., and Stuetzle, W. (1992). Surface reconstruction from unorganized points. In *Proceedings of the 19th annual conference on computer graphics and interactive techniques*, pages 71–78.

[159] Horstemeyer, M. F. (2018). *Integrated computational materials engineering (ICME) for metals: concepts and case studies*. John Wiley & Sons.

[160] Huang, M. (2005). The n-point orientation correlation function and its application. *International Journal of Solids and Structures*, 42(5-6):1425–1441.

[161] Hughes, D., Hansen, N., and Bammann, D. (2003). Geometrically necessary boundaries, incidental dislocation boundaries and geometrically necessary dislocations. *Scripta Materialia*, 48(2):147–153.

[162] Humphreys, F. (1992). Modelling mechanisms and microstructures of recrystallisation. *Materials Science and Technology*, 8(2):135–144.

[163] Humphreys, F. (1997). A unified theory of recovery, recrystallization and grain growth, based on the stability and growth of cellular microstructures—i. the basic model. *Acta Materialia*, 45(10):4231–4240.

[164] Humphreys, F. (1999). Quantitative metallography by electron backscattered diffraction. *Journal of Microscopy*, 195(3):170–185.

[165] Humphreys, F. J. and Hatherly, M. (2012). *Recrystallization and related annealing phenomena*. Elsevier.

[166] Humphreys, J. F. (1993). A microstructural model of recrystallization. In *Materials Science Forum*, volume 113, pages 329–334. Trans Tech Publ.

[167] Hundert, O., Nes, E., and Ryum, N. (1989). On the zener drag—addendum. *Acta Metallurgica*, 37(1):129–133.

[168] Ice, G. E., Budai, J. D., and Pang, J. W. (2011). The race to x-ray microbeam and nanobeam science. *Science*, 334(6060):1234–1239.

[169] Ice, G. E. and Larson, B. C. (2000). 3d x-ray crystal microscope. *Advanced Engineering Materials*, 2(10):643–646.

[170] Ilin, D. N. and Bernacki, M. (2016). Advancing layer algorithm of dense ellipse packing for generating statistically equivalent polygonal structures. *Granular Matter*, 18(3):43.

[171] Iskakov, A., Yabansu, Y. C., Rajagopalan, S., Kapustina, A., and Kalidindi, S. R. (2018). Application of spherical indentation and the materials knowledge system framework to establishing microstructure-yield strength linkages from carbon steel scoops excised from high-temperature exposed components. *Acta Materialia*, 144:758–767.

[172] Ivasishin, O., Shevchenko, S., Vasiliev, N., and Semiatin, S. (2006). A 3-d monte-carlo (potts) model for recrystallization and grain growth in polycrystalline materials. *Materials Science and Engineering: A*, 433(1-2):216–232.

[173] Janssens, K. G. (2003). Random grid, three-dimensional, space-time coupled cellular automata for the simulation of recrystallization and grain growth. *Modelling and Simulation in Materials Science and Engineering*, 11(2):157.

[174] Janssens, K. G. F., Raabe, D., Kozeschnik, E., Miodownik, M. A., and Nestler, B. (2010). *Computational materials engineering: an introduction to microstructure evolution*. Academic Press.

[175] Javaheri, I., Andani, M. T., and Sundararaghavan, V. (2022). Large-scale synthesis of metal additively-manufactured microstructures using markov random fields. *Computational Materials Science*, 206:111228.

[176] Javaheri, I. and Sundararaghavan, V. (2020). Polycrystalline microstructure reconstruction using markov random fields and histogram matching. *Computer-Aided Design*, 120:102806.

[177] Jeulin, D. (1989). Morphological modeling of images by sequential random functions. *Signal Processing*, 16(4):403–431.

[178] Jiao, Y. and Chawla, N. (2014). Modeling and characterizing anisotropic inclusion orientation in heterogeneous material via directional cluster functions and stochastic microstructure reconstruction. *Journal of Applied Physics*, 115(9):093511.

[179] Jin, Y., Bernacki, M., Rohrer, G. S., Rollett, A. D., Lin, B., and Bozzolo, N. (2013). Formation of annealing twins during recrystallization and grain growth in 304l austenitic stainless steel. In *Materials Science Forum*, volume 753, pages 113–116. Trans Tech Publ.

[180] Jivkov, A., Stevens, N., and Marrow, T. (2006). A three-dimensional computational model for intergranular cracking. *Computational Materials Science*, 38(2):442–453.

[181] Johnson, G., King, A., Honnicke, M. G., Marrow, J., and Ludwig, W. (2008). X-ray diffraction contrast tomography: a novel technique for three-dimensional grain mapping of polycrystals. ii. the combined case. *Journal of Applied Crystallography*, 41(2):310–318.

[182] Johnson, W. A. (1939). Reaction kinetics in processes of nucleation and growth. *The American Institute of Mining, Metallurgical, and Petroleum Engineers*, 135:416–458.

[183] Kak, A. and Slaney, M. (1988). Principles of computerized tomographic imaging ieee press. *New York*.

[184] Kak, A. C. and Slaney, M. (2001). *Principles of computerized tomographic imaging*. SIAM.

[185] Kalidindi, S. R. (2015a). Data science and cyberinfrastructure: critical enablers for accelerated development of hierarchical materials. *International Materials Reviews*, 60(3):150–168.

[186] Kalidindi, S. R. (2015b). *Hierarchical materials informatics: novel analytics for materials data*. Elsevier.

[187] Kalidindi, S. R., Bronkhorst, C. A., and Anand, L. (1992). Crystallographic texture evolution in bulk deformation processing of fcc metals. *Journal of the Mechanics and Physics of Solids*, 40(3):537–569.

[188] Kammer, D., Mendoza, R., and Voorhees, P. (2006). Cylindrical domain formation in topologically complex structures. *Scripta Materialia*, 55(1):17–22.

[189] Kammer, D. and Voorhees, P. (2008). Analysis of complex microstructures: Serial sectioning and phase-field simulations. *MRS Bulletin*, 33(6):603–610.

[190] Kaub, T. M., DeHoff, R. T., and Patterson, B. R. (2021). Evaluation of stereological strategies for estimating mean volume, number per unit volume, and grain volume distribution: The disector and selector methods. *Metallurgical and Materials Transactions A*, 52(10):4379–4394.

[191] Kawasaki, K., Nagai, T., and Nakashima, K. (1989). Vertex models for two-dimensional grain growth. *Philosophical Magazine B*, 60(3):399–421.

[192] Keller, C., Calvat, M., Flipon, B., and Barbe, F. (2022). Experimental and numerical investigations of plastic strain mechanisms of aisi 316l alloys with bimodal grain size distribution. *International Journal of Plasticity*, 153:103246.

[193] Keller, T., Cutler, B., Lazar, E. A., Yauney, G., and Lewis, D. J. (2014). Comparative grain topology. *Acta Materialia*, 66:414–423.

[194] Kelly, T. F. and Miller, M. K. (2007). Atom probe tomography. *Review of Scientific Instruments*, 78(3):031101.

[195] Keshavarz, S. and Ghosh, S. (2015). Hierarchical crystal plasticity fe model for nickel-based superalloys: Sub-grain microstructures to polycrystalline aggregates. *International Journal of Solids and Structures*, 55:17–31.

[196] Khosravani, A., Cecen, A., and Kalidindi, S. R. (2017). Development of high throughput assays for establishing process-structure-property linkages in multiphase polycrystalline metals: Application to dual-phase steels. *Acta Materialia*, 123:55–69.

[197] Kim, C.-S., Rollett, A. D., and Rohrer, G. S. (2006a). Grain boundary planes: New dimensions in the grain boundary character distribution. *Scripta Materialia*, 54(6):1005–1009.

[198] Kim, H., Yamamoto, T., Sato, Y., and Inoue, J. (2019). Establishment of structure-property linkages using a bayesian model selection method: Application to a dual-phase metallic composite system. *Acta Materialia*, 176:264–277.

[199] Kim, S. G., Kim, D. I., Kim, W. T., and Park, Y. B. (2006b). Computer simulations of two-dimensional and three-dimensional ideal grain growth. *Physical Review E*, 74(6):061605.

[200] Kim, Y., Park, H. K., Jung, J., Asghari-Rad, P., Lee, S., Kim, J. Y., Jung, H. G., and Kim, H. S. (2021). Exploration of optimal microstructure and mechanical properties in continuous microstructure space using a variational autoencoder. *Materials & Design*, 202:109544.

[201] King, A., Herbig, M., Ludwig, W., Reischig, P., Lauridsen, E., Marrow, T., and Buffière, J. (2010). Non-destructive analysis of micro texture and grain boundary character from x-ray diffraction contrast tomography. *Nuclear Instruments and Methods in Physics Research Section B: Beam Interactions with Materials and Atoms*, 268(3-4):291–296.

[202] King, A., Johnson, G., Engelberg, D., Ludwig, W., and Marrow, J. (2008). Observations of intergranular stress corrosion cracking in a grain-mapped polycrystal. *Science*, 321(5887):382–385.

[203] Kobayashi, S., Tsurekawa, S., Watanabe, T., and Palumbo, G. (2010). Grain boundary engineering for control of sulfur segregation-induced embrittlement in ultrafine-grained nickel. *Scripta Materialia*, 62(5):294–297.

[204] Köhnen, P., Létang, M., Voshage, M., Schleifenbaum, J. H., and Haase, C. (2019). Understanding the process-microstructure correlations for tailoring the mechanical properties of l-pbf produced austenitic advanced high strength steel. *Additive Manufacturing*, 30:100914.

[205] Kolmogorov, A. N. (1937). On the statistical theory of the crystallization of metals. *Bull. Acad. Sci. USSR, Math. Ser*, 1(3):355–359.

[206] Kondo, R., Yamakawa, S., Masuoka, Y., Tajima, S., and Asahi, R. (2017). Microstructure recognition using convolutional neural networks for prediction of ionic conductivity in ceramics. *Acta Materialia*, 141:29–38.

[207] Kotha, S., Ozturk, D., and Ghosh, S. (2019). Parametrically homogenized constitutive models (phcms) from micromechanical crystal plasticity fe simulations, part i: Sensitivity analysis and parameter identification for titanium alloys. *International Journal of Plasticity*, 120:296–319.

[208] Kotha, S., Ozturk, D., Smarslok, B., and Ghosh, S. (2020). Uncertainty quantified parametrically homogenized constitutive models for microstructure-integrated structural simulations. *Integrating Materials and Manufacturing Innovation*, 9(4):322–338.

[209] Kral, M., Mangan, M., Spanos, G., and Rosenberg, R. (2000). Three-dimensional analysis of microstructures. *Materials Characterization*, 45(1):17–23.

[210] Kral, M. and Spanos, G. (1999). Three-dimensional analysis of proeutectoid cementite precipitates. *Acta Materialia*, 47(2):711–724.

[211] Krill Iii, C. and Chen, L.-Q. (2002). Computer simulation of 3-d grain growth using a phase-field model. *Acta Materialia*, 50(12):3059–3075.

[212] Kronberg, M. and Wilson, u. F. (1949). Secondary recrystallization in copper. *JOM*, 1(8):501–514.

[213] Kugler, G. and Turk, R. (2006). Study of the influence of initial microstructure topology on the kinetics of static recrystallization using a cellular automata model. *Computational Materials Science*, 37(3):284–291.

[214] Kühbach, M., Gottstein, G., and Barrales-Mora, L. (2016). A statistical ensemble cellular automaton microstructure model for primary recrystallization. *Acta Materialia*, 107:366–376.

[215] Kuhn, J., Schneider, M., Sonnweber-Ribic, P., and Böhlke, T. (2020). Fast methods for computing centroidal laguerre tessellations for prescribed volume fractions with applications to microstructure generation of polycrystalline materials. *Computer Methods in Applied Mechanics and Engineering*, 369:113175.

[216] Kumar, A., Nguyen, L., DeGraef, M., and Sundararaghavan, V. (2016). A markov random field approach for microstructure synthesis. *Modelling and Simulation in Materials Science and Engineering*, 24(3):035015.

[217] Kumar, S. and Kurtz, S. K. (1994). Simulation of material microstructure using a 3d voronoi tesselation: Calculation of effective thermal expansion coefficient of polycrystalline materials. *Acta Metallurgica et Materialia*, 42(12):3917–3927.

[218] Kumar, S., Kurtz, S. K., and Agarwala, V. K. (1996). Micro-stress distribution within polycrystalline aggregate. *Acta Mechanica*, 114(1):203–216.

[219] Kupka, D., Huber, N., and Lilleodden, E. (2014). A combined experimental-numerical approach for elasto-plastic fracture of individual grain boundaries. *Journal of the Mechanics and Physics of Solids*, 64:455–467.

[220] Lan, Y., Xiao, N., Li, D., and Li, Y. (2005). Mesoscale simulation of deformed austenite decomposition into ferrite by coupling a cellular automaton method with a crystal plasticity finite element model. *Acta Materialia*, 53(4):991–1003.

[221] Larson, B., Yang, W., Ice, G., Budai, J., and Tischler, J. (2002). Three-dimensional x-ray structural microscopy with submicrometre resolution. *Nature*, 415(6874):887–890.

[222] Latypov, M. I., Khan, A., Lang, C. A., Kvilekval, K., Polonsky, A. T., Echlin, M. P., Beyerlein, I. J., Manjunath, B., and Pollock, T. M. (2019). Bisque for 3d materials science in the cloud: microstructure–property linkages. *Integrating Materials and Manufacturing Innovation*, 8(1):52–65.

[223] Latypov, M. I., Kühbach, M., Beyerlein, I. J., Stinville, J.-C., Toth, L. S., Pollock, T. M., and Kalidindi, S. R. (2018). Application of chord length distributions and principal component analysis for quantification and representation of diverse polycrystalline microstructures. *Materials Characterization*, 145:671–685.

[224] Lauridsen, E. M., Schmidt, S., Suter, R., and Poulsen, H. F. (2001). Tracking: a method for structural characterization of grains in powders or polycrystals. *Journal of Applied Crystallography*, 34(6):744–750.

[225] Lavergne, F., Brenner, R., and Sab, K. (2013). Effects of grain size distribution and stress heterogeneity on yield stress of polycrystals: A numerical approach. *Computational Materials Science*, 77:387–398.

[226] Lee, E. H. (1969). Elastic-plastic deformation at finite strains.

[227] Levine, L. E., Larson, B. C., Yang, W., Kassner, M. E., Tischler, J. Z., Delos-Reyes, M. A., Fields, R. J., and Liu, W. (2006). X-ray microbeam measurements of individual dislocation cell elastic strains in deformed single-crystal copper. *Nature Materials*, 5(8):619–622.

[228] Lewiner, T., Lopes, H., Vieira, A. W., and Tavares, G. (2003). Efficient implementation of marching cubes' cases with topological guarantees. *Journal of Graphics Tools*, 8(2):1–15.

[229] Lewis, A., Bingert, J., Rowenhorst, D., Gupta, A., Geltmacher, A., and Spanos, G. (2006). Two-and three-dimensional microstructural characterization of a super-austenitic stainless steel. *Materials Science and Engineering: A*, 418(1-2):11–18.

[230] Lewis, A. and Geltmacher, A. (2006). Image-based modeling of the response of experimental 3d microstructures to mechanical loading. *Scripta Materialia*, 55(1):81–85.

[231] Lewis, A., Qidwai, S., Rowenhorst, D., and Geltmacher, A. (2011). Correlation between crystallographic orientation and mechanical response in a three-dimensional β-ti microstructure. *Journal of Materials Research*, 26(8):957–964.

[232] Li, D. (2014). Review of structure representation and reconstruction on mesoscale and microscale. *Jom*, 66(3):444–454.

[233] Li, D.-F., Davies, C. M., Zhang, S.-Y., Dickinson, C., and O'Dowd, N. P. (2013). The effect of prior deformation on subsequent microplasticity and damage evolution in an austenitic stainless steel at elevated temperature. *Acta Materialia*, 61(10):3575–3584.

[234] Li, D.-F. and O'Dowd, N. P. (2011). On the evolution of lattice deformation in austenitic stainless steels—the role of work hardening at finite strains. *Journal of the Mechanics and Physics of Solids*, 59(12):2421–2441.

[235] Li, D.-F. and O'Dowd, N. P. (2012). Investigating ductile failure at the microscale in engineering steels: A micromechanical finite element model. In *Pressure Vessels and Piping Conference*, volume 55058, pages 137–143. American Society of Mechanical Engineers.

[236] Li, D.-F., O'Dowd, N. P., Davies, C. M., and Zhang, S.-Y. (2011). Microscale prediction of deformation in an austenitic stainless steel under uniaxial loading. *European Journal of Mechanics-A/Solids*, 30(5):748–760.

[237] Li, J., Dillon, S. J., and Rohrer, G. S. (2009). Relative grain boundary area and energy distributions in nickel. *Acta Materialia*, 57(14):4304–4311.

[238] Li, M., Ghosh, S., Richmond, O., Weiland, H., and Rouns, T. (1999). Three dimensional characterization and modeling of particle reinforced metal matrix composites: part i: quantitative description of microstructural morphology. *Materials Science and Engineering: A*, 265(1-2):153–173.

[239] Li, S. and Suter, R. (2013). Adaptive reconstruction method for three-dimensional orientation imaging. *Journal of Applied Crystallography*, 46(2):512–524.

[240] Li, X., Mariethoz, G., Lu, D., and Linde, N. (2016). Patch-based iterative conditional geostatistical simulation using graph cuts. *Water Resources Research*, 52(8):6297–6320.

[241] Li, X., Zhang, Y., Zhao, H., Burkhart, C., Brinson, L. C., and Chen, W. (2018). A transfer learning approach for microstructure reconstruction and structure-property predictions. *Scientific Reports*, 8(1):1–13.

[242] Li, Z., Wen, B., and Zabaras, N. (2010). Computing mechanical response variability of polycrystalline microstructures through dimensionality reduction techniques. *Computational Materials Science*, 49(3):568–581.

[243] Lieberman, E., Rollett, A., Lebensohn, R., and Kober, E. (2015). Calculation of grain boundary normals directly from 3d microstructure images. *Modelling and Simulation in Materials Science and Engineering*, 23(3):035005.

[244] Link, T., Zabler, S., Epishin, A., Haibel, A., Bansal, M., and Thibault, X. (2006). Synchrotron tomography of porosity in single-crystal nickel-base superalloys. *Materials Science and Engineering: A*, 425(1-2):47–54.

[245] Liu, L., Ding, Q., Zhong, Y., Zou, J., Wu, J., Chiu, Y.-L., Li, J., Zhang, Z., Yu, Q., and Shen, Z. (2018a). Dislocation network in additive manufactured steel breaks strength–ductility trade-off. *Materials Today*, 21(4):354–361.

[246] Liu, R., Kumar, A., Chen, Z., Agrawal, A., Sundararaghavan, V., and Choudhary, A. (2015a). A predictive machine learning approach for microstructure optimization and materials design. *Scientific Reports*, 5(1):1–12.

[247] Liu, T., Xia, S., Zhou, B., Bai, Q., and Rohrer, G. S. (2017). Three-dimensional characteristics of the grain boundary networks of conventional and grain boundary engineered 316l stainless steel. *Materials Characterization*, 133:60–69.

[248] Liu, T., Xia, S., Zhou, B., Bai, Q., and Rohrer, G. S. (2018b). Three-dimensional geometrical and topological characteristics of grains in conventional and grain boundary engineered 316l stainless steel. *Micron*, 109:58–70.

[249] Liu, W., Ice, G. E., Larson, B. C., Yang, W., Tischler, J. Z., and Budai, J. D. (2004). The three-dimensional x-ray crystal microscope: A new tool for materials characterization. *Metallurgical and Materials Transactions A*, 35(7):1963–1967.

[250] Liu, X. and Shapiro, V. (2015). Random heterogeneous materials via texture synthesis. *Computational Materials Science*, 99:177–189.

[251] Liu, Y., Cheng, L., Zeng, Q., Feng, Z., and Zhang, L. (2015b). Pclab–a software with interactive graphical user interface for monte carlo and finite element analysis of microstructure-based layered composites. *Advances in Engineering Software*, 90:53–62.

[252] Logé, R., Bernacki, M., Resk, H., Delannay, L., Digonnet, H., Chastel, Y., and Coupez, T. (2008). Linking plastic deformation to recrystallization in metals using digital microstructures. *Philosophical Magazine*, 88(30-32):3691–3712.

[253] Lorensen, W. E. and Cline, H. E. (1987). Marching cubes: A high resolution 3d surface construction algorithm. *Acm Siggraph Computer Graphics*, 21(4):163–169.

[254] Louat, N. (1974). On the theory of normal grain growth. *Acta Metallurgica*, 22(6):721–724.

[255] Louat, N. (1982). The resistance to normal grain growth from a dispersion of spherical particles. *Acta Metallurgica*, 30(7):1291–1294.

[256] Loughnane, G., Groeber, M., Uchic, M., Shah, M., Srinivasan, R., and Grandhi, R. (2014). Modeling the effect of voxel resolution on the accuracy of phantom grain ensemble statistics. *Materials Characterization*, 90:136–150.

[257] Ludwig, W. and Bellet, D. (2000). Penetration of liquid gallium into the grain boundaries of aluminium: a synchrotron radiation microtomographic investigation. *Materials Science and Engineering: A*, 281(1-2):198–203.

[258] Ludwig, W., King, A., Herbig, M., Reischig, P., Marrow, J., Babout, L., Lauridsen, E. M., Proudhon, H., and Buffiere, J.-Y. (2010). Characterization of polycrystalline materials using synchrotron x-ray imaging and diffraction techniques. *Jom*, 62(12):22–28.

[259] Ludwig, W., King, A., Reischig, P., Herbig, M., Lauridsen, E. M., Schmidt, S., Proudhon, H., Forest, S., Cloetens, P., Du Roscoat, S. R., et al. (2009a). New opportunities for 3d materials science of polycrystalline materials at the micrometre lengthscale by combined use of x-ray diffraction and x-ray imaging. *Materials Science and Engineering: A*, 524(1-2):69–76.

[260] Ludwig, W., Reischig, P., King, A., Herbig, M., Lauridsen, E., Johnson, G., Marrow, T., and Buffiere, J.-Y. (2009b). Three-dimensional grain mapping by x-ray diffraction contrast tomography and the use of friedel pairs in diffraction data analysis. *Review of Scientific Instruments*, 80(3):033905.

[261] Ludwig, W., Schmidt, S., Lauridsen, E. M., and Poulsen, H. F. (2008). X-ray diffraction contrast tomography: a novel technique for three-dimensional grain mapping of polycrystals. i. direct beam case. *Journal of Applied Crystallography*, 41(2):302–309.

[262] Lund, A. and Voorhees, P. W. (2003). A quantitative assessment of the three-dimensional microstructure of a γ- γ' alloy. *Philosophical Magazine*, 83(14):1719–1733.

[263] Mackenzie, J. (1958). Second paper on statistics associated with the random disorientation of cubes. *Biometrika*, 45(1-2):229–240.

[264] MacSleyne, J., Simmons, J., and De Graef, M. (2008). On the use of moment invariants for the automated analysis of 3d particle shapes. *Modelling and Simulation in Materials Science and Engineering*, 16(4):045008.

[265] Madej, Ł. and Sitko, M. (2014). Parallelization of the monte carlo static recrystallization model. In *eScience on Distributed Computing Infrastructure*, pages 445–458. Springer.

[266] Mahmud, K., Mariethoz, G., Caers, J., Tahmasebi, P., and Baker, A. (2014). Simulation of earth textures by conditional image quilting. *Water Resources Research*, 50(4):3088–3107.

[267] Mandal, S., Bhaduri, A., and Sarma, V. S. (2011). A study on microstructural evolution and dynamic recrystallization during isothermal deformation of a ti-modified austenitic stainless steel. *Metallurgical and Materials Transactions A*, 42(4):1062–1072.

[268] Mandal, S., Lao, J., Donegan, S., and Rollett, A. D. (2018). Generation of statistically representative synthetic three-dimensional microstructures. *Scripta Materialia*, 146:128–132.

[269] Mangal, A. and Holm, E. A. (2018). Applied machine learning to predict stress hotspots i: Face centered cubic materials. *International Journal of Plasticity*, 111:122–134.

[270] Mangal, A. and Holm, E. A. (2019). Applied machine learning to predict stress hotspots ii: Hexagonal close packed materials. *International Journal of Plasticity*, 114:1–14.

[271] Mann, A. and Kalidindi, S. R. (2022). Development of a robust cnn model for capturing microstructure-property linkages and building property closures supporting material design. *Frontiers in Materials*, 9.

[272] Margulies, L., Lorentzen, T., Poulsen, H., and Leffers, T. (2002). Strain tensor development in a single grain in the bulk of a polycrystal under loading. *Acta Materialia*, 50(7):1771–1779.

[273] Mariethoz, G. and Lefebvre, S. (2014). Bridges between multiple-point geostatistics and texture synthesis: Review and guidelines for future research. *Computers & Geosciences*, 66:66–80.

[274] Martin, G., Ochoa, N., Sai, K., Hervé-Luanco, E., and Cailletaud, G. (2014). A multiscale model for the elastoviscoplastic behavior of directionally solidified alloys: Application to fe structural computations. *International Journal of Solids and Structures*, 51(5):1175–1187.

[275] Martins, R. V., Margulies, L., Schmidt, S., Poulsen, H. F., and Leffers, T. (2004). Simultaneous measurement of the strain tensor of 10 individual grains embedded in an al tensile sample. *Materials Science and Engineering: A*, 387:84–88.

[276] Matouš, K., Geers, M. G., Kouznetsova, V. G., and Gillman, A. (2017). A review of predictive nonlinear theories for multiscale modeling of heterogeneous materials. *Journal of Computational Physics*, 330:192–220.

[277] Mazánová, V., Heczko, M., and Polák, J. (2022). On the mechanism of fatigue crack initiation in high-angle grain boundaries. *International Journal of Fatigue*, 158:106721.

[278] McEwen, B. F., Renken, C., Marko, M., and Mannella, C. (2008). Principles and practice in electron tomography. *Methods in Cell Biology*, 89:129–168.

[279] Meissonnier, F., Busso, E., and O'Dowd, N. (2001). Finite element implementation of a generalised non-local rate-dependent crystallographic formulation for finite strains. *International Journal of Plasticity*, 17(4):601–640.

[280] Mendoza, R., Alkemper, J., and Voorhees, P. (2003). The morphological evolution of dendritic microstructures during coarsening. *Metallurgical and Materials Transactions A*, 34(3):481–489.

[281] Merriman, B., Bence, J. K., and Osher, S. J. (1994). Motion of multiple junctions: A level set approach. *Journal of Computational Physics*, 112(2):334–363.

[282] Metals, C. S. (2012). *China superalloys handbook*. Standards Press of China.

[283] Meyer, F. (1994). Topographic distance and watershed lines. *Signal Processing*, 38(1):113–125.

[284] Meyer, F. and Beucher, S. (1990). Morphological segmentation. *Journal of Visual Communication and Image Representation*, 1(1):21–46.

[285] Midgley, P. A. and Dunin-Borkowski, R. E. (2009). Electron tomography and holography in materials science. *Nature Materials*, 8(4):271–280.

[286] Mika, D. and Dawson, P. (1999). Polycrystal plasticity modeling of intracrystalline boundary textures. *Acta Materialia*, 47(4):1355–1369.

[287] Mika, D. P. and Dawson, P. R. (1998). Effects of grain interaction on deformation in polycrystals. *Materials Science and Engineering: A*, 257(1):62–76.

[288] Miodownik, M., Godfrey, A., Holm, E., and Hughes, D. (1999). On boundary misorientation distribution functions and how to incorporate them into three-dimensional models of microstructural evolution. *Acta Materialia*, 47(9):2661–2668.

[289] Miodownik, M. A. (2002). A review of microstructural computer models used to simulate grain growth and recrystallisation in aluminium alloys. *Journal of Light Metals*, 2(3):125–135.

[290] Miraglia, M., Dawson, P., and Leffers, T. (2007). On the influence of mechanical environment on the emergence of brass textures in fcc metals. *Acta Materialia*, 55(3):799–812.

[291] Mishchenko, Y. (2015). A fast algorithm for computation of discrete euclidean distance transform in three or more dimensions on vector processing architectures. *Signal, Image and Video Processing*, 9(1):19–27.

[292] Mitra, N. J. and Nguyen, A. (2003). Estimating surface normals in noisy point cloud data. In *Proceedings of the nineteenth annual symposium on Computational geometry*, pages 322–328.

[293] Miyazawa, Y., Briffod, F., Shiraiwa, T., and Enoki, M. (2019). Prediction of cyclic stress–strain property of steels by crystal plasticity simulations and machine learning. *Materials*, 12(22):3668.

[294] Moelans, N., Blanpain, B., and Wollants, P. (2008). An introduction to phase-field modeling of microstructure evolution. *Calphad*, 32(2):268–294.

[295] Moelans, N., Wendler, F., and Nestler, B. (2009). Comparative study of two phase-field models for grain growth. *Computational Materials Science*, 46(2):479–490.

[296] Mora, L. B., Gottstein, G., and Shvindlerman, L. (2008a). Three-dimensional grain growth: Analytical approaches and computer simulations. *Acta Materialia*, 56(20):5915–5926.

[297] Mora, L. B., Mohles, V., Shvindlerman, L., and Gottstein, G. (2008b). Effect of a finite quadruple junction mobility on grain microstructure evolution: Theory and simulation. *Acta Materialia*, 56(5):1151–1164.

[298] Morawiec, A. (2000). Method to calculate the grain boundary energy distribution over the space of macroscopic boundary parameters from the geometry of triple junctions. *Acta Materialia*, 48(13):3525–3532.

[299] Morawiec, A. (2004). Symmetry. In *Orientations and Rotations*, pages 93–114. Springer.

[300] Morfa, C. R., Farias, M. M. d., Morales, I. P. P., Navarra, E. O. I. d., and Valera, R. R. (2018). Virtual modeling of polycrystalline structures of materials using particle packing algorithms and laguerre cells. *Computational Particle Mechanics*, 5(2):213–226.

[301] Morgeneyer, T. F., Khadyko, M., Buljac, A., Helfen, L., Helfen, F. H., Benallal, A., Børvik, T., and Hopperstad, O. S. (2021). On crystallographic aspects of heterogeneous plastic flow during ductile tearing: 3d measurements and crystal plasticity simulations for aa7075-t651. *International Journal of Plasticity*, page 103028.

[302] Motaman, S. A. H. and Haase, C. (2021). The microstructural effects on the mechanical response of polycrystals: A comparative experimental-numerical study on conventionally and additively manufactured metallic materials. *International Journal of Plasticity*, 140:102941.

[303] Motaman, S. A. H., Kies, F., Köhnen, P., Létang, M., Lin, M., Molotnikov, A., and Haase, C. (2020a). Optimal design for metal additive manufacturing: An integrated computational materials engineering (icme) approach. *JOM*, 72(3):1092–1104.

[304] Motaman, S. A. H., Roters, F., and Haase, C. (2020b). Anisotropic polycrystal plasticity due to microstructural heterogeneity: a multi-scale experimental and numerical study on additively manufactured metallic materials. *Acta Materialia*, 185:340–369.

[305] Mughrabi, H. (1983). Dislocation wall and cell structures and long-range internal stresses in deformed metal crystals. *Acta Metallurgica*, 31(9):1367–1379.

[306] Mullins, W. W. (1957). Theory of thermal grooving. *Journal of Applied Physics*, 28(3):333–339.

[307] Musinski, W. D. and McDowell, D. L. (2016). Simulating the effect of grain boundaries on microstructurally small fatigue crack growth from a focused ion beam notch through a three-dimensional array of grains. *Acta Materialia*, 112:20–39.

[308] Mustapha, H., Chatterjee, S., Dimitrakopoulos, R., and Graf, T. (2013). Geologic heterogeneity recognition using discrete wavelet transformation for subsurface flow solute transport simulations. *Advances in Water Resources*, 54:22–37.

[309] Naderi, H., Fathianpour, N., and Tabaei, M. (2019a). Morphsim: A new multiple-point pattern-based unconditional simulation algorithm using morphological image processing tools. *Journal of Petroleum Science and Engineering*, 173:1417–1437.

[310] Naderi, S., Dean, J. S., and Zhang, M. (2019b). Three-dimensional virtual microstructure generation of porous polycrystalline ceramics. *Ceramics International*, 45(17):21647–21656.

[311] Nakashima, K., Nagai, T., and Kawasaki, K. (1989). Scaling behavior of two-dimensional domain growth: Computer simulation of vertex models. *Journal of Statistical Physics*, 57(3):759–787.

[312] Neal, F. B. and Russ, J. C. (2012). *Measuring shape*. CRC Press.

[313] Nes, E., Ryum, N., and Hunderi, O. (1985). On the zener drag. *Acta Metallurgica*, 33(1):11–22.

[314] Nestler, B. (2005). A 3d parallel simulator for crystal growth and solidification in complex alloy systems. *Journal of Crystal Growth*, 275(1-2):e273–e278.

[315] Nicholas, M. and Old, C. (1979). Liquid metal embrittlement. *Journal of Materials Science*, 14(1):1–18.

[316] Niezgoda, S. R., Turner, D. M., Fullwood, D. T., and Kalidindi, S. R. (2010). Optimized structure based representative volume element sets reflecting the ensemble-averaged 2-point statistics. *Acta Materialia*, 58(13):4432–4445.

[317] Nolze, G. and Hielscher, R. (2016). Orientations–perfectly colored. *Journal of Applied Crystallography*, 49(5):1786–1802.

[318] Nouri, N., Ziaei-Rad, V., and Ziaei-Rad, S. (2013). An approach for simulating microstructures of polycrystalline materials. *Springer-Verlag New York, Inc.*, 52(1):181–192.

[319] Nygårds, M. (2003). Number of grains necessary to homogenize elastic materials with cubic symmetry. *Mechanics of Materials*, 35(11):1049–1057.

[320] Orloff, J., Swanson, L., and Utlaut, M. (2003). *High resolution focused ion beams: FIB and its applications: Fib and its applications: the physics of liquid metal ion sources and ion optics and their application to focused ion beam technology*. Springer Science & Business Media.

[321] Orowan, E. (1934). Zur kristallplastizität. i. *Zeitschrift für Physik*, 89(9):605–613.

[322] Ozturk, D., Kotha, S., and Ghosh, S. (2021). An uncertainty quantification framework for multiscale parametrically homogenized constitutive models (phcms) of polycrystalline ti alloys. *Journal of the Mechanics and Physics of Solids*, 148:104294.

[323] Ozturk, D., Kotha, S., Pilchak, A. L., and Ghosh, S. (2019). Two-way multi-scaling for predicting fatigue crack nucleation in titanium alloys using parametrically homogenized constitutive models. *Journal of the Mechanics and Physics of Solids*, 128:181–207.

[324] Ozturk, T. and Rollett, A. D. (2018). Effect of microstructure on the elasto-viscoplastic deformation of dual phase titanium structures. *Computational Mechanics*, 61(1):55–70.

[325] Pandey, A. and Pokharel, R. (2021). Machine learning based surrogate modeling approach for mapping crystal deformation in three dimensions. *Scripta Materialia*, 193:1–5.

[326] Pantleon, W. (2008). Resolving the geometrically necessary dislocation content by conventional electron backscattering diffraction. *Scripta Materialia*, 58(11):994–997.

[327] Patala, S., Mason, J. K., and Schuh, C. A. (2012). Improved representations of misorientation information for grain boundary science and engineering. *Progress in Materials Science*, 57(8):1383–1425.

[328] Patala, S. and Schuh, C. A. (2011). A continuous and one-to-one coloring scheme for misorientations. *Acta Materialia*, 59(2):554–562.

[329] Paulson, N. H., Priddy, M. W., McDowell, D. L., and Kalidindi, S. R. (2017). Reduced-order structure-property linkages for polycrystalline microstructures based on 2-point statistics. *Acta Materialia*, 129:428–438.

[330] Paulson, N. H., Priddy, M. W., McDowell, D. L., and Kalidindi, S. R. (2018). Data-driven reduced-order models for rank-ordering the high cycle fatigue performance of polycrystalline microstructures. *Materials & Design*, 154:170–183.

[331] Paulson, N. H., Priddy, M. W., McDowell, D. L., and Kalidindi, S. R. (2019). Reduced-order microstructure-sensitive protocols to rank-order the transition fatigue resistance of polycrystalline microstructures. *International Journal of Fatigue*, 119:1–10.

[332] Pavlyk, V. and Dilthey, U. (2003). Simulation of weld solidification microstructure and its coupling to the macroscopic heat and fluid flow modelling. *Modelling and Simulation in Materials Science and Engineering*, 12(1):S33.

[333] Peczak, P. and Luton, M. (1993). The effect of nucleation models on dynamic recrystallization i. homogeneous stored energy distribution. *Philosophical Magazine B*, 68(1):115–144.

[334] Peczak, P. and Luton, M. (1994). The effect of nucleation models on dynamic recrystallization ii. heterogeneous stored-energy distribution. *Philosophical Magazine B*, 70(4):817–849.

[335] Pereiro-Lopez, E., Ludwig, W., Bellet, D., Cloetens, P., and Lemaignan, C. (2005). Direct evidence of nanometric invasionlike grain boundary penetration in the al/ga system. *Physical Review Letters*, 95(21):215501.

[336] Pinz, M., Weber, G., and Ghosh, S. (2019). Generating 3d virtual microstructures and statistically equivalent rves for subgranular gamma-gamma'microstructures of nickel-based superalloys. *Computational Materials Science*, 167:198–214.

[337] Pinz, M., Weber, G., Lenthe, W., Uchic, M., Pollock, T., and Ghosh, S. (2018). Microstructure and property based statistically equivalent rves for intragranular γ-γ'microstructures of ni-based superalloys. *Acta Materialia*, 157:245–258.

[338] Plimpton, S., Corbett Battaile, M. C., Holm, L., Thompson, A., Tikare, V., Wagner, G., Zhou, X., Cardona, C. G., and Slepoy, A. (2009). Crossing the mesoscale no-man's land via parallel kinetic monte carlo.

[339] Pluim, J. P., Maintz, J. A., and Viergever, M. A. (2003). Mutual-information-based registration of medical images: a survey. *IEEE Transactions on Medical Imaging*, 22(8):986–1004.

[340] Pokharel, R., Pandey, A., and Scheinker, A. (2021). Physics-informed data-driven surrogate modeling for full-field 3d microstructure and micromechanical field evolution of polycrystalline materials. *JOM*, 73(11):3371–3382.

[341] Popat, K. and Picard, R. W. (1993). Novel cluster-based probability model for texture synthesis, classification, and compression. In *Visual Communications and Image Processing'93*, volume 2094, pages 756–768. SPIE.

[342] Popova, E., Staraselski, Y., Brahme, A., Mishra, R., and Inal, K. (2015). Coupled crystal plasticity–probabilistic cellular automata approach to model dynamic recrystallization in magnesium alloys. *International Journal of Plasticity*, 66:85–102.

[343] Pospiech, J., Lücke, K., and Sztwiertnia, K. (1993). Orientation distribution and orientation correlation functions for description of microstructures. *Acta Metallurgica et Materialia*, 41(1):305–321.

[344] Poulsen, H. F. (2004). *Three-dimensional X-ray diffraction microscopy: mapping polycrystals and their dynamics*, volume 205. Springer Science & Business Media.

[345] Poulsen, H. F. (2012). An introduction to three-dimensional x-ray diffraction microscopy. *Journal of Applied Crystallography*, 45(6):1084–1097.

[346] Poulsen, H. F. and Fu, X. (2003). Generation of grain maps by an algebraic reconstruction technique. *Journal of Applied Crystallography*, 36(4):1062–1068.

[347] Poulsen, H. F., Nielsen, S. F., Lauridsen, E. M., Schmidt, S., Suter, R., Lienert, U., Margulies, L., Lorentzen, T., and Juul Jensen, D. (2001). Three-dimensional maps of grain boundaries and the stress state of individual grains in polycrystals and powders. *Journal of Applied Crystallography*, 34(6):751–756.

[348] Provatas, N. and Elder, K. (2011). *Phase-field methods in materials science and engineering*. John Wiley & Sons.

[349] Przybyla, C. P., Musinski, W. D., Castelluccio, G. M., and McDowell, D. L. (2013). Microstructure-sensitive hcf and vhcf simulations. *International Journal of Fatigue*, 57:9–27.

[350] Qin, R. and Bhadeshia, H. (2010). Phase field method. *Materials Science and Technology*, 26(7):803–811.

[351] Quey, R., Dawson, P., and Barbe, F. (2011). Large-scale 3d random polycrystals for the finite element method: Generation, meshing and remeshing. *Computer Methods in Applied Mechanics and Engineering*, 200(17-20):1729–1745.

[352] Quey, R. and Renversade, L. (2018). Optimal polyhedral description of 3d polycrystals: Method and application to statistical and synchrotron x-ray diffraction data. *Computer Methods in Applied Mechanics and Engineering*, 330:308–333.

[353] Raabe, D. (1999). Introduction of a scalable three-dimensional cellular automaton with a probabilistic switching rule for the discrete mesoscale simulation of recrystallization phenomena. *Philosophical Magazine A*, 79(10):2339–2358.

[354] Raabe, D. (2000). Scaling monte carlo kinetics of the potts model using rate theory. *Acta Materialia*, 48(7):1617–1628.

[355] Raabe, D. (2002). Cellular automata in materials science with particular reference to recrystallization simulation. *Annual Review of Materials Research*, 32(1):53–76.

[356] Raabe, D., Roters, F., Barlat, F., and Chen, L.-Q. (2004). *Continuum scale simulation of engineering materials: fundamentals-microstructures-process applications*. John Wiley & Sons.

[357] Raghavan, N., Stump, B. C., Fernandez-Zelaia, P., Kirka, M. M., and Simunovic, S. (2021). Influence of geometry on columnar to equiaxed transition during electron beam powder bed fusion of in718. *Additive Manufacturing*, 47:102209.

[358] Ragnemalm, I. (1992). Fast erosion and dilation by contour processing and thresholding of distance maps. *Pattern Recognition Letters*, 13(3):161–166.

[359] Randle, V. (2010). Role of grain boundary plane in grain boundary engineering. *Materials Science and Technology*, 26(7):774–780.

[360] Randle, V. and Engler, O. (2000). Introduction to texture analysis: Macrotexture. *Microtexture and Orientation Mapping (Gordon Breach, 2000)*.

[361] Rappaz, M. and Gandin, C.-A. (1993). Probabilistic modelling of microstructure formation in solidification processes. *Acta Metallurgica et Materialia*, 41(2):345–360.

[362] Read, W. T. and Shockley, W. (1950). Dislocation models of crystal grain boundaries. *Physical Review*, 78(3):275.

[363] Reddy, K., Adlakha, I., Gupta, S., and Roychowdhury, S. (2022). Crystal elasticity simulations of polycrystalline material using rank-one approximation. *Integrating Materials and Manufacturing Innovation*, 11(1):139–157.

[364] Reid, A. C., Langer, S. A., Lua, R. C., Coffman, V. R., Haan, S.-I., and García, R. E. (2008). Image-based finite element mesh construction for material microstructures. *Computational Materials Science*, 43(4):989–999.

[365] Ritz, H. and Dawson, P. (2008). Sensitivity to grain discretization of the simulated crystal stress distributions in fcc polycrystals. *Modelling and Simulation in Materials Science and Engineering*, 17(1):015001.

[366] Roberts, W. and Ahlblom, B. (1978). A nucleation criterion for dynamic recrystallization during hot working. *Acta Metallurgica*, 26(5):801–813.

[367] Rohrer, G., Li, J., Lee, S., Rollett, A., Groeber, M., and Uchic, M. (2010). Deriving grain boundary character distributions and relative grain boundary energies from three-dimensional ebsd data. *Materials Science and Technology*, 26(6):661–669.

[368] Rohrer, G. S. (2011). Grain boundary energy anisotropy: a review. *Journal of Materials Science*, 46(18):5881–5895.

[369] Rohrer, G. S., Saylor, D. M., El-Dasher, B., Adams, B. L., Rollett, A. D., and Wynblatt, P. (2004). The distribution of internal interfaces in polycrystals. *Z. Metallkd*, 95(4):197–214.

[370] Rollett, A. (1997). Overview of modeling and simulation of recrystallization. *Progress in Materials Science*, 42(1-4):79–99.

[371] Rollett, A. and Raabe, D. (2001). A hybrid model for mesoscopic simulation of recrystallization. *Computational Materials Science*, 21(1):69–78.

[372] Rollett, A. D., Lee, S.-B., Campman, R., and Rohrer, G. (2007). Three-dimensional characterization of microstructure by electron back-scatter diffraction. *Annual Review of Materials Research*, 37:627–658.

[373] Rollett, A. D. and Manohar, P. (2004). The monte carlo method. *Continuum Scale Simulation of Engineering Materials*, pages 77–114.

[374] Roters, F., Eisenlohr, P., Hantcherli, L., Tjahjanto, D. D., Bieler, T. R., and Raabe, D. (2010). Overview of constitutive laws, kinematics, homogenization and multiscale methods in crystal plasticity finite-element modeling: Theory, experiments, applications. *Acta Materialia*, 58(4):1152–1211.

[375] Roucoules, C., Pietrzyk, M., and Hodgson, P. (2003). Analysis of work hardening and recrystallization during the hot working of steel using a statistically based internal variable model. *Materials Science and Engineering: A*, 339(1-2):1–9.

[376] Rowenhorst, D. J., Nguyen, L., Murphy-Leonard, A. D., and Fonda, R. W. (2020). Characterization of microstructure in additively manufactured 316l using automated serial sectioning. *Current Opinion in Solid State and Materials Science*, 24(3):100819.

[377] Russ, J. C. (2006). *The image processing handbook*. CRC press.

[378] Russ, J. C., Matey, J. R., Mallinckrodt, A. J., and McKay, S. (1994). The image processing handbook. *Computers in Physics*, 8(2):177–178.

[379] Rycroft, C. (2009). Voro++: A three-dimensional voronoi cell library in c++. Technical report, Lawrence Berkeley National Lab.(LBNL), Berkeley, CA (United States).

[380] Salehi, M. S. and Serajzadeh, S. (2012). Simulation of static recrystallization in non-isothermal annealing using a coupled cellular automata and finite element model. *Computational Materials Science*, 53(1):145–152.

[381] Saluja, R. S., Narayanan, R. G., and Das, S. (2012). Cellular automata finite element (cafe) model to predict the forming of friction stir welded blanks. *Computational Materials Science*, 58:87–100.

[382] Sarma, G. B. and Dawson, P. R. (1996a). Effects of interactions among crystals on the inhomogeneous deformations of polycrystals. *Acta Materialia*, 44(5):1937–1953.

[383] Sarma, G. B. and Dawson, P. R. (1996b). Texture predictions using a polycrystal plasticity model incorporating neighbor interactions. *International journal of plasticity*, 12(8):1023–1054.

[384] Saylor, D. M., Fridy, J., El-Dasher, B. S., Jung, K.-Y., and Rollett, A. D. (2004). Statistically representative three-dimensional microstructures based on orthogonal observation sections. *Metallurgical and Materials Transactions A*, 35(7):1969–1979.

[385] Saylor, D. M., Morawiec, A., Adams, B. L., and Rohrer, G. S. (2000). Misorientation dependence of the grain boundary energy in magnesia. *Interface Science*, 8(2):131–140.

[386] Saylor, D. M., Morawiec, A., and Rohrer, G. S. (2003). The relative free energies of grain boundaries in magnesia as a function of five macroscopic parameters. *Acta Materialia*, 51(13):3675–3686.

[387] Saylor, D. M. and Rohrer, G. S. (1999). Measuring the influence of grain-boundary misorientation on thermal groove geometry in ceramic polycrystals. *Journal of the American Ceramic Society*, 82(6):1529–1536.

[388] Schmid, B. (2010). *Computational tools for the segmentation and registration of confocal brain images of Drosophila melanogaster*. PhD thesis, Universität Würzburg.

[389] Schmidt, S. (2014). Grainspotter: a fast and robust polycrystalline indexing algorithm. *Journal of Applied Crystallography*, 47(1):276–284.

[390] Schmidt, S., Olsen, U. L., Poulsen, H. F., Sørensen, H. O., Lauridsen, E. M., Margulies, L., Maurice, C., and Jensen, D. J. (2008). Direct observation of 3-d grain growth in al–0.1% mn. *Scripta Materialia*, 59(5):491–494.

[391] Schroeder, W. J., Zarge, J. A., and Lorensen, W. E. (1992). Decimation of triangle meshes. In *Proceedings of the 19th annual conference on Computer graphics and interactive techniques*, pages 65–70.

[392] Schwartz, A. J., Kumar, M., Adams, B. L., and Field, D. P. (2009). *Electron backscatter diffraction in materials science*, volume 2. Springer.

[393] Segurado, J., Lebensohn, R. A., and LLorca, J. (2018). Computational homogenization of polycrystals. *Advances in Applied Mechanics*, 51:1–114.

[394] Sengodan, G. A. (2021). Prediction of two-phase composite microstructure properties through deep learning of reduced dimensional structure-response data. *Composites Part B: Engineering*, 225:109282.

[395] Shen, Y., Gao, T., Tian, X., Chen, X., Xiao, C., and Lu, T. (2015). Constructing three-dimensional (3d) nanocrystalline models of li4sio4 for numerical modeling and simulation. *Scientific Reports*, 5(1):1–9.

[396] Shockley, W. (1952). *Imperfections in Nearly Perfect Crystals: Symposium Held at Pocono Manor, October 12-14, 1950*. Wiley.

[397] Shu, C., He, J., Xue, G., and Xie, C. (2022). Grain knowledge graph representation learning: A new paradigm for microstructure-property prediction. *Crystals*, 12(2):280.

[398] Simmons, J., Chuang, P., Comer, M., Spowart, J., Uchic, M., and De Graef, M. (2008). Application and further development of advanced image processing algorithms for automated analysis of serial section image data. *Modelling and Simulation in Materials Science and Engineering*, 17(2):025002.

[399] Smith, C. S. (1948). Grains, phases, and interfaces: An introduction of microstructure. *Transactions of the Metallurgical Society of AIME*, 175:15–51.

[400] Snigirev, A., Snigireva, I., Kohn, V., Kuznetsov, S., and Schelokov, I. (1995). On the possibilities of x-ray phase contrast microimaging by coherent high-energy synchrotron radiation. *Review of Scientific Instruments*, 66(12):5486–5492.

[401] Soille, P. (2013). *Morphological image analysis: principles and applications*. Springer Science & Business Media.

[402] Spanos, G., Rowenhorst, D., Lewis, A., and Geltmacher, A. (2008). Combining serial sectioning, ebsd analysis, and image-based finite element modeling. *Mrs Bulletin*, 33(6):597–602.

[403] Spittle, J. and Brown, S. (1995). A cellular automaton model of steady-state columnar-dendritic growth in binary alloys. *Journal of Materials Science*, 30(16):3989–3994.

[404] Spowart, J. E. (2006). Automated serial sectioning for 3-d analysis of microstructures. *Scripta Materialia*, 55(1):5–10.

[405] Spowart, J. E., Mullens, H. E., and Puchala, B. T. (2003). Collecting and analyzing microstructures in three dimensions: a fully automated approach. *Jom*, 55(10):35–37.

[406] Srivastava, A., Ghassemi-Armaki, H., Sung, H., Chen, P., Kumar, S., and Bower, A. F. (2015). Micromechanics of plastic deformation and phase transformation in a three-phase trip-assisted advanced high strength steel: Experiments and modeling. *Journal of the Mechanics and Physics of Solids*, 78:46–69.

[407] St-Pierre, L., Héripré, E., Dexet, M., Crépin, J., Bertolino, G., and Bilger, N. (2008). 3d simulations of microstructure and comparison with experimental microstructure coming from oim analysis. *International Journal of Plasticity*, 24(9):1516–1532.

[408] Staraselski, Y., Brahme, A., Mishra, R., and Inal, K. (2014). Reconstruction of the 3d representative volume element from the generalized two-point correlation function. *Modelling and Simulation in Materials Science and Engineering*, 23(1):015007.

[409] Steinbach, I. (2009). Phase-field models in materials science. *Modelling and Simulation in Materials Science and Engineering*, 17(7):073001.

[410] Steinbach, I., Pezzolla, F., Nestler, B., Seeßelberg, M., Prieler, R., Schmitz, G. J., and Rezende, J. L. (1996). A phase field concept for multiphase systems. *Physica D: Nonlinear Phenomena*, 94(3):135–147.

[411] Stopka, K. S., Yaghoobi, M., Allison, J. E., and McDowell, D. L. (2022). Simulated effects of sample size and grain neighborhood on the modeling of extreme value fatigue response. *Acta Materialia*, 224:117524.

[412] Sundararaghavan, V. (2014). Reconstruction of three-dimensional anisotropic microstructures from two-dimensional micrographs imaged on orthogonal planes. *Integrating Materials and Manufacturing Innovation*, 3(1):240–250.

[413] Sundararaghavan, V. and Zabaras, N. (2004). A dynamic material library for the representation of single-phase polyhedral microstructures. *Acta Materialia*, 52(14):4111–4119.

[414] Sundararaghavan, V. and Zabaras, N. (2005). Classification and reconstruction of three-dimensional microstructures using support vector machines. *Computational Materials Science*, 32(2):223–239.

[415] Suter, R., Hennessy, D., Xiao, C., and Lienert, U. (2006). Forward modeling method for microstructure reconstruction using x-ray diffraction microscopy: Single-crystal verification. *Review of Scientific Instruments*, 77(12):123905.

[416] Suzudo, T. and Kaburaki, H. (2009). An evolutional approach to the numerical construction of polycrystalline structures using the voronoi tessellation. *Physics Letters A*, 373(48):4484–4488.

[417] Syha, M. and Weygand, D. (2009). A generalized vertex dynamics model for grain growth in three dimensions. *Modelling and Simulation in Materials Science and Engineering*, 18(1):015010.

[418] Tahmasebi, P., Hezarkhani, A., and Sahimi, M. (2012). Multiple-point geostatistical modeling based on the cross-correlation functions. *Computational Geosciences*, 16(3):779–797.

[419] Tahmasebi, P. and Sahimi, M. (2013). Cross-correlation function for accurate reconstruction of heterogeneous media. *Physical Review Letters*, 110(7):078002.

[420] Tahmasebi, P. and Sahimi, M. (2016). Enhancing multiple-point geostatistical modeling: 2. iterative simulation and multiple distance function. *Water Resources Research*, 52(3):2099–2122.

[421] Tahmasebi, P., Sahimi, M., and Caers, J. (2014). Ms-ccsim: accelerating pattern-based geostatistical simulation of categorical variables using a multi-scale search in fourier space. *Computers & Geosciences*, 67:75–88.

[422] Tallman, A. E., Stopka, K. S., Swiler, L. P., Wang, Y., Kalidindi, S. R., and McDowell, D. L. (2019). Gaussian-process-driven adaptive sampling for reduced-order modeling of texture effects in polycrystalline alpha-ti. *JOM*, 71(8):2646–2656.

[423] Tang, Y., Xiong, Y., Park, S.-i., and Rosen, D. W. (2020). Universal material template for heterogeneous objects with applications to additive manufacturing. *Computer-Aided Design*, 129:102929.

[424] Teferra, K. and Graham-Brady, L. (2015). Tessellation growth models for polycrystalline microstructures. *Computational Materials Science*, 102:57–67.

[425] Tiaden, J., Nestler, B., Diepers, H.-J., and Steinbach, I. (1998). The multiphase-field model with an integrated concept for modelling solute diffusion. *Physica D: Nonlinear Phenomena*, 115(1-2):73–86.

[426] Tikare, V., Holm, E., Fan, D., and Chen, L.-Q. (1998). Comparison of phase-field and potts models for coarsening processes. *Acta Materialia*, 47(1):363–371.

[427] Tiley, J., Searles, T., Lee, E., Kar, S., Banerjee, R., Russ, J., and Fraser, H. (2004). Quantification of microstructural features in α/β titanium alloys. *Materials Science and Engineering: A*, 372(1-2):191–198.

[428] Todinov, M. (2000). On some limitations of the johnson–mehl–avrami–kolmogorov equation. *Acta Materialia*, 48(17):4217–4224.

[429] Torquato, S. and Haslach Jr, H. (2002). Random heterogeneous materials: microstructure and macroscopic properties. *Applied Mechanics Reviews*, 55(4):B62–B63.

[430] Tran, A. and Wildey, T. (2021). Solving stochastic inverse problems for property–structure linkages using data-consistent inversion and machine learning. *JOM*, 73(1):72–89.

[431] Tu, X., Shahba, A., Shen, J., and Ghosh, S. (2019). Microstructure and property based statistically equivalent rves for polycrystalline-polyphase aluminum alloys. *International Journal of Plasticity*, 115:268–292.

[432] Tucker, J. C., Chan, L. H., Rohrer, G. S., Groeber, M. A., and Rollett, A. D. (2012). Tail departure of log-normal grain size distributions in synthetic three-dimensional microstructures. *Metallurgical and Materials Transactions A*, 43(8):2810–2822.

[433] Uchic, M. D., Groeber, M. A., Dimiduk, D. M., and Simmons, J. (2006). 3d microstructural characterization of nickel superalloys via serial-sectioning using a dual beam fib-sem. *Scripta Materialia*, 55(1):23–28.

[434] Uchic, M. D., Holzer, L., Inkson, B. J., Principe, E. L., and Munroe, P. (2007). Three-dimensional microstructural characterization using focused ion beam tomography. *MRS Bulletin*, 32(5):408–416.

[435] Ullah, A., Liu, G., Luan, J., Li, W., ur Rahman, M., and Ali, M. (2014). Three-dimensional visualization and quantitative characterization of grains in polycrystalline iron. *Materials Characterization*, 91:65–75.

[436] Ullah, A., Liu, G., Wang, H., Khan, M., Khan, D. F., and Luan, J. (2013). Optimal approach of three-dimensional microstructure reconstructions and visualizations. *Materials Express*, 3(2):109–118.

[437] Van Houtte, P., Delannay, L., and Kalidindi, S. (2002). Comparison of two grain interaction models for polycrystal plasticity and deformation texture prediction. *International Journal of Plasticity*, 18(3):359–377.

[438] Venkatraman, A., de Oca Zapiain, D. M., Lim, H., and Kalidindi, S. R. (2021). Texture-sensitive prediction of micro-spring performance using gaussian process models calibrated to finite element simulations. *Materials & Design*, 197:109198.

[439] Vieira, R. T., de Bortoli, D., de Carvalho, M. V., and Pires, F. A. (2019). The role of elastic anisotropy on the macroscopic constitutive response and yield onset of cubic oligo-and polycrystals. *International Journal of Plasticity*, 121:153–200.

[440] Vincent, L. and Soille, P. (1991). Watersheds in digital spaces: an efficient algorithm based on immersion simulations. *IEEE Transactions on Pattern Analysis & Machine Intelligence*, 13(06):583–598.

[441] Wall, M. A., Schwartz, A. J., and Nguyen, L. (2001). A high-resolution serial sectioning specimen preparation technique for application to electron backscatter diffraction. *Ultramicroscopy*, 88(2):73–83.

[442] Wang, W., Lee, P. D., and Mclean, M. (2003). A model of solidification microstructures in nickel-based superalloys: predicting primary dendrite spacing selection. *Acta Materialia*, 51(10):2971–2987.

[443] Wang, W., Xu, T., Zhong, J., Guan, K., Shang, Y., and Zhang, X. (2022). Specimen size effect on evaluation of strength properties of 3cr1mov and incoloy 800h using small punch test. *Materials Science and Engineering: A*, 832:142400.

[444] Wang, Y. M., Voisin, T., McKeown, J. T., Ye, J., Calta, N. P., Li, Z., Zeng, Z., Zhang, Y., Chen, W., Roehling, T. T., et al. (2018). Additively manufactured hierarchical stainless steels with high strength and ductility. *Nature Materials*, 17(1):63–71.

[445] Warren, J. A., Kobayashi, R., Lobkovsky, A. E., and Carter, W. C. (2003). Extending phase field models of solidification to polycrystalline materials. *Acta Materialia*, 51(20):6035–6058.

[446] Watanabe, T. (2011). Grain boundary engineering: historical perspective and future prospects. *Journal of Materials Science*, 46(12):4095–4115.

[447] Weber, G., Pinz, M., and Ghosh, S. (2020). Machine learning-aided parametrically homogenized crystal plasticity model (phcpm) for single crystal ni-based superalloys. *JOM*, 72(12):4404–4419.

[448] Wei, L.-Y. and Levoy, M. (2000). Fast texture synthesis using tree-structured vector quantization. In *Proceedings of the 27th annual conference on Computer graphics and interactive techniques*, pages 479–488.

[449] Weins, M., Chalmers, B., Gleiter, H., and Ashby, M. (1969). Structure of high angle grain boundaries. *Scripta Metallurgica*, 3(8):601–603.

[450] Weitkamp, T., Diaz, A., David, C., Pfeiffer, F., Stampanoni, M., Cloetens, P., and Ziegler, E. (2005). X-ray phase imaging with a grating interferometer. *Optics Express*, 13(16):6296–6304.

[451] Wen, B. and Zabaras, N. (2012). A multiscale approach for model reduction of random microstructures. *Computational Materials Science*, 63:269–285.

[452] Weygand, D., Brechet, Y., and Lepinoux, J. (1998). A vertex dynamics simulation of grain growth in two dimensions. *Philosophical Magazine B*, 78(4):329–352.

[453] Weygand, D., Brechet, Y., and Lepinoux, J. (2001). A vertex simulation of grain growth in 2d and 3d. *Advanced Engineering Materials*, 3(1-2):67–71.

[454] Weygand, D., Bréchet, Y., Lépinoux, J., and Gust, W. (1999). Three-dimensional grain growth: a vertex dynamics simulation. *Philosophical Magazine B*, 79(5):703–716.

[455] Wolf, D. (1989). A read-shockley model for high-angle grain boundaries. *Scripta Metallurgica*, 23(10):1713–1718.

[456] Wolf, D. (1990a). Correlation between structure, energy, and ideal cleavage fracture for symmetrical grain boundaries in fcc metals. *Journal of Materials Research*, 5(8):1708–1730.

[457] Wolf, D. (1990b). Structure-energy correlation for grain boundaries in fcc metals—iii. symmetrical tilt boundaries. *Acta Metallurgica et Materialia*, 38(5):781–790.

[458] Wolf, D. (1990c). Structure-energy correlation for grain boundaries in fcc metals—iv. asymmetrical twist (general) boundaries. *Acta Metallurgica et Materialia*, 38(5):791–798.

[459] Wong, L. N. Y. and Zhang, Y. (2018). An extended grain-based model for characterizing crystalline materials: An example of marble. *Advanced Theory and Simulations*, 1(8):1800039.

[460] Wright, S. and Larsen, R. (2002). Extracting twins from orientation imaging microscopy scan data. *Journal of Microscopy*, 205(3):245–252.

[461] Xie, C., Pan, Z., and Shu, C. (2022). Microstructure representation knowledge graph to explore the twinning formation. *Crystals*, 12(4):466.

[462] Yaghoobi, M., Stopka, K. S., Lakshmanan, A., Sundararaghavan, V., Allison, J. E., and McDowell, D. L. (2021). Prisms-fatigue computational framework for fatigue analysis in polycrystalline metals and alloys. *npj Computational Materials*, 7(1):1–12.

[463] Yamanaka, A., Kamijyo, R., Koenuma, K., Watanabe, I., and Kuwabara, T. (2020). Deep neural network approach to estimate biaxial stress-strain curves of sheet metals. *Materials & Design*, 195:108970.

[464] Yang, L., Hou, W., Cui, C., and Cui, J. (2016). Gosim: a multi-scale iterative multiple-point statistics algorithm with global optimization. *Computers & Geosciences*, 89:57–70.

[465] Yazdipour, N., Davies, C. H., and Hodgson, P. D. (2008). Microstructural modeling of dynamic recrystallization using irregular cellular automata. *Computational Materials Science*, 44(2):566–576.

[466] Yuan, M., Paradiso, S., Meredig, B., and Niezgoda, S. R. (2018). Machine learning–based reduce order crystal plasticity modeling for icme applications. *Integrating Materials and Manufacturing Innovation*, 7(4):214–230.

[467] Zaefferer, S., Wright, S., and Raabe, D. (2008). Three-dimensional orientation microscopy in a focused ion beam–scanning electron microscope: A new dimension of microstructure characterization. *Metallurgical and Materials Transactions A*, 39(2):374–389.

[468] Zeghadi, A., N'guyen, F., Forest, S., Gourgues, A.-F., and Bouaziz, O. (2007). Ensemble averaging stress–strain fields in polycrystalline aggregates with a constrained surface microstructure–part 1: Anisotropic elastic behaviour. *Philosophical Magazine*, 87(8-9):1401–1424.

[469] Zeng, X., Zhang, C., Zhu, W., Zhu, M., Wang, Y., and Zhang, X. (2022). Quantitative characterization of short fatigue crack and grain boundary interaction behavior in zirconium. *International Journal of Fatigue*, 161:106894.

[470] Zhang, C., Enomoto, M., Suzuki, A., and Ishimaru, T. (2004). Characterization of three-dimensional grain structure in polycrystalline iron by serial sectioning. *Metallurgical and Materials Transactions A*, 35(7):1927–1933.

[471] Zhang, M., Zhang, J., and McDowell, D. (2007). Microstructure-based crystal plasticity modeling of cyclic deformation of ti–6al–4v. *International Journal of Plasticity*, 23(8):1328–1348.

[472] Zhang, P., Balint, D., and Lin, J. (2011). An integrated scheme for crystal plasticity analysis: Virtual grain structure generation. *Computational Materials Science*, 50(10):2854–2864.

[473] Zhang, P., Karimpour, M., Balint, D., and Lin, J. (2012). Three-dimensional virtual grain structure generation with grain size control. *Mechanics of Materials*, 55:89–101.

[474] Zhang, Z., Wang, Y., Ge, P., and Wu, T. (2022). A review on modelling and simulation of laser additive manufacturing: heat transfer, microstructure evolutions and mechanical properties. *Coatings*, 12(9):1277.

[475] Zhao, J. and Adams, B. (1988). Definition of an asymmetric domain for intercrystalline misorientation in cubic materials in the space of euler angles. *Acta Crystallographica Section A: Foundations of Crystallography*, 44(3):326–336.

[476] Zheng, C. and Raabe, D. (2013). Interaction between recrystallization and phase transformation during intercritical annealing in a cold-rolled dual-phase steel: A cellular automaton model. *Acta Materialia*, 61(14):5504–5517.

[477] Zheng, C., Xiao, N., Li, D., and Li, Y. (2008). Microstructure prediction of the austenite recrystallization during multi-pass steel strip hot rolling: A cellular automaton modeling. *Computational Materials Science*, 44(2):507–514.

[478] Zhong, X., Rowenhorst, D. J., Beladi, H., and Rohrer, G. S. (2017). The five-parameter grain boundary curvature distribution in an austenitic and ferritic steel. *Acta Materialia*, 123:136–145.

[479] Zhu, M. and Hong, C. (2002). A three dimensional modified cellular automaton model for the prediction of solidification microstructures. *ISIJ International*, 42(5):520–526.

[480] Zhu, S. C., Wu, Y., and Mumford, D. (1998). Filters, random fields and maximum entropy (frame): Towards a unified theory for texture modeling. *International Journal of Computer Vision*, 27(2):107–126.